Fabrication and Evaluation of $In_{0.52}Al_{0.48}As/In_{0.53}Ga_{0.47}As/InP$ Quantum Cascade Lasers

Submitted for the degree of

Doctor of Philosophy

to the

Faculty of Engineering,

University of Glasgow

by

Corrie David Farmer

September 2000

Abstract

InP-based quantum cascade (QC) lasers were fabricated following the design reported by Faist *et al.*[1] with the initial aim of applying them in gas sensing applications. The lasers were characterised by our collaborators, Cockburn *et al.*[2] Unfortunately, the performance of our QC lasers (QCLs) did not live up to expectations, and the gas sensing objectives became replaced with resolving the issues of their poor performance. This was achieved through a mixture of laser fabrication, characterisation, and optical and thermal waveguide modelling. The devices fabricated included mesa-etched QCLs, shallow-etched QCLs, and novel native-oxide defined QCLs.

2D thermal modelling using a commercial finite element modelling package was carried out to solve the 2D non-linear thermal diffusion equation for all of the structures listed above, as well as for InP-clad and buried heterostructure configurations. The temperature elevations, distributions and heat flow vectors were calculated under high, but not unrealistic thermal power generation in the active waveguide core. The relative effectiveness at dissipating heat was judged using these results. The modelling indicated the presence of high temperatures and thermal gradients across the active waveguide core under continuous wave (CW) operation. The thermal resistance derived through the use of the thermal modelling agreed very well with that calculated by Faist *et al.*[1] from experimental data.

The optical modelling, which was instrumental in resolving the anomalous behaviour of our QC lasers, comprised of two parts. First, modelling of the dielectric permittivity gave values of n and α for InP, $In_{0.52}Al_{0.48}As$ and $In_{0.53}Ga_{0.47}As$ as a function of the free-carrier density and wavelength. The calculations were made using single and multiple-oscillator models with a free-carrier contribution in the form of a classical Drude expression. The dependencies of the electron mass and electron mobility on the free electron density were taken into account in the calculations. These values were used to perform 2D optical modelling of the waveguide using a commercial, fully vectorial waveguide mode solver. This yielded the effective index, confinement factor, facet reflectivity, waveguide loss and far-field distribution for each mode. These, in turn, were used to calculate the threshold gain for each mode. Perhaps the most important findings were the prediction of the existence of higher order transverse modes, that these modes can have low values of g_{th} (comparable or better than that of the fundamental mode of the waveguide) and that the collection efficiency will vary dramatically from mode to mode. The modelling also indicated that the performance of the QCLs would suffer greatly with an increase in the InP substrate doping level, even just from 1×10^{18} cm^{-3} to 3×10^{18} cm^{-3}.

Subsequent far-field measurements on the mesa-etched QC lasers confirmed the lasing of higher order modes and more importantly, dramatic changes in the far-field distributions with current. Measurement of the threshold current density gave the waveguide losses ~ 30 cm^{-1} which was subsequently traced to an excessive doping level in the substrate.

Novel design and fabrication of QC lasers was demonstrated with the planar selective wet oxidation (PSWOX) QC laser. Despite the high waveguide losses arising from the substrate, the PSWOX QCLs still performed very well. Optically they were far superior to our mesa-etched QC lasers, possessing an output beam with a very low divergence and whose far-field profile was stable with increasing drive current. The lasers' ability to dissipate heat also appeared to be enhanced over its counterparts, as demonstrated by its high characteristic temperature T_0 (~142 K). However, this particular structure was let down by the very poor electrical confinement which led to substantial threshold currents.

[1] J. Faist, F. Capasso, C. Sirtori, D. L. Sivco, J. N. Baillargeon, A. L. Hutchinson, S. G. Chu, A. Y. Cho, 'High power mid-infrared (λ~5 μm) quantum cascade lasers operating above room temperature', *Appl. Phys. Lett.* **68** (26), 24 June 1996.

[2]J. W. Cockburn, P. T. Keightley, L. R. Wilson and D. A. Carder

Acknowledgements

Many thanks go Prof. Charles N. Ironside for his supervision and ever-positive viewpoint. Also many thanks go to Dr. Jane Magill as my second supervisor. Prof. Colin R. Stanley and Dr. Adam Boyd for their excellence in MBE growth and encouragement. Thanks also to my colleagues Michel Garcia and Jeremy Green.

A big thank you to Dr. John Cockburn's and his group including Dr. Luke Wilson, Peter Keightley and Damian A. Carder in the Dept. of Physics and Astronomy at the University of Sheffield for their large contribution to this work.

Special thanks to all the other postgraduates, postdocs, research assistants and academics for sharing with me their vast knowledge and for their invaluable support.

There are so many technicians to thank for their help and their expertise. Many thanks go to all of them in the cleanrooms, Dry Etch, Ultra Small Structures Laboratory, Mechanical and Electrical workshops. The Department of Electronics & Electrical Engineering has seen so many people come and go. It has been a pleasure and an experience to have worked and interact with them all. I wish all of the very best in the future.

Outside the Dept. thanks must go to Claire Gmachl, Bell Labs. and Jerome Faist, Uni. of Neuchâtel for their ever-rapid replies giving technical advice and encouragement - thanks for putting up with my questions. Also to Olga Blum of Sandia Labs. for her help.

Thanks to Edinburgh Sensors for their support through a CASE studentship.

Last, and not least, my love and thanks go to my family and friends who have kept me going. Above all, I dedicate this thesis and my love to Lesley - thanks for keeping me sane with your insanity.

Table of Contents

List of Figures

List of Tables

List of Publications

1. C. D. Farmer, C. N. Ironside, A. Boyd, C. R. Stanley, P. T. Keightley, J. W. Cockburn, "Self-aligned Overhanging Mesas in Quantum Cascade Lasers", *Vertical Transport and Intersubband Processes in Low Dimensional Structures Meeting*, Sheffield, UK, October 1998.

2. C. D. Farmer, C. N. Ironside, J. V. Magill, C. R. Stanley, A. R. Boyd, P. T. Keightley, L. R. Wilson, J. W. Cockburn, M. S. Skolnick, "New Fabrication Techniques for Quantum Cascade Lasers", *Semiconductor and Integrated Optoelectronics* (SIOE) *Conference*, Cardiff, Wales, April 1999.

3. C. D. Farmer, C. N. Ironside, J. V. Magill, C. R. Stanley, A. R. Boyd, P. T. Keightley, L. R. Wilson, J. W. Cockburn, M. S. Skolnick, "Inverted-Mesa Quantum Cascade Lasers", *Conference on Lasers and Electro-Optics* (CLEO), Baltimore, Maryland, May 1999.

4. C. D. Farmer, P. T. Keightley, C. N. Ironside, C. R. Stanley, L. R. Wilson, J. W. Cockburn, 'A quantum cascade laser fabricated using planar native-oxide layers', *Appl. Phys. Lett.* 77 (1), 3 July 2000.

5. C. D. Farmer, P. T. Keightley, C. N. Ironside, A. Boyd, C. R. Stanley, L. R. Wilson, J. W. Cockburn, "A quantum cascade laser using a native-oxide-defined current aperture and optical waveguide", *Conference on Lasers and Electro-Optics* (CLEO) *Europe*, Nice, France, September 2000.

Chapter 1 Introduction

The quantum cascade (QC) laser is a semiconductor laser diode which offers the potential to produce compact, high power light sources within the mid- to sub-millimetre ($\lambda \approx 100$ μm) spectral range.[1] Lasing in pulsed-mode at room temperature has been demonstrated at spectral points between 3.4 and 13 μm, and lasing at 17 μm has been demonstrated at temperatures up to $T = 240$ K.[2, 3] Applications of QC lasers include trace gas analysis for pollution monitoring,[4, 5, 6] and medical diagnostics, as well as possible applications in free-space communications, laser radar and in military applications, such as missile countermeasures.[2] It has a number of advantages over existing technologies such as lead salt and III-V antimonide-based interband diode lasers, particularly in the areas of high temperature operation and emission wavelength selection.[1, 7]

At wavelengths greater than ~ 5 μm, QC lasers are the only semiconductor injection lasers that operate at room temperature. The closest alternative is a PbSrSe/PbSe/PbSrSe double heterostructure laser which was demonstrated very recently and operated in pulsed mode up to 333 K at a wavelength of 4.78 μm.[8] However, many QC lasers have already demonstrated room-temperature operation *without* the assistance of the buried heterostructure configuration. In fact, pulsed operation of a simple mesa-etched QCL up to $T \geq 425$ K at $\lambda \approx$ 8.4 μm was recently reported.[9] The use of the buried heterostructure configuration is only just beginning to be explored in QC lasers, with there already being evidence of significant improvements in heat dissipation.[10]

In comparison to lead salt lasers, the optical output power of QC lasers is at least 100 times more powerful, and the characteristic temperature T_0 is higher by at least a factor of 2, mainly because the performance of interband mid-IR lasers at high temperatures is compromised by severe non-radiative Auger recombination.[11]

The QC laser is the first semiconductor laser that can be tailored to emit light at a predetermined wavelength set at nearly any point over a wide range of the mid-infrared spectrum without having to alter the composition of the constituent semiconductor materials. This ability is important for applications such as pollution monitoring and industrial process control as many hazardous and toxic gases and chemicals have strong optical absorption 'fingerprints' at these wavelengths.[12] To substantially vary the emission wavelength in a conventional semiconductor laser one must develop a laser using a different semiconductor material, whereas the emission wavelength of QC lasers may be continuously tailored over a very wide range by simply changing the active-layer thickness' and without changing the combination of semiconductor materials.

Since the QCL relies only on intersubband electron transitions, wide-gap III-V semiconductor materials can be used. QC lasers were first demonstrated using the $Ga_{0.47}In_{0.53}As/Al_{0.48}In_{0.52}As/InP$ material system,[1] and were later extended to the AlGaAs/GaAs material system.[13] These materials are already employed in high-speed electronics and telecommunications lasers and, as such, they are much easier to process, and more reliable than low-bandgap semiconductors such as lead-salts used for the conventional mid-IR diode lasers.[12]

To achieve this, the principle of operation of the QC laser differs in a fundamental way from conventional diode lasers. It relies on only one type of carrier (hence, 'unipolar' semiconductor laser) and on electronic transitions between conduction subband states (hence, 'intersubband' laser). The emission wavelength of the QC device is determined, not by the band gap, but by the small energy separation of conduction subbands induced by size quantisation in semiconductor heterostructures. Using intersubband transitions in semiconductor quantum well (QW) structures for long wavelength lasers was first suggested in 1971 by Kazarinov and Suris,[14] and was first demonstrated in 1994 by Faist, Capasso, Sivco, Sirtori, Hutchison and

Cho at AT&T Bell Laboratories (Lucent Technologies).[1, 15] In the three year period following their first publication of the QC laser, the group at AT&T Bell Laboratories were still the only group to have demonstrated working type-I QC devices. Furthermore, they had already progressed to room-temperature operation in pulsed mode, lasers with emission at a number of wavelengths in the 4-11μm spectral region,[16] distributed feedback (DFB) QC lasers,[17] dual-wavelength intersubband emitters,[18] QC microdisk lasers,[19] and high power interminiband superlattice lasers,[20] proving the ruggedness and versatility of the QC design.

The emission wavelength and maximum operating temperature for pulsed- and CW-mode operation of a number of intersubband QC lasers demonstrated to date are shown in Figure 1. Comparing the results with the absorption lines of several gases of interest shown in Figure 2,[12] one can see that the QC laser spans an impressive range of wavelengths important for gas sensing.

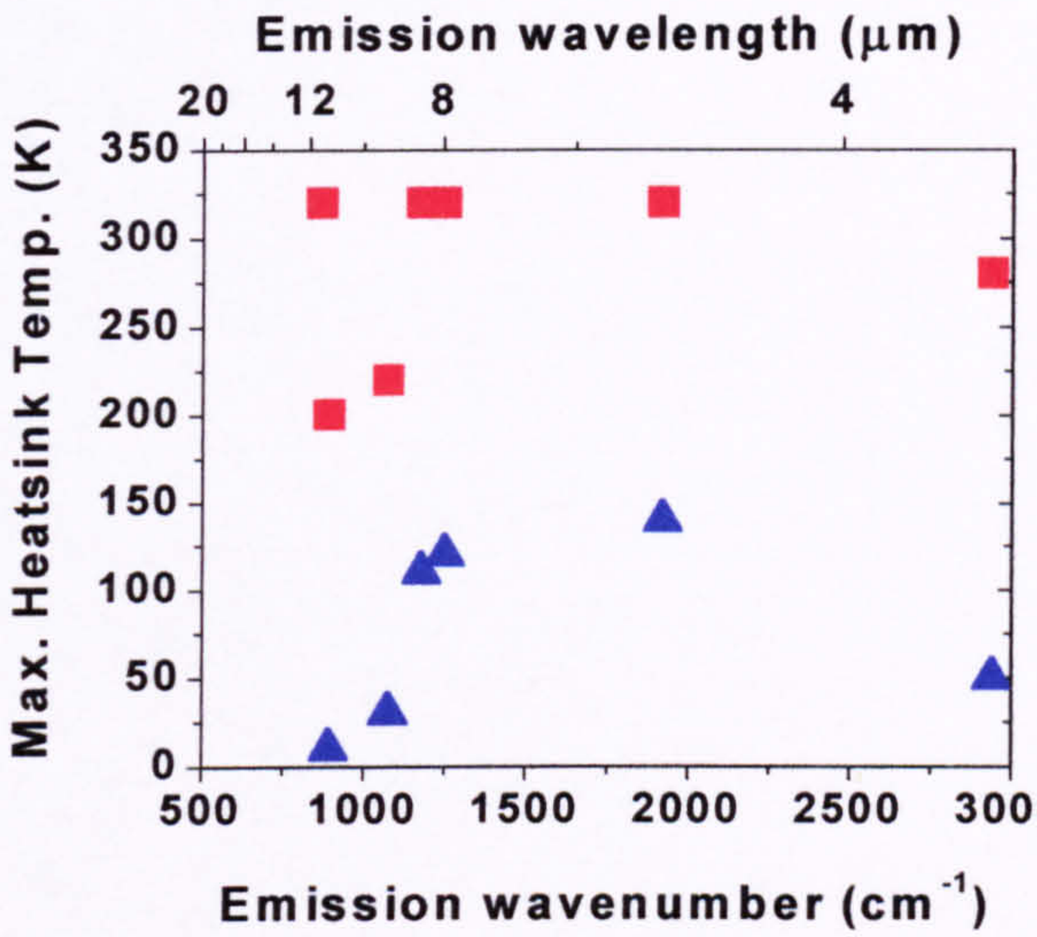

Figure 1 Maximum operating temperatures in pulsed-mode (squares) and CW-mode (triangles) demonstrated for a number of QC lasers.[12]

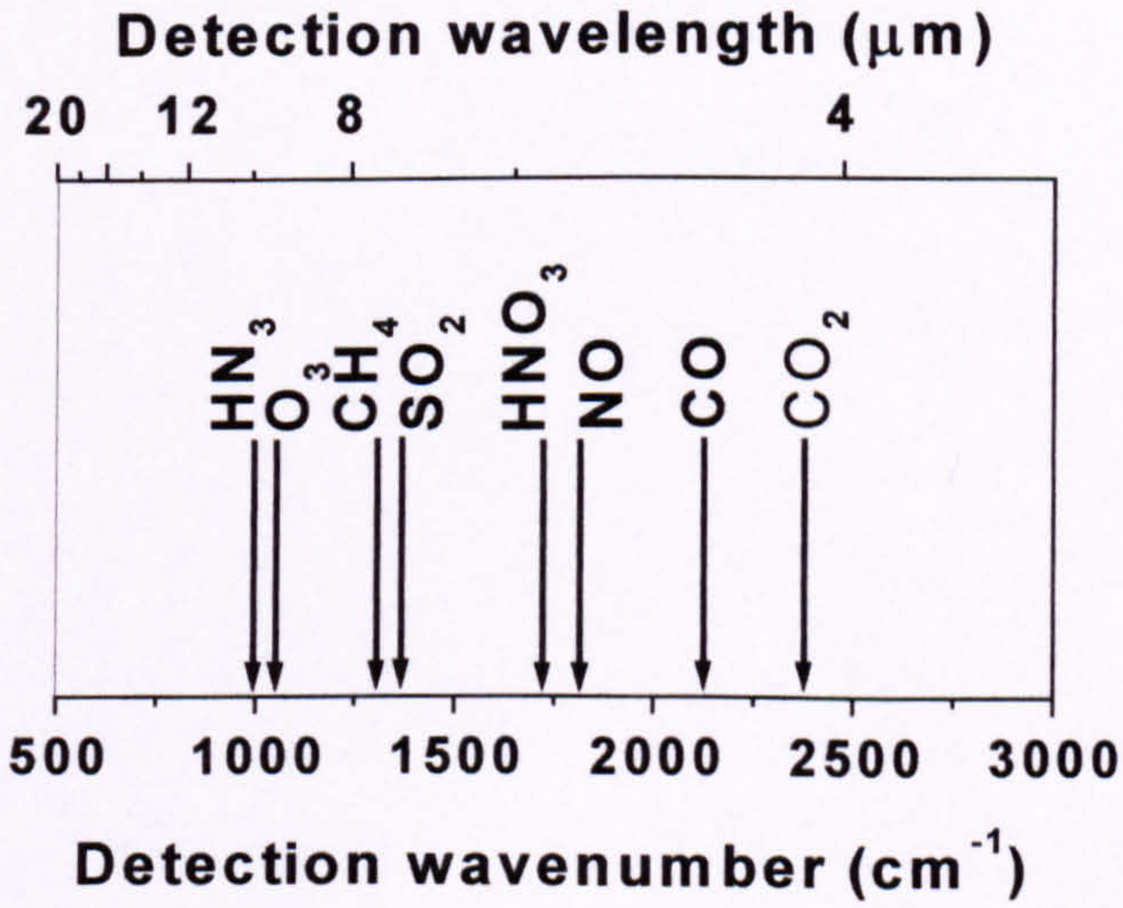

Figure 2 Position of absorption lines of gases of interest in gas sensing.[21]

1.1 Original objectives of this work

At the outset, this work was applications-driven in nature. The overall objective was to produce and use InP-based QC lasers for gas sensing applications. The approach was to use the MBE facility in our department to grow our QC wafers following the designs already demonstrated in the literature. The idea was that this would allow us to progress rapidly to the main objective of using the lasers for gas sensing.

To improve the QC laser performance for practical applications, efforts would be concentrated on the design and fabrication of the laser waveguide and resonator. By considering alternative waveguide structures, designs for improved heat dissipation, and by incorporating Bragg gratings, the project aimed to produce QC lasers with reduced room-temperature threshold currents, power levels in the milliwatt range and with emission at specific wavelengths for incorporation into gas sensors for the collaborating company, Edinburgh Sensors, Ltd.. This company had an interest in exploiting QC devices for the detection of gases and a longer-term interest in QC lasers for trace gas detection.

With the vast majority of the resources and expertise being centred on optoelectronic devices for the telecommunications market (i.e. emission wavelengths of $\lambda \approx 1.3$ and 1.55 μm), the mid-IR emitting QC lasers were a brand new area of research in our department. Although excellent, world-class molecular beam epitaxy (MBE) and fabrication facilities were at hand, a cryogenic mid-IR laser characterisation system, which was really a prerequisite to entering the field of QC lasers and carrying out the objectives, was not. The work started with the high expectation of obtaining outside funding for the acquisition of the required equipment, wafer growths, etc.. Unfortunately, funding was only approved far into the final year of the PhD, too late to make an impact on this work. Fortunately, some of the work was able to continue, owing to an informal collaboration established in the second year with Dr. Cockburn's GaAs/AlGaAs QC group at the University of Sheffield, UK. They had the necessary characterisation system and agreed to characterise our devices.

1.2 Work carried out and outline of thesis

The characterisation by our collaborators revealed that the QC devices fabricated were lasing, but were not performing nearly as well as that reported by Faist *et al.*. Initially, it was unclear whether it was the QC wafer growth, fabrication or characterisation that was to blame, since none of them had really been proven as far QC lasers were concerned. Resolving this issue became one of the main objectives of this work.

Nevertheless, the objectives of developing new waveguide structures, and new designs for improved heat dissipation proceeded. This was done through the comparison the performance of different QC laser structures fabricated from the same wafer, and through thermal modelling.

The different QC lasers structures fabricated included 10 μm-, 15 μm- and 112 μm-wide mesa-etched QCLs, 15 μm-wide shallow-etched QCLs, a mesa-etched QCL array, and 20 μm-wide PSWOX QCLs. The PSWOX QCLs were novel QC devices fabricated using a planar selective wet thermal oxidisation (PSWOX) process. Chapter 6 is devoted to the fabrication procedures that were developed for all the different kinds of devices produced. The collaboration and characterisation techniques are outlined in Chapter 7, before the results of the laser characterisation are presented in Chapter 8. The characterisation results include light-current (LI), current-voltage (IV), spectral and far-field measurements.

The results are explained with the assistance of the basic QC theory from Chapter 2, results of the dielectric permittivity modelling developed in Chapter 3, optical waveguide modelling in Chapter 4, and the thermal modelling Chapter 5.

The modelling of the dielectric permittivity gave values of n and α for InP, $In_{0.52}Al_{0.48}As$ and $In_{0.53}Ga_{0.47}As$ as a function of free-carrier density and wavelength in the mid-infrared spectral region. These values were used in the 2D optical modelling of the waveguide which gave the optical intensity plots of the waveguide modes and their values of effective index, waveguide loss coefficient, confinement factor, facet reflectivity, as well as their far-field distributions.

In Chapter 5 2D thermal modelling using non-linear finite element analysis was carried out for all of the structures listed above, as well as for InP-clad and buried heterostructure configurations. The chapter first discusses the factors limiting CW operation and what efforts (including those of this author) have been made to combat them, then presents the temperature distributions calculated for all of the waveguide designs from which their relative effectiveness at heat dissipation was assessed.

In summary, the work became modelling- and fabrication-based, with an emphasise on comparing a number of different QCL waveguide geometries and resolving the relatively poor performance common to all of our lasers. In the end, it was the combination of all this work which led to a satisfactory solution.

1.3 References

[1] J. Faist, F. Capasso, D. L. Sivco, C. Sirtori, A. L. Hutchinson, A. Y. Cho, 'Quantum Cascade Laser', Science **264** (22 April 1994).

[2] F. Capasso, A. Tredicucci, C. Gmachl, D. L. Sivco, A. L. Hutchinson, A. Y. Cho, G. Scamarcio, "High-Performance Superlattice Quantum Cascade Lasers", *IEEE J. Selected Topics in Quantum Electron.*, **5** (3) 792, May/June 1999.

[3] A. Tredicucci, C. Gmachl, F. Capasso, A. L. Hutchinson, D. L. Sivco, A. Y. Cho, "Single-mode surface-plasmon laser", *Appl. Phys. Lett.* **76** (16) 2164, 17 April 2000.

[4] K. Namjou, S. Cai, E. A. Whittaker, J. Faist, C. Gmachl, F. Capasso, D. L. Sivco, A. Y. Cho, "Sensitive absorption spectroscopy with a room-temperature distributed feedback quantum cascade laser", *Opt. Lett.* **23** 219, 1998 .

[5] S. W. Sharpe, J. F. Kelly, J. S. Hartman, C. Gmachl, F. Capasso, D. L. Sivco, J. N. Baillargeon, A. Y. Cho, "High-resolution (Doppler-limited) spectroscopy using quantum-cascade distributed-feedback lasers", *Opt. Lett.* **23** (17) 1396, September 1998.

[6] B. A. Paldus, T. G. Spence, R. N. Zare, J. Oomens, F. J. M. Harren, D. H. Parker, C. Gmachl, F. Capasso, D. L. Sivco, J. N. Baillargeon, A. Y. Cho, "Photoacoustic spectroscopy using quantum cascade lasers", *Opt. Lett.* **24** (3) 175, 1999.

[7] M. Tacke, "New Developments and Applications of Tuneable IR Lead Salt Lasers", Infrared Phys. Technol. **36** (1) 447, 1995.

[8] Z. Shi, G. Xu, P. J. McCann, X. M. Fang, N. Dai, C. L. Felix, W. W. Bewley, I. Vurgaftman, J. R. Meyer, "IV-VI compound mid-infrared high-reflectivity mirrors and vertical-cavity surface-emitting lasers grown by molecular-beam epitaxy", *App. Phys. Lett.*, **76** (25), pp.3688-3690, 19 June 2000.

[9] C. Gmachl, A. Tredicucci, F. Capasso, A. L. Hutchison, D. L. Sivco, A. M. Sergent, T. Mentzel, A. Y. Cho, 'High temperature ($T \geq 425$ K) pulsed operation of quantum cascade lasers', *Electron. Lett.* **36** (8) 723, 13 April 2000.

[10] M. Beck, J. Faist, A. Muller, U. Oesterle, M. Ilegems, E. Gini, H. Melchior, "High-Performance ($\lambda \approx 10.4$ μm) buried heterostructure quantum cascade lasers", Conference on Lasers and Electro-Optics Europe - Technical Digest, p.265, 2000.

[11] H.K. Choi and G.W. Turner, "InAsSb/InAlAsSb strained quantum-well diode lasers emitting at 3.9μm", Appl. Phys. Lett. **67** (3), 17 July 1995.

[12] F. Capasso, C. Gmachl, A. Tredicucci, A. L. Hutchinson, D. L. Sivco, A. Y. Cho, "High Performance Quantum Cascade Lasers", *Optics & Photonics News*, **10** (10) 31, October 1999.

[13] C. Sirtori, P. Kruck, S. Barbieri, P. Collot, J. Nagle, M. Beck, J. Faist, U. Oesterie, "GaAs/$Al_xGa_{1-x}As$ quantum cascade lasers", *Appl. Phys. Lett.* **73** (24), December 1998.

[14] R. F. Kazarinov and R. A. Suris, "Possibility of the amplification of electromagnetic waves in a semiconductor with a superlattice", *So. Phys. Semicond.* **5** (4) 707, October 1971.

[15] J. Faist, F. Capasso, D. L. Sivco, C. Sirtori, A. L. Hutchinson, A. Y. Cho, 'Quantum cascade laser: An intersub-band semiconductor laser operating above liquid nitrogen temperature', *Electronic Letters* **30** (11) 865, 26 May 1994.

[16] F. Capasso, J. Faist, C. Sirtori, and A. Y. Cho, "Infrared (4 - 11 μm) Quantum Cascade Lasers", *Solid State Communications* **102** (2-3) 231, 1997.

[17] J. Faist, C. Gmachl, F. Capasso, C. Sirtori, D. L. Sivco, J. N. Baillargeon, A. Y. Cho, 'Distributed feedback quantum cascade lasers', *Appl. Phys. Lett.* **70** (20) 2670, 19 May 1997.

[18] C. Sirtori, F. Capasso, J. Faist, A. L. Hutchinson, D. L. Sivco, A. Y. Cho, 'Dual wavelength intersubband emitters', *CLEO'97* p425, 22 May 1997.

[19] J. Faist, C. Gmachl, M. Striccoli, C. Sirtori, F. Capasso, D. L. Sivco, A. Y.Cho, 'Quantum Cascade disk lasers', *Appl. Phys. Lett.* **69** (17) 2456, 21 October 1996.

[20] G. Scamarcio, F. Capasso, C. Sirtori, J. Faist, A. L. Hutchinson, D. L. Sivco, A. Y. Cho,' High-Power Infrared (8-Micrometer Wavelength) Superlattice Lasers', *Science* **276** p773, 2 May 1997.

[21] E. V. Stepanov, A. I. Kouznetsov, P. V. Zyrianov, V. G. Artjushenko, Yu. G. Selivanov, "Multicomponent fiber-optical gas sensor based on MIR tunable diode lasers", Proceedings of the *SPIE*, **2508** pp224-233, 1995.

Chapter 2 Basics of quantum cascade lasers diodes

First of all, this chapter looks at the basic design of the QC laser and at the improvements which were implemented following its initial demonstration at cryogenic temperatures, covering the advances which were involved in achieving room-temperature operation. Following that, there will be an overview of the layer structure and operation of the $\lambda \approx 5$ μm, room-temperature QC laser design which was the design adopted for the majority of this work. Finally, we move to a more in-depth look at the operational characteristics of the QC laser, such as the threshold current density, bias voltage, electrical power dissipation, slope efficiency and external quantum efficiency. The advantages and disadvantages of the lasers are discussed giving the underlying reasons for the behaviour and the implications for their performance.

2.1 Brief history of the development of QC lasers

2.1.1 General concept

The spatial confinement of electrons in the direction normal to the epitaxial layers in nanometer-thick semiconductor heterostructures means that their allowed energy states become quantised. The QC laser is comprised of a series of semiconductor heterostructures or 'quantum wells' (QWs). The basic concept of the QC laser was that, under the application of an external electric field, electrons could be injected by quantum mechanical tunnelling into an upper energy state of a QW, and then make a radiative transition (transition involving emission of a photon) to a state of lower energy located either in the same QW or the adjacent one. The emission energy (or wavelength) is then determined by the energy separation between the upper and lower energy states which could be adjusted by changing the heterostructure layer thickness'. Once the electrons had made the optical transition, they could then be removed from the lower energy state by tunneling, before being injected into an identical series of QWs to repeat the process yet again. The electrons could 'cascade' down the periodic structure with the potential for each one to emit a photon in every period. As in other lasers, one condition which needs to be met before lasing could be established was that the electron population in the upper energy state was greater than that in the lower one, i.e. that a population inversion existed.

2.1.2 QC lasers with a diagonal transition

The first QC lasers only operated up to T = 88-125 K and were based on photon-assisted tunnelling transitions, often referred to as 'diagonal' transitions.[1, 15] A schematic drawing of the conduction band energy diagram under operating bias is given in Figure 3. The intersubband optical-phonon-limited relaxation time of electrons from the $n = 3$ to the $n = 2$ states, τ_{32}, was relatively long as the transition was between states of reduced spatial overlap and accompanied by a large momentum transfer. Very fast inelastic relaxation, by means of optical phonons with nearly zero momentum transfer, occurred between the strongly overlapped and closely spaced $n = 2$ and $n = 1$ subbands to ensure a population inversion. The diagonal nature of the laser transition increased the escape time to the continuum from the $n = 3$ level, thus enhancing the injection efficiency. On the other hand, the diagonal transition design suffered from the effects of interface roughness in the form of a broadening of the luminescence linewidth (FWHM ≈ 22 meV),[2] and as a consequence the peak gain was reduced.[1]

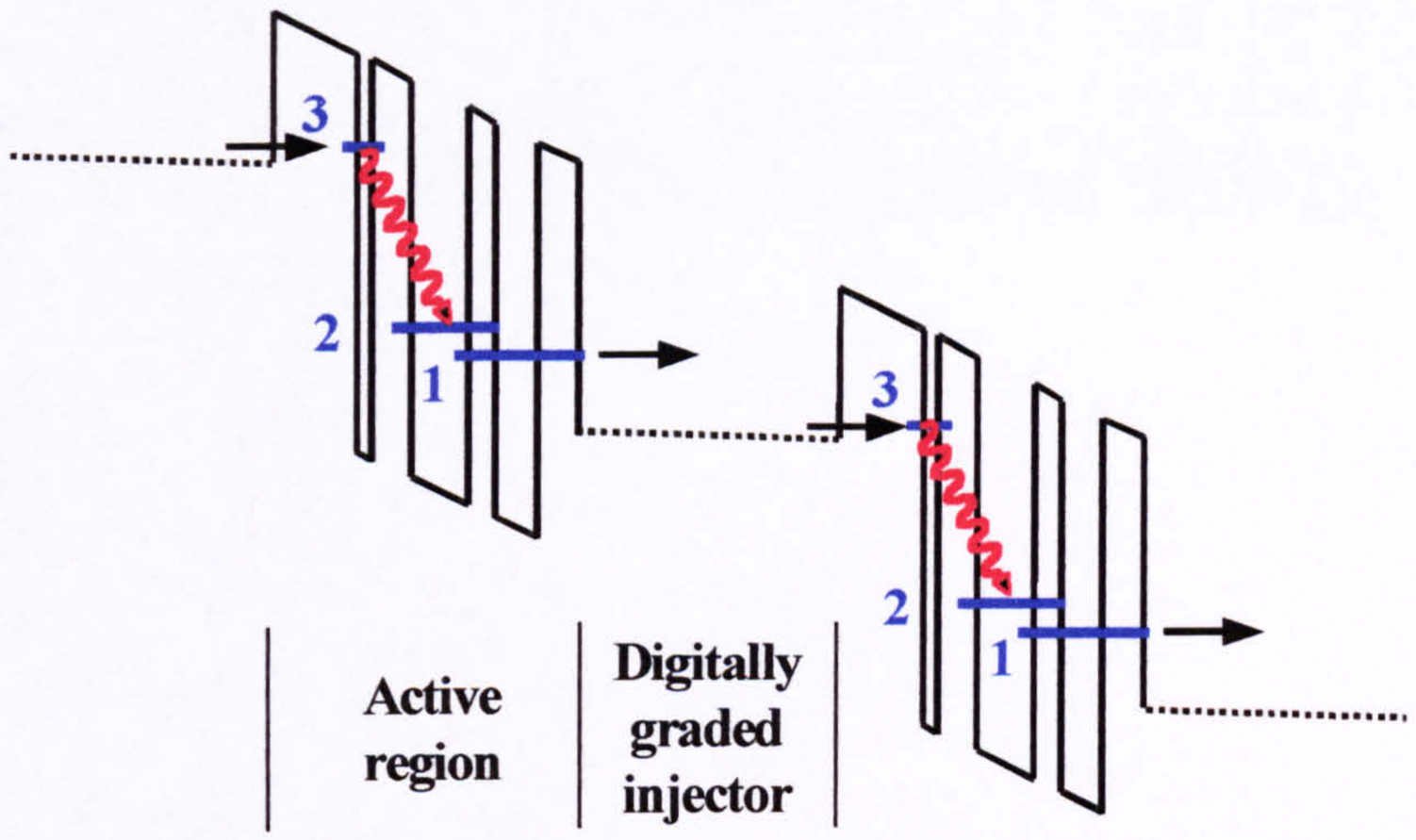

Figure 3 Energy diagram of a QC laser based on a diagonal transition. The solid blue lines represent the lowest energy and approximate spatial extent of the $n = 1$, 2 and 3 subbands in the active region. The black arrows indicate resonant tunnelling of electrons between subband states, and the red wavy arrows represent the radiative transition between the $n = 3$ and $n = 2$ states.

2.1.3 QC lasers with a vertical transition

Intrawell intersubband transitions (vertical) are less sensitive to interface roughness, [3] and the move to vertical transition QC lasers, like that shown in Figure 4, reduced the width of the luminescence spectrum considerably (FWHM $\approx$ 12 meV). [2]

However, the escape time from the excited $n = 3$ state to the continuum is much shorter for the vertical transition, resulting in a reduction in the quantum efficiency. To provide the necessary electron confinement (similar to that provided by the diagonal design), the superlattice of the graded injection/relaxation region was designed as a Bragg reflector for electrons in the $n = 3$ state via a minigap, as well extracting electrons from the $n = 2$ and $n = 1$ states via a miniband (refer to Figure 4).[2]

QC lasers based on a vertical transition showed a dramatic improvement in performance.[16] The threshold current density was approximately halved which led to higher operating temperatures, greatly enhanced peak optical output powers and continuous wave (CW) operation up to heatsink temperatures in excess of 100 K.

2.1.4 Room-temperature operation in pulsed-mode

An advance to pulsed QC laser operation at $T = 300$ K was accomplished by combining a few modest design modifications by the group at AT&T Bell Laboratories.[16] Their aim was to improve the injection efficiency, maintain the population inversion efficiency at higher temperatures, and to increase the heat dissipation capacity of the upper cladding layers.

The use of InP in the upper waveguide cladding (as well as that of the lower) improved the high temperature optical power output by an order of magnitude so that room temperature operation was achieved.[4] This was attributed to the thermal resistance of binary materials such as InP being $\approx$ 20 times smaller than ternaries such as $In_{0.52}Al_{0.48}As$, due to the absence of alloy scattering.

The population inversion in a QC laser was created by maximising the electron injection into the upper excited $n = 3$ level and the carrier lifetime within that level, and minimising the carrier density of the lower $n = 2$ level by maximising extraction to the graded relaxation region. However, at elevated temperatures

'thermal backfilling' of the $n = 2$ state occurs from the relaxation region, which degrades the population inversion.[2] To combat this the energy separation Δ (refer to Figure 4) between the ground state of the injector/relaxation graded region and the lower $n = 2$ level was increased and the doping of the injection/relaxation regions was reduced.[4] This helped maintain the gain at elevated temperatures, and so increased the operating temperature limit.

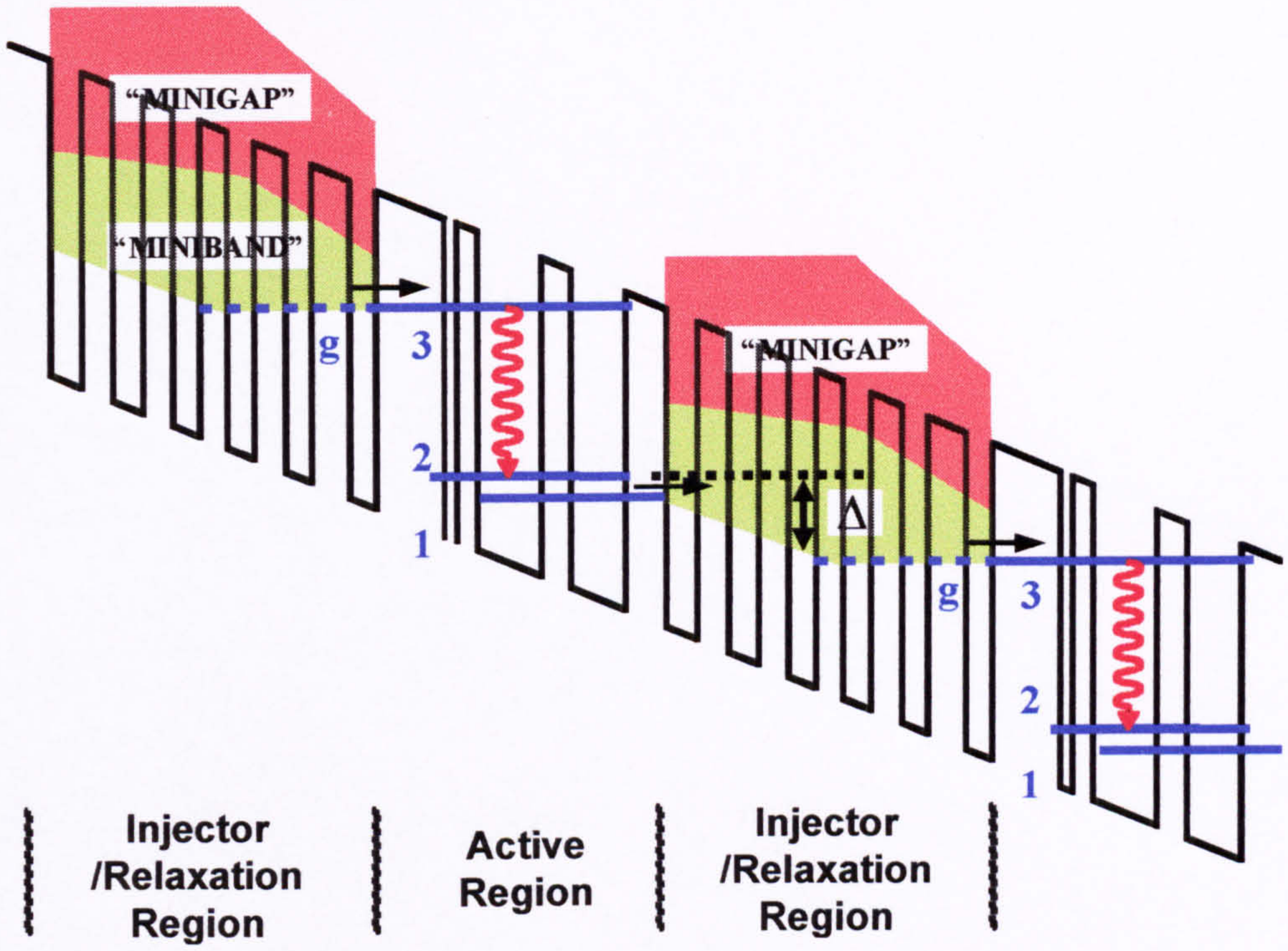

Figure 4 Following Faist *et al.* [4] this figure shows a rough schematic of the conduction band for a portion of the cascade structure of the $Ga_{0.47}In_{0.53}As/Al_{0.48}In_{0.52}As$ QC structure under an operational electric field of 7.6 x10^4 V/cm. The solid and dotted blue lines represent the lowest energy and approximate spatial extent of the $n = 1$, 2 and 3 subbands in the active region, and of the ground state (g) of the injector miniband, respectively. The "miniband" is a manifold of energy levels whose energy and spatial extent is shown by the green shading and the "minigap" which contains a low density of states, is shaded in red. The black arrows indicate resonant tunnelling of electrons between subband states, and the red wavy arrows represent the radiative transition between the $n = 3$ and $n = 2$ states. The energy separation Δ between the quasi-Fermi energy of in the ground state of the injector and the $n = 2$ is shown.

An additional 0.9 nm-thick $Ga_{0.47}In_{0.53}As$ quantum well coupled to the double well by a 1.5 nm barrier was introduced to selectively enhance the amplitude of the wavefunction of the $n = 3$ state in the 5.0 nm injection barrier (see Figure 4). This maximised the injection efficiency by increasing the overlap between the $n = 3$ wavefunction and the ground state wavefunction of the injector, while reducing the latter for the $n = 2$ and $n = 1$ states.[4]

Finally, the width of the miniband of the injector was narrowed towards the 5.0 nm injection barrier so as to 'funnel' the electrons into the injector ground state to maximise injection efficiency at room temperature and above.[4]

With the implementation of these improvements Faist *et al.* demonstrated room-temperature lasing at $\lambda \approx 5.2$ μm in pulsed mode with peak optical output power ≈ 200 mW. CW operation up to $T = 140$ K was also

reported.[4] Demonstration of pulsed-mode room temperature operation of QC lasers emitting at a range of wavelengths between $4.5 < \lambda < 11$ μm followed within a short period.[16] At present, these are still the only semiconductor lasers operating at room-temperature above $\lambda \approx 5$ μm.

Room-temperature operation is important for practical applications, and recalling that the original objectives of this work were to use QC lasers for gas sensing applications, it was the advent of this design which really sparked off the project. Replicating the above design was the ideal place to start.

2.2 Layer structure and fundamental operation of the room-temperature, $\lambda \approx 5$ μm $In_{0.52}Al_{0.48}As$-clad QC laser design

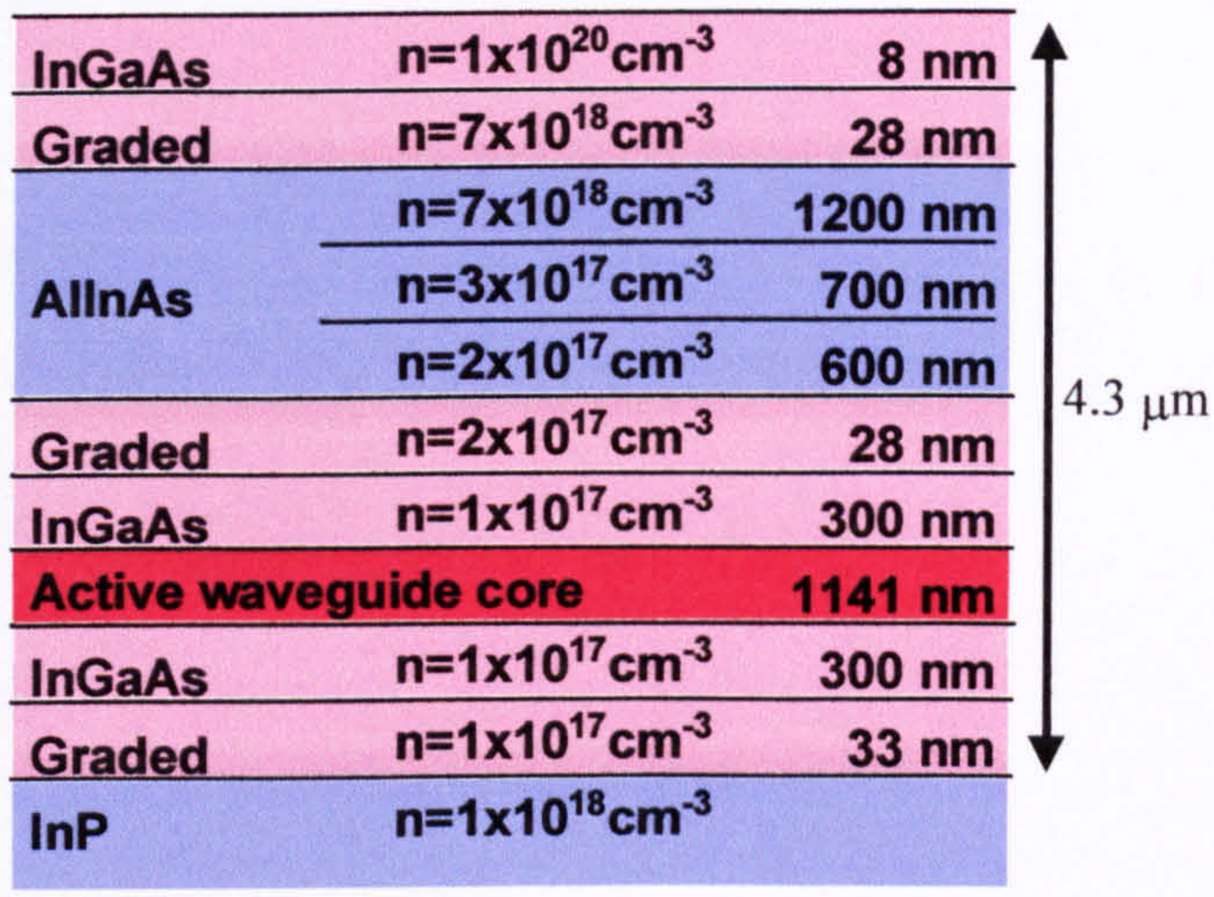

Figure 5 Layer structure of QC laser ($\lambda \approx 5\mu m$).[4]

The first priority of this project at the University of Glasgow, which is still ongoing, was to replicate the pulsed room-temperature operating QC (vertical transition) laser emitting at wavelength $\lambda \approx 5\mu m$ as designed by Faist *et al.*.[4] Since InP could not be grown at the MBE facility of the University of Glasgow, it was the structure with the $In_{0.52}Al_{0.48}As$ upper cladding layer which was grown for our work. The $In_{0.53}Ga_{0.47}As$/ $In_{0.52}Al_{0.48}As$/InP layer structure of the device is shown in Figure 5, including the layer thickness' and doping levels. The active waveguide core consisted of the 25 identical periods of the radiative transition and injection/relaxation regions (see Figure 6) sandwiched between two thin $In_{0.53}Ga_{0.47}As$ layers. The purpose of the two $In_{0.53}Ga_{0.47}As$ layers was increase the average refractive index of the core. The layer structure of one of the 25 periods of the active waveguide core is shown in Figure 6.

A schematic conduction band diagram of two periods of the active region of the structure under positive bias is shown in Figure 3. The diagram, and the following discussion, were based on that reported in the literature.[4, 5, 12, 16] Under an applied electric field of ≈ 76 kV/cm the conduction band diagram takes on a staircase appearance as the electric field exceeds the quasi-electric field associated with the graded conduction band relaxation/injection regions. Electrons tumbling down this potential staircase sequentially emit photons at each coupled-well radiative region. Electrons relax in the graded regions and are then injected by tunnelling into the $n = 3$ excited state. The radiative (TM polarised) intersubband transitions occur between the $n = 3$ and $n = 2$ subbands. The lower $n = 2$ state is designed to be separated from the $n = 1$ state by an energy equal to one optical phonon so that the relaxation time τ_{21} is considerably less than that

between the $n = 3$ and $n = 2$ levels, thus ensuring population inversion. The chirped superlattice relaxation/injection regions are designed to act as Bragg reflectors for electrons in the n = 3 excited states to prevent electron escape to the continuum and to simultaneously facilitate swift electron extraction from the lower $n = 1$ and $n = 2$ states via a miniband facing them.[3]

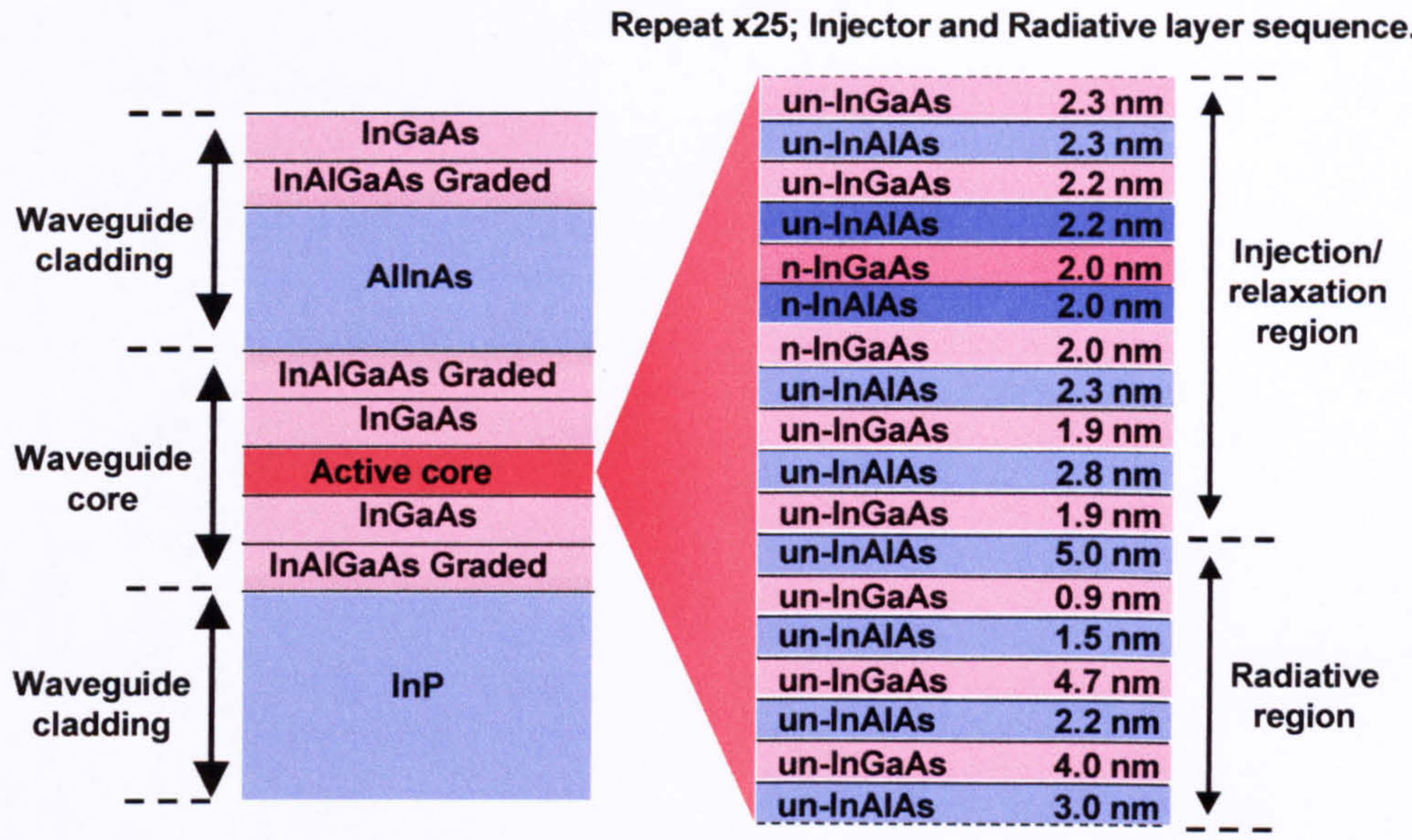

Figure 6 Expanded view the layer sequence of the active waveguide core. There were 25 repeats of this QC stage in the core. Each stage consisted of an injector/relation region and a radiative region.

The 25 period active region and the two InGaAs layers are sandwiched between a thick InP substrate and $In_{0.52}Al_{0.48}As$ cladding layer to provide an optical waveguide parallel to the material layers. Processing the wafer structure into 10 to 20μm wide, 0.5 to 3 mm long ridge waveguides with cleaved, uncoated facets and electrical contacts produces an edge-emitting QC laser diode. This design was reported by Faist *et al.* to operate in CW-mode up to 121 K with 16 mW at 80 K, and to operate in pulsed-mode (50 ns pulses with a 4.5 kHz repetition rate) up to 320 K with ~ 23 mW at 300 K.[4]

A major drawback of the existing lattice-matched InGaAs/AlInAs QC laser is the great complexity of its layer structure. The precision growth of its 500 layers demands very high standards in MBE growth. Despite this, the QC laser has now been replicated by a handful of groups world-wide including our own (see Ref. [12]) and, contrary to initial speculation, the design appears fairly robust and reproducible.

The predominant limitation of the present intersubband QC lasers is the relatively low radiative efficiency below threshold ($\eta_R \approx 1\times10^{-4}$)[6] owing primarily to a fast non-radiative phonon relaxation between the subbands. This leads to a high threshold current density ($J_0 \approx 10$ kA/cm^2 at $T = 300$ K) and substantial heating unless low duration, low duty cycle pulses are used.[4] As we saw earlier, consideration of heat dissipation in the design of the optical waveguide, and tweaking of the active region design to lower the threshold current density by Faist *et al.* led to considerable improvements so that room temperature operation was achieved.[4] Further improvements in performance are expected with the development of structures which can remove heat more efficiently. [7]

2.3 Basic theory of QC lasers

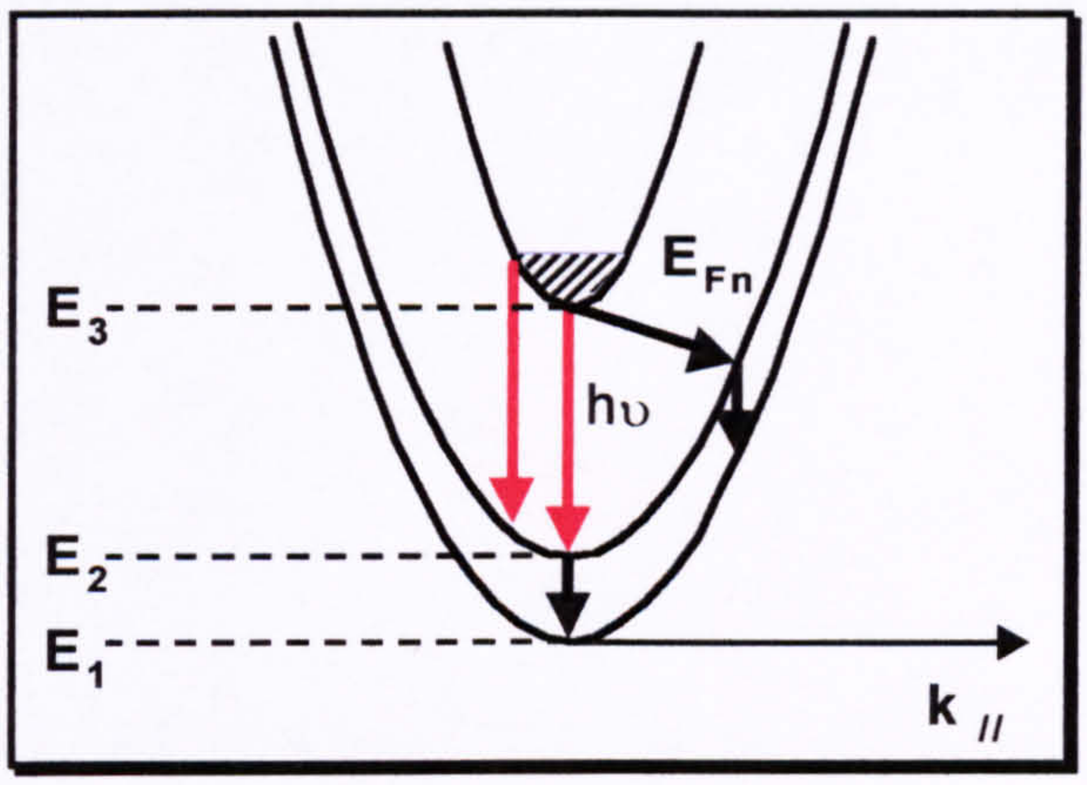

Figure 7 Schematic diagram of the in-plane dispersion of the active region subbands and some of the electron transitions that occur.[8] The black and red arrows represent the non-radiative and radiative electron transitions, respectively.

2.3.1 Threshold current density

The threshold current required to establish lasing in QC lasers is high ($J_{th} \approx 1$kA/cm^2 at $T = 10$ K, $J_{th} \approx 10$ kA/cm^2 at $T = 300$K). The fundamental reason behind this is that, in contrast to interband lasers, the electronic transitions in a QCL (see Figure 7) are between states which have very similar magnitudes and identical signs of electron effective mass. As a consequence, the active region does not possess an electronic bandgap between the n = 3 and n = 2 states, which in turn permits fast non-radiative electron transitions such as electron-phonon, electron-electron, and impurity scattering.[7] The main culprit is the emission of longitudinal optical (LO) phonons ($\tau \sim 0.5 - 2$ ps) which rapidly depopulate the excited state $n = 3$. Nevertheless, by ensuring that the lifetime of electrons in the lower level of the lasing transition ($n = 2$) is shorter, a population inversion can still be established. The short lifetime of electrons in the $n = 3$ level lowers the magnitude of the population inversion, the radiative efficiency (below threshold), and can lead to high non-equilibrium phonon populations,[7] all of which contribute to a high threshold current. In its favour though, since the QCL is a unipolar device, the Auger recombination which plagues mid-IR interband laser diodes is not a concern in QCLs.[7] Further major advantages of the cascade scheme will emerge as we discuss the threshold current and voltage, and slope efficiency.

Following Faist *et al.*,[4] the gain coefficient for a QC active region can be calculated from,

$$g = \tau_3 \left(1 - \tau_2 / \tau_{32}\right) \frac{4\pi e z_{32}^2}{\varepsilon_0 n_{eff} L_p \lambda (2\gamma_{32})}, \qquad (2\text{-}1)$$

where the parameters and their respective values are given in Table 1. Substituting these values into the expression for the gain coefficient yields $g \approx 32\times10^{-3}$ cm/A at $T = 10$ K.

The threshold current density J_{th} (kA/cm^2) is related to the laser threshold current I_{th} (A) by the simple expression,

$$J_{th} = 100 \frac{I_{th}}{L_{cav} W}, \qquad (2\text{-}2)$$

where L_{cav} (mm) and W (μm) are the length and width of the laser cavity, respectively.

From the gain coefficient, the threshold current density J_{th} (kA/cm^2) can be determined using,

$$J_{th} = \frac{\alpha_m + \alpha_w}{g\Gamma}, \tag{2-3}$$

where Γ is the overlap between the optical mode and the QC stage(s), α_m and α_w are the optical losses associated with the laser facets (mirror loss) and waveguide (waveguide loss), respectively. The mirror losses experienced by an optical mode with effective index n_{eff} in a cavity of length L_{cav} with as-cleaved facets are calculated using,

$$\alpha_m = -\frac{\ln(R)}{L_{cav}}, \tag{2-4}$$

where R is the facet reflectivity. Using the reported values of α_m, α_w and Γ shown in Table 1 gives a value of $J_{th} = 0.94$ kA/cm^2. This compares to a value of $J_{th} \approx 0.93$ kA/cm^2 ($I_{th} \approx 0.25$ A) measured by Faist *et al.* on an actual laser based on this design.

Parameter	Value	Description
z_{32}	1.6 nm	matrix element of the lasing transition
$2\gamma_{32}$	16 meV	broadening of the gain spectrum
L_p	45.3 nm	length of the QC active region stage
$\tau_3 \approx \tau_{32}^{-1} + \tau_{31}^{-1}$	1.3 ps	electron lifetime in the $n = 3$ state
$\tau_2 \approx \tau_{21}$	0.4 ps	electron lifetime in the $n = 2$ state
τ_{32}	2.1 ps	electron scattering time from $n = 3$ to $n = 2$
Δ	110 meV	energy separation between quasi-Fermi of injector ground state and level $n = 2$
n_g	1.24×10^{11} cm^{-2}	electron sheet density in cascade stages
λ	5.2 μm	free-space emission wavelength
n_{eff}	3.22	effective refractive index of the mode
α_m	4.5 cm^{-1}	mirror loss coefficient
α_w	12 cm^{-1}	waveguide loss coefficient
Γ	0.55	overlap factor for the fundamental mode
W	9 μm	laser cavity width
L_{cav}	3 mm	laser cavity length
k_B	8.617×10^{-5} eVK^{-1}	Boltzman Constant
e	1.609×10^{-19} C	electron charge
ε_0	8.85×10^{-12} Fm^{-1}	permittivity of free space

Table 1 Parameters used in the calculations (such as of the gain coefficient) and their values which were taken from [4].

One of the major benefits of the cascade scheme is to curtail the current required to reach threshold. By cascading N_p periods of active region in series, each electron has N_p chances at producing photons (note that it also has N_p times more chances to emit phonons as well!). The overall quantum efficiency is therefore multiplied by the number of active regions N_p; the same flow of current can produce N_p times as much optical gain. However, this additional gain is only of benefit if it overlaps with the optical waveguide mode. Fortunately, this is not difficult since the length of a single QC stage is only $L_p \approx 0.043$ μm, whereas the wavelength of light inside the waveguide is $\lambda/n_{eff} \approx 1.6$ μm. The waveguide core must be about this width anyway in order to guide the fundamental mode of the optical waveguide, so there is plenty of room for a series of QC stages. Cascading 25 QC stages forms an active waveguide core roughly 1.2 μm in width and the waveguide core is completed by sandwiching this between the two 0.3 μm $In_{0.53}Ga_{0.47}As$ layers.

The cascading therefore enhances Γ and reduces J_{th} according to Eq. (2-3). Of course, Γ cannot be increased above unity, so that J_{th} cannot be lowered indefinitely with N_p; it will level out once the majority of the optical mode becomes confined to the active waveguide core. According to measurements on a similar QC structure emitting at $\lambda \approx 8$ μm by Gmachl *et al.*,[9] Γ scales approximately linearly with the number of stages up to $N_p \approx 30$ but the growth begins to saturate beyond this point. Additional stages added above this point begin to become detrimental to the QCL performance since additional voltage is required to bias them, yet little decrease in J_{th} is gained by their presence.

A secondary advantage of reduction in current will be discussed in Section 2.3.4 on the power dissipation.

2.3.1.1 Temperature dependence of the threshold current density

Before discussing the underlying causes of the rise of J_{th} with temperature in QCLs, we will define a general, empirical parameter which is often used to characterise the temperature dependence of the threshold current of a semiconductor laser. The characteristic temperature, T_0 (K) is given by, [10, 11]

$$J_{th} \propto \exp\left(T/T_0\right). \tag{2-5}$$

The T_0 is an phenomenological parameter which can be used to describe the exponential rise in J_{th} with increasing temperature. Its value is an amalgamation of all of the temperature-dependent characteristics that go together to determine $J_{th}(T)$ (such as non-radiative transition rates, the thermal resistance, broadening of the gain spectrum, waveguide losses, confinement factor etc.). For any device, it can be measured from the slope of a plot of the T versus Ln(J_{th}). Since the temperature dependencies of the underlying contributions change with temperature, so too does T_0, as it is actually a temperature-dependant parameter itself. Consequently the T_0 is usually only quoted for a certain range of temperature, or even given several values covering different temperature regions.

The increase in the threshold current density with temperature can be accounted for by considering three effects.[12] First, the phonon emission rate τ_{ph}^{-1} increases with temperature which brings about a decrease in the electron lifetime of the $n = 3$ state. The temperature-dependence of τ_{ph} can be accounted for by using the Bose-Einstein factor n_B (also known as the phonon Planck function) associated with the emission of LO phonons of energy $E_{LO} = 34$ meV, [4, 12]

$$\tau_{ph} \propto (2n_B + 1) = \frac{2}{\exp\left(E_{LO}/k_B T\right) - 1} + 1. \tag{2-6}$$

To have an idea of the magnitude of this effect, $(2n_B+1) \approx 1$ at $T = 10$ K, and $(2n_B+1) \approx 0.43$ at $T = 300$ K. Secondly, the population n_2 of the lower lasing level ($n = 2$) rises with temperature due to the thermal activation of electrons ('thermal backfilling') from the ground state g of the injector of the next stage. This population of thermally activated carriers is given by, [4]

$$n_2^{therm} = n_g \exp\left(-\Delta/k_B T\right), \tag{2-7}$$

where Δ is defined as the energy separation between the quasi-Fermi energy in the ground state of the injector g and the lowest state ($n = 2$) of the lasing transition, n_g is the sheet density of electrons arising from the n-type doped sections of the injectors. Since this structure was designed to be optimised for room

temperature operation, a relatively large value of $\Delta \approx 110$ meV and low value of n_g were chosen. Note that the value of Δ is only ~110 meV when a field of 7.6×10^4 V/cm exists across the cascade. The value of Δ is not a fixed parameter; it is proportional to the applied electric field.[13] The device may reach lasing threshold at an electric field lower than 7.6×10^4 V/cm, especially at lower temperatures (see 2.3.2).

The thermally activated population n_2^{therm} contribute to the threshold current density J_{th} according to,[4]

$$J_{th} = \frac{\alpha_m + \alpha_w}{g\Gamma_m} + \frac{q n_2^{therm}}{\tau_3 \left(1 - \tau_2/\tau_{32}\right)}. \tag{2-8}$$

However, this equation is based on a greatly simplified kinetic model of the conduction band states which does not take into account the presence of non-equilibrium phonons and their effect on the inter- and intrasubband scattering rates.[7] It has been shown that to accurately predict the J_{th} and optical gain spectra these processes must be included in the calculation electron state lifetimes and population distributions.[7, 14, 15] This is beyond the scope of this thesis.

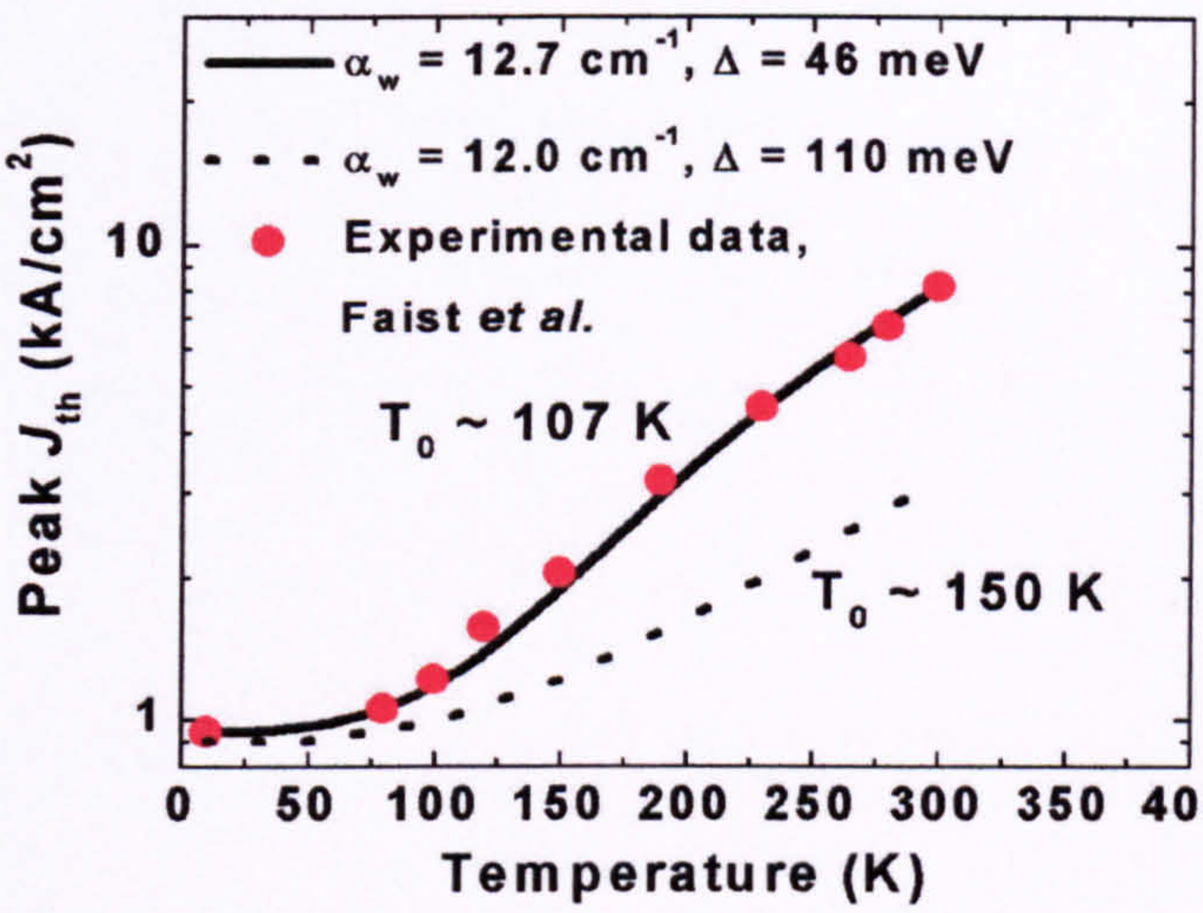

Figure 8 The figure shows the data taken from Faist *et al.*[4] for the threshold current density J_{th} as a function of temperature of a QCL ($\lambda \sim 5$ μm design). The measurements were made with low duty cycle ≈ 0.02%, 50 ns current pulses to prevent heating of the device during the current pulse. Also shown are the temperature dependencies of J_{th} calculated using Eq. (2-8) and the design parameters reported by Faist *et al.*[4] (dashed line), and then using parameters that provide a better fit of the data (solid line).

The observed range of validity of Eq. (2-8) varied with QCL design and was useful up to ~200 K in one case,[16] but only up to ~ 80 K in the case of the $\lambda \approx 5$ μm QCL design.[4] Referring to Figure 8, which plots the experimental temperature-dependence of J_{th} measured by Faist *et al.*[4] and the calculated $J_{\text{th}}(T)$ using Eq. (2-8) (using the parameters listed in Table 1), there was good agreement between them below $T \approx 80$ K, but above this temperature the value of T_0 was underestimated by ~ 43 K. Interestingly, this author notes that if one uses a lower value of $\Delta \approx 46$ meV, a very close fit of the data can be obtained over the entire range.

2.3.2 Bias voltage

Of course, you rarely get something for nothing and there is a penalty incurred by increasing N_p. Since the operational electric field across each period must be maintained, the voltage that must be applied across the cascade is multiplied by N_p. Essentially, the cascading scheme acts in a similar manner to a current to voltage transformer. In exchange for an additional voltage bias, the current required for operation is reduced. The voltage drop across the entire N_p-stage cascade (when the ground state of the injector g is in resonance with the $n = 3$ level of the lasing transition) can be approximated using,

$$V_{active} \approx \frac{E_{32} + \Delta}{e} N_p . \qquad (2\text{-}9)$$

Using values for the $\lambda \approx 5$ μm QCL used in this work ($E_{32} \approx 242$ meV, $\Delta \approx 110$ meV and $N_p = 25$), we calculate $V_{active} \approx 8.8$ V. As we will see, lasing can actually commence before reaching this level of voltage bias, especially at low temperature. In the current-voltage curves reported by Faist *et al.* for this design,[5] their QC laser exhibited a voltage at laser threshold of $V \approx 7.95$ V at $T = 22$ K which is ~ 1 V lower than that calculated above. If the difference is divided by $N_p = 25$, a value equivalent to 40 meV is obtained per stage. This indicates that either the device had commenced lasing before the ground state of the injector was aligned, or that Δ was ~70 meV at lasing threshold.

As for conventional interband laser diodes, a turn-on voltage $V_{t\text{-}o}$ (the voltage for which current begins to flow through the laser diode) can be applied. In addition to the voltage drop across the cascade V_{active}, this must also include the additional voltage offset, V_{offset}, which is the sum of the voltages required to overcome any other internal built-in fields in series with cascade within the laser diode.[9]

$$V_{t-o} = V_{active} + V_{offset} . \qquad (2\text{-}10)$$

Such built-in electric fields can occur at the graded-gap regions which lie between the semiconductor heterojunctions in the waveguide cladding layers. Ideally, the metal contact-semiconductor interface should not contribute to V_{offset} since, it should supposedly be ohmic. However, a contribution to V_{offset} by them has been reported (for $V_{offset} = 0.3$ V, ~ 0.1 V was attributed to the non-alloyed contacts)[9] which implies that they are not strictly ohmic in practice. Taking $V_{offset} = 0.3$ V and $V_{active} = 8.8$ V, this gives $V_{t\text{-}o} = 9.1$ V.

Returning briefly to our discussion of the non-alloyed metal contacts, it is desirable that they should have a low resistance and be ohmic in nature. To achieve this in other semiconductor devices, thermal alloying of the metal contact to the semiconductor has been used extensively.[17] However, this approach is thought not to be appropriate in QC lasers and non-alloyed metal contacts are generally used in conjunction with a very highly doped semiconductor ($n > 2\times10^{19}$ cm^{-3}). Having a high electron density in the semiconductor means that the depletion layer at the semiconductor-metal interface becomes very thin and allows the electrons to tunnel through the barrier so that a very low-resistance, ohmic contact can be obtained.[18, 19] However, in practice it has been shown that non-alloyed contacts which rely on tunnelling can be difficult to realise as they require a very high quality interface between the semiconductor and metal layers. Even mild damage/contamination to the semiconductor surface during fabrication stages (such as Si_3N_4 deposition and removal by dry or wet etching) has been shown to result in a high contact resistance and non-ohmic behaviour.[20] It is strongly suspected that this may have been the case in the QCLs fabricated in this work, leading to a large values of R_s and V_{offset} in our devices (see Sections 6.4 and 8.6).

That brings us nicely on to the next topic of discussion; the subject of the electrical resistance of the QCL devices for bias above $V_{t\text{-}o}$. For $V > V_{t\text{-}o}$ we assume that all of the built-in electric fields have been overcome and the electron levels in the QC stages aligned so that large currents can flow. In this region of bias the current can be increased without much of a further increment in the applied voltage since the differential resistance $\partial V/\partial I$ of the laser above $V_{t\text{-}o}$ can be low. Typically values of $\partial V/\partial I$ are < 1 Ω according to the literature,[9] which agrees with measurements on some of the devices in this work (see Section 8.6).

There are three main sources of resistance which contribute to the differential resistance, namely the resistance associated with the transit of the electrons across the cascade (determined by the electron tunnelling and scattering times therein) which scales with N_p, the resistance of the semiconductor cladding layers and the interfaces between them, and the resistance presented by metal contact-semiconductor interfaces.[9] Since $P=I^2R$, each of these contributions should be minimised to avoid any unnecessary dissipation of power within the QCL, which will otherwise degrade its performance.

Given a knowledge of $V_{t\text{-}o}$, I_{th} and $\partial V/\partial I$, the voltage at laser threshold V_{th} can be estimated from,

$$V_{th} = V_{t-o} + I_{th}\frac{\partial V}{\partial I}. \qquad (2\text{-}11)$$

Using the value of I_{th} = 2.2 A measured by Faist *et al.* at T = 300 K and assuming $V_{t\text{-}o}$ = 9.1 V and $\partial V/\partial I$ = 1 Ω, the voltage at laser threshold works out to be $V_{th} \approx$ 11.3 V at $T \approx$ 300 K. Assuming that $\partial V/\partial I$ and $V_{t\text{-}o}$ do not vary with temperature,[9] V_{th} will decrease with temperature in keeping with the drop in I_{th} and in Δ, hence the value of $V_{th} \sim$ 8 V measured by Faist *et al.* at T = 20 K.

These operational voltages are roughly an order of magnitude greater than that found in conventional interband laser diodes, which has several undesirable implications. One of the most important, i.e. the high electrical power dissipated in the device as heat, will be reviewed in the forthcoming Section 2.3.4. The second, perhaps more easily overlooked consideration is that in emulating the existing conventional laser diode waveguide designs and construction, care must be taken not to exceed the dielectric strength of insulating layers used (see Section 6.1). This is a simple, yet crucial consideration since ignoring it can lead to catastrophic device failure. Lastly, the high voltage and high current requirements of QCLs make many conventional laser diode drivers unsuitable. Although they are often capable of supplying large currents, the compliance voltage of these power supplies is typically less than a couple of volts. This is insufficient for the operation of QCLs.

2.3.3 Slope Efficiency and External Quantum Efficiency

The slope efficiency $\partial P/\partial I$ (W/A) of a laser is the observed increase in output power per ampere of additional current injected above threshold. For a QC laser it may be expressed as, [5]

$$\frac{\partial P}{\partial I} = \frac{1}{2}E_{32}\frac{\alpha_m}{\alpha_m+\alpha_w}\left(1-\frac{\tau_2}{\tau_{32}}\right)N_p. \qquad (2\text{-}12)$$

where E_{32} is the photon energy in electron volts. We see from Eq. (2-12) that the slope efficiency is directly proportional to the number of QC stages, which is one of the greatest attributes of the cascade design. [21,

Substituting in the parameter values from Table 1 gives $\partial P/\partial I \approx$ 0.67 W/A per facet. Devices reported in [5] which were based on the same active region design exhibited $\partial P/\partial I \approx$ 0.582 W/A per facet in CW mode. In

this second design, a waveguide loss of $\alpha_w = 13.3$ cm^{-1} had been measured which when substituted into Eq. (2-12) yields $\partial V/\partial I \approx 0.624$ W/A, in fair agreement the measured value. It would seem that a value $0.58 < \partial P/\partial I < 0.67$ should actually be expected for the design we have used.

Another important parameter is the number of photons exiting from the laser cavity per injected electron which is called the external differential quantum efficiency, η_d.[22] The value of η_d per laser facet can be determined from the slope efficiency using the following expression,

$$\eta_d = \frac{1}{E_{32}} \frac{\partial P}{\partial I}, \qquad (2\text{-}13)$$

where, once again, the units of E_{32} are electron volts. Since $\partial P/\partial I$ scales with N_p, so does η_d and so a large differential quantum efficiency can be realised by using a large number of QC stages. This is a fundamental difference between intersubband and conventional interband bipolar semiconductor laser diodes. In these conventional interband lasers η_d cannot exceed unity since in the process of emitting a photon of light an electron combines with a hole. In that case, it obviously cannot produce more than one photon.

Using the value of $\partial P/\partial I \sim 0.58$ W/A per facet measured by Faist *et al.*[5] and $E_{32} \approx 242$ meV, we obtain $\eta_d \approx 2.4$ *per facet* which is greater than unity.

2.3.4 Electrical power dissipation

For a mathematical formula of the power dissipated at threshold for CW operation, the reader is referred to [4]. The intention here is only to highlight the various factors contributing to power dissipation and heating.

Since the radiative efficiency η_R below threshold is very low ($\eta_R \approx 1\times10^{-4}$)[6] virtually all of the input electrical power at threshold $P_{th} = I_{th}V_{th}$ will be converted into phonons.[9, 23] On achieving threshold, much of the additional electrical power dissipated in the cascade will be converted into photons as the slope efficiency indicates, but further electrical power will still create phonons in each injector/relaxation region according to,

$$P_\Delta \approx (I - I_{th})\Delta . \qquad (2\text{-}14)$$

Irrespective of whether the laser is operating above or below threshold, electrical power will be dissipated in the series resistance R_s (e.g. the cladding layers and contacts) according to,

$$P_s = I^2 R_s . \qquad (2\text{-}15)$$

Since the power dissipation associated with R_s scales with the square of the current, it is obvious that P_s could become severe at high currents. Since QCLs usually operate with high currents (as much as 12 A has been used in pulsed mode)[21], it is obvious that efforts should be made to minimise the series resistance of the device. As an example, for $R_s = 0.5\ \Omega$ (measured value from one of the devices presented in Section 8.6) and $I = 5$ A (CW), a power of 12.5 W would be dissipated in the QCL due to R_s alone. As will be seen from the thermal modelling carried out in Chapter 5, this would cause considerable heating of the QCL and should definitely be avoided, if at all possible, by minimising R_s. This was addressed by the pioneers of the QC laser when they designed the waveguide e.g. the use of a highly doped contact layer, and of conduction band smoothing at semiconductor interfaces to reduce the series resistance. However, past the design phase care must be still be taken not to inadvertently increase the series resistance during the QCL fabrication process.

In particular, the formation of metal contacts with low specific contact resistance requires some care and forethought.[20]

In pulsed mode, where 50 ns-long pulses are typically used with a repetition rate of 5 kHz (≡ 0.025 % duty cycle), the heating of the device is thought to be negligible.[4] Using again the values of I_{th} = 2.2A and V_{th} = 11.3 V for pulsed-mode operation at room temperature gives $P_{th} \approx 2.2 \times 11.3 \times 2.5 \times 10^{-4} \approx 6$ mW. However, if we are to assume for a moment that we can use the same values of I_{th} and V_{th} in CW-mode at a heatsink temperature of T = 300 K, then $P_{th} \approx 2.2 \times 11.3 \approx 25$ W! We will see in Chapter 5 that, due to the finite thermal resistance R_{th} between the QCL active waveguide core and the heatsink, such a high power dissipation in the active waveguide core will elevate its temperature high above that of the heatsink. Of course, the existence of this temperature difference in CW-mode will mean that we cannot even assume that value of P_{th} is the same as in pulsed mode, as we did above. In CW-mode, P_{th} will correspond to the temperature of the active waveguide core, which may be considerably higher than the heatsink temperature owing to the presence of a positive feedback loop in the temperature i.e. the temperature of the active waveguide core depends upon the power dissipated and the thermal resistance of the device, but both the thermal resistance and the threshold power depend upon the temperature of the cascade. This can send the temperature, thermal resistance and threshold power all spiralling upwards. Evidence of this thermal runaway effect has been observed.[23]

These effects limit operation in CW mode to cryogenic temperatures. At present, room temperature operation is only accessible in a pulsed mode which keeps the active waveguide core below the maximum temperature of operation. The maximum temperature of CW operation of intersubband QCLs with emission wavelength 5 < λ (μm) < 8 has been around 140 K.[2] Lasing in pulsed mode persists to temperatures above room temperature, with the reported measurements usually being limited to T < 320 K owing to the restraints of the equipment used. Having surmounted these restraints, pulsed operation of a QCL up to $T \geq 425$ K at $\lambda \approx 8.4$ μm was recently reported. [13]

The thermal resistance of the device should be made as small as possible in order to minimise the heating in laser and initiation of thermal runaway.

2.3.5 Spectral dependencies

The non-parabolicity of the quantum-well energy states means that the n = 3 and n = 2 states are not completely parallel on the E-k diagram (energy as a function of the in-plane momentum, see Figure 7). With an increasing value of k the energy separation between the two states (and therefore the emission energy), E_{32}, gradually decreases. The electron distribution in these bands is dependent on both the temperature and injection current. Hence, the gain spectrum of the QC laser is also be temperature- and current-dependent. [24, 25, 26]

With increasing temperature, the emission is expected to red-shift (decrease in energy), as well as broaden and reduce in intensity. The red-shift has been explained by changes in the semiconductor material band structure and in the thermal distribution of the carriers the in-plane states (energy levels n = 1, 2 and 3).[24, 25, 26] The broadening and intensity decrease in the gain spectrum has been explained as a combination of the thermal distribution and electron-LO phonon scattering.[24, 25, 26]

With increasing drive current, the emission peak is expected to blue-shift (increase in energy), and its peak intensity grows approximately linearly.[26] The blue-shift was attributed to the Stark effect of the intersubband transition and to the increasing quasi-Fermi level in the $n = 3$ state with increasing injection current.[26]

2.4 Summary

An overview of the layer structure and operation of the $\lambda \approx 5$ μm, room-temperature QC laser design was given. The operational characteristics of QC lasers, such as the threshold current density, operational voltage, electrical power dissipation, and slope efficiency were introduced along with their dependencies and the implications for the performance of the QCLs.

The design was selected owing to the reported room-temperature operation by Faist *et al.*. Typical performance parameters reported for the design are summarised in Table 2. These will be used as the standard to which we compare the performance of the devices fabricated and characterised in this work.

Parameter	Value at T = 10 K	Value at T = 300 K
J_{th} (kA/cm^2)	0.93 [4]	8 [4]
V_{th} (kA/cm^2)	8 [5]	11
$\partial V/\partial I$ (Ω) above threshold	< 1 [5]	-
$\partial P/\partial I$ (W/A)	0.6 [5]	-
Peak output power (mW)	-	23 [4]

Table 2 Typical performance parameters for the $\lambda \approx 5$ μm design operating in pulsed mode.

The electrical and thermal resistances of the lasers were highlighted as having a detrimental effect on the laser performance, and both should be minimised. The high threshold current density and voltage, along with near-zero radiative efficiency below threshold leads to the generation of a large population of phonons in the active core. A low thermal resistance is desirable to swiftly remove these phonons to minimise the degradation of the laser performance and to extend the maximum temperature of CW operation.

2.5 Reference

[1] J. Faist, F. Capasso, D. L. Sivco, A. L. Hutchinson, C. Sirtori, S. G. Chu, A. Y. Cho, 'Quantum cascade laser: Temperature dependence of the performance characteristics and High T_0 operation', *Appl. Phys. Lett.* **65** (23) 2901, 5 December 1994.

[2] J. Faist, F. Capasso, C. Sirtori, D. L. Sivco, A. L. Hutchinson, A. Y. Cho, 'Vertical transition quantum cascade laser with Bragg confined excited state', *Appl. Phys. Lett.* **66** (5) 539, 30 January 1995.

[3] J. Faist, F. Capasso, C. Sirtori, D. L. Sivco, A. L. Hutchinson, A. Y. Cho, 'Vertical transition quantum cascade laser with Bragg confined excited state', *Appl. Phys. Lett.* **66** (5) 539, 30 January 1995.

[4] J. Faist, F. Capasso, C. Sirtori, D. L. Sivco, J. N. Baillargeon, A. L. Hutchinson, S. G. Chu, A. Y. Cho, 'High power mid-infrared (λ~5 μm) quantum cascade lasers operating above room temperature', *Appl. Phys. Lett.* **68** (26), 24 June 1996.

[5] J. Faist, A. Tredicucci, F. Capasso, C. Sirtori, D. L. Sivco, J. N. Baillargeon, A. L. Hutchison, A. Y. Cho, 'High-Power Continuous-Wave Quantum Cascade Lasers', *IEEE J. Quantum Electron.*, 34 (2) 336, February 1998.

[6] J. Faist, F. Capasso, C. Sirtori, D. L. Sivco, A. L. Hutchinson, S. G. Chu, A. Y. Cho, 'Mid-infrared field-tuneable intersubband electroluminescence at room temperature by photon-assisted tunnelling in coupled-quantum wells', *Appl. Phys. Lett.* **64** (9) 1144, 28 February 1994.

[7] M. Razeghi, "Kinetics of quantum states in quantum cascade lasers: device design principles and fabrication", *Microelectronics Journal.* **30** 1019-1029, 1999.

[8] F. Capasso, J. Faist, C. Sirtori, and A. Y. Cho, "Infrared (4 - 11 μm) Quantum Cascade Lasers", *Solid State Communications* **102** (2-3) 231, 1997.

[9] C. Gmachl, F. Capasso, A. Tredicucci, D. L. Sivco, R. Kohler, A. L. Hutchison, A. Y. Cho, 'Dependence of the Device Performance on the Number of Stages in Quantum-Cascade Lasers', *IEEE J. Selected Topics in Quantum Electron.*, **5** (3) 808, May/June 1999.

[10] H. P. Zappe, *Introduction to Semiconductor Integrated Optics*, Artech House, 1995.

[11] J. Gowar, *Optical Communication Systems,* Second Edition, p. 397, Prentice Hall International (UK) Ltd., 1993.

[12] J. Faist, F. Capasso, D. L. Sivco, A. L. Hutchinson, C. Sirtori, S. G. Chu, A. Y. Cho, 'Quantum cascade laser: Temperature dependence of the performance characteristics and High T_0 operation', *Appl. Phys. Lett.* **65** (23) 2901, 5 December 1994.

[13] C. Gmachl, A. Tredicucci, F. Capasso, A. L. Hutchison, D. L. Sivco, A. M. Sergent, T. Mentzel, A. Y. Cho, 'High temperature ($T \geq 425$ K) pulsed operation of quantum cascade lasers', *Electron. Lett.* **36** (8) 723, 13 April 2000.

[14] V. B. Gorfinkel, S. Luryi, 'Theory of Gain Spectra for Quantum Cascade Lasers and Temperature Dependence of their Characteristics at Low and Moderate Carrier Concentrations', *IEEE J. Quantum Electron.*, 32 (11) 1995, November 1996.

[15] S. Slivken, V. I. Litinov, M. Razeghi, 'Relaxation kinetics in quantum cascade lasers', *J. Appl. Phys.* **85** (2) 665, 15 January 1999.

[16] C. Sirtori, J. Faist, F. Capasso, D. L. Sivco, A. L. Hutchinson, A. Y. Cho, 'Mid-Infrared (8.5 μm) Semiconductor Laser Operating at Room Temperature', *IEEE Photon. Technol. Lett.* **9** (3) 294, 3 March 1997.

[17] T. C. Shen, G. B. Gao, H. Morkoc, "Recent developments in ohmic contacts for III-V compound semiconductors", *J. Vac. Sci. Technol. B*, **10** (5), pp.2113-2132, 1992.

[18]G. Stareev, H. Kunzel "Tunneling behaviour of extremely low resistance nonalloyed Ti/Pt/Au contacts to n(p)-In0.53Ga0.47As and n-InAs/InGaAs", *J. Appl, Phys.*, **74** (12), pp. 7592-7595, 15 Dec. 1993.

[19]G. Stareev, H. Kunzel, G. Dortmann "A controllable mechanism of forming extremely low-resistance nonalloyed ohmic contacts to III-V compound semiconductors", *J. Appl, Phys.*, **74** (12), pp. 7344-7356, 15 Dec. 1993.

[20] D. L. Marcy, E. W. Maby, P. G. Newman, R. Khanna, "Specific resistivity of delta-doped contacts in n-GaAs", *J. Appl, Phys.*, **70** (1), pp. 514-516, 1 July 1991.

[21] C. Gmachl, A. Tredicucci, F. Capasso, A.L. Hutchinson, D.L. Sivco, J.N. Baillargeon, A. Y. Cho, 'High-power $\lambda \approx 8$ μm quantum cascade lasers with near optimum performance', *Appl. Phys. Lett.* **72** (24), 15 June 1998.

[22] L. A. Coldren, S. W. Corzine, *Diode Lasers and Photonic Integrated Circuits*, John Wiley & Sons, Inc., New York, 1995.

[23] C. Gmachl, A. Michael Sergent, A. Tredicucci, F. Capasso, , A. L. Hutchison, D. L. Sivco, J. N. Baillargeon, S. N. George Chu, A. Y. Cho, 'Improved CW Operation of Quantum Cascade Lasers with Epitaxial-Side Heat-Sinking', *IEEE Photon. Technol. Lett.*, **11** (11) 1369, November 1999.

[24] V. B. Gorfinkel, S. Luryi, B. Gelmont, 'Theory of Gain Spectra for Quantum Cascade Lasers and Temperature Dependence of their Characteristics at Low and Moderate Carrier Concentrations', *IEEE J. Quantum Electron.*, **32** (11) 1995, November 1996.

[25] B. Gelmont ,V. B. Gorfinkel, S. Luryi, 'Theory of the spectral line shape and gain in quantum wells with intersubband transitions", *Apl. Phys. Lett.*, **68** (16) 2171, April 1996.

[26] Q. K. Yang, A. Z. Li, "Calculation of spontaneous emission and gain spectra for quantum cascade lasers", *J. Phys.: Condens. Matter.* **12** 1907, 2000.

Chapter 3 Modelling of the dielectric permittivity of *n*-type doped InP, $In_{0.53}Ga_{0.47}As$ and $In_{0.52}Al_{0.48}As$ in the mid-infrared spectral region

A knowledge of the optical properties of the semiconductor layers is essential for the design of the optical waveguide in any semiconductor laser. Obtaining accurate values of the refractive index n and absorption coefficient α (cm^{-1}) is a prerequisite to modelling and optimising the optical modes of the laser waveguide. For the design of InP/$In_{0.52}Al_{0.48}As$ /$In_{0.53}Ga_{0.47}As$ QC lasers we are interested in the optical properties of these semiconductors at wavelengths greater than $\lambda \approx 4.6$ μm. Unfortunately, it seems that experimental data on the dielectric constant of ternary semiconductor compounds does not exist in the literature for the mid- to far-infrared spectra region. In this chapter, theory and experimental material parameters will be used to model the plasma frequency, refractive index and loss in *n*-type doped InP, $In_{0.52}Al_{0.48}As$ and $In_{0.53}Ga_{0.47}As$ in the mid-infrared spectral region.

Before proceeding, some mention of the special nature of the optical confinement employed in InP-based QC lasers must be made. The long wavelength of emission of QC lasers mediates against good confinement of the optical mode to the waveguide core; using the standard method of optical confinement based on the intrinsic refractive index contrast between core and cladding semiconductor materials would require the growth of a prohibitively thick epilayer (6 to 8 μm thick).[1] To reduce the thickness of material required, a greater contrast in the refractive index between the waveguide core and the cladding layers is needed. To overcome this problem the pioneers of the QC laser took advantage of the anomalous dispersion of the refractive index near the plasma frequency.[2] By increasing the free-electron density in the cladding layers, the plasma frequency could be brought nearly to resonance with the optical frequency. This resulted in a large drop in the refractive index of the cladding layers and provided the necessary improvement in the refractive index contrast to permit a reduction in their thickness'. This form of optical confinement was referred to as 'plasma-enhanced' waveguiding. However, this solution is not without its disadvantages; the drop in refractive index is accompanied by an increase in the free-carrier loss which scales rapidly with wavelength and free-electron density. Excessive doping will lead to a high loss waveguide and elevated laser threshold current densities, which should be avoided.

We can see then that it is important to calculate the refractive index, loss coefficient and the plasma frequency of the semiconductor materials as a function of the free-carrier density as well of the wavelength if we are to obtain the necessary information to optically model the waveguides of QC lasers.

3.1 Spectral regions of interaction between light and a semiconductor medium

Moving from high to low wavelength, the optical spectrum of an intrinsic semiconductor can be divided up into several regions: static and far-infrared, reststrahlen, transparent, bandgap, and visible and ultraviolet (visible-UV).[3] In the bandgap region, the electromagnetic radiation frequency is resonant with interband electron transitions. Photons with energy $\hbar\omega > E_g$ can be annihilated by excitation of electrons from the valence band to the conduction band, so that this region is characterised by high values of absorption and refractive index. In the reststrahlen region, the electromagnetic radiation field interacts with optical phonons;

fundamental lattice vibrations of the semiconductor crystal. This is possible since the frequency of the lattice vibrations is resonant with the frequency of the light travelling through the semiconductor. Energy is then exchanged between the propagating radiation field and crystal lattice.[4] Between the bandgap and reststrahlen regions lies the "transparent" region, broadly defined as the spectral region for which the absorption coefficient, $\alpha < 1\text{cm}^{-1}$.[4] In this region, the imaginary part ε_2 of the dielectric constant $\varepsilon = (\varepsilon_1 + i\varepsilon_2)$, tends to zero and consequently the refractive index $n \approx (\varepsilon)^{1/2}$.

At these long wavelengths, the dielectric permittivities of binary and ternary semiconductors are highly sensitive to the doping density. This is due to an additional resonance of the electromagnetic field with free-carriers plasma excitations (plasmons).[4] A plasma is a large, electrically neutral collection of charged particles possessing opposite signs. A plasma oscillation is an organised motion of a collection of charged particles resulting from the long-range correlations caused by Coulomb interactions.[5]

Several theoretical tools are at hand to help predict the dielectric constant at energies below the band-gap energy:

- interpolation from empirical binary semiconductor values (but only undoped data exists in general), [4, 6]
- multiple-oscillator models to account for optical phonon contributions, [3, 4, 6, 7, 8, 9]
- a classical Drude model to account for free-carrier contributions. [4, 6, 8, 9]

They may be used in combination to best determine the optical constants of the material under study.

3.2 Interpolation

The relative permittivity of a medium containing a mixture of dipoles of i^{th} type, having polarizability of α_i and occurring with a density N_i per unit volume is given by the Clausius-Mosotti relation, [4, 6]

$$\frac{\varepsilon - 1}{\varepsilon - 2} = \frac{1}{3}\sum_i N_i \alpha_i . \qquad (3\text{-}1)$$

From this relationship we can obtain $\varepsilon(x)$ for a ternary semiconductor $A_{1-x}B_xC$ where A and B each represent a group III element and C represents a group V element from The Periodic Table, [4, 6]

$$\frac{\varepsilon(x) - 1}{\varepsilon(x) + 2} = (1 - x)\frac{\varepsilon_{AC} - 1}{\varepsilon_{AC} + 2} + x\frac{\varepsilon_{BC} - 1}{\varepsilon_{BC} + 2}. \qquad (3\text{-}2)$$

3.3 Dielectric permittivity of a medium

The complex dielectric function which describes the optical properties of a medium at all photon energies, $E = \hbar\omega$, can be written as, [6]

$$\varepsilon(\omega) = \varepsilon_1(\omega) + i\varepsilon_2(\omega), \qquad (3\text{-}3)$$

where ε_1 and ε_2 are the real and imaginary parts of ε, respectively, and ω is the optical frequency (rad s^{-1}). Similarly, the complex refractive index is given by,[6]

$$n^*(\omega) = n(\omega) + ik(\omega) = \left[\varepsilon_1(\omega) + i\varepsilon_2(\omega)\right]^{1/2}, \tag{3-4}$$

where $n(\omega)$ is the real refractive index and $k(\omega)$ is the extinction coefficient.

It follows that $n(\omega)$ and $k(\omega)$ may be calculated from,[6]

$$n(\omega) = \left(\frac{\left[\varepsilon_1(\omega)^2 + \varepsilon_2(\omega)^2\right]^{1/2} + \varepsilon_1(\omega)}{2} \right)^{1/2}, \tag{3-5}$$

and

$$k(\omega) = \left(\frac{\left[\varepsilon_1(\omega)^2 + \varepsilon_2(\omega)^2\right]^{1/2} - \varepsilon_1(\omega)}{2} \right)^{1/2}. \tag{3-6}$$

The frequency-dependent absorption coefficient $\alpha(\omega)$ (units: cm^{-1}) in the material is then given by, [6]

$$\alpha(\omega) = \frac{4\pi}{\lambda} k(\omega), \tag{3-7}$$

where λ is the free-space wavelength (m). Therefore, from a knowledge of $\varepsilon(\omega)$ we can calculate n and α for the medium at any frequency.

3.4 Modelling of the dielectric permittivity of binary semiconductors

3.4.1 Single harmonic oscillator model for reststrahlen regime

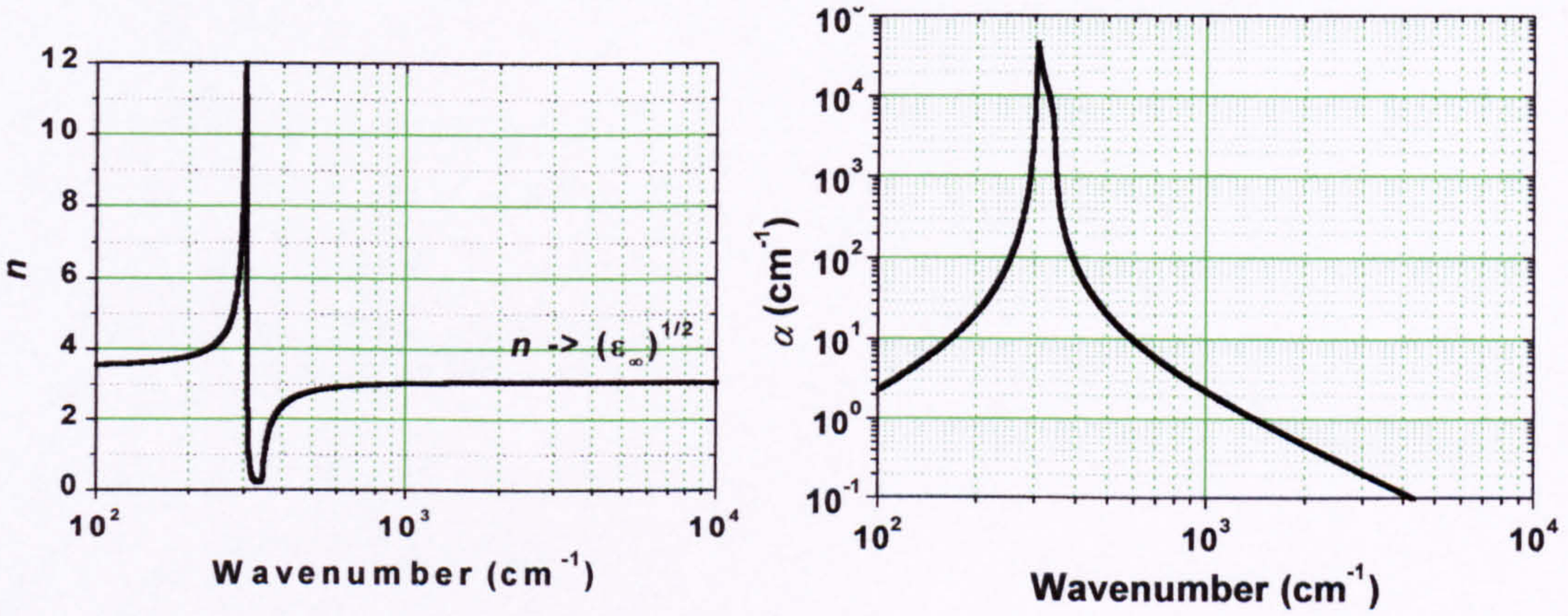

Figure 9 Refractive index n and absorption coefficient α calculated for InP at T = 300 K using Eq. (3-8) and the material parameters listed in Table 3.

For a pure binary semiconductor (e.g. semiinsulating InP or GaAs), the complex dielectric permittivity in the reststrahlen region can be described using a single harmonic oscillator model, [3, 4, 6]

$$\varepsilon(\omega)=\varepsilon_{\infty}\left(1+\frac{\omega_{LO}^2-\omega_{TO}^2}{\omega_{TO}^2-\omega^2-i\omega\gamma_{ph}}\right), \tag{3-8}$$

where ω_{LO} and ω_{TO} are, respectively, the long-wavelength longitudinal-optical and transverse-optical phonon frequencies. The phonon damping constant γ_{ph}, is a phenomenological term that is introduced to approximate phonon-phonon coupling.[10] Owing to the anharmonicity of the lattice motion in real crystals, energy is exchanged between phonons so that the oscillations are damped. To the first approximation, this can be expressed by the inclusion of a velocity-dependant damping term. The high-frequency permittivity ε_{∞} of the semiconductor represents the contribution from bound electrons which, at photon energies well below the band-gap, can be considered dispersion-free in the long-wavelength limit.

Figure 9 shows $n(\omega)$ and $\alpha(\omega)$ calculated using Eq. (3-8) and the material parameters listed in Table 3 for non-conducting InP at $T = 300$ K. Below the reststrahlen region (i.e. $\omega \lesssim 300$ cm^{-1}) the absorption falls off towards zero and the refractive index asymptotically approaches $(\varepsilon_0)^{1/2}$ as ε tends to the low frequency (static) dielectric constant ε_0. In the reststrahlen region, centred near $\omega \approx 300$ cm^{-1}, photons can be annihilated by excitation of long wavelength optical mode phonons, producing a strong absorption peak in this vicinity. Above the reststrahlen region lies the transparent region, where $\alpha(\omega) \approx 0$ and $n \approx (\varepsilon)^{1/2}$. In the spectra range $\omega = 1000 - 2000$ cm^{-1}, the ranges $n = 3.054 - 3.089$ and $\alpha = 2.3 - 0.5$ cm^{-1} were calculated.

Of course, this model does not account for the rise in absorption and refractive index for frequencies nearing the bandgap region, but as we will soon see, the bandgap region is far enough beyond the area of interest as to have negligible effect, especially when the semiconductor is doped.

3.4.2 Comparison with measured data

In the case of InP we are fortunate enough to have some actual experimental data on $n(\omega)$ from the literature. This provides an opportunity to examine the validity of the reststrahlen model. Pikhtin and Yas'kov used a semiempirical method for the calculation of the refractive index in semiconductors in the transparent region.[11] They obtained the following equation for the refractive index,

$$n=\sqrt{1+\frac{A}{\pi}\ln\frac{E_1^2-(\hbar\omega)^2}{E_0^2-(\hbar\omega)^2}+\frac{G_1}{E_1^2-(\hbar\omega)^2}+\frac{G_2}{E_2^2-(\hbar\omega)^2}+\frac{G_3}{E_3^2-(\hbar\omega)^2}}\,. \tag{3-9}$$

The parameter G_3 was determined using,

$$G_3=\left(1+\frac{2A}{\pi}\ln\frac{E_1}{E_0}+\frac{G_1}{E_1^2}+\frac{G_2}{E_2^2}\right)\left[(\hbar\omega_{LO})^2-(\hbar\omega_{TO})^2\right]. \tag{3.10}$$

Generally, with all of the other parameters being known through existing experimental data, the parameters G_1 and G_2 were the only remaining unknowns, and were regarded as being adjustable. Pikhtin and Yas'kov found their values by fitting measured refractive index data to Eq. (3-9). The values of the parameters which were obtained by Pikhtin and Yas'kov by fitting to published refractive index data of Pettit and Turner for $T = 298$ K, and Voronkova *et al.* for $T = 77$ K are given in Table 4.

Material	Parameter	Value at T=77K	Value at T=300 K	Unit
InP	Conduction band edge electron effective mass m_{CBEeff} / m_e	0.084 [7]	0.079 [7]	-
	Band gap energy Eg	1.412 [12]	1.344 [7]	meV
	Spin-off spilt-off energy gap Δ_0	-	0.108 at T = 5 K [7]	meV
	ε_∞	9.3 [13]	9.52 [13]	-
	ω_{LO}	-	345.0 [7]	cm^{-1}
	ω_{TO}	-	303.7 [7]	cm^{-1}
	γ_{ph}	-	3.5	cm^{-1}
InAs	ε_∞	-	12.25 [6, 7]	-
	ω_{LO}	-	238.6 [7]	cm^{-1}
	ω_{TO}	-	217.3 [7]	cm^{-1}
	γ_{ph}	-	2.9 [28]	cm^{-1}
AlAs	ε_∞	-	8.16 [14]	-
	ω_{LO}	403.6 [15]	401.7 [15]	cm^{-1}
	ω_{TO}	363.8 [15]	361.8 [15]	cm^{-1}
	γ_{ph}	7.1 [15]	8.0 [15]	cm^{-1}
GaAs	Conduction band edge electron effective mass m_{CBEeff} / m_e	0.0666 [7]	0.063 [7]	-
	Band gap energy Eg	1.508 [7]	1.424 [7]	meV
	Spin-off spilt-off energy gap Δ_0		0.341 at T = 4.2K [7]	meV
	ε_∞	10.67 [16]	10.88 [16]	-
	ω_{LO}	294.0 [16]	291.4 [16]	cm^{-1}
	ω_{TO}	271.5 [16]	268.2 [16]	cm^{-1}
	γ_{ph}	-	2 [16]	cm^{-1}
$In_{0.53}Ga_{0.47}As$	Conduction band edge electron effective mass m_{CBEeff} / m_e	0.043 [17, 18]	0.04	-
	Band gap energy Eg	806 [20]	735 [19]	meV
	Spin-off spilt-off energy gap Δ_0	375 [20]	375 [20]	meV
	ε_∞	11.09 [22], 11.36 [21]	11.57 [a], 11.61 [6]	-
	ω_{LO} (InAs-like)		233.1 [22]	cm^{-1}
	ω_{TO} (InAs-like)		225.2 [22]	cm^{-1}
	ω_{LO} (GaAs-like)		269.1 [22]	cm^{-1}
	ω_{TO} (GaAs-like)		254.6 [22]	cm^{-1}
$In_{0.52}Al_{0.48}As$	Conduction band edge electron effective mass m_{CBEeff} / m_e	0.069 at 60 K [17] 0.072 at 5 K [18]	0.065	-
	Band gap energy Eg	1.529 [19]	1.447 [19]	meV
	Spin-off spilt-off energy gap Δ_0		338 [19]	meV
	ε_∞	9.65	9.94 [a], 9.84 [22]	-
	ω_{LO} (InAs-like)	-	238 [23]	cm^{-1}
	ω_{TO} (InAs-like)	-	222	cm^{-1}
	ω_{LO} (AlAs-like)	-	372 [23]	cm^{-1}
	ω_{TO} (AlAs-like)	-	333	cm^{-1}

Table 3 Table of material parameters for InP, InAs, AlAs, GaAs, $In_{0.53}Ga_{0.47}As$ and $In_{0.52}Al_{0.48}As$ taken from various sources (referenced individually in the table).

[a] Interpolated from the binary values for InAs and GaAs using the Clausius-Mosotti relation.

T (K)	Spectral range (μm)	E_0 (eV)	E_1 (eV)	E_2 (eV)	E_3 (meV)	G_1 (eV^2)	G_2 (eV^2)	G_3 (eV^2)	Ref.
298	0.811-2.05	1.345	3.2	5.1	37.65	57.889	65.937	0.00392	11
77	2.0-28.5	1.421	3.2	5.1	37.65	97.199	37.009	0.00382	11
293	0.96-13.0	1.345	2.9	5.0	-	38.122	91.732	-	24

Table 4 Fit parameters of the semiempirical formula describing the refractive index of InP at energies above the bandgap energy.

The spectral range ($0.811 < \lambda < 2.05$) of the fit for $T = 298$ K by Pikhtin and Yas'kov did not extend very far into the transparent region, and so is not particularly useful here. However, Bogdanov *et al.* followed the work by measuring the refractive index of lightly doped ($n < 1.5\times10^{16}$ cm^{-3}) InP at $T = 293$ K and fitted their data to the oscillator approximation in Eq. (3-9) over the range $\lambda = 0.96$-13 μm.[24]

Using these parameters, the $n(\omega)$ of InP at $T = 77$K and 293 K is plotted in Figure 10. Both curves compare well with the values of refractive index obtained using the reststrahlen oscillator model back in Section 3.4.1, which is also plotted in Figure 10 for a direct comparison. As one expects, the reststrahlen model becomes inaccurate as the wavenumber moves closer to the bandgap region ($E_g = 1.344$ eV, $\omega \approx 1.08\times10^4$ cm^{-1}), but in the case of InP the deviation is negligible in the wavelength region of interest i.e. $\lambda \geq 5$ μm, or equivalently $\omega \leq 2000$ cm^{-1}.

In the fit of Bogdanov *et al.*, the curve also deviates from the reststrahlen model in the long-wavelength region, $\omega \lesssim 1400$ cm^{-1}. Bogdanov *et al.* elected not to include the contribution of lattice vibrations in the reststrahlen region to the dispersion of n (i.e. $G_3 = 0$), but nevertheless they reported that the mean square deviation between theoretical and experimental data in the range of $769 \leq \omega \leq 10417$ was just $\sqrt{(\Delta n)^2} \approx 0.005$. The discrepancy between our reststrahlen model and their curve is $\Delta n = 0.068$ at $\omega = 766$ cm^{-1}. However, measurements of $n(\omega)$ by Reynolds *et al.* in the overlapping spectral region $500 < \omega < 833$ cm^{-1} agree much better with our reststrahlen model and point to problems with the fit of Bogdanov *et al.* for $\omega \lesssim 1400$ cm^{-1}.

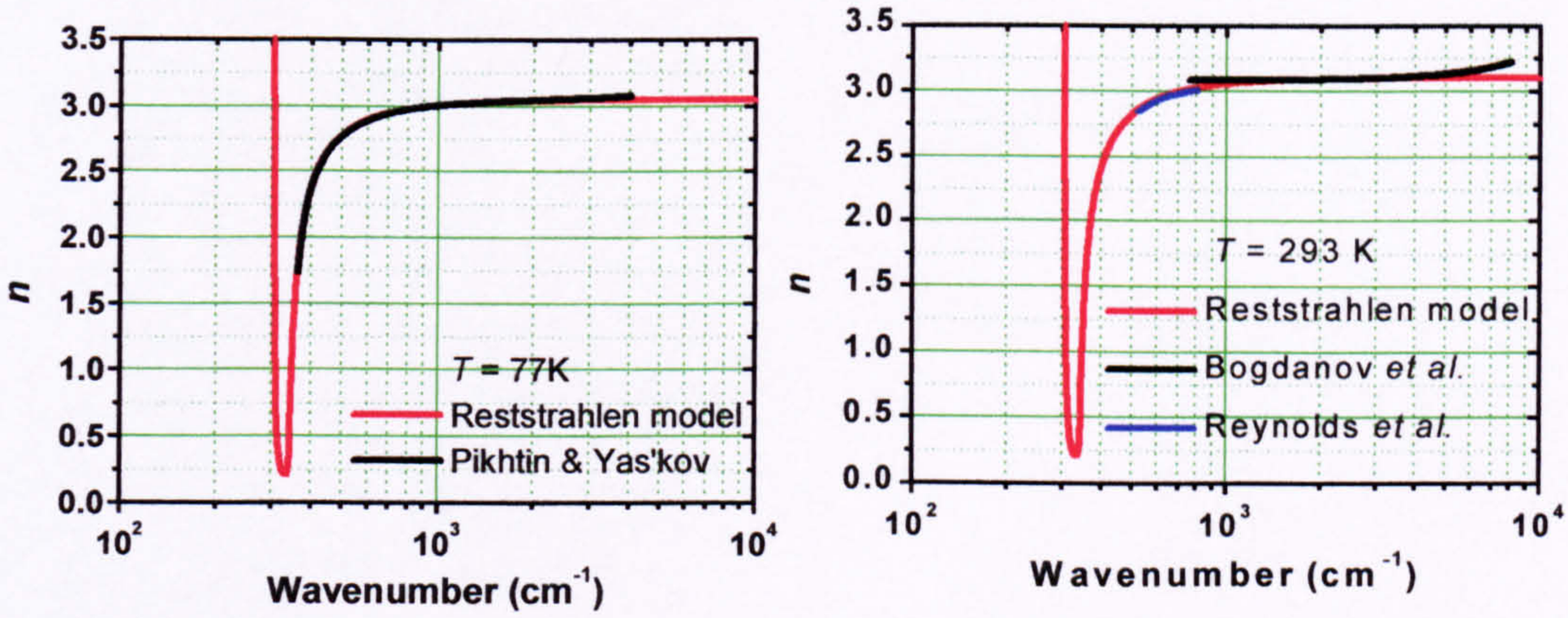

Figure 10 Comparison of the results from the single oscillator model for InP with experimental data at $T = 77$ K and at $T \approx 300$ K.

So, in summary, the reststrahlen model used for the binary InP agreed very well with the available experimental data. We now go on to extend the modelling to ternary semiconductors.

3.5 Modelling the dielectric permittivity of ternary compound semiconductors

Long-wavelength optical phonons in ternary III-V semiconductor lattices commonly exhibit "two-mode" behaviour. [4, 6] That is, two distinct sets of optical phonons exist with frequencies characteristic of each binary member of the compound, and the relative strengths of each component is roughly proportional to the respective concentration. For example, an $In_{0.47}Ga_{0.53}As$ lattice exhibits a set of InAs-like LO and TO phonon modes along with a set of GaAs-like ones.

In the case of this multimode behaviour, the dielectric permittivity can be explained by the use of a multiple oscillator model, [4, 6]

$$\varepsilon(\omega) = \varepsilon_{\infty}\left(1+\left(\sum_{j}\frac{w_{LO_j}^2 - w_{TO_j}^2}{w_{TO_j}^2 - w^2 - iw\gamma_{ph\,j}}\right)\right) \qquad (3\text{-}11)$$

where $\gamma_{ph\,j}$, ω_{LOj} and ω_{TOj}, are the phonon damping constant, and the LO and TO phonon frequencies of the j^{th} oscillator, respectively.

When two binary semiconductors AC and BC, are 'combined' to form a ternary compound $A_{1-x}B_xC$, the phonon frequencies of compounds AC and BC are modified to give "AC-like" and "BC-like" phonon frequencies. The frequency values used for the individual binary compounds should no longer be used. In general, the data is extremely scarce for these parameters. Those which were uncovered are given in Table 3 and are for $T = 300$ K (the same parameters were assumed for $T = 77$ K).

Using the parameter values for $T = 300$ K listed in Table 3, $n(\omega)$ and $\alpha(\omega)$ were calculated for $In_{0.53}Ga_{0.47}As$ and $In_{0.52}Al_{0.48}As$ using Eq. (3-11). The results for $In_{0.53}Ga_{0.47}As$ are given in Figure 11. In the spectra region $\omega = 1000$ to 2000 cm^{-1}, the ranges $n = 3.385$ to 3.401 and $\alpha = 0.6$ to 0.14 cm^{-1} were calculated. In the case of $In_{0.52}Al_{0.48}As$, for which the results are given in Figure 12, $n = 3.085$ to 3.132 and $\alpha = 6.1$ to 1.3 cm^{-1} were calculated.

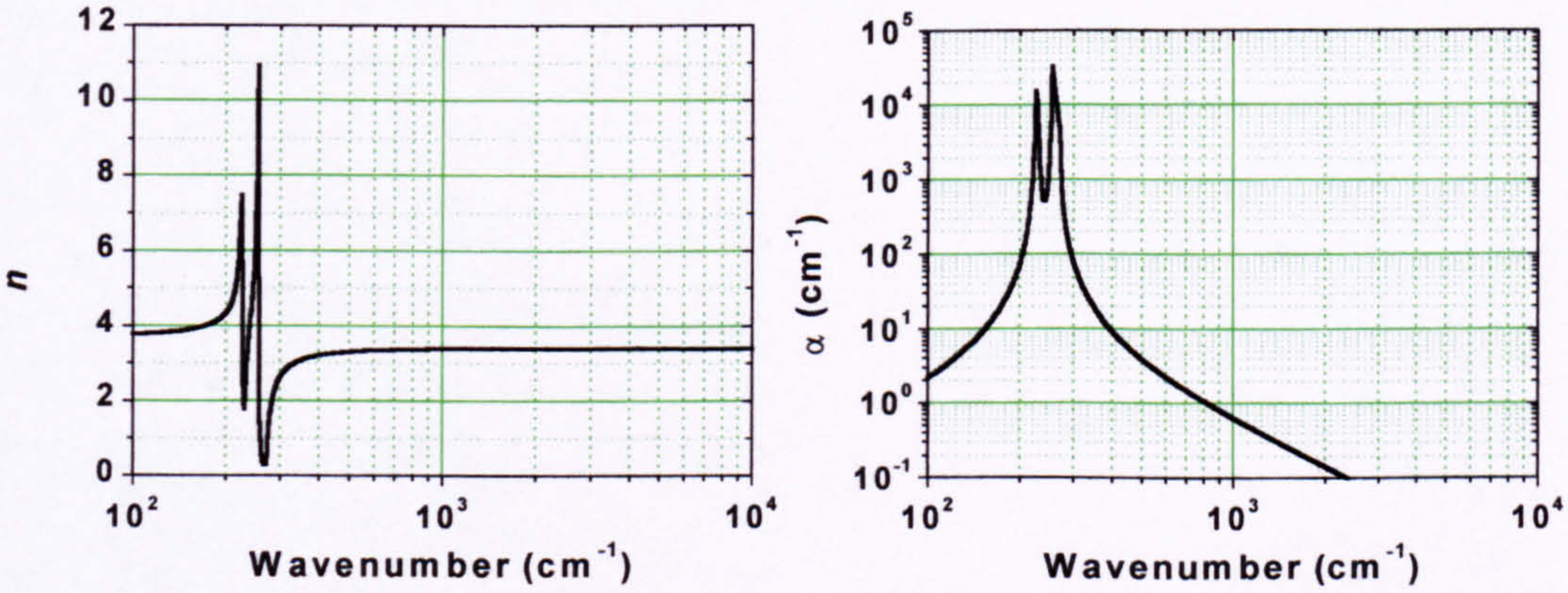

Figure 11 Refractive index n and absorption coefficient α calculated in the long-wavelength limit for $In_{0.53}Ga_{0.47}As$ at $T = 300$K.

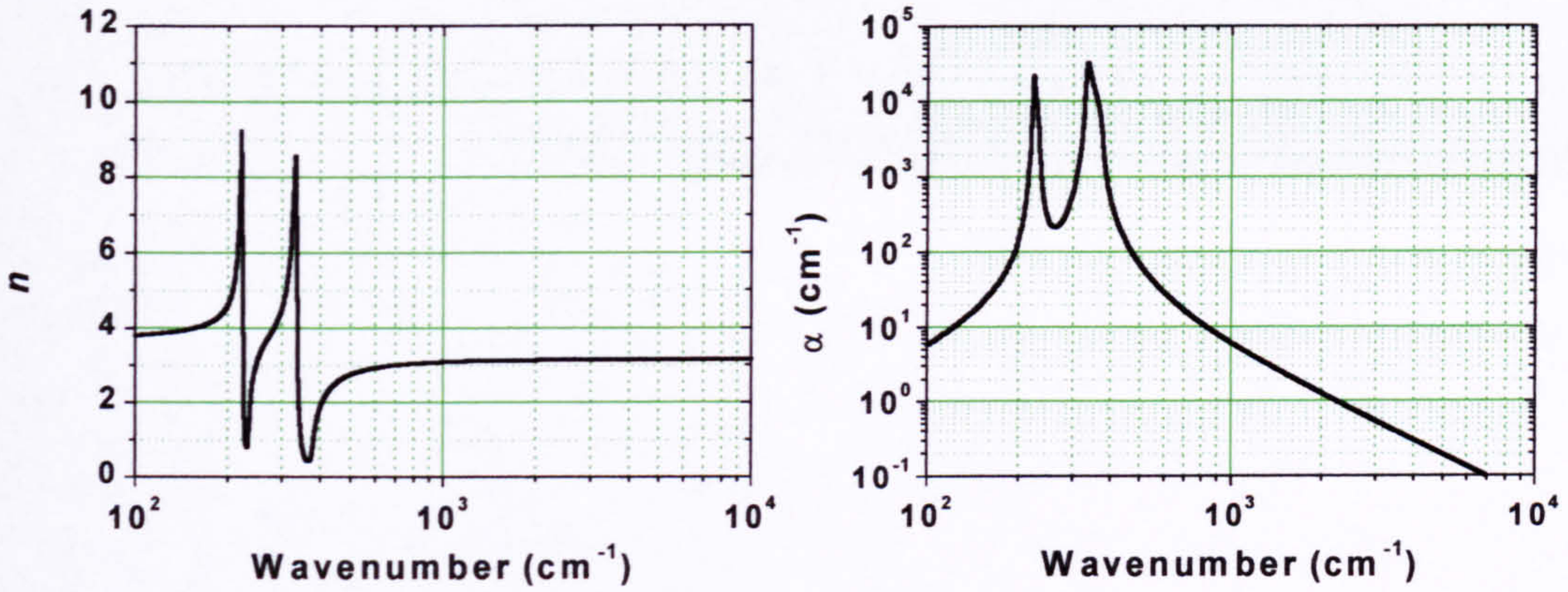

Figure 12 Refractive index n and absorption coefficient α calculated in the long-wavelength limit for $In_{0.52}Al_{0.48}As$ at $T = 300K$.

We do have one means of testing whether the values of the refractive indices are about right for these ternaries. The values of the refractive indices of the binary compounds InAs, GaAs and AlAs have been reported for the transparent region. Since $\varepsilon \approx n^2$ in the transparent region, we have the dielectric constant for each binary and so we can use the Clausius-Mosotti relation (outlined back in Section 3.2) to interpolate between the known values to find the ternary values of $n \approx \varepsilon^{1/2}$. At $\lambda = 5$ μm the values of n for InAs, GaAs and AlAs are 3.45, 3.30, and 3.38, respectively.[25, 26] Using the Clausius-Mosotti relation (Eq. (3-2)) we find $n \approx 3.13$ for $In_{0.52}Al_{0.48}As$ and $n \approx 3.38$ for $In_{0.53}Ga_{0.47}As$, in good agreement with our values calculated using the multiple-oscillator model.

Selected results for non-conducting InP, $In_{0.53}Ga_{0.47}As$, and $In_{0.52}Al_{0.48}As$ are brought together in Table 5. From these results we can see that the multiple-oscillator model predicts that the absorption of $In_{0.52}Al_{0.48}As$ will be relatively high compared to InP and $In_{0.53}Ga_{0.47}As$. The intrinsic material absorption of all three semiconductors increases by a factor of about 5 in moving from $\omega = 2000$ to 1000 cm^{-1} ($\lambda = 5$ to 10 μm). The results have interesting implications in the choice of the upper cladding semiconductor material for the QC laser. Either InP or $In_{0.52}Al_{0.48}As$ has been employed in the past. On the basis of its intrinsically lower material loss (especially at longer wavelengths), the InP would be a better choice and should give lower waveguide loss and threshold currents. Such an improvement has in fact been reported by Faist *et al.* for a QC laser with emission at $\lambda \approx 11.5$ μm.[27]

	$\omega = 2000\ cm^{-1}$		$\omega = 1000\ cm^{-1}$	
Semiconductor	***n***	**α (cm^{-1})**	***n***	**α (cm^{-1})**
InP	3.089	0.5	3.054	2.3
$In_{0.53}Ga_{0.47}As$	3.401	0.14	3.385	0.6
$In_{0.52}Al_{0.48}As$	3.132	1.3	3.085	6.1

Table 5 Refractive index and loss of undoped InP, $In_{0.53}Ga_{0.47}As$, and $In_{0.52}Al_{0.48}As$ at $\lambda = 5$ and 10 μm.

Up until now, we have been looking at undoped semiconductor materials, but the layers in a QC laser are highly doped and this has a large effect on ε. The contribution of free carriers to ε is now addressed.

3.6 Doped semiconductors and the free carrier contribution to the dielectric permittivity

If free carriers are present, as is usually the case when the semiconductor is doped, then plasma contributions to $\varepsilon(\omega)$ must also be included. The collective excitation of the free-carrier electron gas (plasma) modifies the infrared absorption by phonons since the two excitations interaction via their macroscopic electric fields. The following expression for the complex permittivity can then be used, [6, 8]

$$\varepsilon(\omega) = \varepsilon_\infty \left(1 + \left(\sum_j \frac{w_{LO_j}^2 - w_{TO_j}^2}{w_{TO_j}^2 - w^2 - iw\gamma_{ph\,j}}\right) - \frac{w_p^2}{\omega\left(\omega + i\gamma_{pl}\right)}\right), \tag{3-12}$$

where ω_p is the plasma frequency and γ_{pl} is the plasmon damping constant (rad s^{-1}). γ_{pl} can be calculated using, [8]

$$\gamma_{pl} = \frac{e}{\mu m^*}, \tag{3-13}$$

where e, μ , m^* are, respectively, the charge, mobility, and effective mass of the electrons in the semiconductor. In the case where the semiconductor is n-type doped with an free electron density of n_e (cm^{-3}) the plasma frequency, ω_p (rad s^{-1}) is given by, [6]

$$\omega_p = \sqrt{\frac{n_e e^2}{m^* \varepsilon_\infty \varepsilon_0}}. \tag{3-14}$$

However, the plasma frequency is not the only free electron density-dependant term; both the electron mobility μ and electron effective mass m^* are also dependant on n_e.[9, 28, 29, 30, 31, 32, 33] The contribution of impurity scattering to electron scattering increases with the density of dopant ions, leading to a reduction in μ. In the forthcoming section we develop empirical formulae to describe $\mu(n_e)$ for each material considered. Then, in Section 3.6.2, we introduce a theoretical approach to calculate $m^*(n_e)$, and hence $\omega_p(n_e)$. Once all that has been done we will be able proceed with the calculation of the refractive index and loss for each material, beginning in Section 3.6.3.

3.6.1 Dependence of the Electron Mobility on Free-carrier Density

3.6.1.1 Electron mobility in $In_{0.53}Ga_{0.47}As$

Data was extracted from plots of existing experimental data for MBE grown $In_{0.53}Ga_{0.47}As$ and $In_{0.52}Al_{0.48}As$.[34] The dependence of the Hall mobility, μ ($cm^2\ s^{-1}\ V^{-1}$), on the free-carrier density n_e, was fitted to polynomials. With $N = n_e / 1\times10^{17}$ cm^{-3}, polynomial regression of the data for $In_{0.53}Ga_{0.47}As$ doped with silicon over the range $0.1 < N < 100$ yielded,

$$\log_{10}\mu = 3.91743 - \left(0.2585\times\log_{10}N\right) + \left(0.0657\times\left(\log_{10}N\right)^2\right) - \left(0.03539\times\left(\log_{10}N\right)^3\right), \tag{3-15}$$

for the $T = 77$ K data and,

$$\log_{10}\mu = 3.77898 - (0.12786 \times \log_{10} N) + (2.73356 \times 10^{-4} \times (\log_{10} N)^2) - (0.02739 \times (\log_{10} N)^3) \quad (3\text{-}16)$$

for the data at $T = 300$ K.

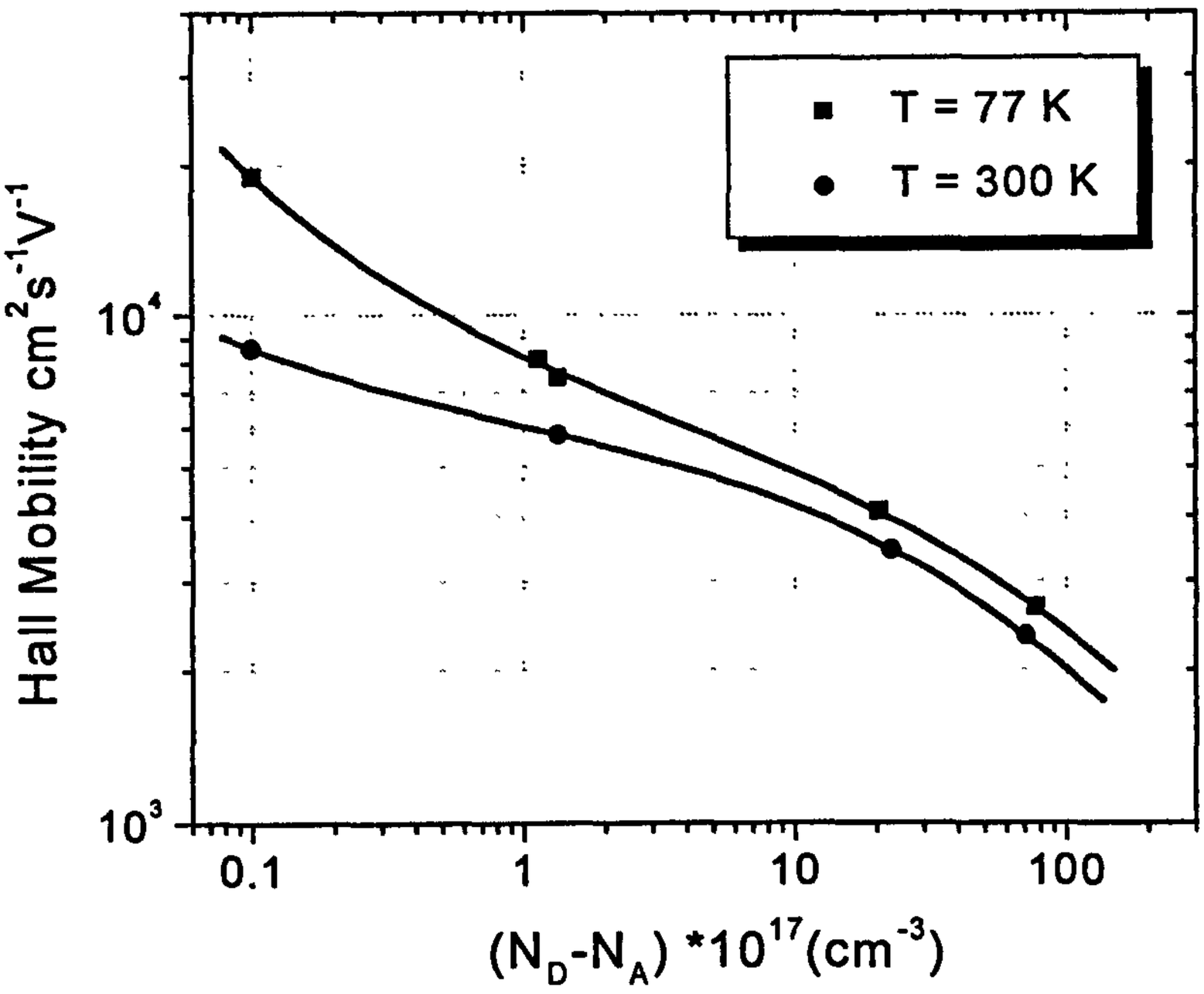

Figure 13 The dependence of the Hall mobility of $In_{0.53}Ga_{0.47}As$ on free-carrier density at $T = 77$ and 300 K.[34]

3.6.1.2 Electron mobility in $In_{0.52}Al_{0.48}As$

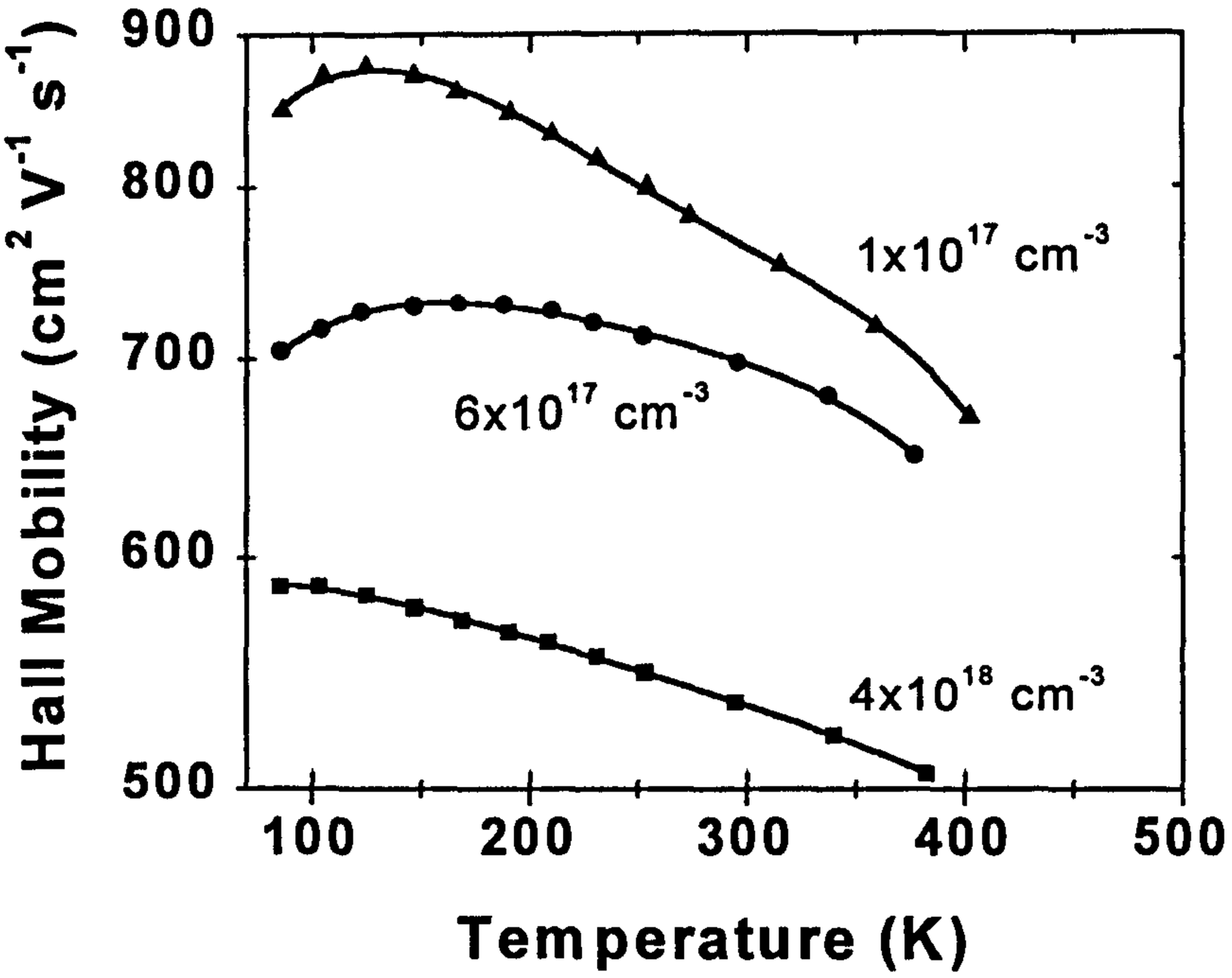

Figure 14 Temperature dependence of the Hall mobility of $In_{0.52}Al_{0.48}As$ as a function of doping level for samples doped at 1×10^{17}, 6×10^{17} and 4×10^{18} cm^{-3}.[35]

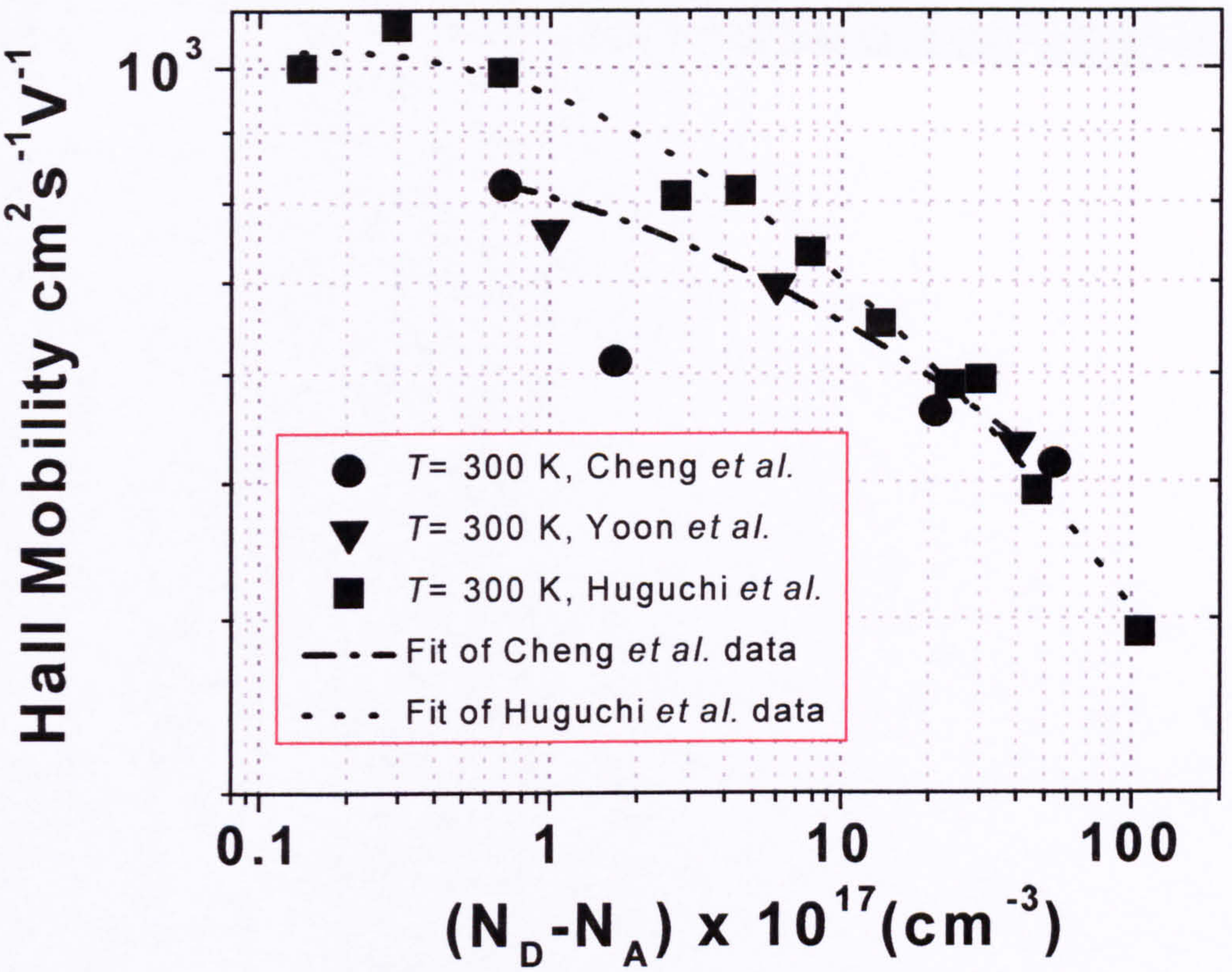

Figure 15 The dependence of the Hall mobility of $In_{0.52}Al_{0.48}As$ on free-carrier density. Three sets of points are shown which are taken from Yoon *et al.*[35], Cheng *et al.* [34], and Higuchi *et al.* Two polynomial fits are shown, one of the Cheng *et al.* data and one of the data of Higuchi *et al.*.

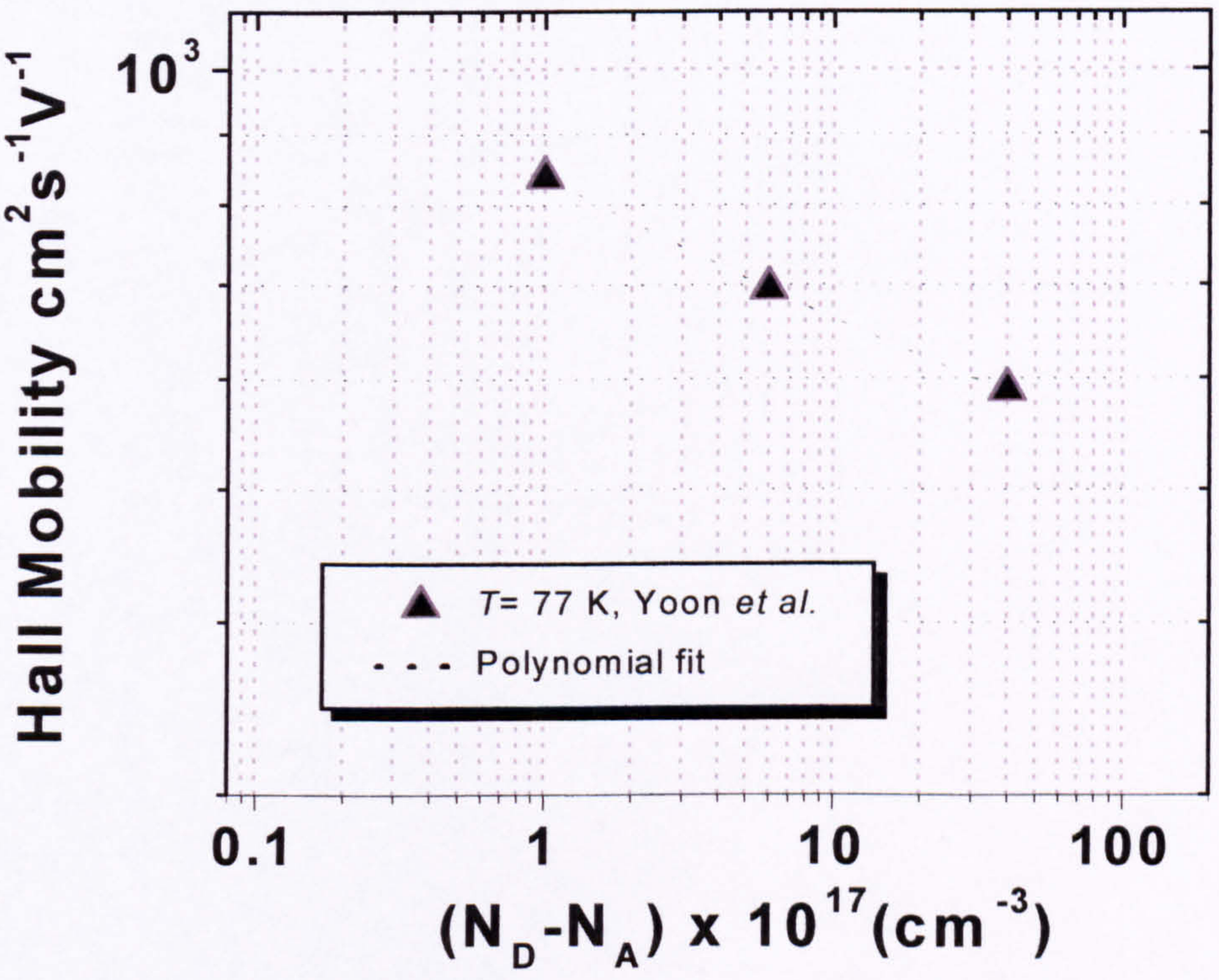

Figure 16 The dependence of the Hall mobility of $In_{0.52}Al_{0.48}As$ on free-carrier density at T = 77K. The data points were calculated from data extracted from plots made by Yoon *et al.*.[35]

Hall measurements made by Yoon *et al.* on $In_{0.52}Al_{0.48}As$ samples Si-doped at 1×10^{17}, 6×10^{17} and 4×10^{18} cm^{-3} give the values of the electron mobility at a number of temperatures between 85 and 400 K. The data points (see Figure 14) for each doping level were taken from the Ref. 35 and fitted by the following polynomial expressions:

$$\mu = 551 + (6.38133 \times T) - (0.04223 \times T^2) + (1.0811 \times 10^{-4} \times T^3) - (1.01369 \times 10^{-7} \times T^4) \quad (3\text{-}17)$$

$$\mu = 539 + (3.26823 \times T) - (0.01956 \times T^2) + (4.9396 \times 10^{-5} \times T^3) - (4.89281 \times 10^{-8} \times T^4) \quad (3\text{-}18)$$

$$\mu = 575 + (0.42388 \times T) - (0.00409 \times T^2) + (1.04038 \times 10^{-5} \times T^3) - (1.00894 \times 10^{-8} \times T^4) \quad (3\text{-}19)$$

From these polynomials, the mobilities at $T = 77$ K and 300 K were estimated. The points for $T = 300$ K are plotted in Figure 15 along with data taken from Cheng *et al.*[34] and Higuchi *et al.*.[36] There was a significant difference between the data of Higuchi *et al.* and Cheng *et al.*, particularly at lower doping levels. It was decided to make separate polynomial fits for the two sets of data and try both of them to gauge the sensitivity of the calculated n and α to the electron mobility data used. The polynomial fit of the Cheng *et al.* data gave,

$$\log_{10}\mu = 2.9072 - (0.05941 \times \log_{10} N) - (0.03159 \times (\log_{10} N)^2), \quad (3\text{-}20)$$

for $0.7 < N < 60$, where N is $n_e / 1\times10^{17}$ (cm^{-3}).

The data of Higuchi et al. covered a greater range of carrier density, $0.2 < N < 100$, and gave,

$$\log_{10}\mu = 2.98058 - (0.08133 \times \log_{10} N) - (0.05225 \times (\log_{10} N)^2). \quad (3\text{-}21)$$

The polynomial fit of the data for $T = 77$ K yielded,

$$\mu = 837.8 - (208.5089 \times \log_{10} N) + (32.78418 \times (\log_{10} N)^2),$$

for $1 \le N \le 40$. The data points and polynomial fit are shown in Figure 16.

3.6.1.3 Electron mobility in InP

The electron mobility in InP was found by Anderson *et al.* to be nearly identical for all n-type dopants, Si, Sn, S, Se and Ge.[30] The data showed very little spread, except at doping levels below ~$1*10^{16}$ cm^{-3}. The mean of all measurements at $T = 77$ K and at $T = 300$ K made were tabulated by Anderson *et al.*. Polynomial regressions were performed on the data which yielded,

$$\log_{10}\mu = 3.63262 - (0.48681 \times \log_{10} N) + (0.14559 \times (\log_{10} N)^2) + (0.00288 \times (\log_{10} N)^3) - (0.01235 \times (\log_{10} N)^4) \quad (3\text{-}22)$$

for the $T = 77$ K data and,

$$\log_{10}\mu = 3.53769 - (0.14926 \times \log_{10} N) - (0.04904 \times (\log_{10} N)^2) \quad (3\text{-}23)$$

for the data at $T = 300$ K, where N is $n_e / 1\times10^{17}$ (cm^{-3}) and μ (cm^2 s^{-1} V^{-1}). The data is plotted in Figure 17 along with the polynomial fitting expressions.

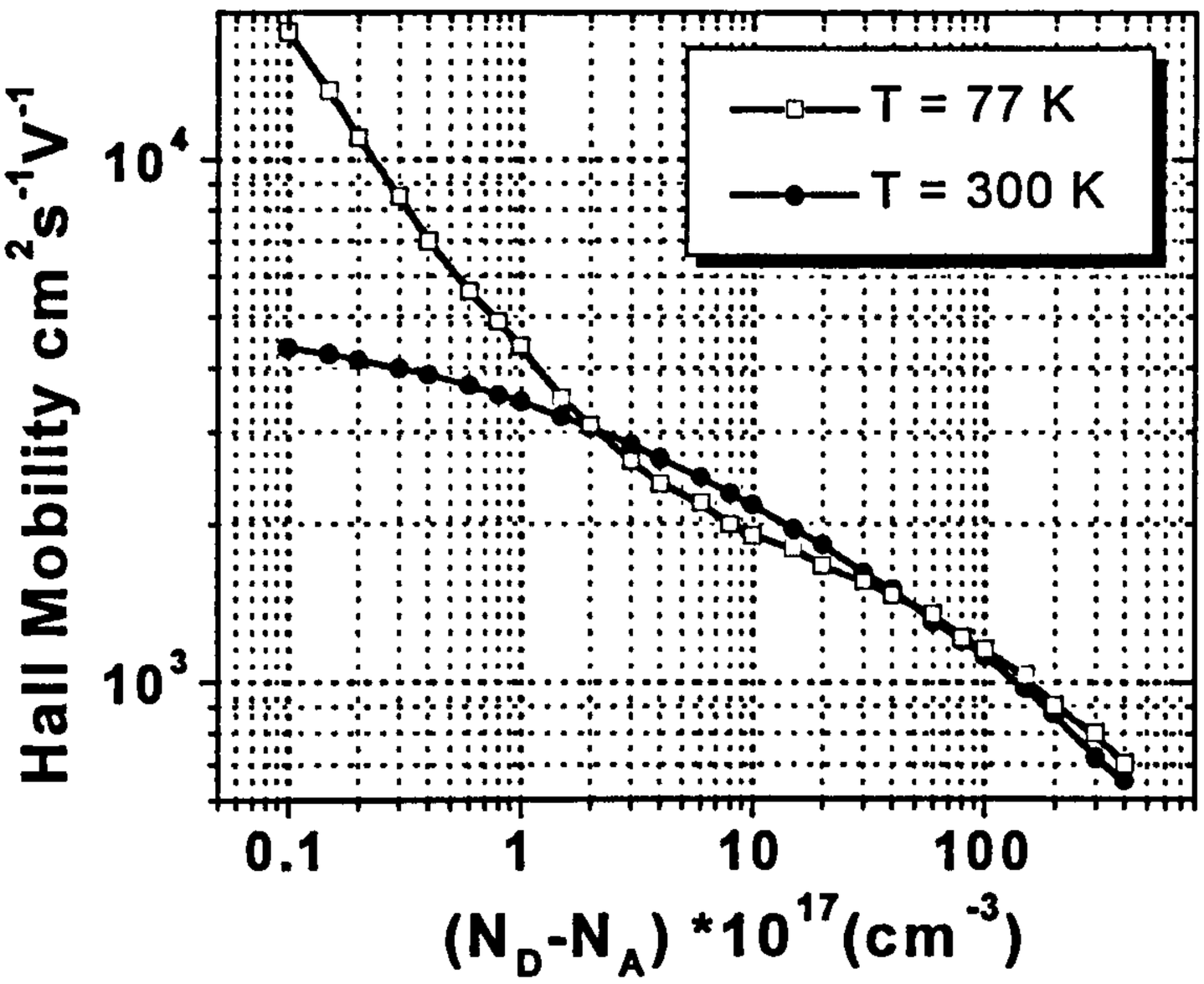

Figure 17 The dependence of the Hall mobility of InP on free-carrier density at $T = 77$ and 300 K. [30]

3.6.2 Dependence of the Electron Mass on Free-carrier Density

If the effective mass term was unchanged by the free-carrier density n_e, then Eq. (3-14) implies that there would be a linear increase in ω_p^2 with n_e and that this increase would continue indefinitely. In practise, this is not the case, and ω_p^2 has been reported to saturate at high doping levels.[31] This is because there is an increase in the *average* effective mass of the electrons with increasing n_e which curbs the shift in the plasma frequency.

The effects of high doping levels on the bandstructure and electron distributions can be split into two categories;[37]

1. the effects which become apparent at high free-carrier densities such as:
   - the effects of band filling (the Burstein-Moss shift), and
   - the effects of conduction-band non-parabolicity;
2. the effects brought about by high impurity concentrations which actually perturb the electronic bandstructure such as:
   - the effects of bandgap narrowing/shrinkage/renormalisation,
   - the effects of band tails, and impurity bands.

The conduction band of a bulk semiconductor has a finite density of states, $N(E) \propto (m_{opt}^*)^{3/2}E^{1/2}$. At high doping levels, the Fermi-energy moves out of the bandgap and up into the conduction band. The finite density of states means that the lower energy states of the conduction band become filled. This results in an effective shift in the fundamental absorption edge of the semiconductor to higher energies, known as the Burstein-Moss shift or band filling.

If the conduction band is non-parabolic, as is the case to differing degrees in real semiconductors, the effective mass will be energy-dependant, denoted as the optical effective mass, $m_{opt}^*(E)$. The large population

of electrons occupying the conduction band will now exhibit a range of effective masses depending on their individual energy. In these cases the average electron effective mass, denoted here as m^*, needs to be used rather than just the conduction band edge effective mass, m_0^*. The average effective mass depends on the energy dispersion of the conduction band, $E(k)$, and the electron distribution therein.

Since the density of states $N(E) \propto (m_{opt}^*)^{3/2}E^{1/2}$ band-filling is more severe in materials with a low value of conduction-band edge effective mass, m_0^*. In these cases, the bottom of the conduction band will fill up more rapidly with increasing free-carrier density, n_e, because there are less states for the electrons at lower energies. Consequently, the Burstein-Moss shift will be more pronounced and m^* will increase more rapidly with n_e.

The semiconductor compounds under consideration in this work possess a range of values of conduction-band edge effective mass from $m_0^* = 0.043m_0$ for $In_{0.47}Ga_{0.53}As$ to $m_0^* = 0.79m_0$ for AlAs. $In_{0.52}Al_{0.48}As$ lies between the two with $m_0^* = 0.072m_0$.

It can be seen from Eq. (3-14) that for any given rise in n_e we would expect that the upwards shift in ω_p would be greater in materials which have a relatively low value of m_0^*, such as $In_{0.53}Ga_{0.47}As$, rather than that seen in a material with a higher m_0^*, such as $In_{0.52}Al_{0.48}As$. Indeed, this is the case at low doping levels; however, band-filling is more severe in the semiconductors which have small m_0^*, so that m^* will increase more rapidly with n_e at high doping levels. It is therefore possible that the m^* of the $In_{0.47}Ga_{0.53}As$ will become greater than the m^* of the $In_{0.52}Al_{0.48}As$ for high n_e. In that situation, the plasma frequency shift becomes greater in the $In_{0.52}Al_{0.48}As$. So, although the initial rise in ω_p will be greater in $In_{0.47}Ga_{0.53}As$, the value of ω_p will reach saturation earlier, and to achieve a large shift in ω_p requires a material with a higher m_0^*.

A calculation of m^* requires a description of the conduction-band energy E, as a function of momentum k, for each semiconductor considered. In the semiconductors considered here, it has been shown that, in order to obtain reasonable agreement between theory and experimental data for m^*, modelling of the bandstructure must be performed which accounts for non-parabolicity and band-filling, when using doping levels up to at least 2×10^{18} cm^{-3}. Methods such as a three-band Kane model,[28] and a triple-band effective-mass equations describing coupled conduction-band, light-hole band and the spin-split-off bands,[29] have been demonstrated in the literature. These models have shown varied success depending on which one was used, the material investigated and the doping level. Generally, the models deviate from the experimental values at very high doping levels (greater than ~ 1×10^{19} cm^{-3}). Materials which exhibit relatively low values of E_g and m_0^* become inaccurate first. Band gap narrowing, and the increasing influence of higher order bands have been suggested as the probable cause. [31]

We use a three level Kane model to describe the conduction band for this work owing to its simplicity, and accept that we will only be able to calculate the optical constants of $In_{0.53}Ga_{0.47}As$ below a doping level of ~ 5×10^{18} cm^{-3}, owing to the limitations of the Kane theory at high values of k.

3.6.2.1 Three Level Kane Model - Conduction band calculation

Following Raymond *et al.*[18] the conduction and valence bands can be described by the following equation developed by Kane:[38]

$$E'\left(E'-E_g\right)\left(E'+\Delta\right)-\hbar^2k^2p^2\left(E'+\frac{2}{3}\Delta\right)=0, \tag{3-24}$$

where,

$$E'=E-\frac{\hbar^2k^2}{2m_0^*}. \tag{3-25}$$

This assumes that the effect of higher order bands is negligible and takes $E=0$ at the top of the valence band. A development of the solution of Eq. (3-24) in powers of k up to order k^6 gives the energy of the conduction band E,[32]

$$E(k)=\frac{\hbar^2k^2}{2m_0^*}-\left(\frac{\hbar^2k^2}{2m_0^*}\right)^2\left(\frac{1+x+\frac{1}{4}x^2}{1+\frac{4}{3}x+\frac{4}{9}x^2}\right)\frac{1}{E_g} \tag{3-26}$$

where $x=\Delta/E_g$, and $E=0$ at the bottom of the conduction band. The parameter Δ is the spin-orbit splitting.

The conduction band energy dispersion calculated for InP, $In_{0.52}Al_{0.48}As$ and $In_{0.53}Ga_{0.47}As$ using Eq. (3-26) and the material parameters ($T=300$ K) listed in Table 3, are plotted in Figure 18, Figure 19 and Figure 20, respectively. The parabolic energy dispersion (i.e. $E(k)=\hbar^2k^2/2m_0^*$) are provided for comparison. The aforementioned limitations of the Kane theory in describing the energy dispersion at high values of k, especially for materials with low E_g and m_0^*, such as $In_{0.53}Ga_{0.47}As$, can be observed in the plots. At high k, one can see that the slope of the dispersion begins to move rapidly towards zero, eventually becoming negative. At this point the theory breaks down completely and is only useful for the range of k below this point. This range of k is relatively low (about half) for $In_{0.53}Ga_{0.47}As$ as compared with the InP and $In_{0.52}Al_{0.48}As$.

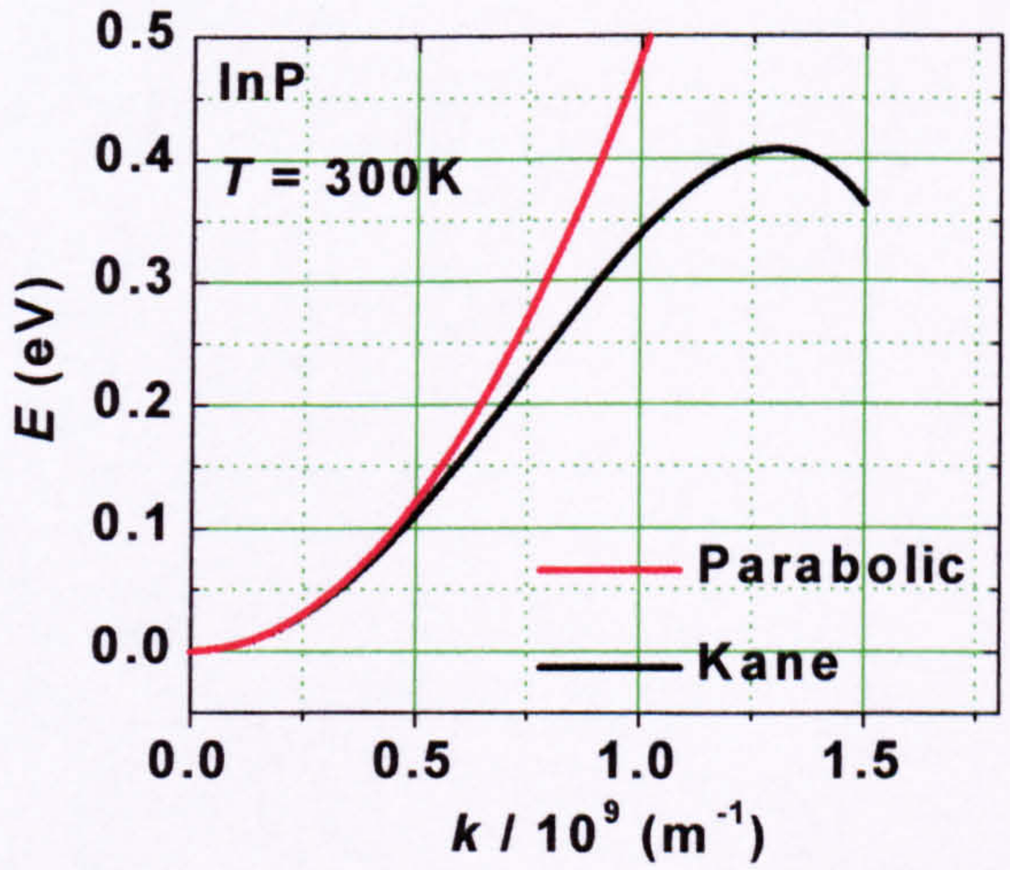

Figure 18 Calculated conduction band energy dispersion $E(k)$ for InP at T = 300K. The dispersion calculated using the Kane theory is compared with the parabolic approximation.

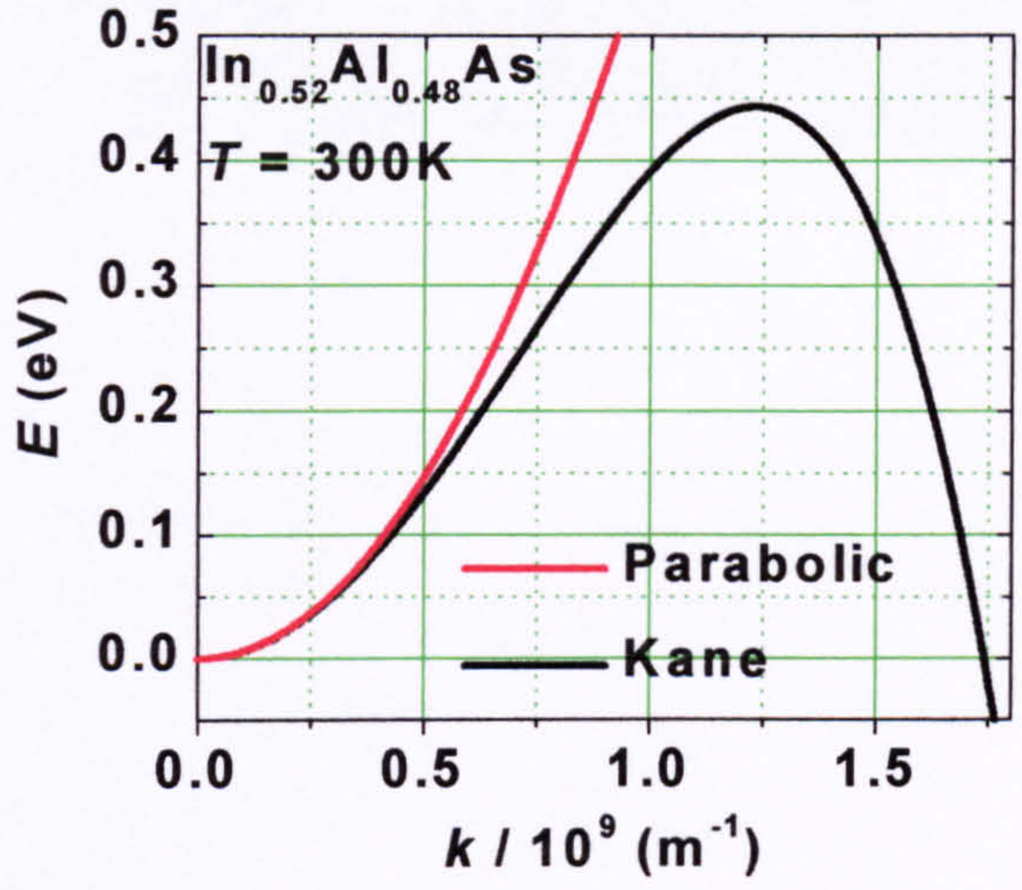

Figure 19 Calculated conduction band energy dispersion $E(k)$ for $In_{0.52}Al_{0.48}As$ at T = 300K. The dispersion calculated using the Kane theory is compared with the parabolic approximation.

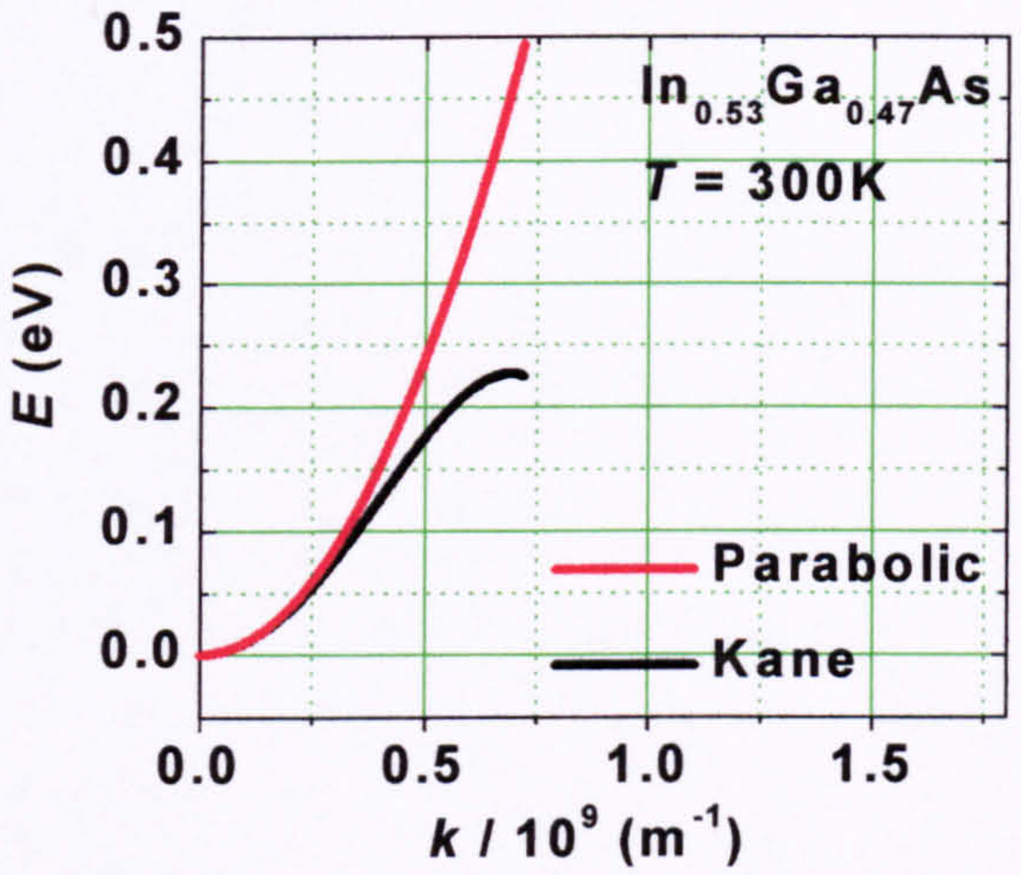

Figure 20 Calculated conduction band energy dispersion $E(k)$ for $In_{0.53}Ga_{0.47}As$ at T = 300K. The dispersion calculated using the Kane theory is compared with the parabolic approximation.

3.6.2.2 Optical effective mass

From the calculated conduction band dispersion, we can determine the optical effective mass by using the following expression,

$$m^*_{opt}(k) = \hbar^2 k \left(\frac{d}{dk} E(k) \right)^{-1} . \qquad (3\text{-}27)$$

As with all of the calculations, the differentiation of $E(k)$ was performed internally by Mathcad. Again the theory can be seen to become erroneous for large k.

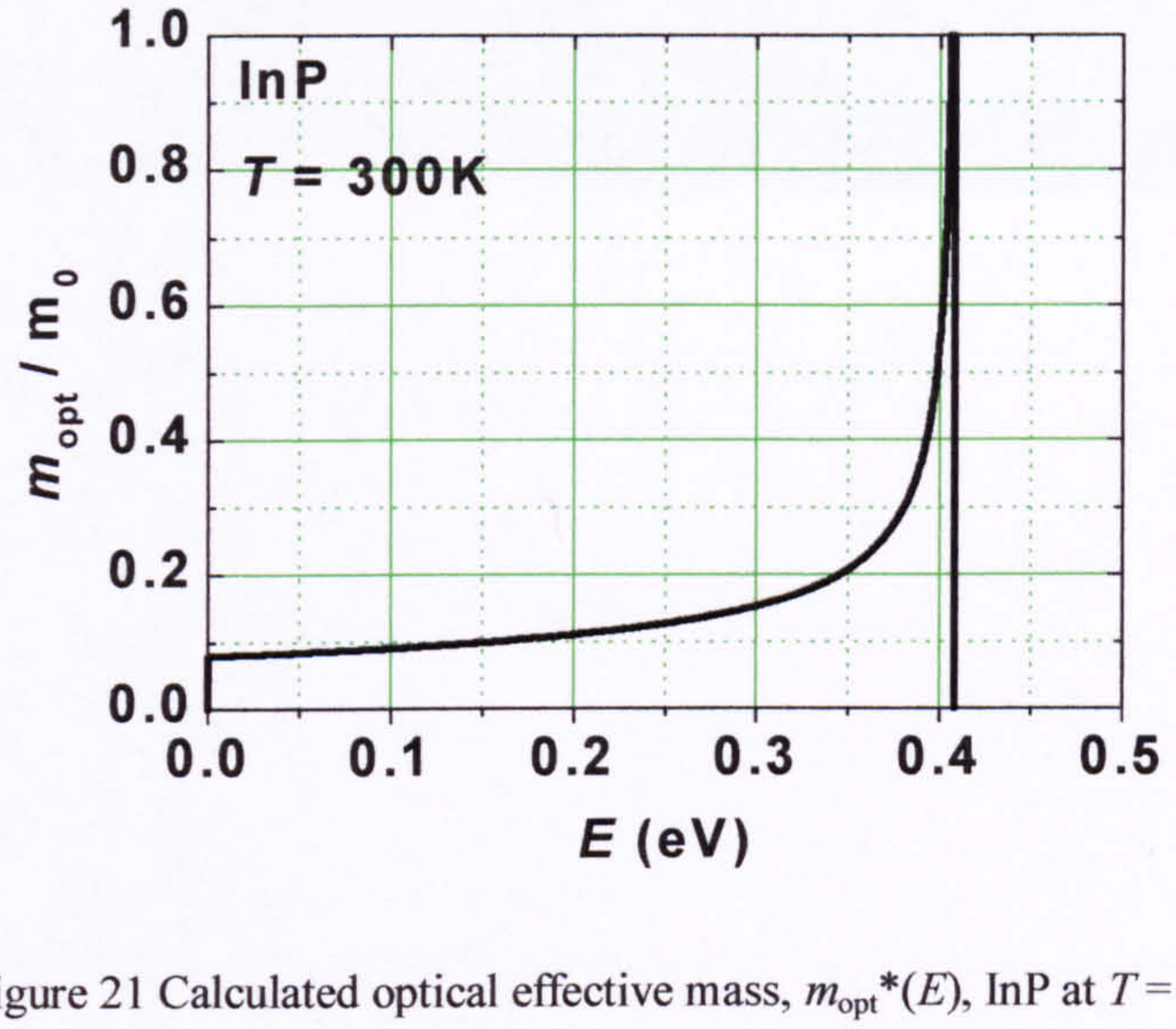

Figure 21 Calculated optical effective mass, $m_{opt}^*(E)$, InP at $T = 300$K.

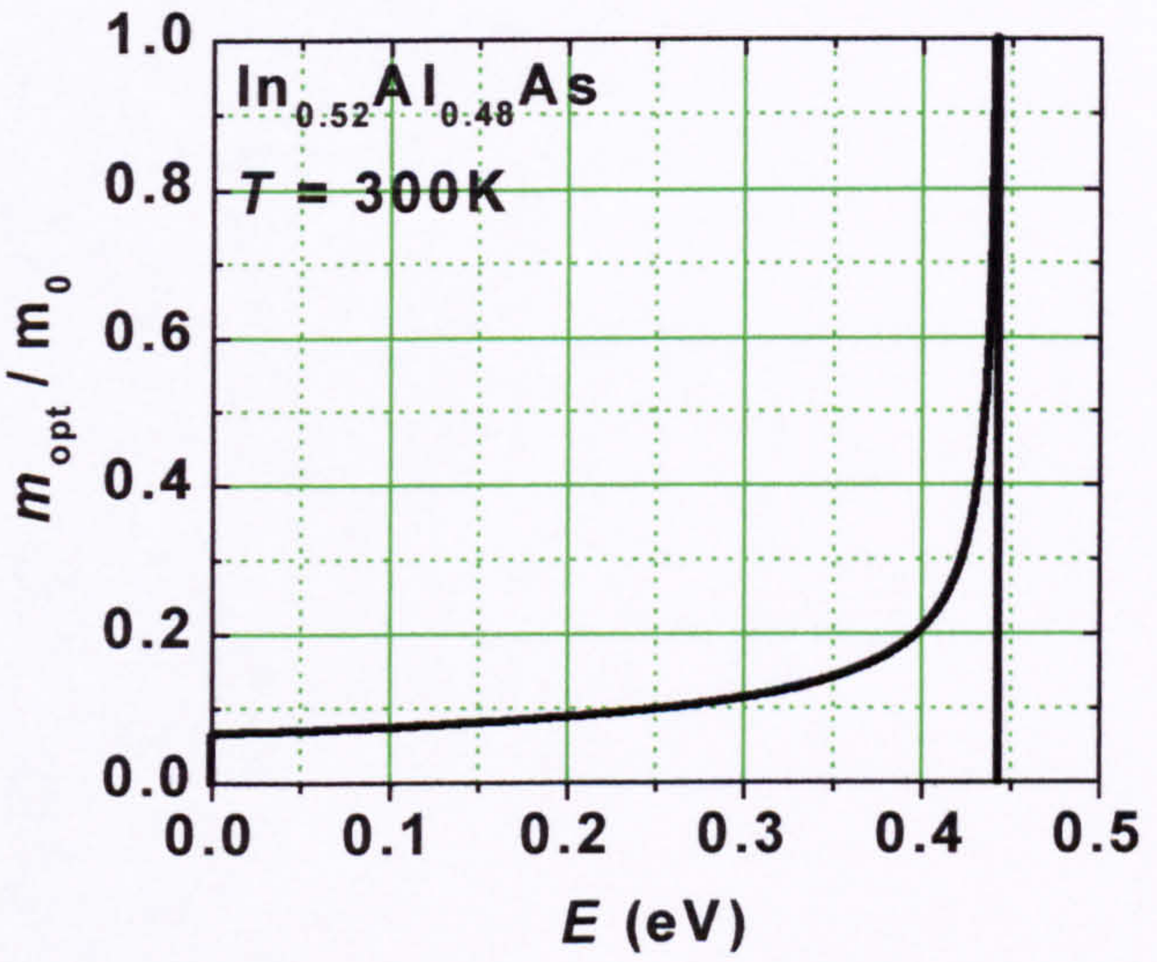

Figure 22 Calculated optical effective mass, $m_{opt}^*(E)$, for $In_{0.52}Al_{0.48}As$ at $T = 300$K.

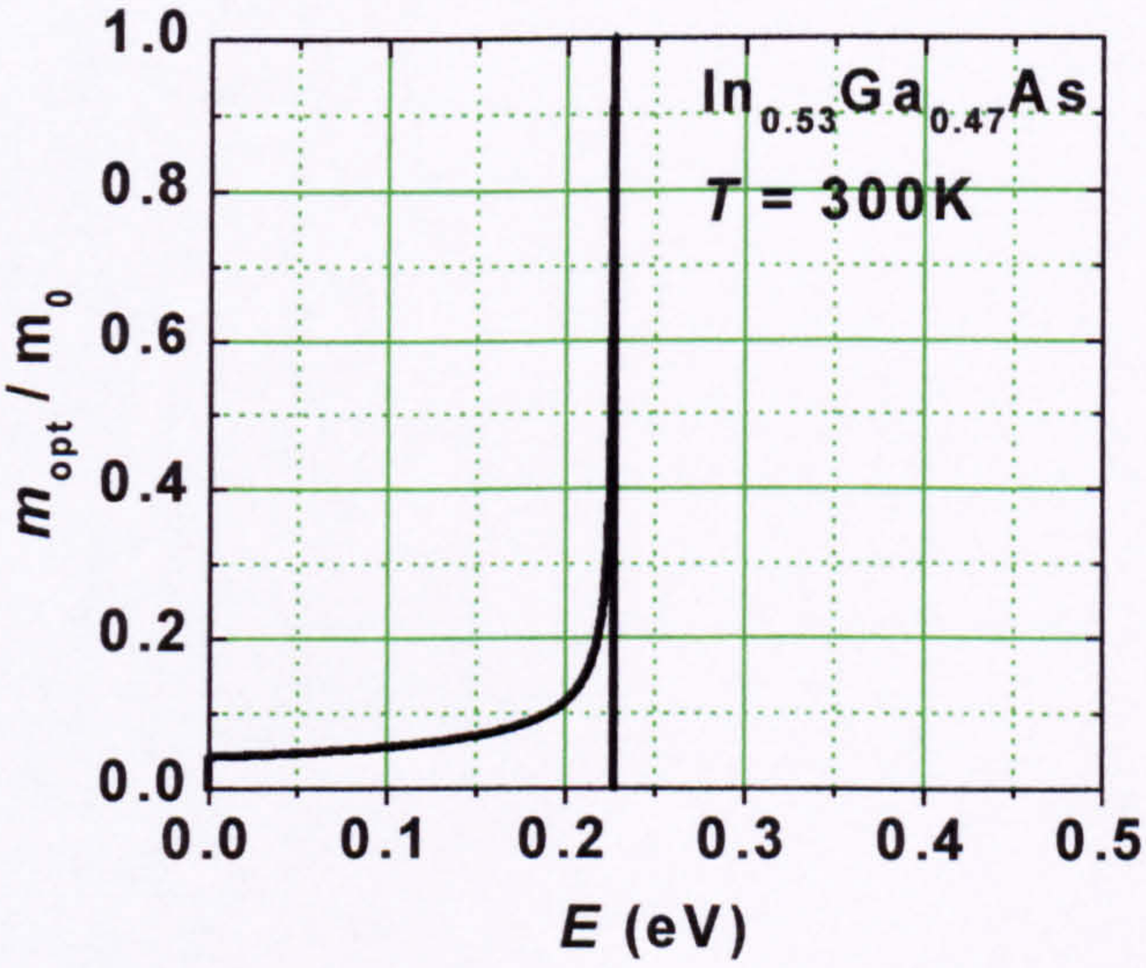

Figure 23 Calculated optical effective mass, $m_{opt}^*(E)$, for $In_{0.53}Ga_{0.47}As$ at $T = 300$K.

3.6.2.3 Density of states

Following the derivation in Appendix A, the density of states in the conduction band $N(k)$ may be expressed as,

$$N(k) = \frac{k^2}{\pi^2}\left(\frac{d}{dk}E(k)\right)^{-1}. \tag{3-28}$$

Rearranging Eq. (3-27) to obtain the expression for dE/dk and substituting it into Eq.(3-28) gives,

$$N(k) = \frac{m^*_{opt}(k)k}{\pi^2\hbar^2}. \tag{3-29}$$

This expression permits a quick way of calculating $N(k)$ given that $m_{opt}{}^*(k)$ has already been calculated.

3.6.2.4 Free-carrier density

Next we need to calculate the free-carrier density for any given value of Fermi energy E_F. This may be calculated using,

$$n_e(E_F) = \int_{E_c}^{E_b} f(k, E_F)N(k)\,dk, \tag{3-30}$$

where $f(E(k), E_F)$ is the Fermi-Dirac distribution function,

$$f(E(k), E_F) = \left[1 + \exp\left(\frac{E(k) - E_F - E_{offset}}{k_B T}\right)\right]^{-1}. \tag{3-31}$$

For $T = 0$ K, $f(E(k), E_F) = 1$ for $E \le E_F$, and $f(E) = 0$ for $E > E_F$. This means that at $T = 0$ K all of the electron states of energy $E \le E_F$ will be filled, and all electron states with energy $E \ge E_F$ will be empty. However, for $T > 0$ K a redistribution of electrons occurs and energy states above $E = E_F$ have a non-zero probability of being occupied, while the states below E_F now have a non-unity probability of being filled. As T increases the distribution moves to higher energies, so that the average effective mass increases. By including the Fermi-Dirac function inside the integral, this dependence of m^* on T is accounted for. The parameter E_{offset} permits us to investigate non-degenerate positions of the Fermi energy i.e. when E_F is in the bandgap below the conduction band minimum E_c.

In our case, we cannot evaluate the integral in Eq. (3-30) from E_c to ∞, as our expression for $E(k)$ has a limited range of validity. This is due ultimately to the limitations of the Kane theory in describing the conduction band dispersion away from $k = 0$. As discussed previously, the Kane theory looses accuracy with increasing k and breaks down completely at high k. For the sake of discussion, let us denote the energy at which the model completely breaks down as E_b (using material parameters for $T = 300$ K, $E_b \approx 400$ meV for InP, $E_b \approx 440$ meV for $In_{0.52}Al_{0.48}As$, $E_b \approx 227$ meV for $In_{0.53}Ga_{0.47}As$). Instead of $E = \infty$, we must take the upper limit as $E \le E_b$.

Unfortunately, the inclusion of $f(E(k), E_F)$ further reduces the range of E_F which can be used, and so the range of free-carrier concentrations which can be investigated. To explain, for $T = 0$ K we may use the full range $0 \le E_F < E_b$ as all of the electrons will occupy energy states below E_b. However, as soon as $T > 0$ K using $0 \le E_F < E_b$ would lead to errors since $f(E(k), E_F) > 0$ for $E > E_b$ and $f(E(k), E_F) < 1$ for $E < E_b$. Since the upper limit of the integral for $n_e(E_F)$ is restricted to $E < E_b$, this would place a part of the electron distribution

outside the range of the integral limits, obviously leading to errors. This forces us to re-examine the upper limit placed on E_F depending on the material and temperature considered. It was decided that the upper limit of $E_F = E_{lim}$ should be chosen such that $f(E_b(k), E_F) \leq 10^{-2}$ i.e. that there is an occupational probability of less than 1% at the energy E_b. For $In_{0.53}Ga_{0.47}As$ the upper limit of E_{lim} was chosen as 0.2 eV for $In_{0.53}Ga_{0.47}As$, and 0.4 eV for InP and $In_{0.52}Al_{0.48}As$.

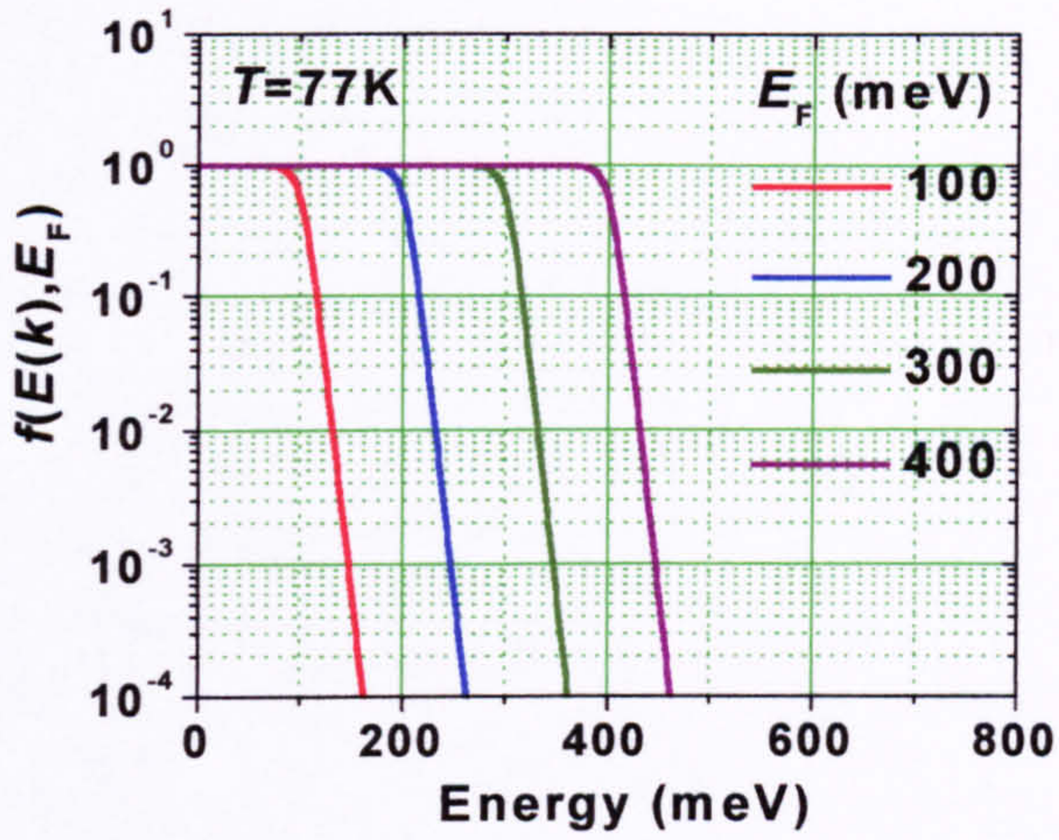

Figure 24 Fermi-Dirac function for $T = 77$ K and for $E_F = 0.1$, 0.2, 0.3 and 0.4 eV.

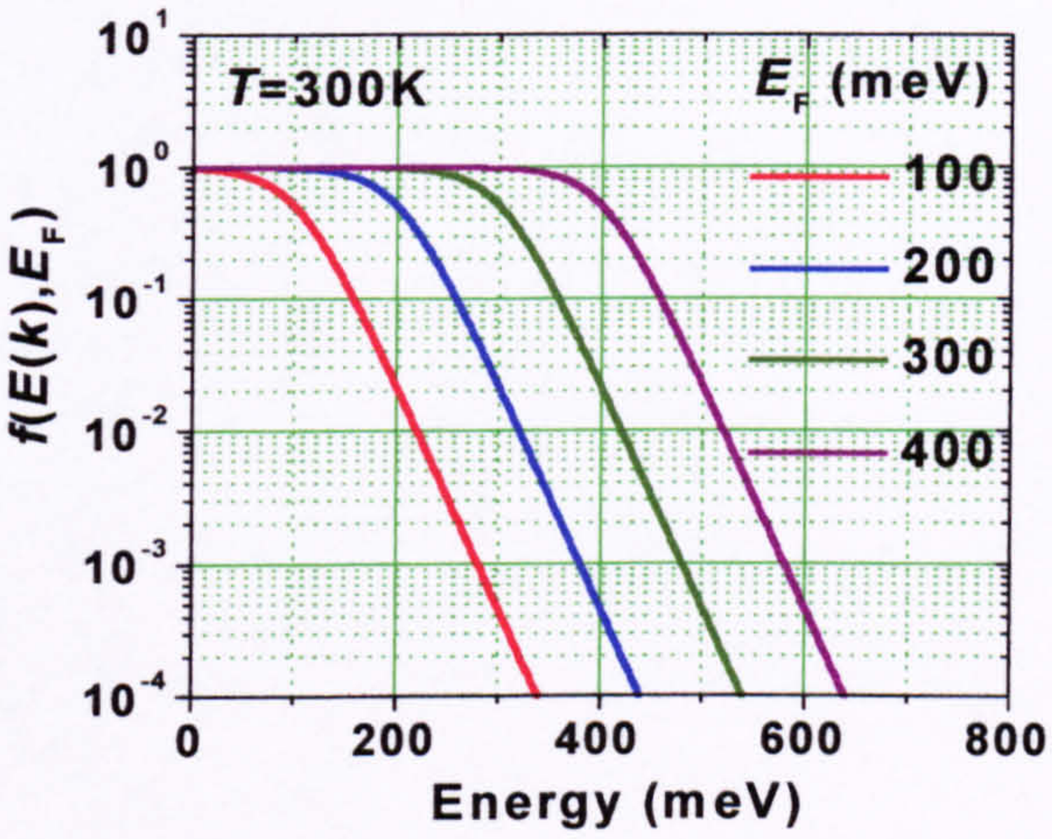

Figure 25 Fermi-Dirac function for $T = 300$ K and for $E_F = 0.1$, 0.2, 0.3 and 0.4 eV.

3.6.2.5 Average effective mass

The average effective mass is then,

$$m^*(E_F) = \frac{1}{n_e(E_F)} \int_0^{E_{lim}} f(k, E_F) N(k) m_{opt}^*(k) dk . \qquad (3\text{-}32)$$

The average effective masses calculated for InP, $In_{0.52}Al_{0.48}As$ and $In_{0.53}Ga_{0.47}As$ using the material parameters ($T = 300$ K) listed in Table 3, are plotted in Figure 26, Figure 27 and Figure 28, respectively. Experimental data points from Kesamanly *et al.* [33] for $m^*(n_e)$ of InP at room temperature are plotted along with our calculated values in Figure 26. There is a very good match between the theory and these published values of m^*. No experimental data for $m^*(n_e)$ could be found in the literature for $In_{0.52}Al_{0.48}As$ or $In_{0.53}Ga_{0.47}As$ so that a comparison with experimental values is not possible here.

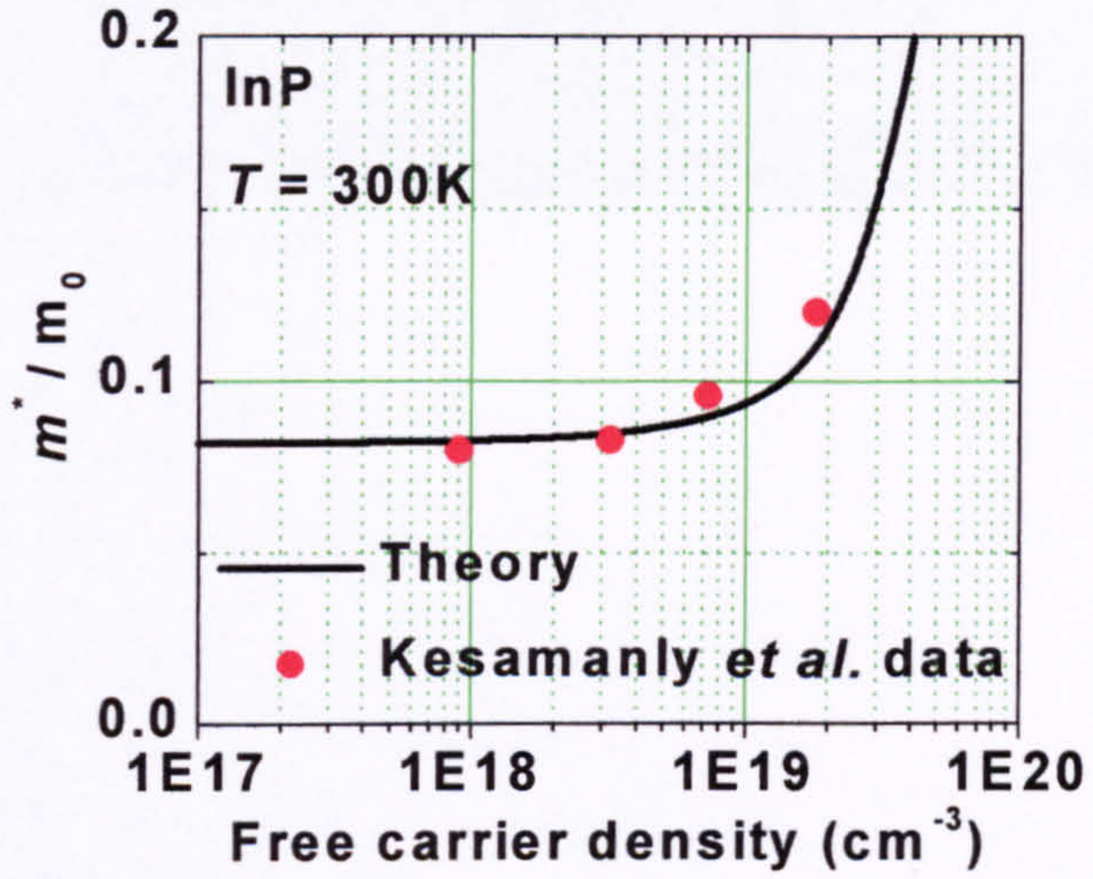

Figure 26 Calculated average effective mass, m^*, for InP at $T = 300$K.

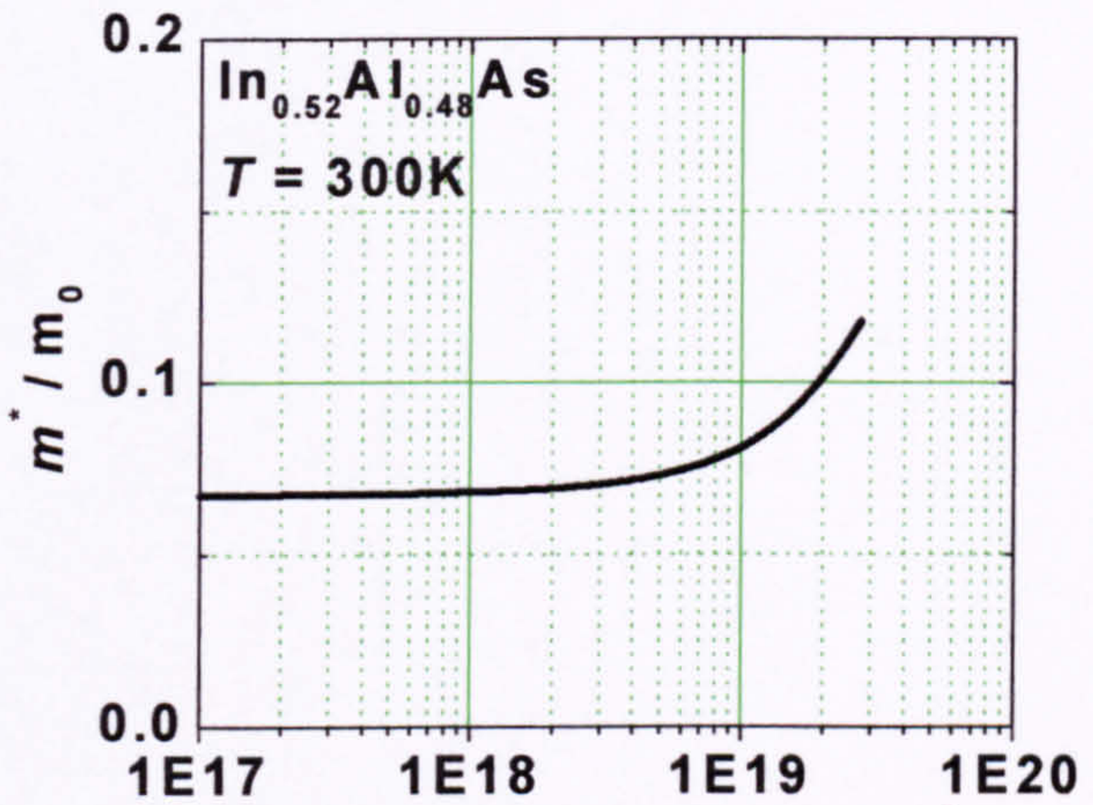

Figure 27 Calculated average effective mass, m^*, for $In_{0.52}Al_{0.48}As$ at $T = 300$K.

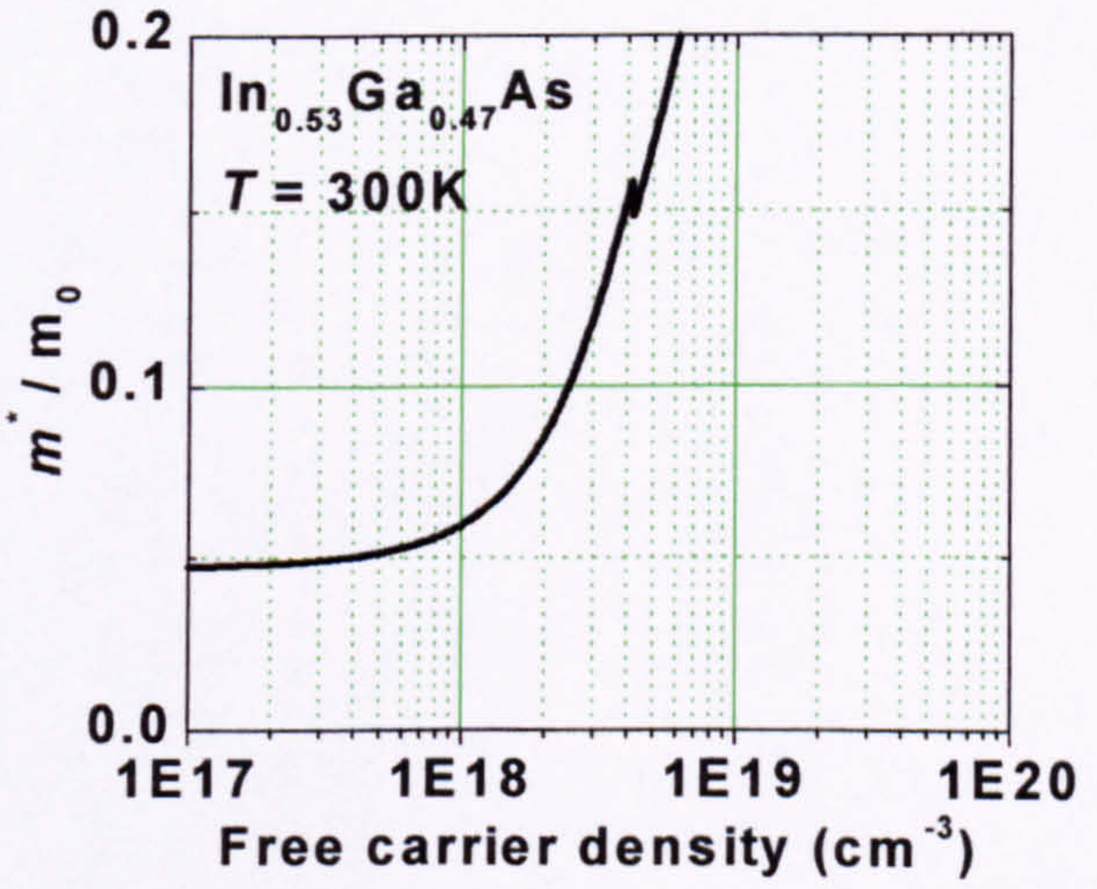

Figure 28 Calculated average effective mass, m^*, for $In_{0.53}Ga_{0.47}As$ at $T = 300$K.

3.6.2.6 Free-carrier dependant plasma frequency

The plasma frequency as a function of E_F may then be found from,

$$\omega_p(E_F) = \sqrt{\frac{q^2 n_e(E_F)}{m^*(E_F)\varepsilon_\infty \varepsilon_0}}. \tag{3-33}$$

The plasma wavelength, $\lambda_p = (\omega_p \times 100)^{-1}$, for InP, $In_{0.52}Al_{0.48}As$ and $In_{0.53}Ga_{0.47}As$ at $T = 77$ K and 300 K which were calculated using the material parameters listed in Table 3, are plotted in Figure 26, Figure 27 and Figure 28, respectively. Published values of ω_p at room temperature in n-type InP from Pickering *et al.* [9] (calculated by fitting to reflectivity measurements) are plotted along with the calculated values in Figure 29. Again there is a very good match between the theory and the published values which were available.

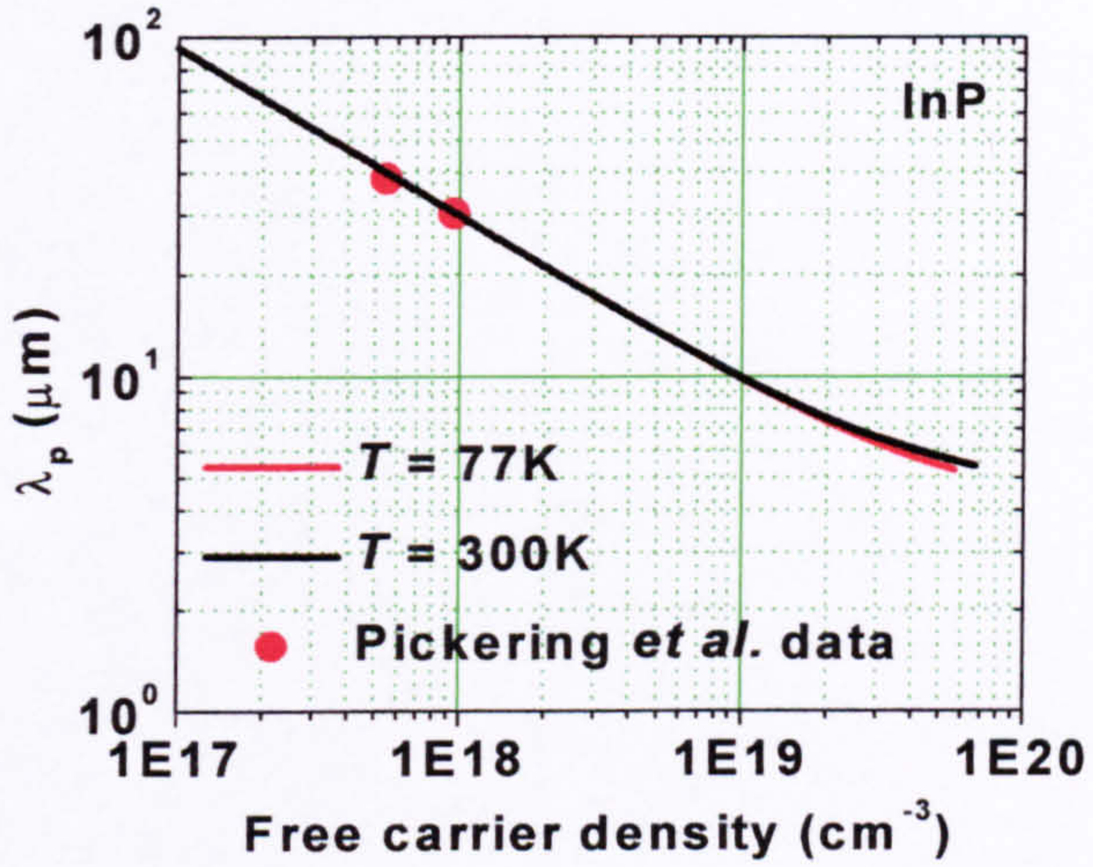

Figure 29 Calculated plasma wavelength, λ_p, for InP at $T = 77$K and 300K.

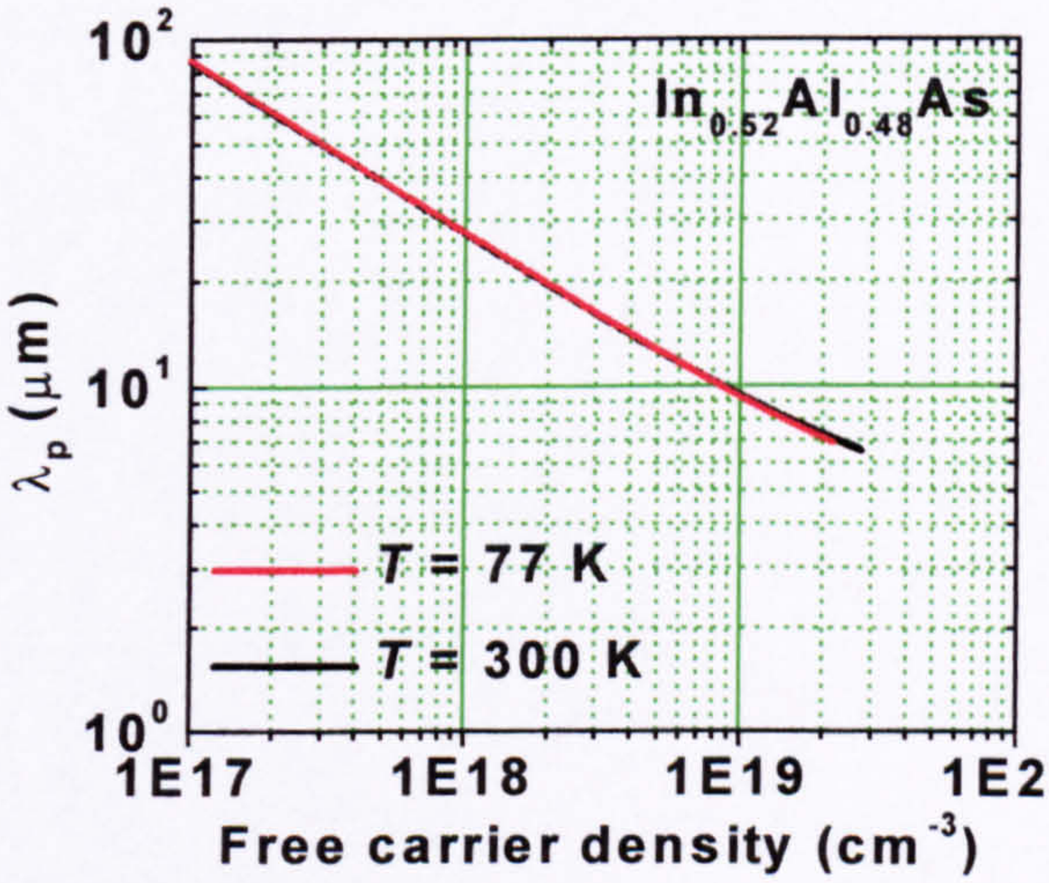

Figure 30 Calculated plasma wavelength, λ_p, for $In_{0.52}Al_{0.48}As$ at $T = 77$K and 300K.

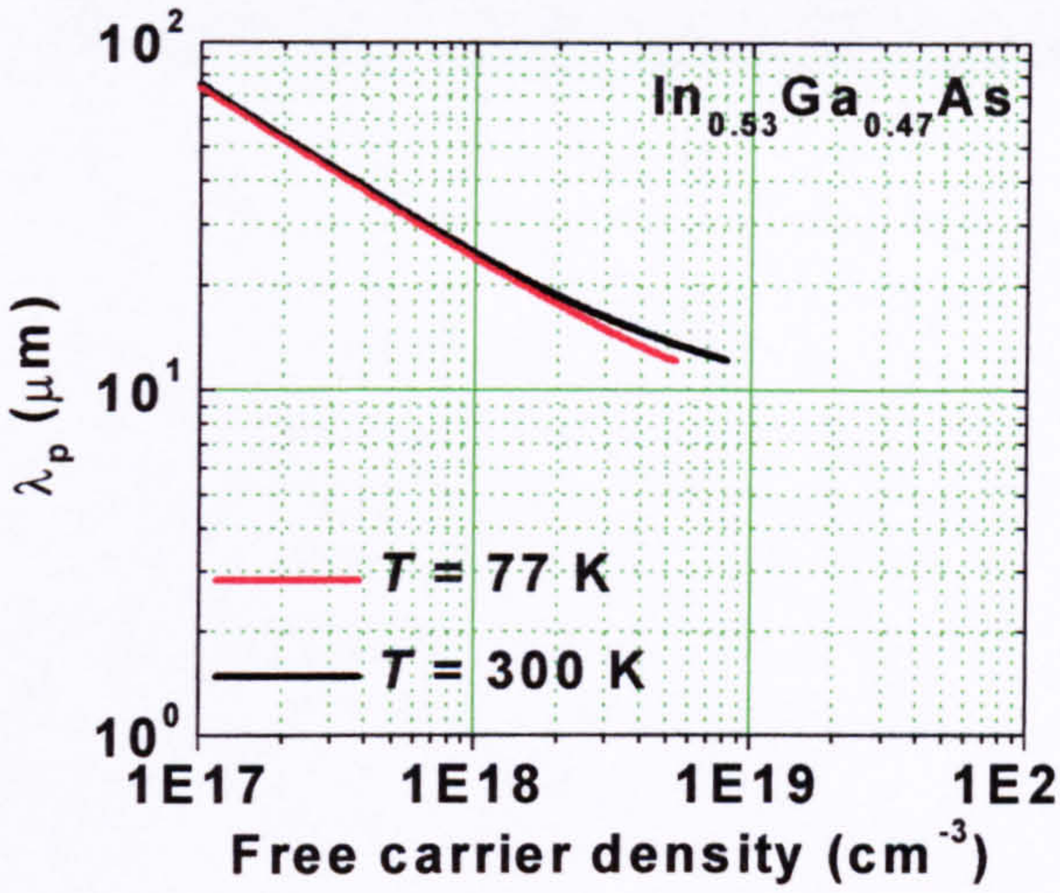

Figure 31 Calculated plasma wavelength, λ_p, for $In_{0.53}Ga_{0.47}As$ at $T = 77K$ and 300K

As we touched upon at the beginning of this chapter, the plasma frequency is quite an important parameter in the design of the 'plasma-enhanced' optical waveguide used in QC lasers. As we have just seen, by increasing the doping level, the plasma frequency can be reduced to a value close to the frequency of laser emission. In the next section, we will see that this can result in a large reduction in the refractive index, which is exactly the effect we wish to achieve in order obtain a 'plasma-enhanced' waveguide. Below in Table 6 we see the calculated free-electron densities required to shift the plasma frequency/wavelength down to the optical frequencies $\lambda = 8.85$, 6.39 and 5.00 μm.

λ_p (μm)	InP doping (cm^{-3})	$In_{0.52}Al_{0.48}As$ doping (cm^{-3})	$In_{0.53}Ga_{0.47}As$ doping (cm^{-3})
8.85	1.3×10^{19}	1.1×10^{19}	-
6.39	3.0×10^{19}	$\sim2.8\times10^{19}$	-
5.00	5.7×10^{19}	-	-

Table 6 Calculated free-electron densities need to achieve λp = 8.85, 6.39 and 5.00 μm for the different semiconductor materials considered.

Using our expression for $\omega_p(E_F)$ in Eq. (3-33) in place of that in Eq. (3-14), we are now in a position to calculate $n(\omega, n_e)$ and $\alpha(\omega, n_e)$ for InP, $In_{0.52}Al_{0.48}As$, and $In_{0.53}Ga_{0.47}As$ at $T = 77K$ and 300K. For clarity, all of the equations required for this task have been brought together in one place on the next page. The remaining material specific parameters used such as ε_∞, $\omega_{LO\,j}$, $\omega_{TO\,j}$, $\gamma_{ph\,j}$, m_0^*, Δ, and E_g are given in Table 3 and $\mu(n_e)$ in Section 3.6.1.

The results of the calculations of n and α for InP, $In_{0.53}Ga_{0.47}As$ and $In_{0.52}Al_{0.48}As$ follow in Sections 3.6.3 to 3.6.6. In each case, n and α have been calculated for three wavelengths $\lambda = 5$, 6.39 and 8.85 μm at $T = 77$ K, and for $\lambda = 5.3$ μm at $T = 300$ K.

$$n(\omega)=\frac{\left[\varepsilon_1(\omega)^2+\varepsilon_2(\omega)^2\right]^{1/2}+\varepsilon_1(\omega)}{2}, \tag{3-34}$$

$$\alpha(\omega)=4\pi\omega\, k(\omega),\ (\mathrm{cm}^{-1}) \tag{3-35}$$

$$k(\omega)=\frac{\left[\varepsilon_1(\omega)^2+\varepsilon_2(\omega)^2\right]^{1/2}-\varepsilon_1(\omega)}{2}. \tag{3-36}$$

$$\varepsilon_1(\omega)+i\varepsilon_2(\omega)=\varepsilon_\infty\left(1+\left(\sum_j\frac{w_{LO_j}^2-w_{TO_j}^2}{w_{TO_j}^2-w^2-iw\gamma_{pk\,j}}\right)-\frac{w_p^2(E_F)}{\omega\left(\omega+i\gamma_{pl}(E_F)\right)}\right), \tag{3-37}$$

$$\gamma_{pl}(n_e)=\frac{e}{\mu(n_e)m^*(n_e)}\frac{1}{200\pi c},\ (\mathrm{cm}^{-1}) \tag{3-38}$$

$$\omega_p(E_F)=\sqrt{\frac{q^2n_e(E_F)}{m^*(E_F)\varepsilon_\infty\varepsilon_0}}\frac{1}{200\pi c},\ (\mathrm{cm}^{-1}) \tag{3-39}$$

$$m^*(E_F)=\frac{1}{n_e(E_F)}\int_0^{E_{kmax}}f(k,E_F)N(k)m_{opt}^*(k)dk, \tag{3-40}$$

$$m_{opt}^*(k)=\hbar^2k\left(\frac{d}{dk}E(k)\right)^{-1}. \tag{3-41}$$

$$n_e(E_F)=\int_0^{E_{kmax}}f(k,E_F)N(k)dk, \tag{3-42}$$

$$f(k,E_F)=\left[1+\exp\left(\frac{E(k)-E_F-E_{offset}}{k_BT}\right)\right]^{-1}. \tag{3-43}$$

$$N(k)=\frac{m_{opt}^*(k)k}{\pi^2\hbar^2}. \tag{3-44}$$

$$E(k)=\frac{\hbar^2k^2}{2m_0^*}-\left(\frac{\hbar^2k^2}{2m_0^*}\right)^2\left(\frac{1+x+\frac{1}{4}x^2}{1+\frac{4}{3}x+\frac{4}{9}x^2}\right)\frac{1}{E_g} \tag{3-45}$$

$$x=\Delta/E_g. \tag{3-46}$$

3.6.3 Calculated values of *n* and α for InP

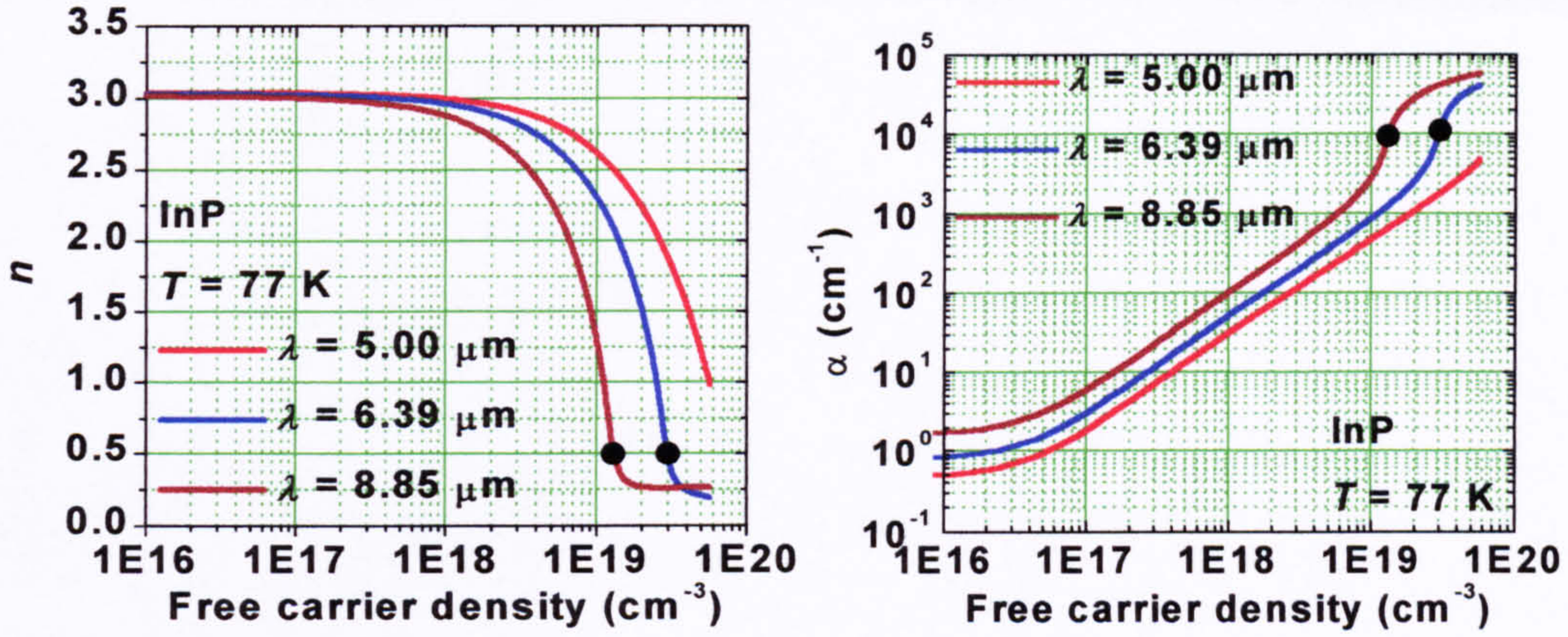

Figure 32 Calculated n and α of InP versus the free electron density at $T = 77$ K for three wavelengths $\lambda = 5$, 6.39 and 8.85 μm. The black dots represent the point at which $\lambda_p = \lambda$.

To make initial comments on the general trends seen in the results for InP, we see that the refractive index does drop with increasing free-carrier density, as expected. The drop becomes very sharp above approximately $n_e \approx 1\times10^{18}$ cm^{-3}. At longer wavelengths the same drop in refractive index can be achieved with a smaller free-carrier density as less of a shift in the plasma frequency is required to bring it close to the optical frequency. The minimum refractive index which can be achieved can be very low with $n \geq 0.25$ for $\lambda \approx 8.85$ μm. However, the minimum was reached after the plasma frequency had crossed the optical frequency e.g. $\lambda_p \approx 8.85$ μm at $n_e \approx 1.3\times10^{19}$ cm^{-3}, which should be avoided if low waveguide losses are to be achieved.

Turning our attention to the calculated loss coefficients now, we see that for any given free-carrier density, the loss increased rapidly with λ_p and n_e. There was a pronounced enhancement of the loss when the plasma frequency approached the optical frequency. Obviously, the doping level should be chosen so as to avoid this regime, since the objective is to achieve low refractive index, but without incurring high free-carrier losses.

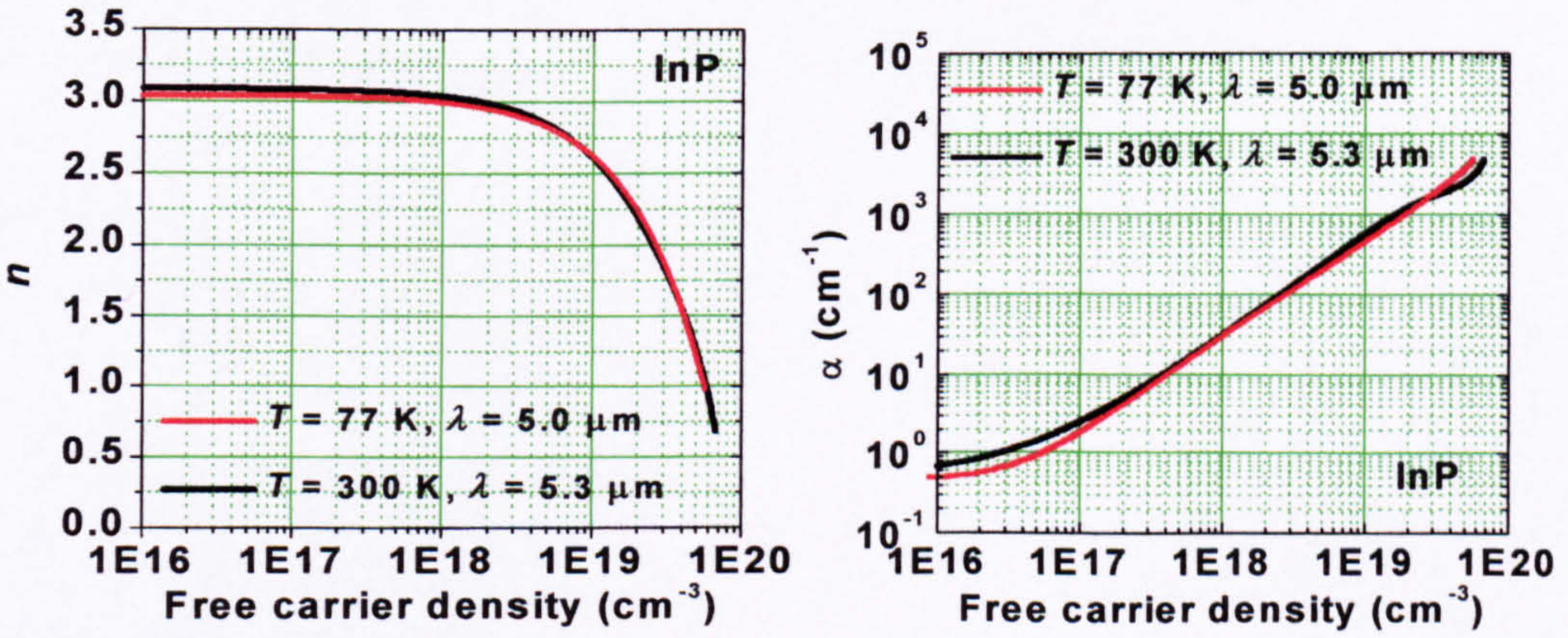

Figure 33 Calculated n and α of InP versus the free electron density for the combinations $T = 77$ K, $\lambda = 5$ μm and $T = 300$ K, $\lambda = 5.3$ μm.

3.6.4 Calculated values of n and α for $In_{0.52}Al_{0.48}As$

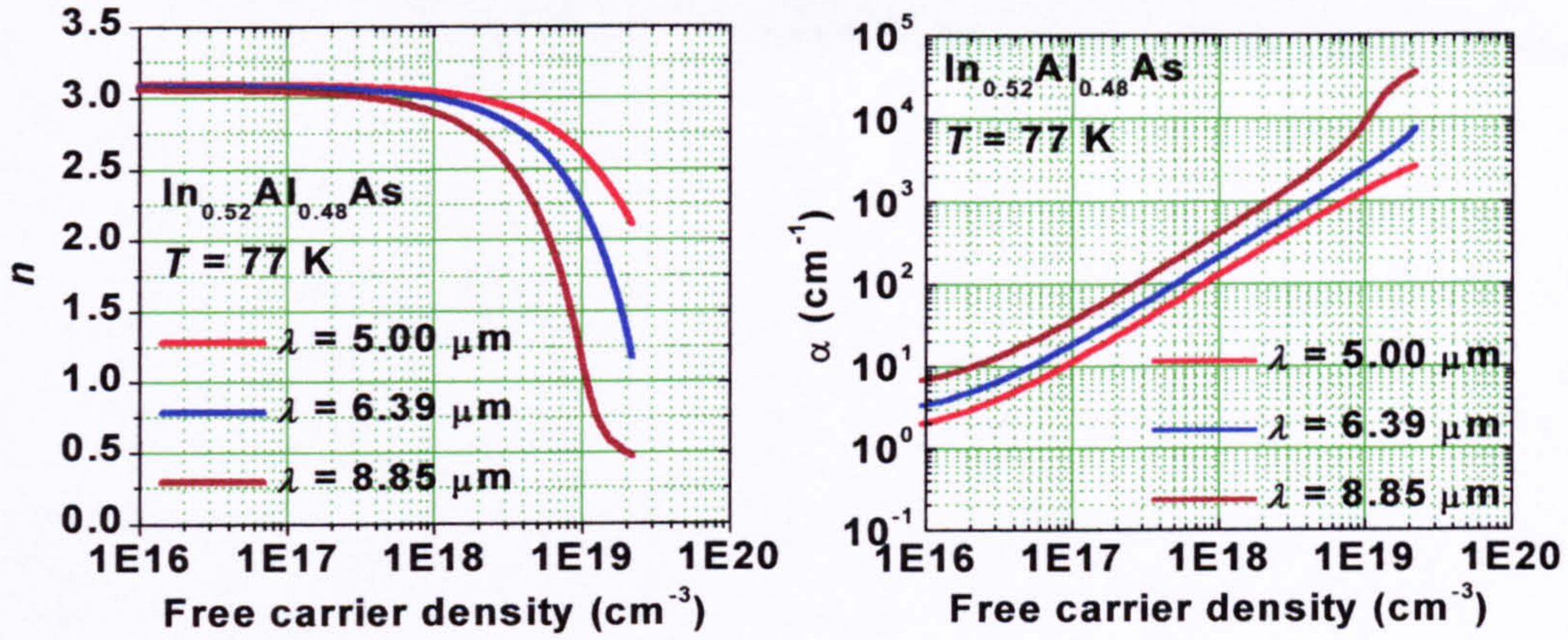

Figure 34 Calculated refractive index n and α of $In_{0.52}Al_{0.48}As$ versus the free electron density at T = 77 K for three wavelengths λ = 5, 6.39 and 8.85 μm.

The calculated behaviour of the n and α of the $In_{0.52}Al_{0.48}As$ with free-carrier density and wavelength was much the same as that for the InP. There were some quantitative differences though. Although the refractive index versus n_e and λ was very similar for the two materials, the loss coefficient of the $In_{0.52}Al_{0.48}As$ was significantly higher. This can be attributed to the much lower electron mobility of the $In_{0.52}Al_{0.48}As$ as compared to that of the InP. This is a very interesting result which suggests that InP should be used as for the cladding layers of the QC laser rather than $In_{0.52}Al_{0.48}As$ as this should lead to waveguides with lower loss, and therefore to lasers with lower values of J_{th}.

More generally, the electron mobility should be maximised to reduce the free-carrier loss, and high electron mobilities are subject to the quality of the epitaxial growth. This emphasises the importance of high quality semiconductor growth not only for the precision growth of the QC superlattice core, but also of the waveguide cladding layers to minimise the waveguide losses.

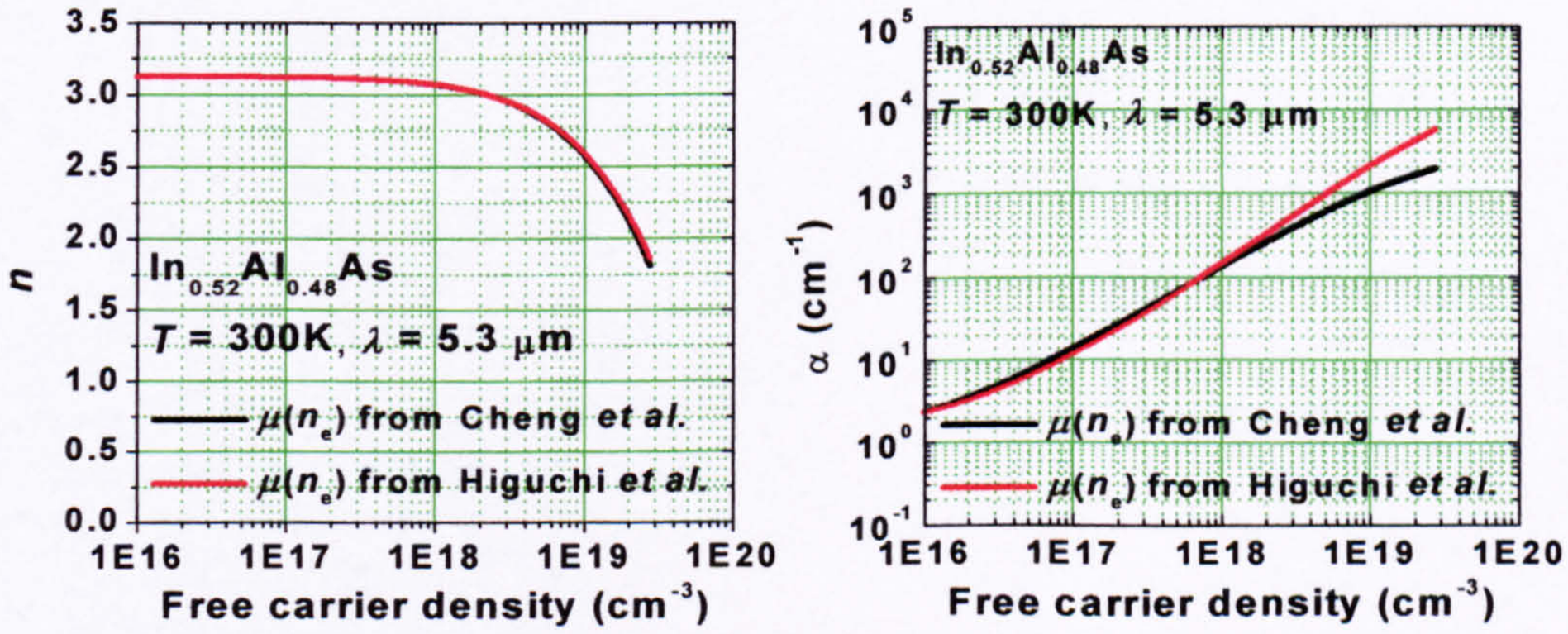

Figure 35 Calculated n and α of $In_{0.52}Al_{0.48}As$ versus the free electron density at T = 300 K using the electron mobility data of either Cheng *et al.* or Higuchi *et al.*.

The only additional point to make here is to point out the difference in the results at T = 300 K when using the two possible sets of data for the electron mobility. Again we see that poor electron mobility leads to higher losses, but little apparent change in the refractive index. Yet again this highlights the sensitivity of the optical loss to the electrical quality of the semiconductor.

3.6.5 Calculated values of n and α for $In_{0.53}Ga_{0.47}As$

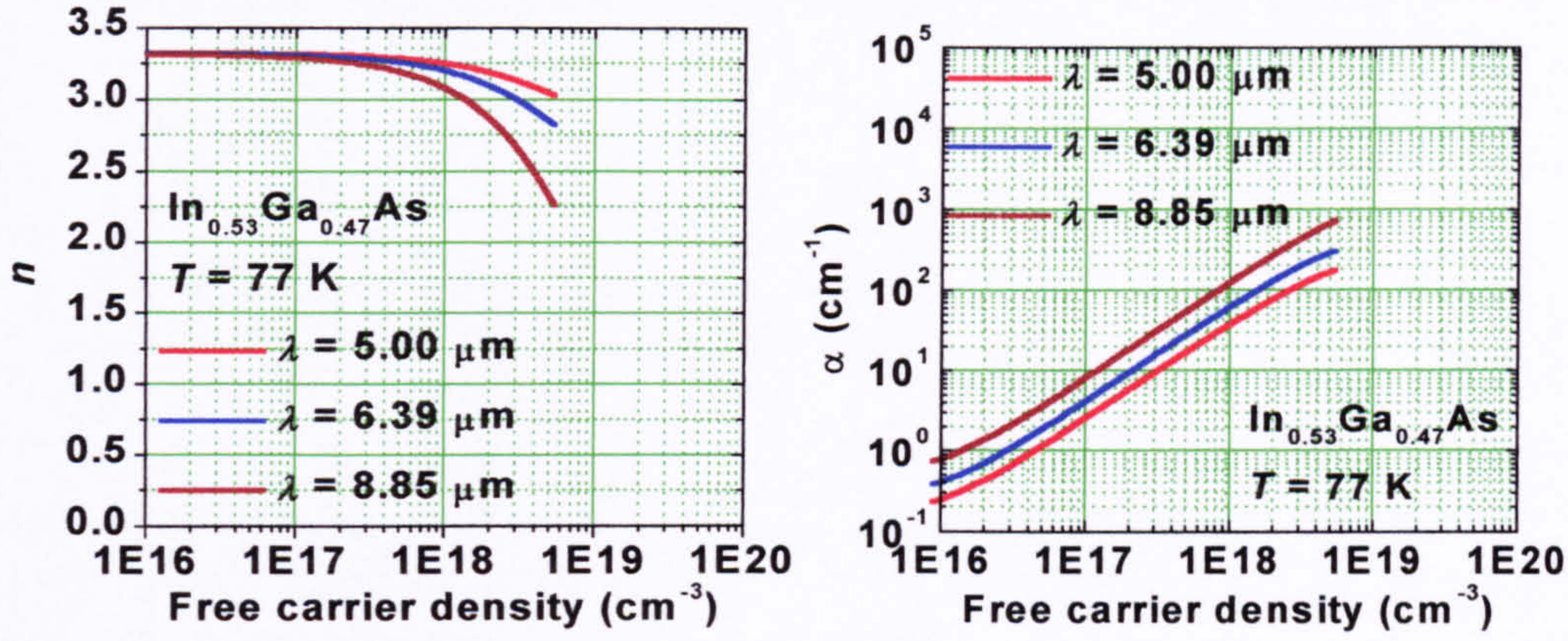

Figure 36 Calculated n and α of $In_{0.53}Ga_{0.47}As$ versus the free electron density at $T = 77$ K for three wavelengths $\lambda = 5$, 6.39 and 8.85 μm.

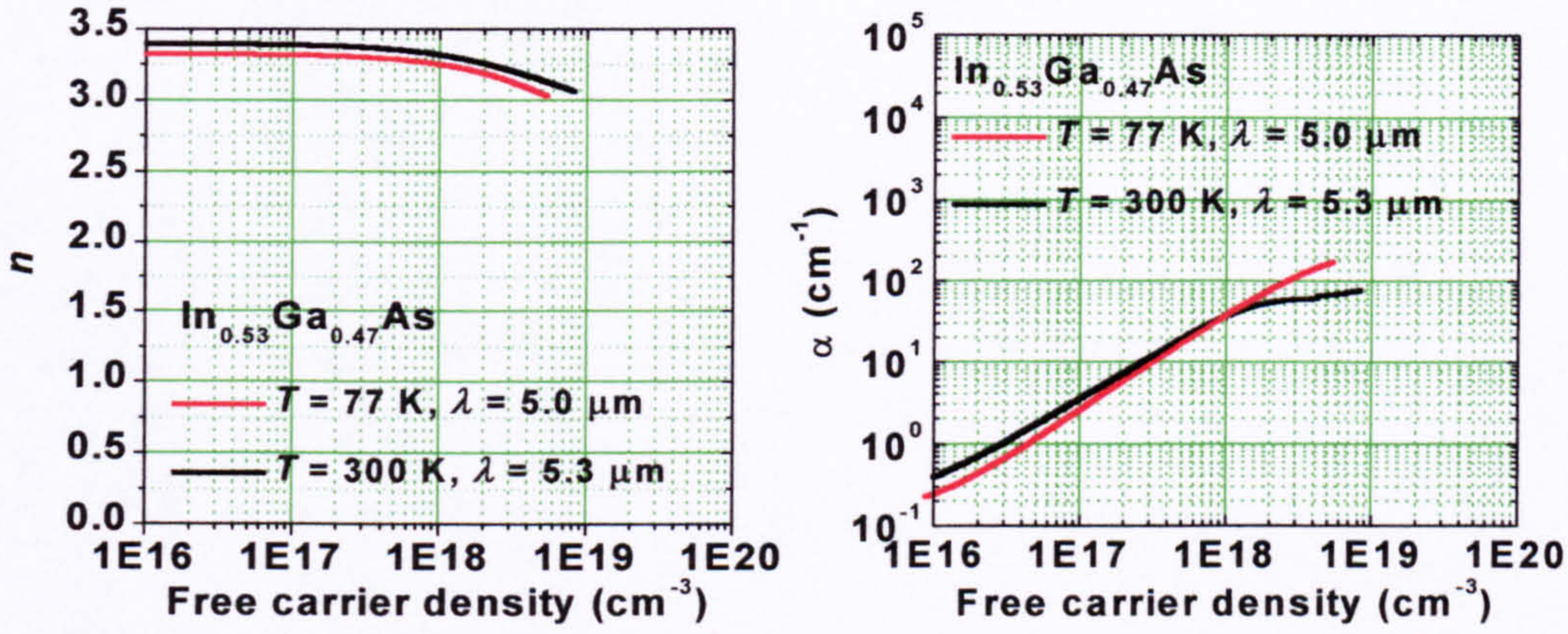

Figure 37 Calculated n and α of $In_{0.53}Ga_{0.47}As$ versus the free electron density for the combinations $T = 77$ K, $\lambda = 5$ μm and $T = 300$ K, $\lambda = 5.3$ μm.

3.6.6 Tables of values of n and α for InP, $In_{0.52}Al_{0.48}As$ and $In_{0.53}Ga_{0.47}As$ for QCL optical modelling

The calculated values of n and α at doping levels specific to those found in our $\lambda \approx 5$ μm QC laser design are given in Table 7 to Table 10 below for $T = 77$K, $\lambda = 5$ μm, and $T = 300$ K, $\lambda \approx 5.3$ μm. The values in these tables were used in the optical modelling of the QC laser waveguide in the next chapter.

Material	Free-carrier density (cm^{-3})							
	2×10^{16}	1×10^{17}	2×10^{17}	3×10^{17}	1×10^{18}	2×10^{18}	3×10^{18}	7×10^{18}
InP	3.039	3.035	3.030	3.026	2.955	2.952	2.910	2.741
InAlAs	3.092	3.087	3.083	3.077	3.041	2.990	2.940	2.748
InGaAs	3.326	3.319	3.312	3.304	3.254	3.190	3.134	-

Table 7 Calculated refractive index n of InP, $In_{0.52}Al_{0.48}As$ and $In_{0.53}Ga_{0.47}As$ for λ=5 μm, T= 77 K and at various values of free-carrier density, n_e.

Material	Free-carrier density (cm^{-3})							
	2×10^{16}	1×10^{17}	2×10^{17}	3×10^{17}	1×10^{18}	2×10^{18}	3×10^{18}	7×10^{18}
InP	0.6	1.9	4.3	7.1	32	73	117	315
InAlAs	3.0	12	24	36	132	277	422	989
InGaAs	0.4	2.6	6.0	9.7	38	79	115	-

Table 8 Calculated absorption coefficient α (cm^{-1}) of InP, $In_{0.52}Al_{0.48}As$ and $In_{0.53}Ga_{0.47}As$ for λ=5 μm, T= 77 K and at various values of free-carrier density, n_e.

Material	Free-carrier density (cm^{-3})							
	2×10^{16}	1×10^{17}	2×10^{17}	3×10^{17}	1×10^{18}	2×10^{18}	3×10^{18}	7×10^{18}
InP	3.087	3.083	3.078	3.073	3.038	2.989	2.940	2.748
InAlAs	3.129	3.125	3.119	3.113	3.071	3.012	2.955	2.733
InAlAs 2	3.130	3.125	3.119	3.113	3.071	3.013	2.956	2.740
InGaAs	3.399	3.392	3.383	3.375	3.332	3.260	3.212	3.091

Table 9 Calculated refractive index n of InP, $In_{0.52}Al_{0.48}As$ and $In_{0.53}Ga_{0.47}As$ for λ =5.3 μm, T= 300 K and at various values of free-carrier density, n_e. 'InAlAs' and 'InAlAs 2' refer to the use of the electron mobility data of Cheng *et al.* and Higuchi *et al.*, respectively.

Material	Free-carrier density (cm^{-3})							
	2×10^{16}	1×10^{17}	2×10^{17}	3×10^{17}	1×10^{18}	2×10^{18}	3×10^{18}	7×10^{18}
InP	2.0	2.6	5.2	8.0	33	78	131	381
InAlAs	3.7	14	28	42	137	268	392	912
InAlAs 2	3.5	12	25	40	148	334	539	1440
InGaAs	0.7	3.6	7.6	12	37	-	-	-

Table 10 Calculated absorption coefficient α (cm^{-1}) of InP, $In_{0.52}Al_{0.48}As$ and $In_{0.53}Ga_{0.47}As$ for λ=5.3 μm, T= 300 K and at various values of free-carrier density, n_e. 'InAlAs' and 'InAlAs 2' refer to the use of the electron mobility data of Cheng *et al.* and Higuchi *et al.*, respectively.

3.7 Dielectric constants of SiO_2, Al_2O_3 and gold in the mid-infrared

Also relevant to the waveguide design are the refractive indices and extinction coefficients (related to the loss coefficient) of the dielectrics and metals used in the construction of the lasers. The dielectrics silicon dioxide and silicon nitride, which are widely employed in the fabrication of conventional interband near-infrared lasers, are so chosen for their high transparency in that spectral region as well as for their excellent electrical insulation properties and adhesion to semiconductors. This changes in the mid-IR spectral region however, as in this region they posses strong, frequency-dependent absorption and an associated dispersion of the refractive index. Plots of n and α taken from published data are shown for SiO_2 (glass) in Figure 38, and for Al_2O_3 (crystalline) in Figure 39. Unfortunately, data for amorphous alumina does not cover the wavelength range of interest, and so data for crystalline Al_2O_3 has been used. Note that in the wavelength range $5 < \lambda < 10$ μm Al_2O_3 exhibits significantly lower losses compared to that of SiO_2.

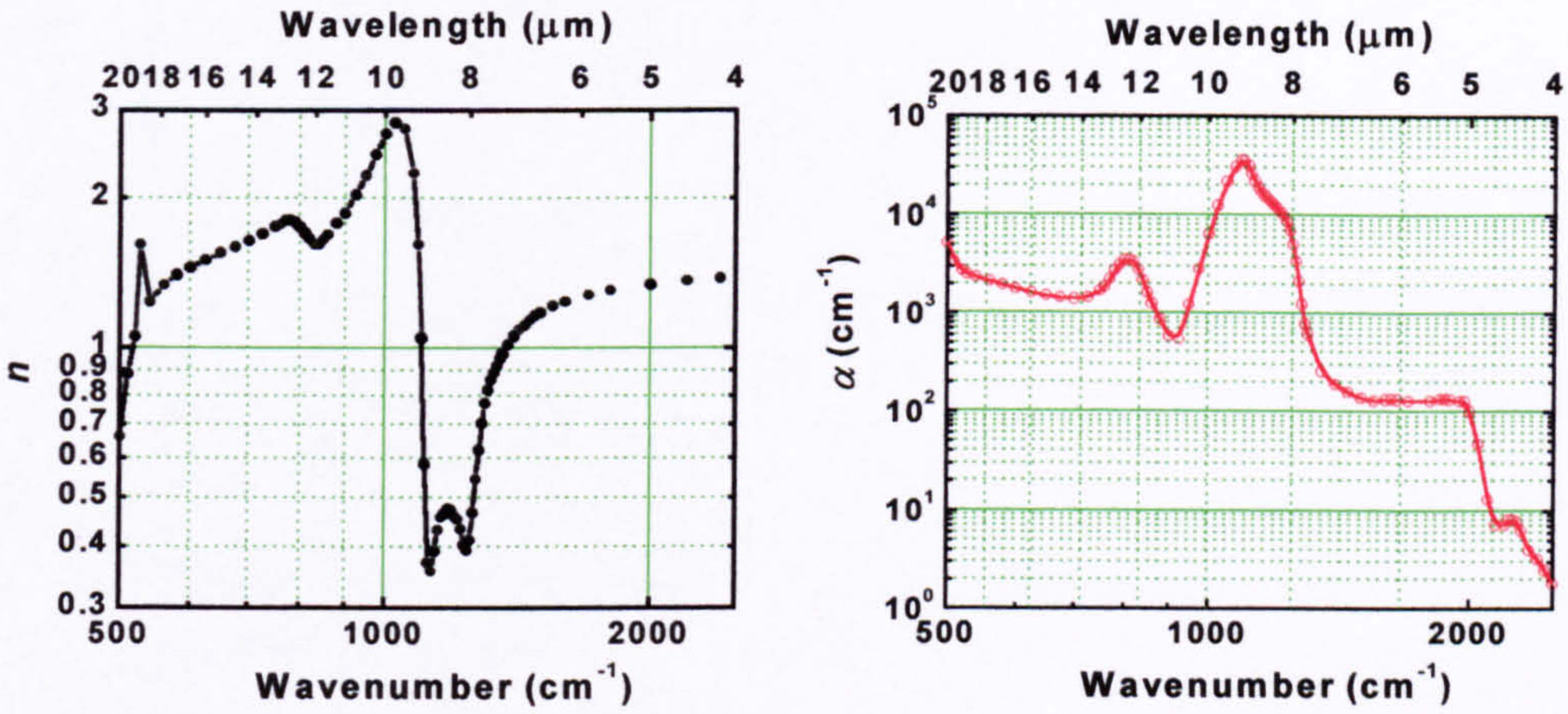

Figure 38 $n(\omega)$ and $\alpha(\omega)$ for silicon dioxide (glass) at room temperature.[25]

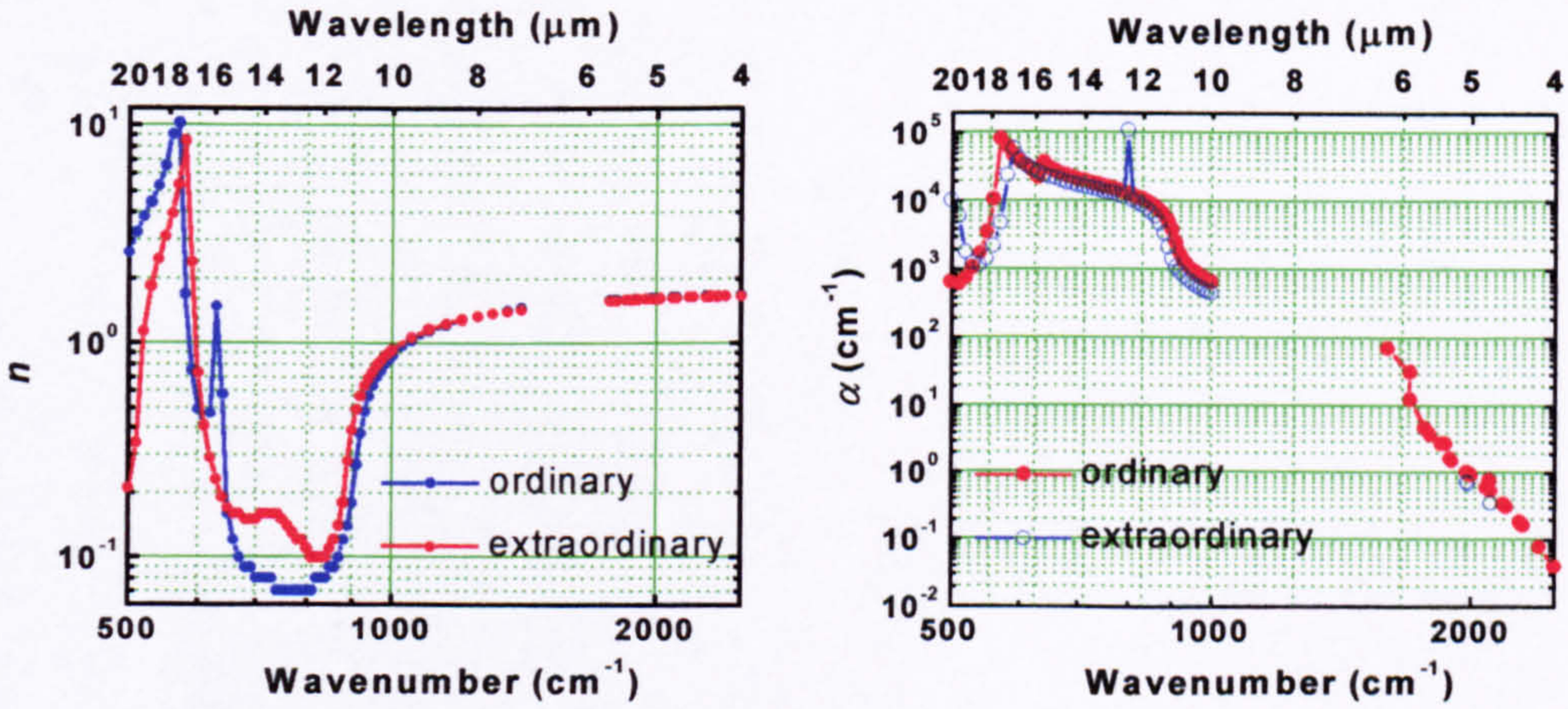

Figure 39 $n(\omega)$ and $\alpha(\omega)$ for aluminium oxide (crystalline) at room temperature.[26]

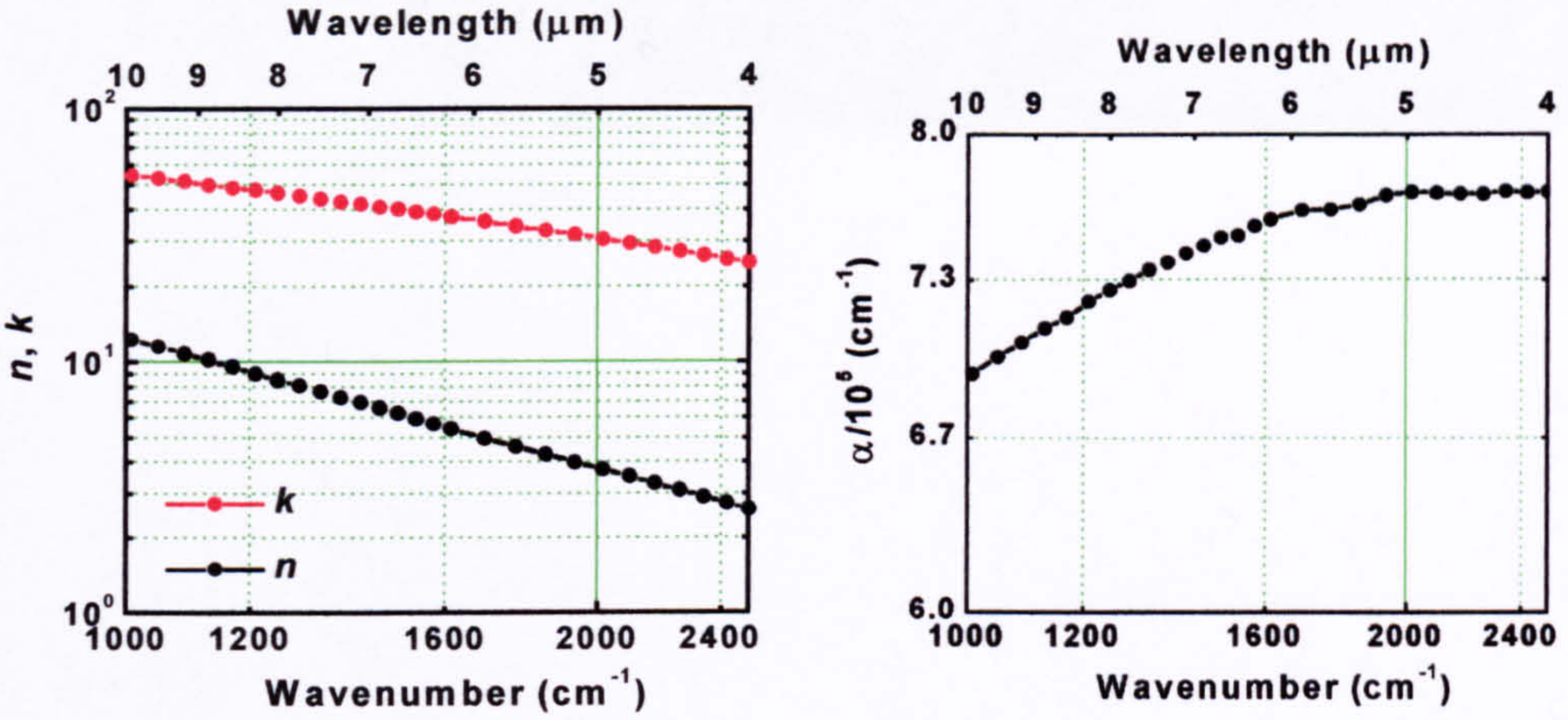

Figure 40 $n(\omega)$ and $k(\omega)$, and $\alpha(\omega)$ for gold.[25]

3.8 Summary

The refractive index and loss coefficient of the semiconductor materials used in our QC laser (InP, $In_{0.52}Al_{0.48}As$ and $In_{0.53}Ga_{0.47}As$) were calculated as a function of the free-electron density, n_e, and optical wavelength, λ. These values were essential for the optical modelling of the QC laser waveguide modes which will be presented in the forthcoming chapter.

The calculations were achieved by using single and multiple-oscillator models which included a free-carrier contribution in the form of a classical Drude expression. The dependence of the electron mass and mobility on the free electron density were taken into account in the calculations. For the electron mass, this was done by calculating the average effective mass of electrons in the conduction band through the use of a three band Kane model. The dependence of the electron mobility on the free-carrier density was obtained by making polynomial fits to published data of $\mu(n_e)$. The calculated values of n and α were for temperatures of $T = 77$ or 300 K depending on which set of material parameters was used in the calculations. Modelling of the $In_{0.53}Ga_{0.47}As$ material was restricted to doping levels below $n_e \approx 1\times10^{18}$ cm^{-3} at $T = 300$ K, which is below that used in the contact layer of the $\lambda \approx 5$ μm design. The restriction was due to the limitations of the three band Kane model in describing the conduction band energy at high wavevectors.

A few interesting findings were uncovered by the modelling which have implications in the design and performance of the QC laser waveguide. First of all, the plasma frequency is an important parameter in the design of the optical waveguide used in QC lasers. As we have just seen, by increasing the doping level in the semiconductors, the plasma frequency can be moved to a value close to the frequency of laser emission. The motivation for doing so is that this can result in a large reduction in the refractive index, which can be harnessed to improve the confinement of the optical mode in the QC laser waveguide. This is the principle of the so-called 'plasma-enhanced' waveguide normally used in QC lasers. However, we see from the modelling that great care must be exercised not to elevate the free-carrier density so high as to force the plasma frequency to drop below the optical frequency. The modelling shows that this leads to a sharp increase in α which will lead to high J_{th} in the lasers.

Secondly, either InP or $In_{0.52}Al_{0.48}As$ can be used as an upper cladding material for the QC laser. The modelling in this chapter indicated that the loss coefficient of the $In_{0.52}Al_{0.48}As$ was significantly greater than that of InP for both intrinsic and extrinsic material, but had roughly the same refractive index. For instance,

for a free electron density $n_e = 1\times10^{18}$ cm^{-3} and wavelength $\lambda = 5$ μm the refractive index and loss coefficient obtained are given in Table 11. A low loss coefficient is desirable since it will ultimately lead to a lower laser threshold current density and higher slope efficiency. With the InP also possessing a much superior thermal conductivity, it would seem to be the material of choice for use as the upper cladding material.

Material	n	α (cm^{-1})
$In_{0.52}Al_{0.48}As$	3.04	133
InP	2.99	33

Table 11 Comparison of the calculated values of n and α of InP and $In_{0.52}Al_{0.48}As$ for $n_e = 1\times10^{18}$ cm^{-3} and wavelength $\lambda = 5$ μm

One last significant finding was that poor electron mobility at high n_e was found to increase the loss coefficient by a large amount (by over 55% in the case considered). Hence, in order to obtain low loss 'plasma-enhanced' waveguides with high optical confinement, it is important to grow high quality semiconductor material with high values of electron mobility. Poor quality semiconductor material will ultimately lead to a high J_{th} and poor slope efficiency.

Future work in this area could include experimental work, such as reflectivity measurements using FTIR spectrometry, to determine the refractive index and loss coefficient of InP, $In_{0.52}Al_{0.48}As$ and $In_{0.53}Ga_{0.47}As$ in the mid-IR as a function of the doping level and wavelength. Fitting experimental reflection spectra to theory has also been shown to provide information on the plasma frequency, the average effective electron mass, mobility and concentration. [28, 31, 9] Measurements of these parameters would extend the validity of the refractive index calculations to higher doping levels.

3.9 References

[1] C. Sirtori, C. Gmachl, F. Capasso, J. Faist, D. L. Sivco, A. L. Hutchinson, A. Y. Cho, "Long-wavelength ($\lambda \approx$ 8-11.5 μm) semiconductor lasers based on surface plasmons", *Optics Letters* **23** (17) 1366, 1 September 1998.

[2] C. Sirtori, J. Faist, F. Capasso, D. Sivco, A. L. Hutchinson, A. Y. Cho, 'Quantum cascade laser with plasmon-enhanced waveguide operating at 8.4 μm wavelength', *Appl. Phys. Lett.* **66** (24), 12 June 1995.

[3] A. R. Forouhi, I. Blommer in, *Properties of Indium Phosphide*, Institute of Electrical Engineers, 1991.

[4] S. S. Mitra, in *Handbook of Optical Constants of Solids*, E. D. Palik, Ed, Academic Press, Orlando London, 1985.

[5] B. Ancker-Johnson, in *Semiconductors and Semimetals – Vol. I Physics of III-V Compounds*, R. K. Williardson, A. C. Beer, Ed, Academic Press Inc, London, 1966.

[6] S. Adachi, *Physical Properties of III-V Semiconductor Compounds - InP, InAs, GaAs, GaP, InGaAs, and InGaAsP* (Wiley, New York, 1992).

[7] O. Madelung, Ed., *Semiconductors: Group IV Elements and III-V Compounds*, (Springer-Verlag, Berlin Heidleberg, 1991).

[8] P. S. Spencer, K. A. Shore, 'Surface plasmon effects and waveguide properties of quantum cascade lasers' *IEE Proc. Optoelectron.* **144** (1) 48, February 1997.

[9] C. Pickering, "Non-destructive characterisation of n-type InP epitaxial layers by infrared reflectivity measurements", *J. Phys. D: Appl. Phys.*, **16**, pp.213-223, (1983).

[10] M. Balkanski, in *Optical Properties of Solids*, F. Abelès, Ed, North-Holland Publishing Company, Amsterdam, 1972.

[11] A. N. Pikhtin, A. D. Yas'kov, "Dispersion of the refractive index of semiconductors with diamond and zinc-blende structures", *Sov. Phys. –Semicond.*, **12** (6) pp.622-626, (1978).

[12] V. Swaminathan, in *Indium Phosphide and Related Materials: Processing, Technology, and Devices*, A. Katz, Ed. (Artech House, Boston, 1992).

[13] A. N. Pikhtin, A. D. Yas'kov, "Dispersion of the refractive index of semiconductors with diamond and zinc-blend structures", *Sov. Phys. –Semicond.*, **12** (6) pp.622-626, (1978).

[14] R. E. Fern, A. Onton, "Refractive Index of AlAs", *J. Appl. Phys.*, **42** (9), pp. 3499-3500, 1971.

[15] S. Perkowitz, R. Sudharsanan, T. J. Drummond, "AlAs PHONON PARAMETERS AND HETEROSTRUCTURE CHARATERIZATION", *Solid State Communications*, **62** (9), pp. 645-647, 1987.

[16] J. S. Blakemore, "Semiconducting and other major properties of gallium arsenide", *J. Appl. Phys.*, **53** (10), pp. R123-R143, October 1982.

[17] L. A. Cury, J. Beerens, J. P. Praseuth, "Dependence of conduction-band effective mass on quaternary alloy composition of $(In_{0.52}Al_{0.48}As)_z(In_{0.53}Ga_{0.47}As)_{1-z}$ lattice matched to InP", *Appl. Phys. Lett.*, **63** (13), September 1993.

[18] Y. F. Chen, Y. T. Dai, J. C. Fan, T. L. Lee, H. H. Lin, "Dependence of electron effective-mass on alloy composition of InAlGaAs lattice-matched to InP studied by optically detected cyclotron-resonance", *Appl. Phys. Lett.*, **67** (9), pp.1256-1258, 1995.

[19] D. K. Gaskill, N. Bottka, L. Aina, M. Mattingly, 'Band-gap determination by photoreflectance of In0.53Ga0.47As and In0.52Al0.48As lattice matched to InP', *Appl. Phys. Lett.*, **56**, pp. 1269-1271, 1990.

[20]K. Bouamama, W. Horig, H. Neumann, "Temperature dependence of photoreflectance measurements in $Ga_{0.47}In_{0.53}As$ epitaxial layers", *Semicond. Sci. Technol.*, **13** (1), pp.75-78, 1998.

[21] H. Lobentanzer, W. W. Rühle, W. Stolz, K. Ploog, "HOT CARRIER—PHONON INTERACTION IN THREE- AND TWO-DIMENSIONAL $Ga_{0.47}In_{0.53}As$", *Solid State Communications*, **62** (1), pp. 53-56, 1987.

[22] P. Bhattacharya, Ed., *Properties of Lattice-Matched and Strained Indium Gallium Arsenide*, (INSPEC, 1993).

[23] R. Borroff, R. Merlin, A. Chin, P. K. Bhattacharya, "Raman scattering by optical phonons in $In_{1-y-z}Al_yGa_zAs$ lattice matched to InP", *Appl. Phys. Lett.*, **53** (17), pp. 1652-1653, 1988.

[24] V. B. Bogdanov, V. T. Prokopenko, A. D. Yaskov, "Refractive index of indium phosphide in the 0.96-13-μm wavelength range", *Opt. Spectrosc. (USSR)*, **60** (1), pp.68-69, (1986).

[25] *Handbook of Optical Constants of Solids*, E. D. Palik, Ed, Academic Press, Orlando London, 1985.

[26] *Handbook of Optical Constants of Solids II*, E. D. Palik, Ed, Academic Press, Orlando London, 1991.

[27] J. Faist, C. Sirtori, F. Capasso, D. L. Sivco, J. N. Baillargeon, A. L. Hutchinson, A. Y. Cho, "High-Power Long-Wavelength ($\lambda \sim 11.5$ μm) Quantum Cascade Lasers Operating Above Room Temperature", *IEEE Photon. Technol. Lett.*, **10** (8) 1100, August 1998.

[28] Y. B. Li, R. A. Stradling, T. Knight, J. R. Birch, T. H . Thomas, C. C. Phillips, and I. T. Ferguson, "Infrared reflection and transmission of undoped and Si-doped InAs grown on GaAs by molecular beam epitaxy", *Semicond. Sci. Technol.*, **8**, pp. 101-111, 1993.

[29] J. Steins and R. Vounchx, "Calculations of plasma wavelength in highly doped III-V semiconductor alloys", *J. Appl, Phys.*, **76** (6), pp. 3526-3533, 15 Sept. 1994.

[30] D. A. Anderson, N. Apsley, P. Davies, P. L. Giles, "Compensation in heavily doped *n*-type InP and GaAs", *J. Appl. Phys*, **58** (8), pp. 3059-3067, 1985.

[31] G. W. Charache, D. M. DePoy, J. E. Raynolds, P. F. Baldasaro, K. E. Miyano, T. Holden, F. H. Pollak, P. R. Sharps, M. L. Timmons, C. B. Geller, W. Mannstadt, R. Asahi, A. J. Freeman, W. Wolf, "Moss-Burstein plasma reflection characteristics of heavily doped *n*-type $In_xGa_{1-x}As$ and InP_yAs_{1-y}", *J. Appl. Phys.*, **86** (1), pp. 452-458, 1 July 1999.

[32] A. Raymond, J. L. Robert, C. Bernard, "The electron effective mass in heavily doped GaAs", *J. Phys. C: Solid State Phys.*, **12** , pp. 2289-2293, 1979.

[33] F. P. Kesamanly, D. N. Nasledov, A. Ya. Nashel'skii, V. A. Skripkin, "DEPENDENCE OF THE EFFECTIVE MASS OF ELECTRONS ON THEIR DENSITY IN INDIUM PHOSPHIDE CRYSTALS", *Sov. Phys. –Semicond.*, **2** (10) pp.1221-1224, (1969).

[34] K. Y. Cheng, A.Y. Cho, "Silicon doping and impurity profiles in $Ga_{0.47}In_{0.53}As$ and $Al_{0.48}In_{0.52}As$ grown by molecular beam epitaxy ", J.Appl. Phys., **53**, (6), June 1982.

[35] S. F. Yoon, Y. B. Miao, K. Radhakrishnan, H. L. Duan, "The effects of Si doping in $In_{0.52}Al_{0.48}As$ layers grown lattice matched on InP substrates", *J. Appl. Phys.*, **78** (3), pp. 1812-1817, August 1995.

[36] M. Higuchi, T. Ishikawa, K. Imanishi, K. Kondo, "Doping characteristics of Si into molecular-beam-epitaxially grown InAlAs layers", *J. Vac. Sci. Technol. B*, **9** (6), pp.2802-2894, 1991.

[37] E. Fred Schubert, Doping in III-V Semiconductors, Cambridge University Press, 1993.

[38] E. O. Kane, *J. Phys. Chem. Solids.*, **1** p.248, 1957.

Chapter 4 Optical waveguide modelling

In this chapter the properties of the optical waveguide of the QC laser have been modelled. The optical constants which were derived in the last chapter and the waveguide geometries of interest were entered into a commercially available optical waveguide solver. The optical modes of the waveguides were found and we present their individual intensity distributions inside the waveguide, effective indices n_{eff}, waveguide losses α_w, confinement factors Γ, modal facet reflectivity R, and far-field profiles. These are all important parameters which play a large part in determining the performance of the lasers. For instance, the threshold gain for lasing is dependant on n_{eff}, α_w, Γ, and on R (see Eq. **(2-3)**). In this work the results were used to calculate the threshold gain g_{th} for each mode which gave information on which modes were expected to lase, and in which order with increasing gain. Using the values of g_{th} in combination with the equations introduced in Section 2.3 which described the gain provided by the QC core, the expected values of J_{th} and I_{th} were also calculated. The far-fields profiles were very interesting and explained many features which were observed in the measured light-current characteristics of real QC lasers fabricated in this work.

To the author's knowledge this is the first time that 2D optical modelling of the QC laser waveguides have been reported. 1D waveguide mode field profiles of QC lasers in the vertical direction (perpendicular to the layers) have been reported a number of times, but gave no information on the horizontal transverse modes. [1, 2] As far as the author is aware, the existence of higher order horizontal transverse modes has been acknowledged just once in the extensive literature on QC lasers,[1] and it was only in passing. The publication stated that any higher order modes were suppressed in their devices by virtue of their greater overlap with the lossy metal-covered waveguide sidewalls. Further, they reported that they were only observed occasionally in their QC lasers and only in ones with wide ridges i.e. ≥ 15 μm, operating under high pumping conditions.

As will become clear, this author's findings were a little different, both experimentally and theoretically. We will see in the chapter of the measurements performed on actual QC lasers that higher order transverse modes were frequently observed in this work (even in narrow devices) and, moreover, they had a considerable effect on the measured laser performance. Further, the measurements indicated that the higher-order modes may even have been the first modes to achieve lasing threshold, rather than the fundamental mode. The modelling in this chapter is used to explain this behaviour of our QC lasers.

4.1 Optical Waveguide Mode Solver

The software used, called FIMMWAVE and FIMMPROP-3D (by Photon Design (Europe) Ltd.), was a generic, fully vectorial mode finder which could be used to model virtually any 3D waveguide structure geometery. The heart of the program used a 2D waveguide solver based on the film mode matching method developed by Sudbo, [3, 4] and was capable of solving structures with complex refractive index. The solver modelled an arbitrary shaped waveguide as a set of rectangular slices, each being laterally uniform, but composed vertically of a number of layers. The eigenvalues (waveguide modes) were found by FIMMWAVE by solving a discrete eigenproblem. The effective index n_{eff}, loss coefficient α_w and 2D intensity plot of each guided mode were given directly from these solutions. Please note that, since the emission from a QC laser is transverse magnetically (TM) polarised due to the selection rules of the intersubband transition,[5] we were only interested in the guided modes with near 100 % TM component.

FIMMPROP-3D, the bi-directional optical propagation tool was used to calculate the facet reflectivity R for each mode found by FIMMWAVE. FIMMPROP-3D calculated the reflection coefficient at the facet by

calculating the Fresnel reflection for each point across the facet and then working out the total coupling of the reflected light back into the original mode.

FIMMWAVE also had built-in routines to calculate the 2D (and 1D) farfield profiles. According to the FIMMWAVE manual, the algorithm used a rigorous vectorial formula, taking into account the mixing of the 3 electric and magnetic field components. First it approximated the near-field profile outside the facet, then performed 2D fast Fourier transforms (FFT's) on all four transverse components $E_x(x, y)$, $H_y(x, y)$. $E_y(x, y)$ and $H_x(x, y)$. Finally, it generated the 2D farfield profile from the FFT data, taking into account the mixing of the field components.[6]

Owing to the extremely high loss ($\alpha \approx 800{,}000$ cm^{-1} at $\lambda = 5$ μm) of the metal layers they could not be included in the representation of the waveguide as FIMMWAVE was unable to calculate the 1D modes of the metal slabs. However, the lossy silica layer ($\alpha \approx 110$ cm^{-1} at $\lambda = 5$ μm) between the sidewall and the metal was included. Additionally, the coupling to the surface-plasmon mode was not calculated. Modes with higher spatial overlap with the plasmon mode, or with a refractive index closer to the effective index of the surface-plasmon mode will experience greater coupling to this lossy mode. However, according to the literature the coupling of the waveguide mode to the surface-plasmon mode is very small in the 'plasma-enhanced' waveguide and so it has been assumed that we can safely ignore it.[7]

4.2 Structures modelled

In the original $\lambda \approx 5$ μm QC laser design by Faist *et al.* the doping level of the InP substrate was specified as $n_e = 1\times10^{18}$ cm^{-3}. This posed a small problem to our MBE growers since they did not have InP substrates doped to this level, nor could they grow InP. At the time this modelling was carried out it was understood that the doping level of the InP substrate which was used by our MBE group lay somewhere in the range $n_e = 1\times10^{18}$ to 3×10^{18} cm^{-3}. For this reason the modelling was carried out twice for each structure; once with values for an InP substrate doped $n_e = 1\times10^{18}$ cm^{-3} and then again with those for an InP substrate doped $n_e = 3\times10^{18}$ cm^{-3}. This was to investigate, what was thought of at the time, as the best and worst case scenarios. However, it was discovered during the final stages of the write-up of this thesis that the InP substrates which had been used for our growths had actually been doped between 4×10^{18} and 8×10^{18} cm^{-3}. We can see from the data in Table 12 (which were taken from the results of the previous chapter) that the optical constants of InP at these doping levels will be very different from that of the design specification. The loss coefficient is around an order of magnitude greater at 7×10^{18} cm^{-3} and the refractive index has also suffered a large drop. We can therefore expect that the losses in our lasers will rise accordingly, and that the confinement factor and the number of vertical transverse modes will also change. Overall, we can expect that our lasers will have high J_{th}, low $\partial P/\partial I$, and may not achieve room-temperature operation as a consequence.

Doping Level (cm^{-3})	n	α (cm^{-1})
1×10^{18}	2.95	32
3×10^{18}	2.91	117
8×10^{18}	2.74	315

Table 12 Refractive index and loss coefficient of InP at $\lambda = 5$ μm for several levels of free-carrier density ($T = 77$ K).

Given this knowledge we can see that the results of the modelling which used $n_e = 3\times10^{18}$ cm^{-3} now represent the very best that we can expect from the QC lasers in this work, with there being plenty of margin for the devices to perform significantly worse than predicted. The results using the $n_e = 1\times10^{18}$ cm^{-3} data for the InP substrate are still extremely useful since they show us what to expect when the proper substrate doping is used, which will be no doubt be carried out in the future. Referring to the data in Table 12 and making a comparison of the results for two cases will give an indication of how much further we could expect the performance to decrease if $n_e = 7\times10^{18}$ cm^{-3}.

QC lasers with a number of different waveguide geometries were fabricated during the course of this work, and most of them have been optically modelled to gain insight into their performance. The structures modelled and presented in this chapter are:

- 15 μm-wide mesa-etched QC laser with 55 ° sidewall angle at $T = 77$ K and $\lambda = 5$ μm,
- 9 μm-wide mesa-etched QC laser with 55 ° sidewall angle at $T = 77$ K and $\lambda = 5$ μm,
- 80 μm-wide mesa-etched QC laser with 55 ° sidewall angle at $T = 77$ K and $\lambda = 5$ μm,
- 15 μm-wide shallow-etched QC laser with 55 ° sidewall angle at $T = 77$ K and $\lambda = 5$ μm,
- 20 μm-wide PSWOX QC laser (native oxide depth = 0.6 μm) at $T = 77$ K and $\lambda = 5$ μm,
- 15 μm-wide mesa-etched QC laser with 55 ° sidewall angle at $T = 300$ K and $\lambda = 5.3$ μm,
- 15 μm-wide mesa-etched QC laser with vertical sidewalls at $T = 300$ K and $\lambda = 5.3$ μm.

The last structure with vertical sidewalls was not fabricated, and was simply modelled to see what differences existed between a QC laser with vertical and sloping sidewalls. The sloping sidewalls were approximated as a series of waveguide slices with a varying depth of replacement of the epilayer with silica, as required by the software. The width of each waveguide refers to the width at the base of the mesa (see Figure 41). For the mesa-etched structures the average width of the active region (used in the calculation of I_{th}) will be ~1.2 μm narrower owing to the sloping sidewalls.

For each structure, a table is given showing the list of layers used in the their representation in FIMMWAVE, with their composition, thickness, doping level, refractive index and loss coefficient. The values of n and α were taken from the results of the last chapter (see Table 7 to Table 10). The layers are listed in reverse order of epitaxial growth i.e. the first layers are the upper cladding layers and the last layer is the InP substrate. The refractive index and loss of the active waveguide core was taken as the average of all of the ~500 $In_{0.53}Ga_{0.47}As/In_{0.52}Al_{0.48}As$ layers contained within.

Next to this, a second table is given with a list of the optical modes found for the waveguide. The modes were numbered 0, 1, 2, ... which refers to the order of decreasing modal effective index n_{eff}. In every case mode '0' was the fundamental mode of the waveguide and the others were the higher order transverse modes. The n_{eff}, α_w and Γ found for each mode is given along side its number.

Below the tables for each structure are the intensity plots of each mode inside the waveguide i.e. $|E_y(x, y)|^2$ versus (x, y), like the one displayed in Figure 41 (a). High intensity light was shown as a bright yellow/green colour which scaled down to a dark colour for low intensity light. The blue colour was only a background and had no significance. In these plots the superimposed horizontal lines referred to the interfaces between the epitaxial layers. The bottom layer was the InP substrate and the top layer was silica with $n = 1.36$, α =

110 cm^{-1} (see Section 3.7). The two sloping (or vertical in one case) lines superimposed on the plot represented the sidewalls of the QC waveguide. The plots exported by FIMMWAVE were slightly misleading as to the actual structures modelled. The plot in Figure 41 (a) was been altered using a drawing package and is shown in Figure 41 (b) to help explain. Outside the waveguide, and above the InP substrate, the region was entirely SiO_2, although this is not clear in the plots made by FIMMWAVE. Secondly, the size scales in the vertical and horizontal were different, often with the horizontal scale being compressed so that the waveguide appears much narrower than it really was.

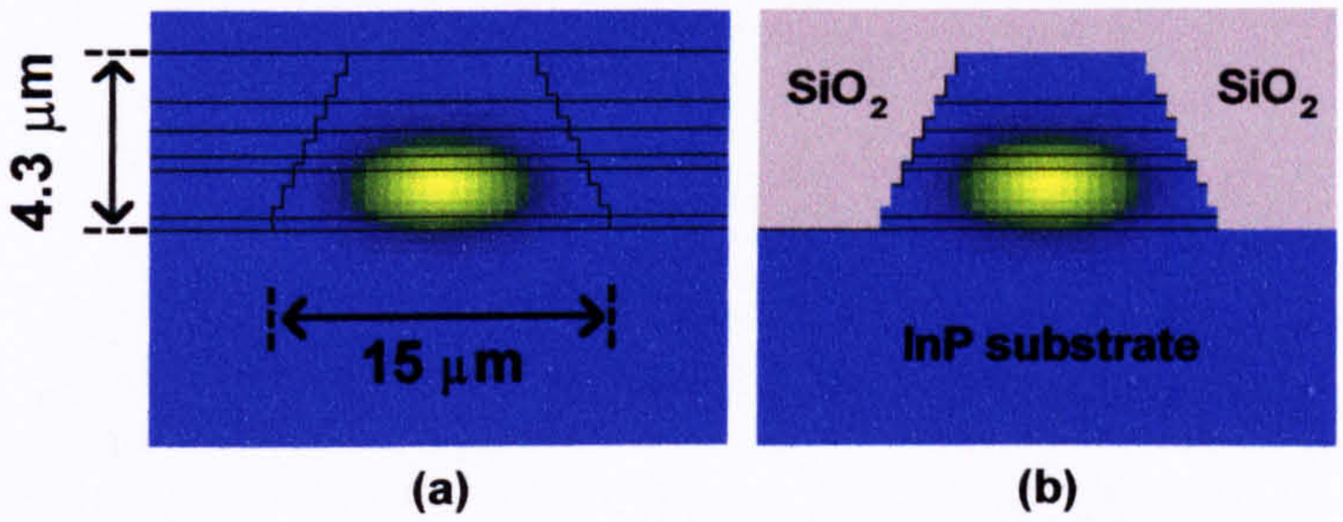

Figure 41 (a) Example of an intensity plot of the fundamental mode inside a '15 µm-wide' mesa-etched QC laser waveguide and (b) an altered plot to show more clearly the structure which was actually modelled.

In the case of the shallow-etched mesa (see Figure 42), the region of silica was only extended down to waveguide core i.e. it only replaced the top three InAlAs layers, and the three layers comprising the waveguide core were left intact extending fully from left to right. Some of the optical modes of interest, like the one in Figure 42, were more spread out horizontally than in the mesa-etched structures, and so the boundaries of the calculation had to be moved further away from the mesa so they did not influence the solution (the entire width modelled was 500 µm). To avoid large graphic files FIMMWAVE's intensity plots were of a limited resolution, which in the case of the rib mesa, was not sufficient to give a good view of the higher order modes. In this case it was decided to output the intensity data $I(x, y)$ for the full 500 µm-wide calculation space to file before plotting the central 100 µm in high resolution using external graphing software (see Figure 42). In these plots, the colour scales from white to red for low to high intensity, and the background is white.

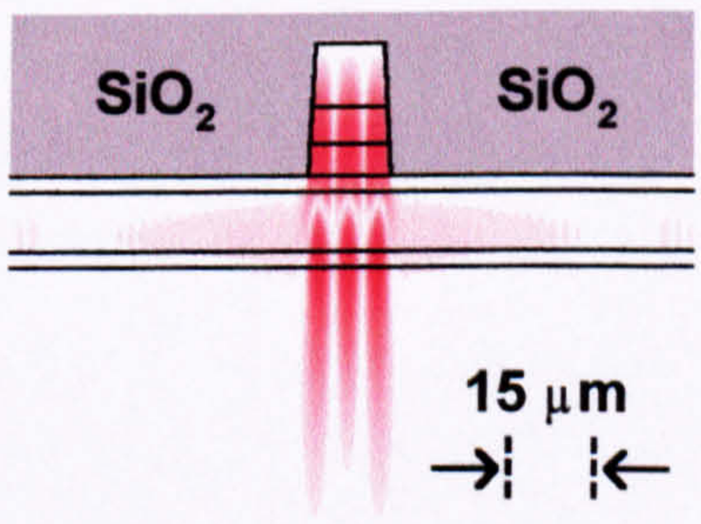

Figure 42 Example of an intensity plot of a high order transverse mode inside a rib-mesa QC laser waveguide. The plot was altered graphically to show more clearly the structure which was actually modelled.

Finally, to the PSWOX structure. In this case the structure was emulated by replacing 0.6 µm of the top InAlAs layer in the slices either side of the 20 µm-wide waveguide with the optical constants for Al_2O_3

(given in Section 3.7). Owing to the weaker optical confinement, these structures also needed to have the calculation boundaries place quite far from the waveguide (again a 500 μm width was modelled) to allow the mode to decay fully before reaching them. These device did not exhibit many higher order modes and so it was not really necessary to improve the resolution of the intensity plots. The direct output from FIMMWAVE is given here, so please forgive the poor quality of the plot.

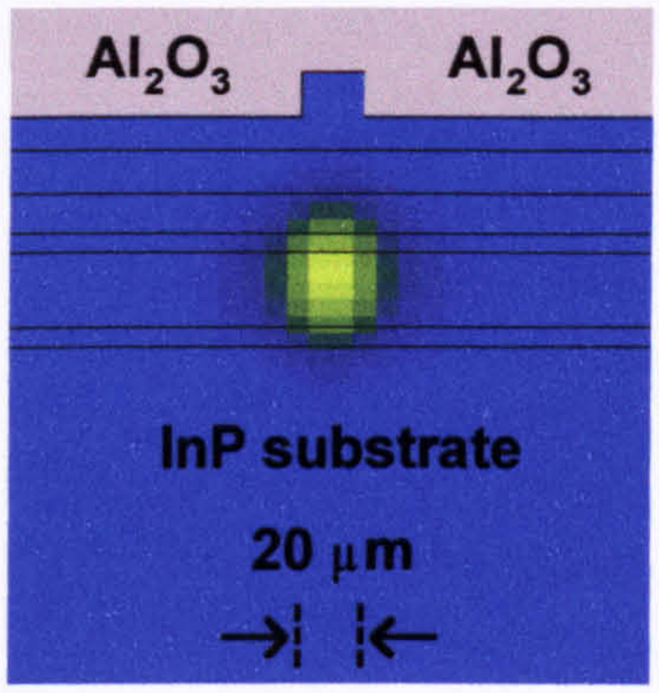

Figure 43 Example of an intensity plot of the fundamental mode inside a PSWOX QC laser waveguide. The plot was altered graphically to show more clearly the structure which was actually modelled.

4.3 Calculation of g_{th}, J_{th} and I_{th}

Once the values of Γ, α_w, and R had been determined, the threshold gain g_{th} (cm^{-1}) for each mode was easily calculated using,[8]

$$g_{th} = \frac{\alpha_m + \alpha_w}{\Gamma}, \tag{4-1}$$

where the mirror loss per cm, α_m, for a cavity of length L_{cav} (cm) with two facets with equal reflectivity R was found with the usual formula given in Eq. **(2-4)**. A cavity length L_{cav} = 3 mm was used for all calculations of J_{th} and I_{th}. The threshold gain gives information on how much gain must be produced by the QC active regions in order to bring a mode to lasing threshold. By comparing the values g_{th} for each mode, we can see which mode should be brought to threshold first. Further, if the difference in g_{th} between the modes is not too high, we can say which modes we might expect to lase given additional gain is provided in the cavity for that mode.

Going a step further, we may use Eq. **(2-8)** to calculate the expected value of J_{th} of each optical mode. This was carried out for all of calculated modes presented in this chapter, except those for T = 300 K since Eq. **(2-8)** has been shown not to work particularly well for high temperatures. The values of the parameters used in the calculation were those given in Table 3 except that a value of Δ = 46 meV was used for the reasons already given in Section 2.3.1.1. The threshold current I (A) was also calculated from,

$$I_{th} = \frac{1}{100} J_{th} L_{cav} W, \tag{4-2}$$

where units were kA/cm^2, mm, and μm for J_{th}, L_{cav}, and the waveguide width W, respectively.

4.4 Results of the optical modelling

4.4.1 Waveguide mode effective indices, waveguide losses, confinement factors, and field intensity plots

4.4.1.1 Mesa-etched QC laser with 55 ° sidewall angle, λ = 5 μm, width = 15 μm, T = 77 K, $n_e = 1\times10^{18}$ cm^{-3} substrate doping

Layer	Doping (cm^{-3})	Thickness (nm)	n	α (cm^{-1})
InAlAs	7E18	1215	2.748	989
InAlAs	3E17	700	3.077	36
InAlAs	2E17	615	3.083	24
InGaAs	1E17	315	3.319	2.6
Active Core	2E16	1141	3.205	1.7
InGaAs	1E17	315	3.319	2.6
InP sub	1E18	10000	2.955	32

Table 13 The layers used in the simulation together with their thickness, n and α..

Mode	n_{eff}	α_w (cm^{-1})	Γ (%)	R (%)	α_m (cm^{-1})	g_{th} (cm^{-1})	J_{th} (kA/cm^2)	I_{th} (A)
0	3.131	14.7	55.4	27.33	4.32	34.3	1.01	0.42
1	3.115	14.0	56.0	27.31	4.33	32.7	0.96	0.40
2	3.090	13.3	56.7	27.27	4.33	31.1	0.90	0.37
3	3.055	13.2	57.0	27.20	4.34	**30.8**	**0.88**	**0.37**
4	3.012	14.4	55.7	27.07	4.36	33.7	0.95	0.39
5	2.966	19.4	47.4	26.74	4.40	50.2	1.39	0.57
6	2.956	51.2	6.9	25.38	4.57	808.3	22.0	9.11

Table 14 Modes found by FIMMWAVE along with their respective values of n_{eff}, α_w, Γ and R. Width for threshold calculations = 13.8 μm. The mode with the lowest g_{th} is highlighted in bold.

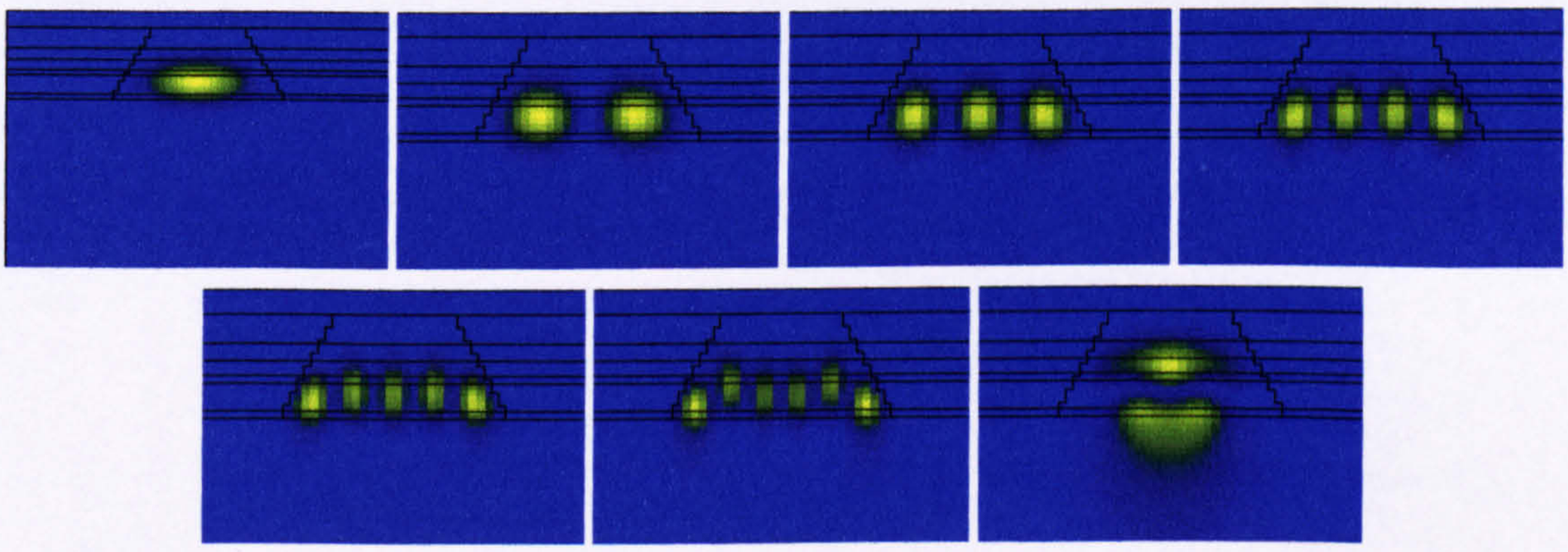

Figure 44 Intensity plots for the TM modes numbered 0 to 6 in Table 14.

The first feature that stands out is the large number of modes supported by the waveguide, especially in the horizontal direction. There was even a second order mode in the vertical direction, but this was only very weakly guided (its n_{eff} =2.956 was very close to that of the substrate n = 2.955) and it had such a high loss that we would never expect it to reach threshold (J_{th} calculated as 9.11 A).

The second interesting feature was that these calculations showed that the fundamental mode should not be the first mode to lase, but rather that honour will go to one of the higher order transverse modes. The order of low to high g_{th} in this case was mode 3, 2, 4, 1, 0, 5, then 6. As will become clear when we see the results for

the waveguide structure with vertical sidewalls in Section 4.4.1.11, this was a consequence of the sloping sidewalls. Close to the sloping sidewalls, the mode was more tightly confined to the active waveguide core in the vertical direction owing to the gradual reduction in the epilayer thickness. For the higher order horizontal modes which had a greater presence at the sidewalls, this meant they had higher values of Γ and lower α, both of which helped reduce J_{th}. The difference in g_{th} between modes 0 to 5 was not very large, which suggested that the devices might well be susceptible to the competition of modes for dominance and/or to changes in number lasing transverse modes with increasing laser bias.

Comparison of the calculated α_w and J_{th} with those reported in the literature was very encouraging. Mode 3 was calculated here to have $\alpha_w = 13.3$ cm^{-1} and $J_{th} = 0.88$ kA/cm^2 for the 15 μm × 3mm device. The only set of experimental data reported for this device was by Faist *et al.* for a 9 μm × 3 mm QCL where the measured J_{th} data of device indicated $\alpha_w = 12.7$ cm^{-1} and $J_{th} \approx$ 1kA/cm2 at $T = 77$ K (see Figure 8). It is thought that the QCLs fabricated by Faist *et al.* had more vertical sidewalls, which is one of the numerous factors that could explain the small discrepancy in the measured and predicted J_{th}.

4.4.1.2 Mesa-etched QC laser with 55 ° sidewall angle, $\lambda = 5$ μm, width = 15 μm, $T = 77$ K, $n_e = 3\times10^{18}$ cm^{-3} substrate doping

Layer	Doping (cm^{-3})	Thickness (nm)	n	α (cm^{-1})
InAlAs	7E18	1215	2.748	989
InAlAs	3E17	700	3.077	36
InAlAs	2E17	615	3.083	24
InGaAs	1E17	315	3.319	2.6
Active core	2E16	1143	3.205	1.7
InGaAs	1E17	315	3.319	2.6
InP sub	3E18	10000	2.910	117

Table 15 The layers used in the simulation together with their thickness, n and α..

Mode	n_{eff}	α_w (cm^{-1})	Γ (%)	R (%)	α_m (cm^{-1})	g_{th} (cm^{-1})	J_{th} (kA/cm^2)	I_{th} (A)
0	3.127	21.4	55.8	27.33	4.32	46.1	1.34	0.56
1	3.111	20.9	56.4	27.31	4.33	44.7	1.30	0.54
2	3.085	20.6	57.3	27.27	4.33	**43.5**	**1.25**	**0.52**
3	3.050	21.2	58.0	27.21	4.34	44.0	1.25	0.52
4	3.007	23.7	57.5	27.09	4.35	48.8	1.37	0.57
5	2.957	30.4	53.2	26.87	4.38	65.4	1.80	0.74
6	2.935	99.4	12.2	25.66	4.53	852	23.0	9.53
7	2.915	93.5	13.8	25.61	4.51	710	19.1	7.89

Table 16 Modes found by FIMMWAVE along with their respective values of n_{eff}, α_w, Γ and R. Width for threshold calculations = 13.8 μm. The mode with the lowest g_{th} is highlighted in bold.

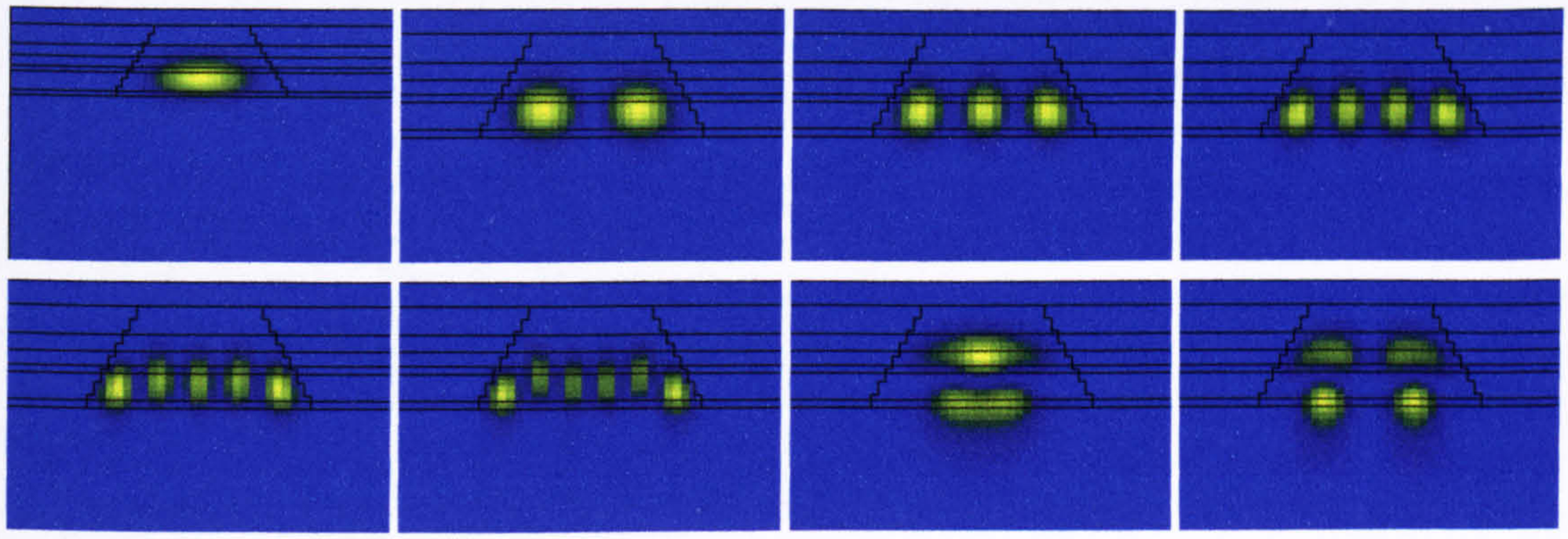

Figure 45 Intensity plots for the TM modes numbered 0 to 7 in Table 16.

Owing to the higher loss and stronger confinement provided by the excessively doped InP layer, we can see a corresponding rise in the J_{th} by ~ 30 to 40 % and the appearance of a another 2nd order vertical mode. These thresholds are very close to the ones measured in this work for 15 μm × 3 mm QCLs ($I_{th} \approx 0.5$ to 1A), which indicates that the source of our problems was simply with the incorrect doping level of the InP substrate. Another effect of the high loss in the InP substrate was to change the mode with lowest threshold gain from mode number 3 to number 2. We can see from the values of Γ and α_w that this happened because, even although mode 3 still had the superior Γ, its greater overlap with the lossy InP substrate raised its value of α_w.

4.4.1.3 Mesa-etched narrow QC laser with 55 ° sidewall angle, λ = 5 μm, width = 9 μm, T = 77 K, $n_e = 1\times10^{18}$ cm^{-3} substrate doping

Layer	Doping (cm^{-3})	Thickness (nm)	n	α (cm^{-1})
InAlAs	7E18	1215	2.748	989
InAlAs	3E17	700	3.077	36
InAlAs	2E17	615	3.083	24
InGaAs	1E17	315	3.319	2.6
Active core	2E16	1141	3.205	1.7
InGaAs	1E17	315	3.319	2.6
InP sub	1E18	10000	2.955	32

Table 17 The layers used in the simulation together with their thickness, n and α..

Mode	n_{eff}	α_w (cm^{-1})	Γ (%)	R (%)	α_m (cm^{-1})	g_{th} (cm^{-1})	J_{th} (kA/cm^2)	I_{th} (A)
0	3.120	13.6	56.3	27.25	4.33	31.9	0.93	0.22
1	3.073	11.7	58.1	27.21	4.34	**27.6**	**0.80**	**0.19**
2	3.005	14.0	54.9	26.98	4.37	33.5	0.94	0.22

Table 18 Modes found by FIMMWAVE along with their respective values of n_{eff}, α_w, Γ and R. Width for threshold calculations = 7.8 μm. The mode with the lowest g_{th} is highlighted in bold.

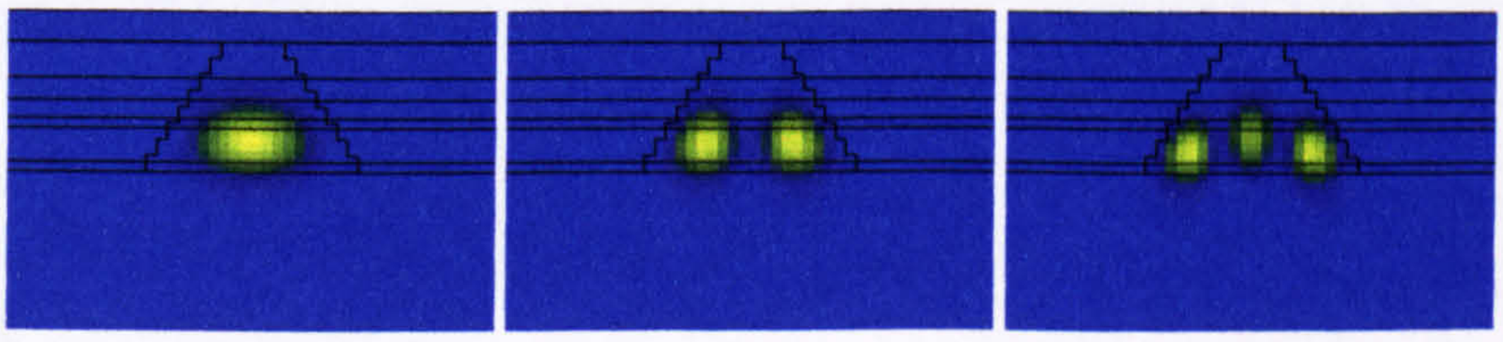

Figure 46 Intensity plots for the TM modes numbered 0 to 2 in Table 18.

Moving to a slightly narrower waveguide geometry greatly reduced the number of transverse modes and threshold current, not only due to the reduction in laser width, but also because of the value of J_{th} being reduced to just 0.8 kA/cm^2. This was again a consequence of sidewalls acting to increase Γ. We must concede here that some contributions which were not accounted for in these calculations, such as possible overlap of the modes with the metal layers or possible imperfections/roughness of the sidewalls, would preferentially increase the waveguide losses of the higher order modes. In this case, they might suffer from increased loss and threshold currents over the fundamental and lower order modes.

4.4.1.4 Mesa-etched narrow QC laser with 55 ° sidewall angle, λ = 5 μm, width = 9 μm, T = 77 K, n_e = 3×10^{18} cm^{-3} substrate doping

Layer	Doping (cm^{-3})	Thickness (nm)	n	α (cm^{-1})
InAlAs	7E18	1215	2.748	989
InAlAs	3E17	700	3.077	36
InAlAs	2E17	615	3.083	24
InGaAs	1E17	315	3.319	2.6
Active core	2E16	1143	3.205	1.7
InGaAs	1E17	315	3.319	2.6
InP sub	3E18	10000	2.952	73

Table 19 The layers used in the simulation together with their thickness, n and α..

Mode	n_{eff}	α_w (cm^{-1})	Γ (%)	R (%)	α_m (cm^{-1})	g_{th} (cm^{-1})	J_{th} (kA/cm^2)	I_{th} (A)
0	3.116	20.5	56.8	27.33	4.32	43.7	1.27	0.30
1	3.068	19.8	59.2	27.29	4.33	**40.8**	**1.18**	**0.28**
2	2.998	25.9	57.8	27.10	4.35	52.3	1.47	0.35
3	2.920	45.3	42.1	26.48	4.43	118	3.19	0.75
4	2.918	90.7	12.5	25.53	4.55	762	20.47	4.79

Table 20 Modes found by FIMMWAVE along with their respective values of n_{eff}, α_w, Γ and R. Width for threshold calculations = 7.8 μm. The mode with the lowest g_{th} is highlighted in bold.

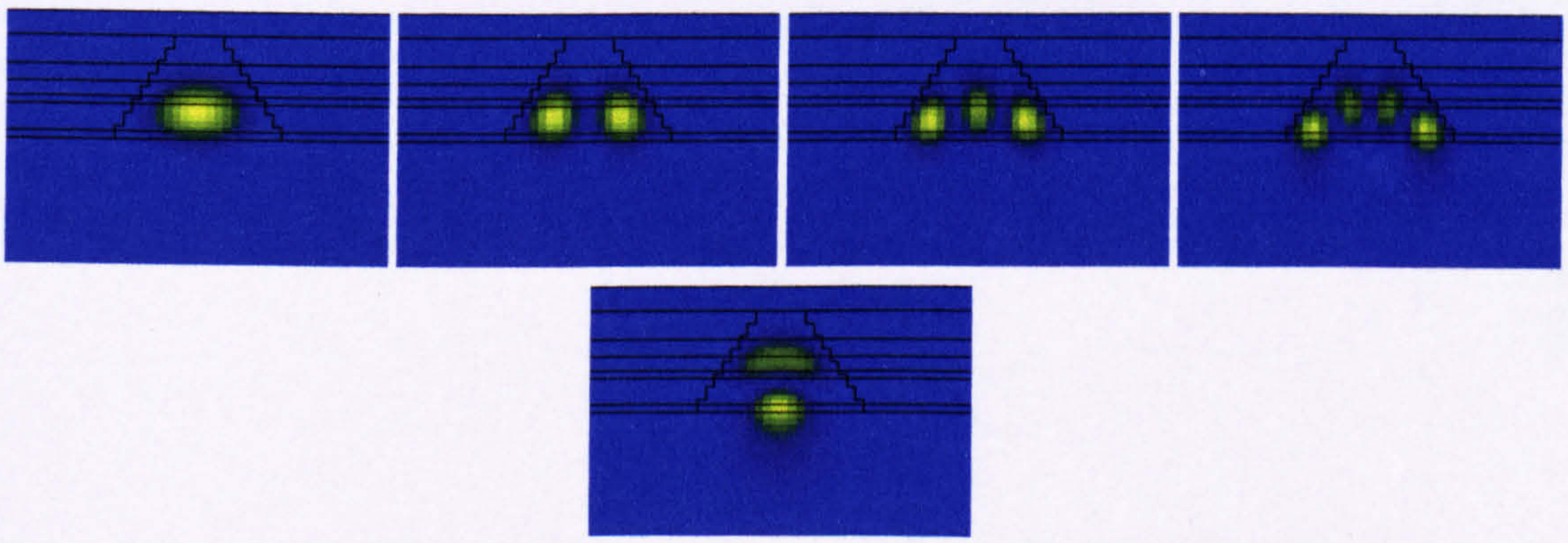

Figure 47 Intensity plots for the TM modes numbered 0 to 4 in Table 20.

Again we see that the highly doped InP substrate causes considerable degradation in performance, with nearly a 50 % increase in J_{th}, as well as the appearance of additional higher order modes. Again, these results compare well with measured values. A QC laser measuring 10 μm × 2.15 mm (see Section **8.2**) exhibited a threshold current of $I_{th} \approx 340$ mA, which translated to $J_{th} \approx 1.6$ kA/cm^2 c.f. the calculated values of $J_{th} \approx 1.2$ kA/cm^2 above. The slightly higher value of J_{th} observed in the actual device is expected, since the doping level of the InP substrate in the real device was higher than the value 3×10^{18} cm^{-3} used in the calculations.

4.4.1.5 Mesa-etched broad QC laser with 55 ° sidewall angle, λ = 5 μm, width = 80 μm, T = 77 K, $n_e = 3\times10^{18}$ cm^{-3} substrate doping

Layer	Doping (cm^{-3})	Thickness (nm)	n	α (cm^{-1})
InAlAs	7E18	1215	2.748	989
InAlAs	3E17	700	3.077	36
InAlAs	2E17	615	3.083	24
InGaAs	1E17	315	3.319	2.6
Active core	2E16	1143	3.205	1.7
InGaAs	1E17	315	3.319	2.6
InP sub	3E18	10000	2.910	117

Table 21 The layers used in the simulation together with their thickness, n and α..

Mode	n_{eff}	α_w (cm^{-1})	Γ (%)	R (%)	α_m (cm^{-1})	g_{th} (cm^{-1})	J_{th} (kA/cm^2)	I_{th} (A)
0	3.133	21.7	55.5	27.33	4.32	46.9	1.37	3.24
1	3.132	21.7	55.5	27.33	4.32	46.9	1.37	3.24
15	3.097	21.7	55.5	27.32	4.33	**46.9**	**1.35**	**3.20**
39	2.941	102	11.9	25.66	4.53	895	24.2	57.3

Table 22 Modes found by FIMMWAVE along with their respective values of n_{eff}, α_w, Γ and R. Width for threshold calculations = 78.8μm. The mode with the lowest g_{th} is highlighted in bold.

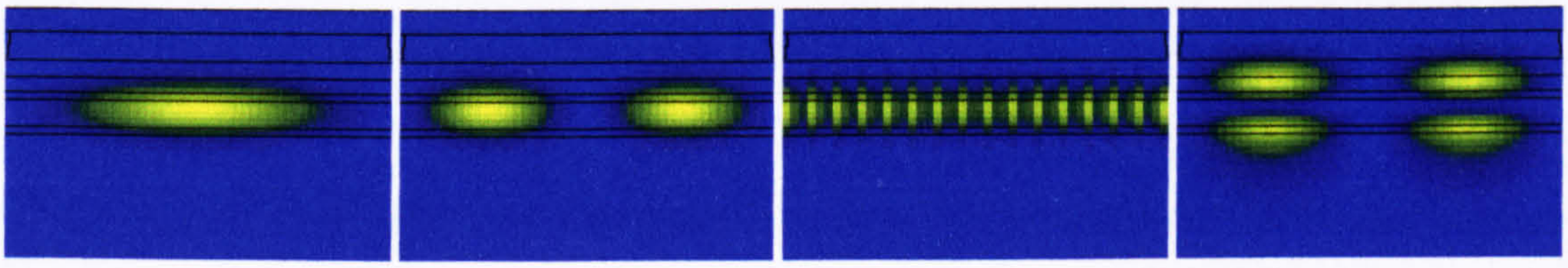

Figure 48 Intensity plots for the TM modes numbered 0, 1, 15 and 39 in Table 22.

In the case of a broad-area QCL, the large width of the waveguide permitted the existence of a very large number of horizontal transverse modes. More than 57 modes were found by FIMMWAVE for this structure. Only four examples, modes 0, 1, 15 and 39 are shown for simplicity. Since only a low percentage of each mode interacted with the sidewalls, there was very little difference between the horizontal fundamental and higher order transverse modes, both in terms of effective index and in threshold gain. The fundamental mode had the lowest gain owing to slowly decreasing facet reflectivity with increasing mode order. It may be possible that many modes may reach threshold sequentially and lase simultaneously. The modes which were second order in the vertical direction all had much higher α_w and lower Γ so that the threshold of these modes was very high indeed.

4.4.1.6 Shallow-etched QC laser with 55 ° sidewall angle, λ = 5 μm, width = 15 μm, T = 77 K, $n_e = 3\times10^{18}$ cm^{-3} substrate doping

Layer	Doping (cm^{-3})	Thickness (nm)	n	α (cm^{-1})
InAlAs	7E18	1215	2.748	989
InAlAs	3E17	700	3.077	36
InAlAs	2E17	615	3.083	24
InGaAs	1E17	315	3.319	2.6
Active core	2E16	1143	3.205	1.7
InGaAs	1E17	315	3.319	2.6
InP sub	3E18	10000	2.910	117

Table 23 The layers used in the simulation together with their thickness, n and α..

Mode	n_{eff}	α_w (cm^{-1})	Γ (%)	R (%)	α_m (cm^{-1})	g_{th} (cm^{-1})	J_{th} (kA/cm^2)	I_{th} (A)
0	3.130	21.6	55.6	27.33	4.32	46.6	1.36	0.61
1	3.123	21.4	55.9	27.33	4.32	45.7	1.34	0.60
2	3.110	21.2	56.3	27.33	4.32	45.3	1.32	0.59
3	3.093	21.1	57.0	27.33	4.32	44.6	1.29	0.58
4	3.072	21.7	58.2	27.33	4.32	44.7	1.28	0.58
5	2.939	98.7	14.1	26.88	4.38	731	19.8	8.91
6	2.930	95.8	15.2	25.68	4.53	660	17.8	8.01
7	2.914	88.9	19.8	25.64	4.54	472	12.7	5.70

Table 24 Modes found by FIMMWAVE along with their respective values of n_{eff}, α_w, Γ and R. Width for threshold calculations = 15 μm.

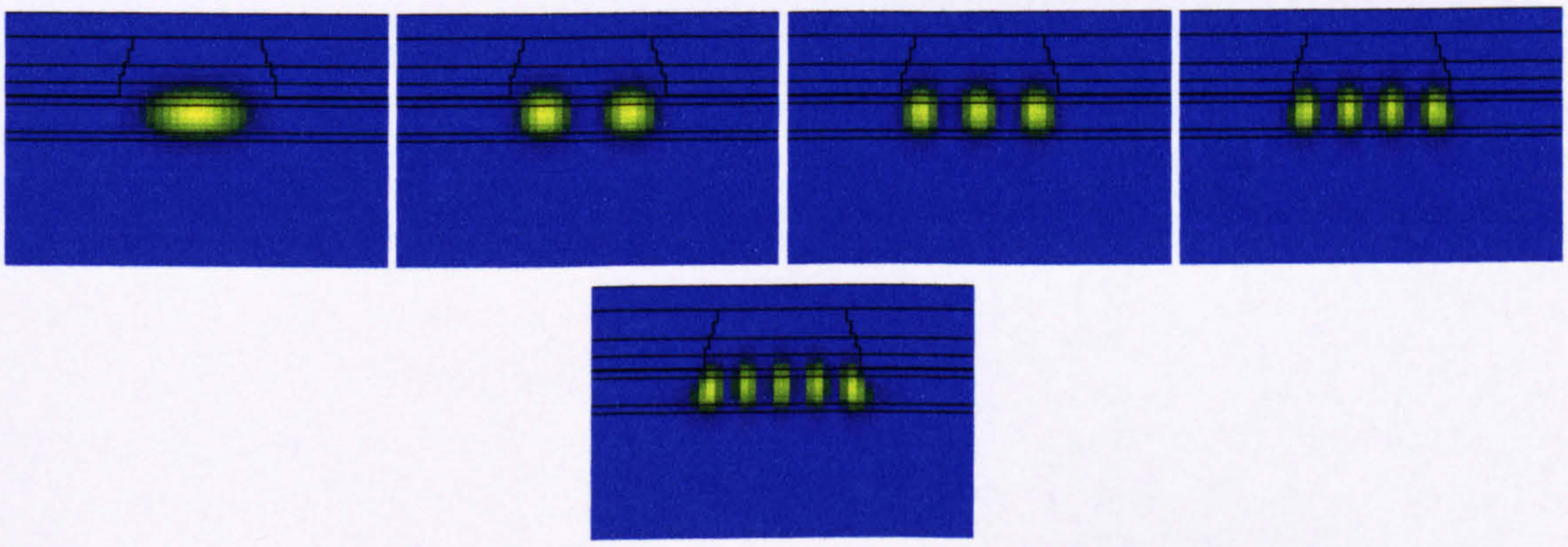

Figure 49 Intensity plots exported directly from FIMMWAVE for the TM modes numbered 0 to 4 in Table 24.

Even though the horizontal optical confinement was not as strong as in the mesa-etched devices (owing to the reduced contrast in effective index), the calculations showed that there was still a fair number of transverse modes supported in the shallow-etched QCL geometry.

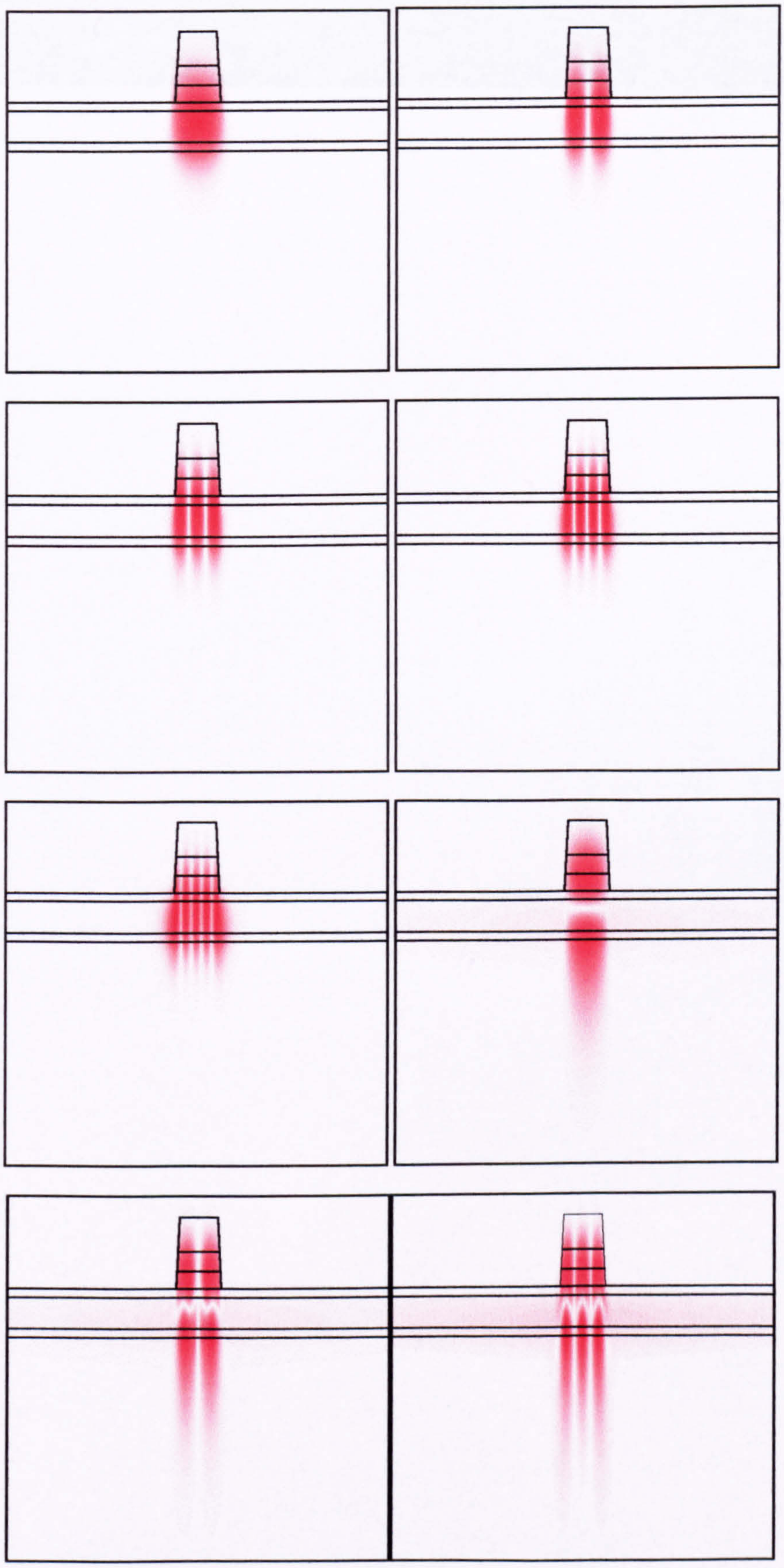

Figure 50 Intensity plots exported as a data file, then plotted at high resolution for the TM modes numbered 0 to 7 in Table 24.

In the calculation of the I_{th} of the devices it was assumed that there was no current spreading so that the width used was that of the rib width i.e. 15 μm. This has been shown not to be the case as a high I_{th} for real devices reported in this work and elsewhere, indicated that there was significant lateral current spreading. The lateral current spreading in actual rib structures was estimated by Gmachl *et al.* to increase the effective stripe width of a ~15 μm-wide rib to ~60 μm.[9] There was no claim, nor evidence (such as that which could perhaps be obtained from farfield measurements) in that publication to indicate that the entire area into which current was injected was emitting stimulated light. It is suggested here that the excess current required to reach threshold may be considered as leakage current which does not contribute to output power.

4.4.1.7 PSWOX QC laser, λ = 5 μm, width = 20 μm, T = 77 K, $n_e = 1\times10^{18}$ cm^{-3} substrate doping

Layer	Doping (cm^{-3})	Thickness (nm)	n	α (cm^{-1})
InAlAs	7E18	1215	2.748	989
InAlAs	3E17	700	3.077	36
InAlAs	2E17	615	3.083	24
InGaAs	1E17	315	3.319	2.6
Active core	2E16	1141	3.205	1.7
InGaAs	1E17	315	3.319	2.6
InP sub	1E18	10000	2.955	32

Table 25 The layers used in the simulation together with their thickness, n and α..

Mode	n_{eff}	α_w (cm^{-1})	Γ (%)	R (%)	α_m (cm^{-1})	g_{th} (cm^{-1})	J_{th} (kA/cm^2)	I_{th} (A)
0	3.136	14.0	54.4	27.34	4.32	**33.7**	**0.99**	**0.59**
1	2.960	53.8	6.9	25.44	4.56	846	23.1	13.8

Table 26 Modes found by FIMMWAVE along with their respective values of n_{eff}, α_w, Γ and R. Width for threshold calculations = 20 μm. The mode with the lowest g_{th} is highlighted in bold.

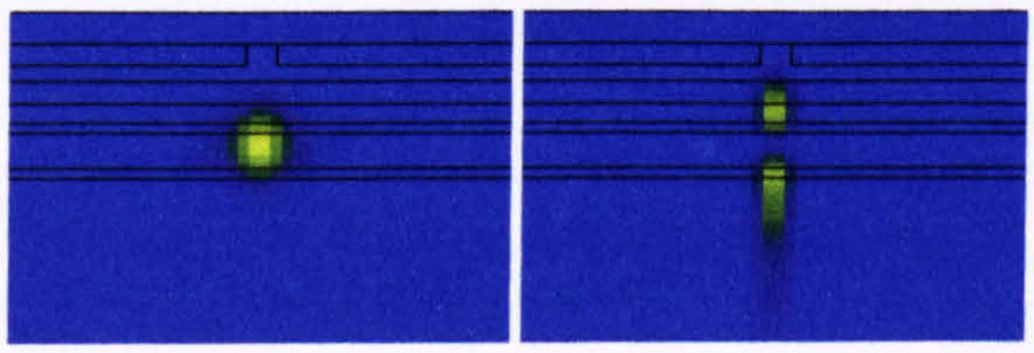

Figure 51 Intensity plots for the TM modes numbered 0 to 1 in Table 26. Note that the poor resolution is only of the displayed information, not an indication of the resolution of the calculations.

The PSWOX structure only exhibited two guided modes localised to the aperture, with only one of them having a threshold current within usual operation limits. From a purely optical point of view, this structure exhibited excellent performance for a 20 μm-wide QCL device. However, in terms of electrical confinement it is as bad, or worse, than the rib-mesa structure (see Section 8.6).

4.4.1.8 PSWOX QC laser, λ = 5 μm, width = 20 μm, T = 77 K, $n_e = 3 \times 10^{18}$ cm^{-3} substrate doping

Layer	Doping (cm^{-3})	Thickness (nm)	n	α (cm^{-1})
In0.52Al0.48As	7E18	1215	2.748	989
InAlAs	3E17	700	3.077	36
InAlAs	2E17	615	3.083	24
InGaAs	1E17	315	3.319	2.6
Active core	2E16	1143	3.205	1.7
InGaAs	1E17	315	3.319	2.6
InP sub	3E18	10000	2.910	117

Table 27 The layers used in the simulation together with their thickness, n and α..

Mode	n_{eff}	α_w (cm^{-1})	Γ (%)	R (%)	α_m (cm^{-1})	g_{th} (cm^{-1})	J_{th} (kA/cm^2)	I_{th} (A)
0	3.132	20.7	55.7	27.34	4.41	**45.1**	**1.31**	**0.79**
1	2.941	101	11.8	25.66	4.53	894	24.2	14.5
2	2.937	94.5	11.7	25.66	4.53	846	22.9	13.7

Table 28 Modes found by FIMMWAVE along with their respective values of n_{eff}, α_w, Γ and R. Width for threshold calculations = 20 μm. The mode with the lowest g_{th} is highlighted in bold.

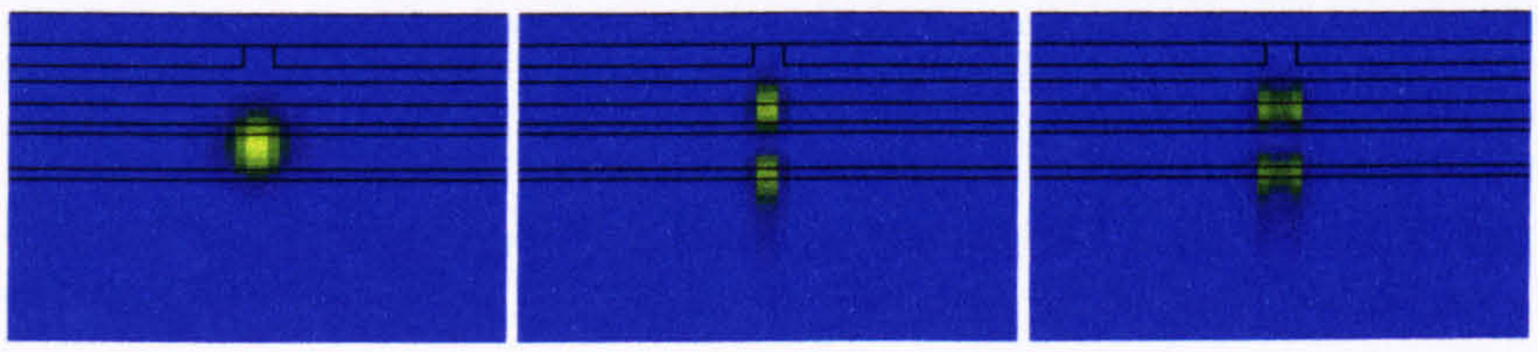

Figure 52 Intensity plots for the TM modes numbered 0 to 2 in Table 28. Note that the poor resolution is only of the displayed information, not an indication of the resolution of the calculations.

The much higher $J_{th} \approx 9$ kA/cm^2 measured in this work for these devices (see Section **8.6**), indicated the presence of strong current spreading. The current spreading effectively decreased the overlap Γ of the optical mode with the gain so that J_{th} and I_{th} increased. The actual J_{th} measured in our PSWOX QCLs was a factor of ~ 7 times the value which was predicted by the calculations here, but it must also be remembered that the InP substrate doping level was greater than 3×10^{18} cm^{-3} in the real devices. This indicated that current spreading had led to an effective width at threshold of ~ 100 μm. However, analysis of measured slope efficiency suggested that most of the current injected above threshold was consumed by the lasing mode, and that the fraction lost to spreading decreased above threshold.

4.4.1.9 Mesa-etched QC laser with 55 ° sidewall angle, λ = 5.3 μm, width = 15 μm, T = 300 K, $n_e = 1\times10^{18}$ cm^{-3} substrate doping

Layer	Doping (cm^{-3})	Thickness (nm)	n	α (cm^{-1})
InAlAs	7E18	1215	2.740	1440
InAlAs	3E17	700	3.113	40
InAlAs	2E17	615	3.119	25
InGaAs	1E17	315	3.392	3.6
Active core	2E16	1141	3.260	2.2
InGaAs	1E17	315	3.392	3.6
InP sub	1E18	10000	3.038	33

Table 29 The layers used in the simulation together with their thickness, n and α..

Mode	n_{eff}	α_w (cm^{-1})	Γ (%)	R (%)	α_m (cm^{-1})	g_{th} (cm^{-1})
0	3.183	17.1	54.9	27.97	4.25	38.9
1	3.166	16.2	55.2	27.94	4.25	37.0
2	3.139	15.2	55.5	27.89	4.26	**35.1**
3	3.101	15.2	55.1	27.80	4.27	35.3
4	3.059	17.0	52.7	27.62	4.46	40.4

Table 30 Modes found by FIMMWAVE along with their respective values of n_{eff}, α_w, Γ and R. Width for threshold calculations = 13.8 μm. The mode with the lowest g_{th} is highlighted in bold.

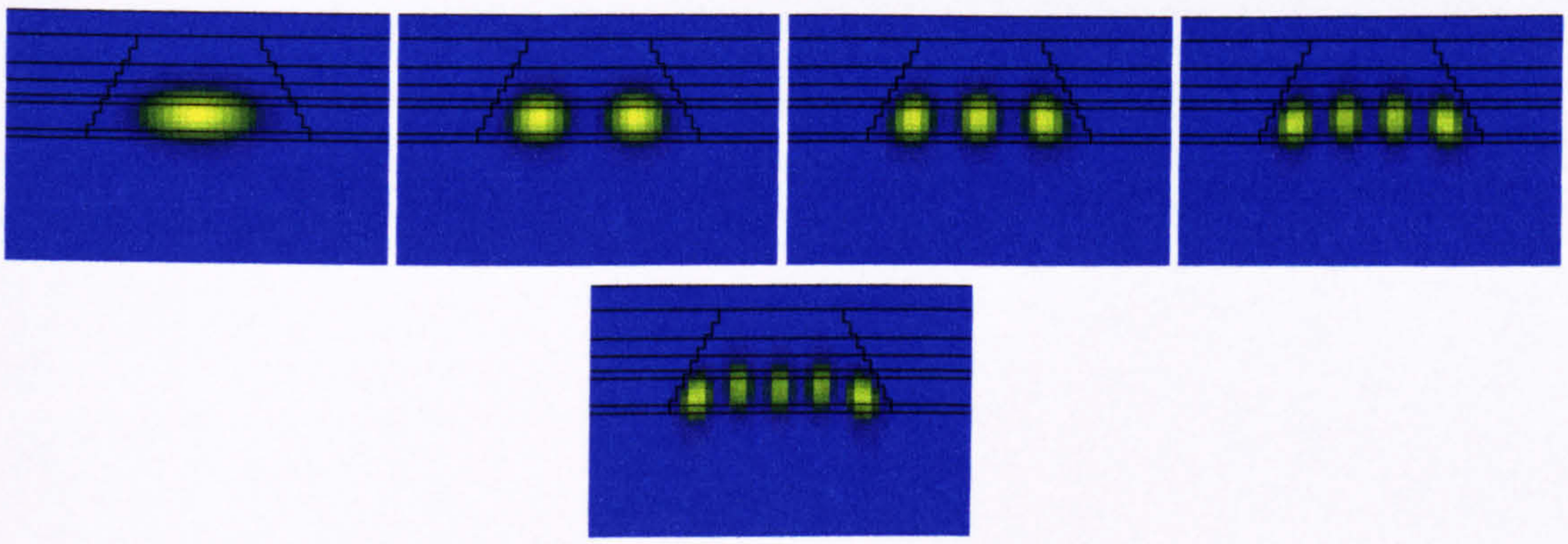

Figure 53 Intensity plots for the TM modes numbered 0 to 4 in Table 30.

The room temperature calculations showed a few slight differences to those for liquid nitrogen temperature. The effective indices of the modes were a little higher at T = 300 K; n_{eff} = 3.131 at T = 77 K compared to n_{eff} = 3.183 at T = 300 K for the fundamental mode. The values waveguide losses had also increased; α_w = 14.7 at T = 77 K compared to α_w = 17.1 at T = 300 K. Γ had dropped slightly, but R had increased slightly. Overall, the threshold gain had increased by around 14 %. Lastly, because the lower contrast in refractive index between the InP substrate and the guided mode, the number of modes supported had decreased. In the vertical direction, the waveguide had become single mode.

4.4.1.10 Mesa-etched QC laser with 55 ° sidewall angle, λ = 5.3 μm, width = 15 μm, T = 300 K, n_e = 3 ×10^{18} cm^{-3} substrate doping

Layer	Doping (cm^{-3})	Thickness (nm)	n	α (cm^{-1})
InAlAs	7E18	1215	2.740	1440
InAlAs	3E17	700	3.113	40
InAlAs	2E17	615	3.119	25
InGaAs	1E17	315	3.392	3.6
Active core	2E16	1143	3.260	2.2
InGaAs	1E17	315	3.392	3.6
InP sub	3E18	10000	2.940	131

Table 31 The layers used in the simulation together with their thickness, n and α..

Mode	n_{eff}	α_w (cm^{-1})	Γ (%)	R (%)	α_m (cm^{-1})	g_{th} (cm^{-1})
0	3.174	26.3	56.2	27.96	4.25	54.4
1	3.156	25.9	56.9	27.94	4.25	53.0
2	3.128	25.8	57.7	27.89	4.26	**52.1**
3	3.089	26.7	58.3	27.81	4.48	53.5
4	3.044	28.0	57.9	27.68	4.28	55.8
5	2.986	39.0	53.2	27.44	4.31	81.4
6	2.961	125	11.2	26.04	4.49	1156
7	2.940	117	12.4	25.93	4.50	980

Table 32 Modes found by FIMMWAVE along with their respective values of n_{eff}, α_w, Γ and R. Width for threshold calculations = 13.8 μm. The mode with the lowest g_{th} is highlighted in bold.

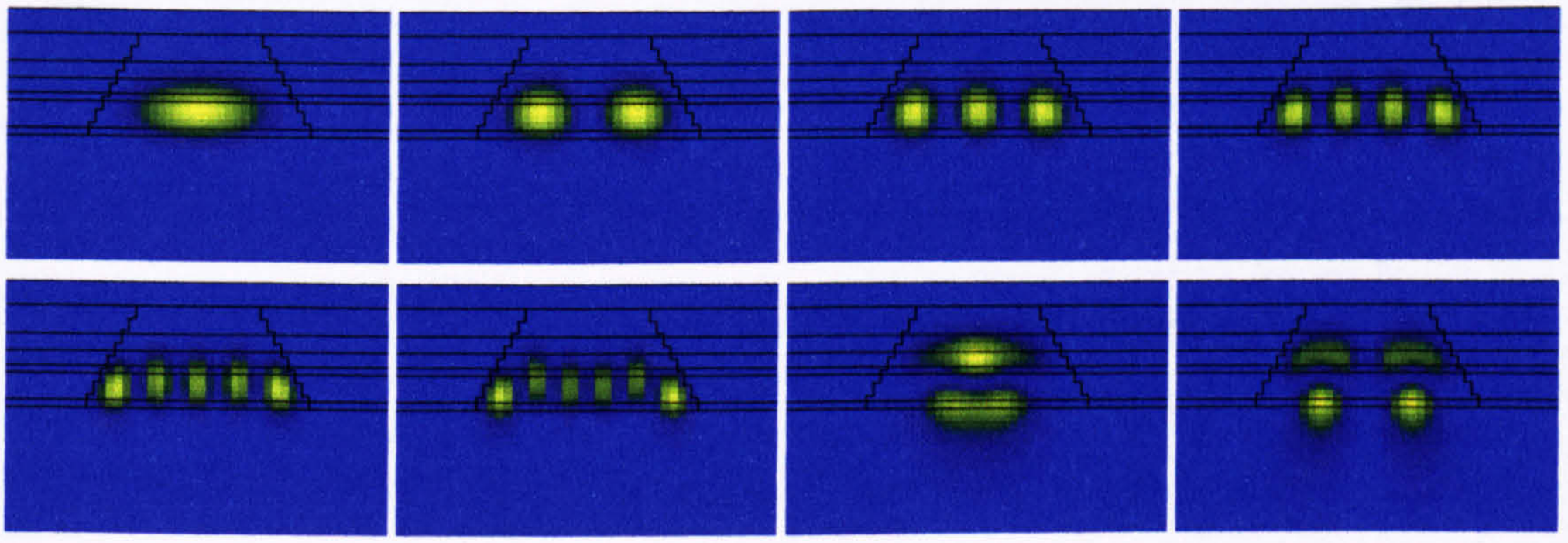

Figure 54 Intensity plots for the TM modes numbered 0 to 7 in Table 32.

With the use of the excessively doped InP substrate there was a reappearance of the lossy 2nd order modes in the vertical direction and an increase in the threshold gain by ~50 % over the structure with the correct doping level.

4.4.1.11 Mesa-etched QC laser with vertical sidewalls, λ = 5.3 μm, width = 15 μm, T = 300 K, $n_e = 1\times10^{18}$ cm^{-3} substrate doping

Layer	Doping (cm^{-3})	Thickness (nm)	n	α (cm^{-1})
InAlAs	7E18	1215	2.740	1440
InAlAs	3E17	700	3.113	40
InAlAs	2E17	615	3.119	25
InGaAs	1E17	315	3.392	3.6
Active core	2E16	1141	3.260	2.2
InGaAs	1E17	315	3.392	3.6
InP sub	1E18	10000	3.038	33

Table 33 The layers used in the simulation together with their thickness, n and α..

Mode	n_{eff}	α_w (cm^{-1})	Γ (%)	R (%)	α_m (cm^{-1})	g_{th} (cm^{-1})
0	3.185	17.5	54.7	27.96	4.25	**39.8**
1	3.171	17.6	54.6	27.92	4.25	40.1
2	3.148	17.7	54.5	28.01	4.24	40.3
3	3.116	17.9	54.3	27.98	4.25	40.8
4	3.074	18.3	54.0	27.67	4.28	41.8

Table 34 Modes found by FIMMWAVE along with their respective values of n_{eff}, α_w, Γ and R. Width for threshold calculations = 13.8 μm. The mode with the lowest g_{th} is highlighted in bold.

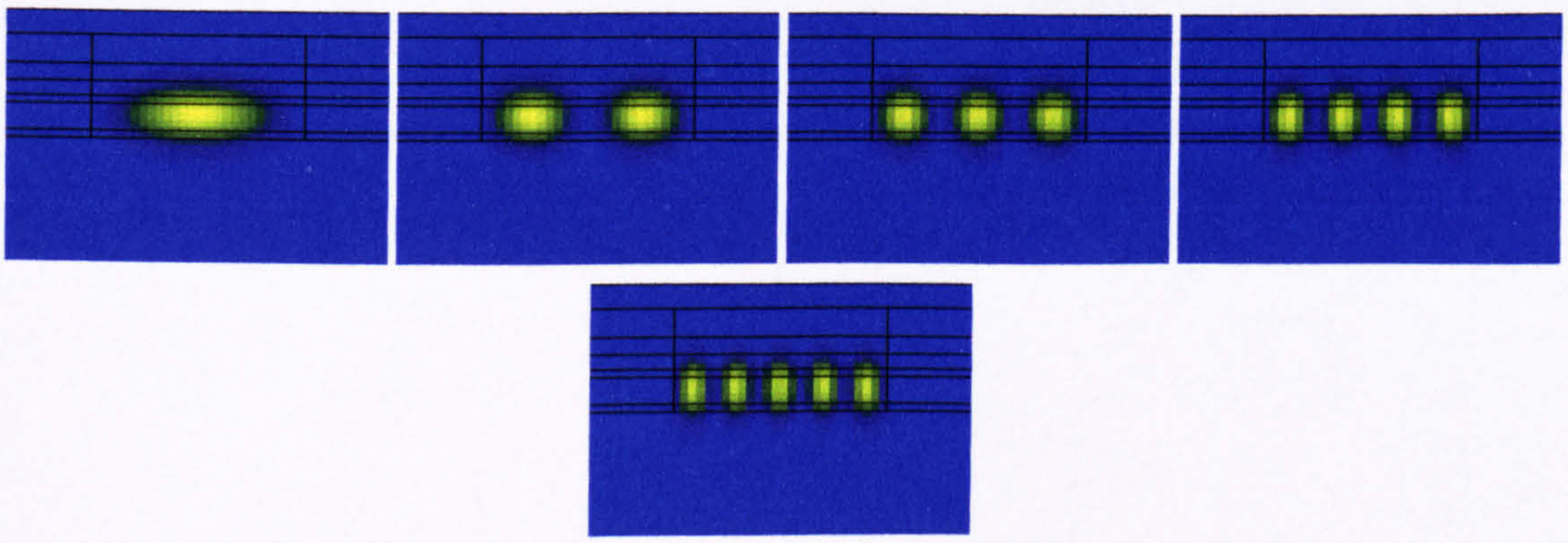

Figure 55 Intensity plots for the TM modes numbered 0 to 4 in Table 34.

	Sloping sidewalls				*Vertical sidewalls*			
Mode	n_{eff}	α_w (cm^{-1})	Γ (%)	R (%)	n_{eff}	α_w (cm^{-1})	Γ (%)	R (%)
0	3.183	17.1	54.9	27.97	3.185	17.5	54.7	27.96
1	3.166	16.2	55.2	27.94	3.171	17.6	54.6	27.92
2	3.139	15.2	55.5	27.89	3.148	17.7	54.5	28.01
3	3.101	15.2	55.1	27.80	3.116	17.9	54.3	27.98
4	3.059	17.0	52.7	27.62	3.074	18.3	54.0	27.67

Table 35 Comparison of the results of the optical modelling for a mesa-etched QCL with vertical and sloping sidewalls.

The modelling showed that in a mesa-etched QCL structure with vertical sidewalls, the fundamental mode should be the first mode to lase since it now had the lowest threshold gain. Table 35 compares the values of n_{eff}, α_w, Γ and R obtained for the structure with sloped sidewalls (see Section 4.4.1.9) with those found for the one with vertical sidewalls. We see that the fundamental mode was essentially unaffected by the

sidewalls, whereas the higher order modes had enhanced Γ and lower α_w in the case of the mesa with sloping sidewalls.

4.4.2 Far-field intensity profiles

FIMMWAVE's built-in far-field tool was used to calculate the far-field of each of the modes from Section 4.4.1. The far-field gave the distribution of the output beam at the plane (x, y, L) where x was the direction parallel to the epitaxial layers of the QCL (horizontal direction) and to the laser facet, y was the direction perpendicular the epitaxial layers and parallel to the laser facet (vertical direction), and z was the direction of beam propagation which was perpendicular to the laser facet. $z = L$ was the distance between the laser facet and the plane of the far-field i.e. the distance propagated by the mode outside the laser cavity.

The results of the calculations were exported from FIMMWAVE as data files and then used to create greyscale intensity plots in an external graphing program. Each plot scales from black to white for 0 to maximum intensity (meaning that they are all normalised). The axes have the units mm/L as the spread of the beam depends on the distance propagated. Hence, if the far-field plane was at a distance $L = 42$ mm from the laser facet, the area of the far-field plots would be $4L \times 4L = 168 \times 168$ mm.

The characterisation system and far-field measurements will be fully discussed Chapter 7. However, before moving on to the results of the far-field calculations it is useful to point out that in the light-current (LI) measurements performed on our QC lasers, the light was collected from the facet using a parabolic mirror with f-number ≈ 1.7. This mirror only collected the emission within a cone of ±16 degrees. On the far-field plots this will correspond to a circle with a radius of only L/mm = 0.29 centred at (0, 0) which has been superimposed on the plots as a red dotted circle. While inspecting the calculated far-fields we will see that the collection efficiency (i.e. the ratio of emission inside the circle radius 0.29, to that outside it) changes for each mode. A white dotted circle was also superimposed on the plots to represent the optical access to the cryostat (f/0.8). Any light outside the white dotted circle would not even escape the cryostat.

4.4.2.1 Mesa-etched QC laser with 55 ° sidewall angle, λ = 5 μm, width = 15 μm, T = 77 K, n_e = 1×10^{18} cm^{-3} substrate doping

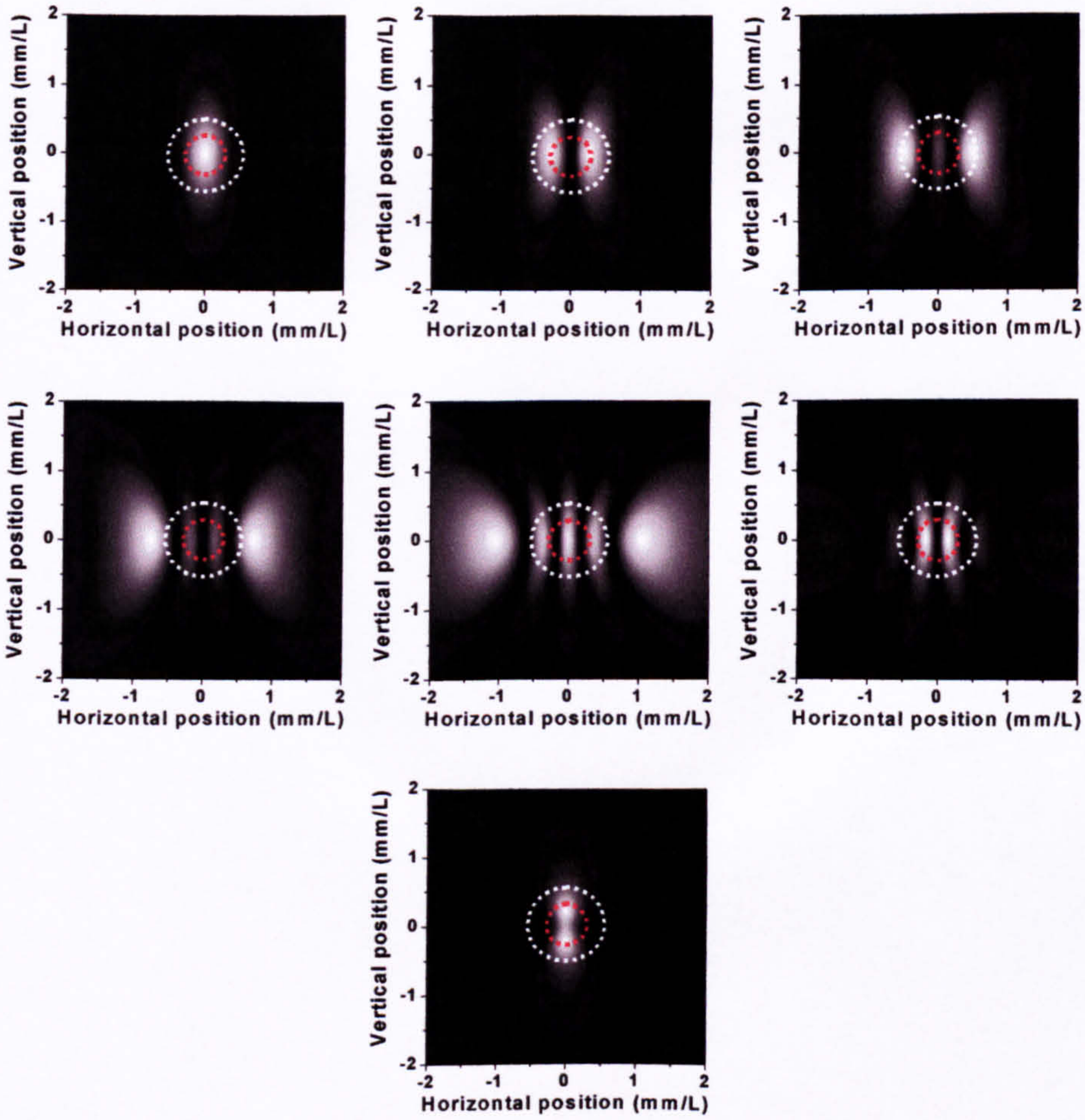

Figure 56 3D intensity plots of the far-field distributions of the TM modes numbered 0 to 6 in Table 13. The white dotted circle represents an f/0.8 cryostat window and the red dotted circle f/1.7 parabolic collection.

The fundamental mode (mode 0) had a FWHM divergence of ~24 degrees in the horizontal and ~ 66 degrees in the vertical direction which corresponds very well to values reported for other QC lasers (29 and 64 degrees) [10]. The collection efficiency has not been calculated for each mode (perhaps it should be at a later date), but it is obvious from the calculated far-fields that it is different for each mode. If the laser were to operate on mode 2 or 3, for example, the collection efficiency would be much lower than if it were to be lasing on the fundamental mode (mode 0). This is very important since the modelling results in Section 4.4.1.1 showed that modes 2 and 3 exhibited the lowest threshold currents for this structure. Further, if the laser were to switch between modes (or lase with additional modes) during operation, we would expect changes in collection efficiency and so fluctuations in the collected power in the LI curves. This behaviour was evident in the experimental results of this work, which we will see later on in Chapter 8.

4.4.2.2 Mesa-etched QC laser with 55 ° sidewall angle, λ = 5 μm, width = 15 μm, T = 77 K, $n_e = 3\times10^{18}$ cm^{-3} substrate doping

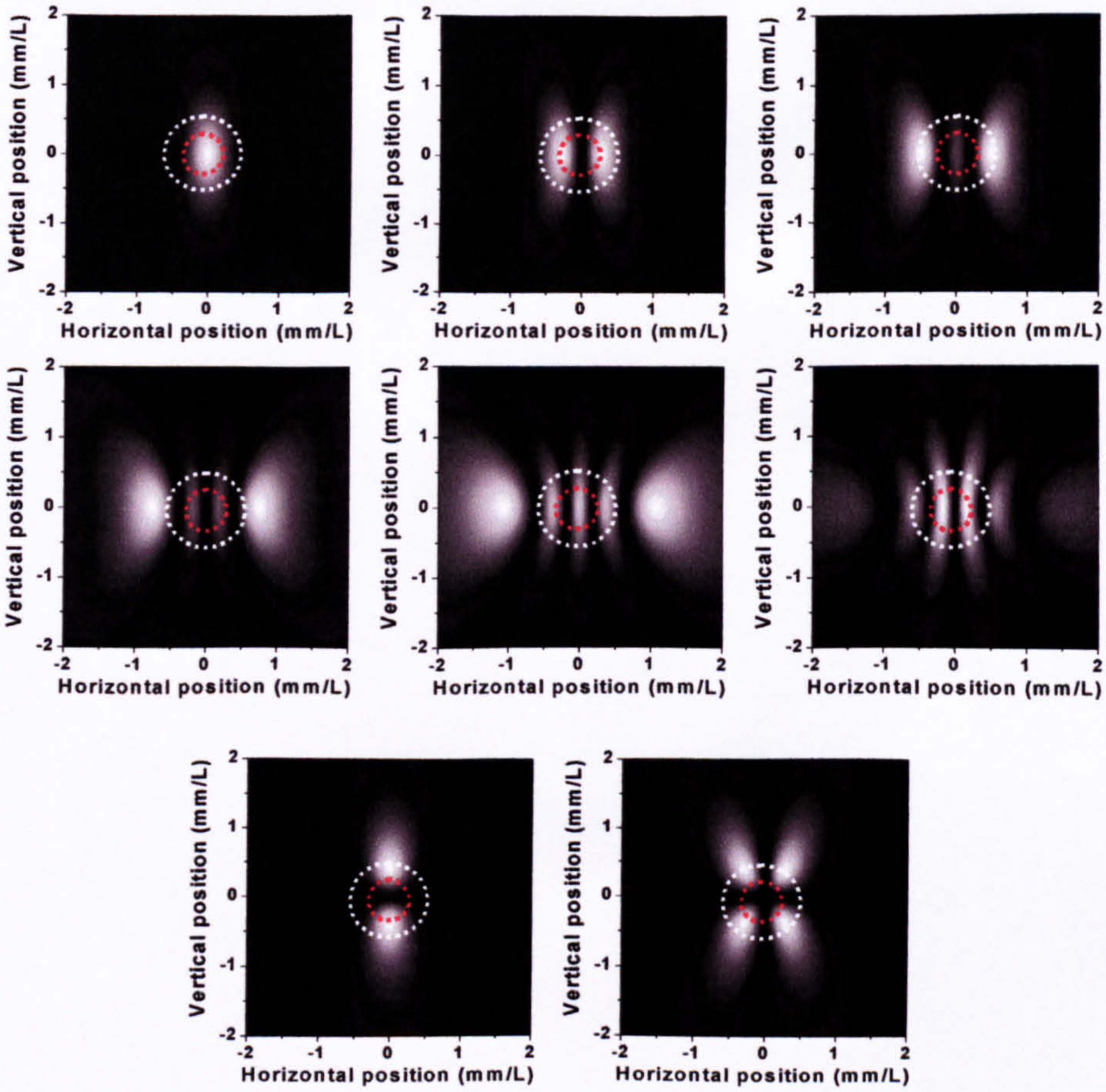

Figure 57 3D intensity plots of the far-field distributions for the TM modes numbered 0 to 7 in Table 15. The white dotted circle represents an f/0.8 cryostat window and the red dotted circle f/1.7 parabolic collection.

The only addition comment that needs to made here is that, owing to the increased optical confinement provided by the excessively doped InP substrate, the divergence in the vertical direction was increased. The fundamental mode (mode 0) had a FWHM divergence of ~24 degrees in the horizontal and ~ 69 degrees in the vertical direction, which will further reduce the collection efficiency.

4.4.2.3 Mesa-etched narrow QC laser with 55 ° sidewall angle, λ = 5 μm, width = 9 μm, T = 77 K, n_e = 1×10^{18} cm^{-3} substrate doping

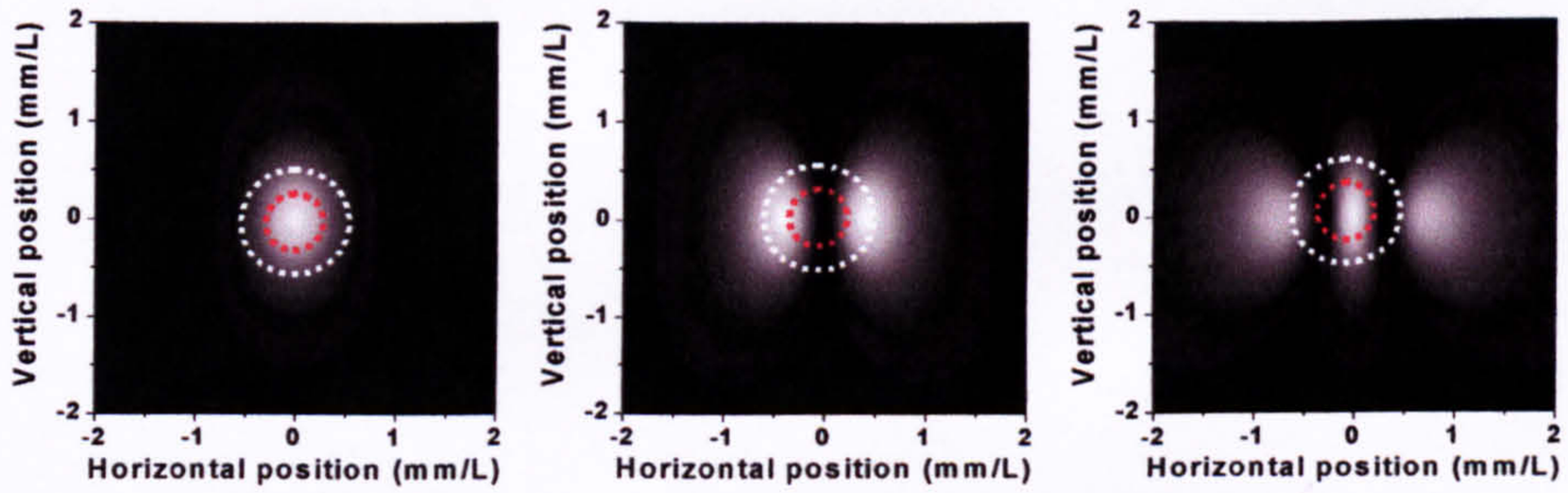

Figure 58 3D intensity plots of the far-field distributions for the TM modes numbered 0 to 2 in Table 17. The white dotted circle represents an f/0.8 cryostat window and the red dotted circle f/1.7 parabolic collection.

Comparing the far-field of this 9 μm-wide QCL with that of the 15 μm-wide one, it was found that the beam divergence in the horizontal plane had risen, as would be expected for a narrower device. The fundamental mode (mode 0) had a FWHM divergence of ~ 39 degrees in the horizontal and ~ 67 degrees in the vertical direction. The collection efficiency for mode 0 and mode 1 therefore dropped accordingly, with the collection for mode 1 being very small. An unexpected finding was that the collection efficiency of mode 3 was improved as there was a greater concentration of the mode to the centre of the profile.

4.4.2.4 Mesa-etched narrow QC laser with 55 ° sidewall angle, λ = 5 μm, width = 9 μm, T = 77 K, n_e = 1×10^{18} cm^{-3} substrate doping

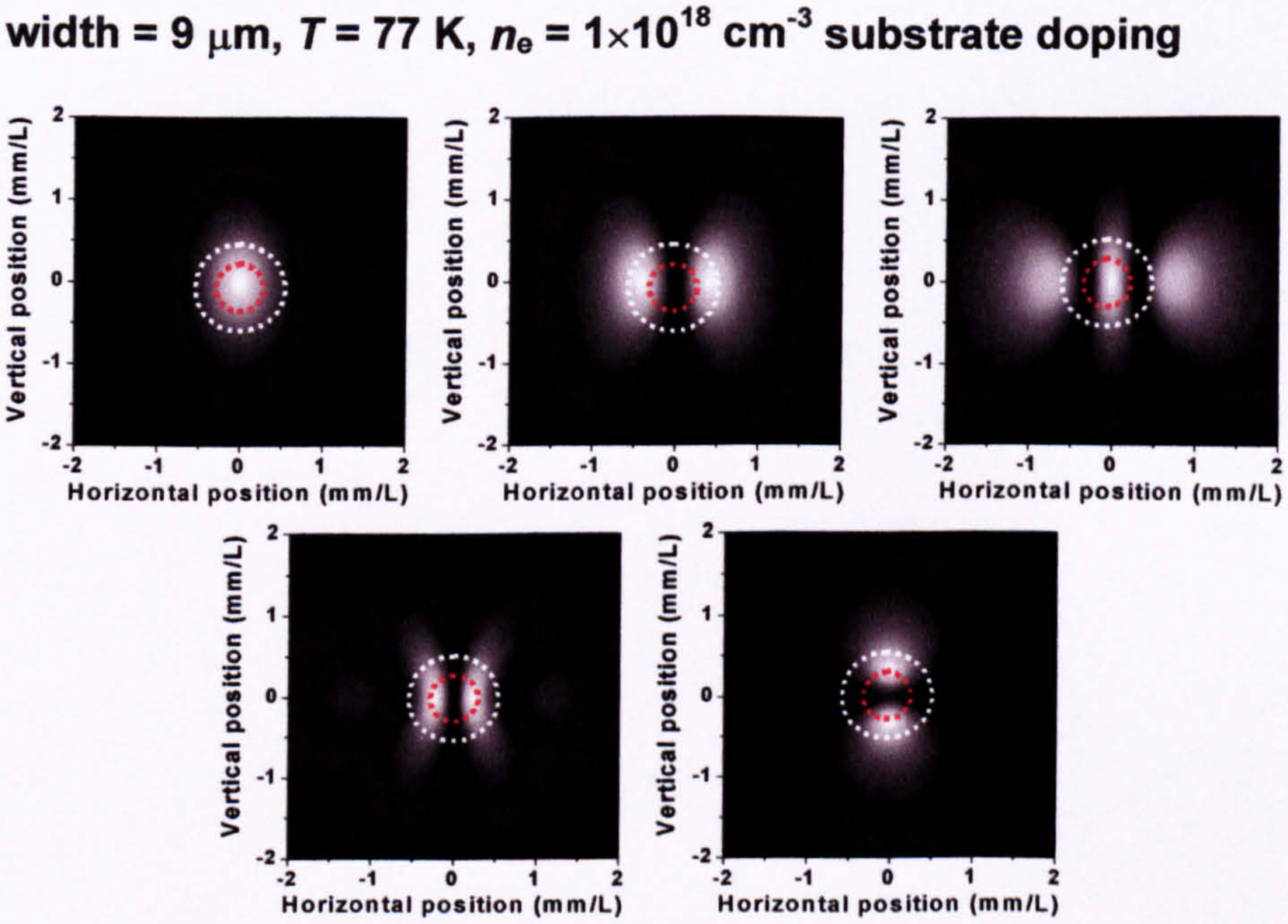

Figure 59 3D intensity plots of the far-field distributions for the TM modes numbered 0 to 4 in Table 19. The white dotted circle represents an f/0.8 cryostat window and the red dotted circle f/1.7 parabolic collection.

The comments for this structure follow those in Sections 4.4.1.2 and 4.4.1.3. The fundamental mode (mode 0) had a FWHM divergence of ~ 40 degrees in the horizontal and ~ 69 degrees in the vertical direction.

4.4.2.5 Mesa-etched broad QC laser with 55 ° sidewall angle, λ = 5 μm, width = 80 μm, T = 77 K, n_e = 3×10^{18} cm^{-3} substrate doping

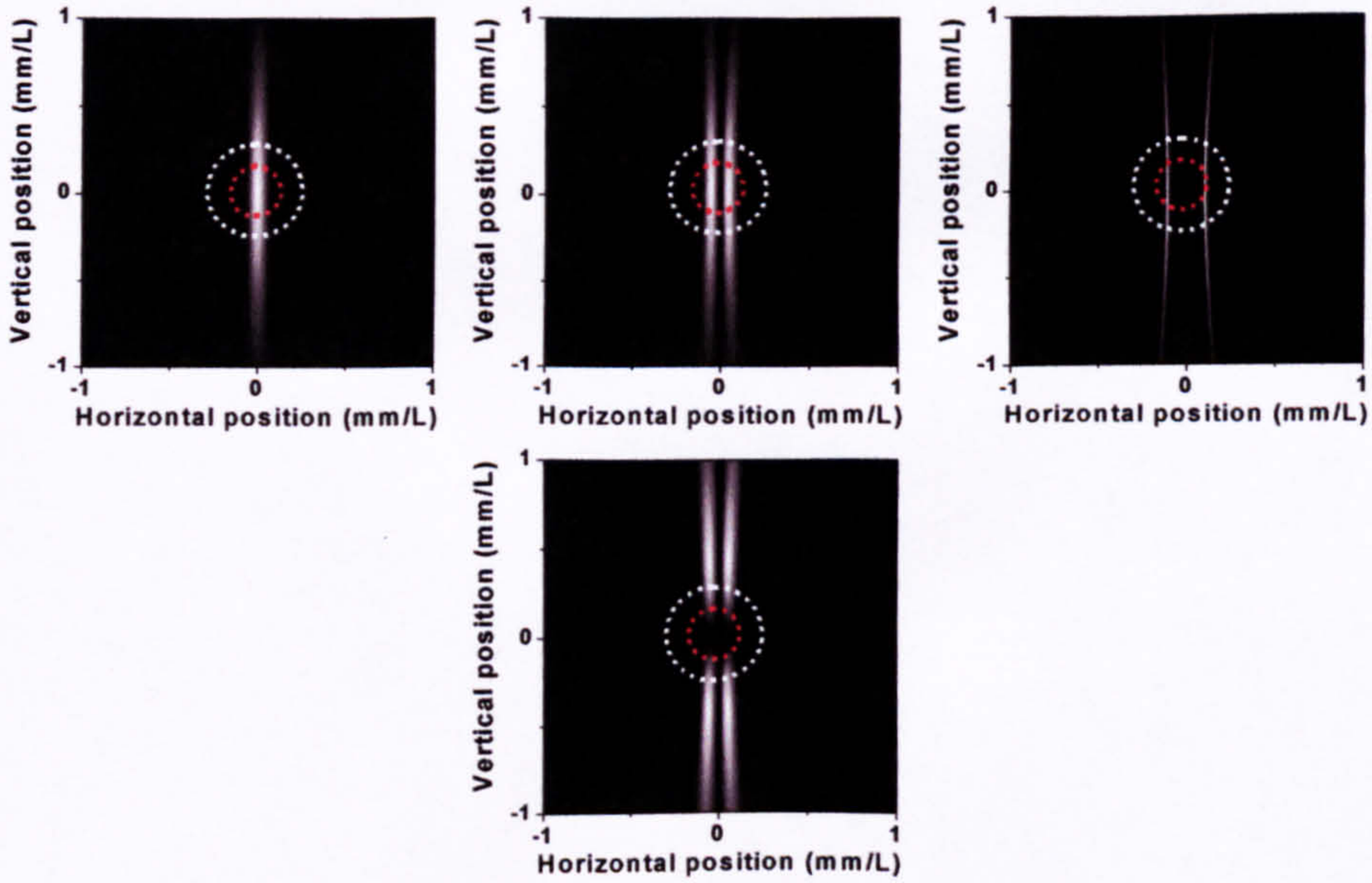

Figure 60 3D intensity plots of the far-field distributions for the TM modes numbered 0, 1, 15 and 39 in Table 21. The white dotted circle represents an f/0.8 cryostat window and the red dotted circle f/1.7 parabolic collection.

The far-field distributions for the broad-area QCL had a very narrow divergence in the horizontal direction owing to the weak optical confinement imposed by the broad mesa. The fundamental mode (mode 0) had a FWHM divergence of just ~ 4 degrees in the horizontal and ~ 68 degrees in the vertical direction. A relatively high collection efficiency might be expected for this laser, but we must remember that there were many other modes which had low thresholds and could lase perhaps all simultaneously.

4.4.2.6 Shallow-etched QC laser with 55 ° sidewall angle, λ = 5 μm, width = 15 μm, T = 77 K, $n_e = 3\times10^{18}$ cm^{-3} substrate doping

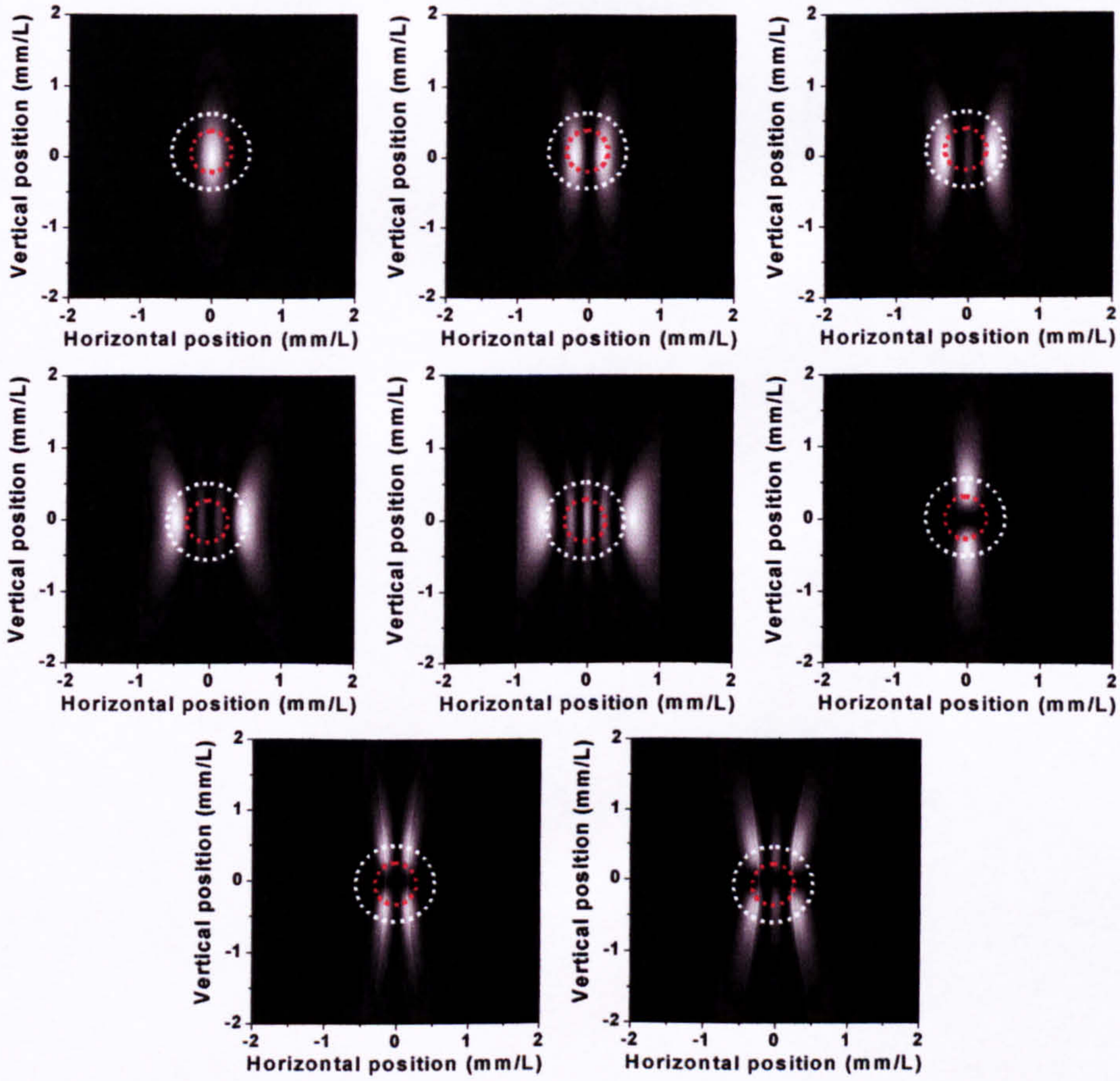

Figure 61 3D intensity plots of the far-field distributions for the TM modes numbered 0 to 7 in Table 23. The white dotted circle represents an f/0.8 cryostat window and the red dotted circle f/1.7 parabolic collection.

The shallow-etched QCL had a far-field distribution with a character somewhere between that of a broad-area and a mesa-etched QCL, with their being a medium beam divergence in the horizontal direction. The fundamental mode (mode 0) had a FWHM divergence of ~ 13 degrees in the horizontal and ~ 68 degrees in the vertical direction.

4.4.2.7 PSWOX QC laser, λ = 5 μm, width = 20 μm, T = 77 K, $n_e = 1\times10^{18}$ cm^{-3} substrate doping

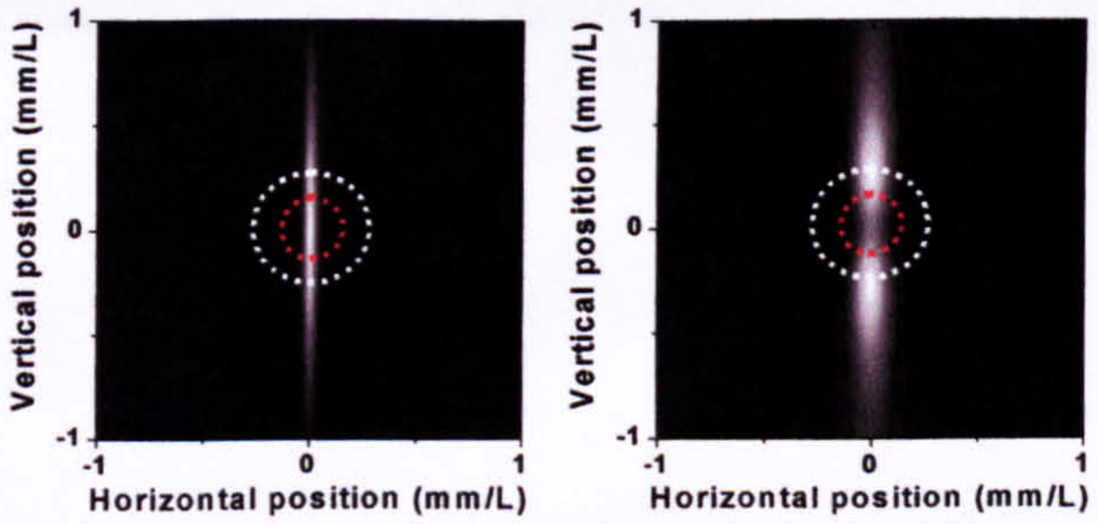

Figure 62 3D intensity plots of the far-field distributions for the TM modes numbered 0 to 1 in Table 25. The white dotted circle represents an f/0.8 cryostat window and the red dotted circle f/1.7 parabolic collection.

The far-field distribution of the PSWOX QCL exhibited a FWHM divergence of only ~ 3 degrees in the horizontal and ~ 67 degrees in the vertical direction. Since the second mode had such a high threshold, it was not expected to ever reach lasing threshold. This meant that the structure was more or less single mode and that there should not be any changes in collection efficiency during the its operation, even under high current injection conditions. This was confirmed by the experimental far-field profiles which are presented in Chapter 8.

4.4.2.8 PSWOX QC laser, λ = 5 μm, width = 20 μm, T = 77 K, $n_e = 3\times10^{18}$ cm^{-3} substrate doping

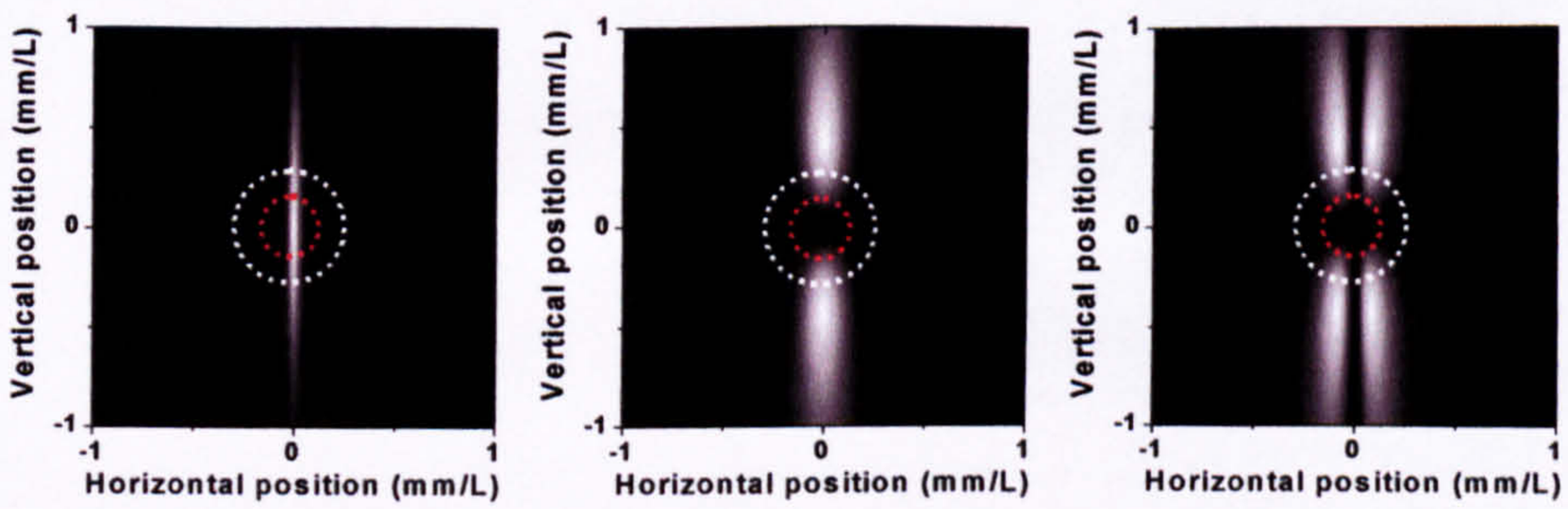

Figure 63 3D intensity plots of the far-field distributions for the TM modes numbered 0 to 2 in Table 27. The white dotted circle represents an f/0.8 cryostat window and the red dotted circle f/1.7 parabolic collection.

The fundamental mode (mode 0) had a FWHM divergence of ~ 3 degrees in the horizontal and ~ 69 degrees in the vertical direction. The comments on these results follow those made in the previous section.

4.4.2.9 Mesa-etched QC laser with 55 ° sidewall angle, λ = 5.3 μm, width = 15 μm, T = 300 K, $n_e = 1\times10^{18}$ cm^{-3} substrate doping

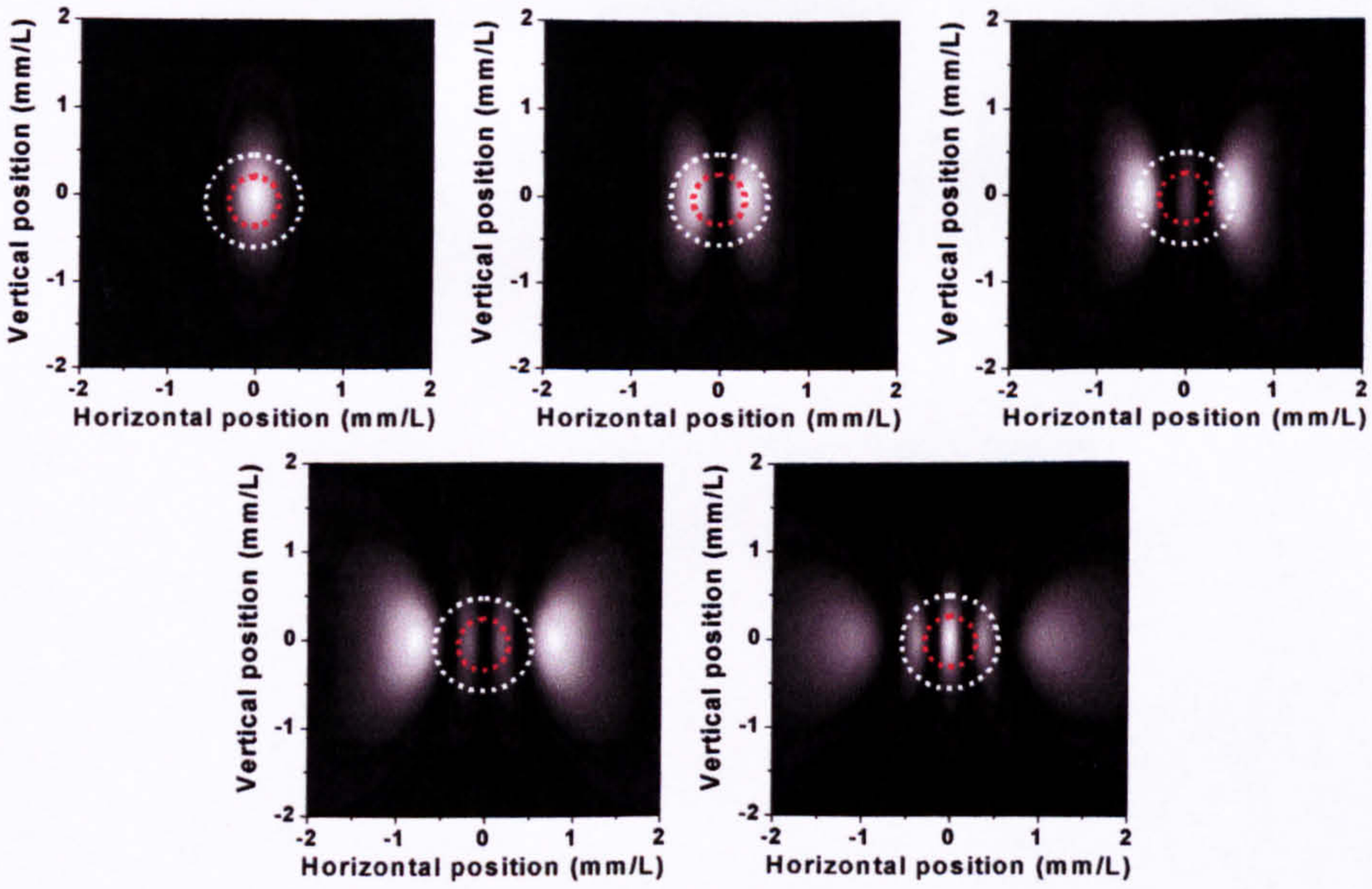

Figure 64 3D intensity plots of the far-field distributions for the TM modes numbered 0 to 4 in Table 29. The white dotted circle represents an f/0.8 cryostat window and the red dotted circle f/1.7 parabolic collection.

The fundamental mode (mode 0) had a FWHM divergence of ~ 25 degrees in the horizontal and ~ 66 degrees in the vertical direction.

4.4.2.10 Mesa-etched QC laser with 55 ° sidewall angle, λ = 5.3 μm, width = 15 μm, T = 300 K, n_e = 3×10^{18} cm^{-3} substrate doping

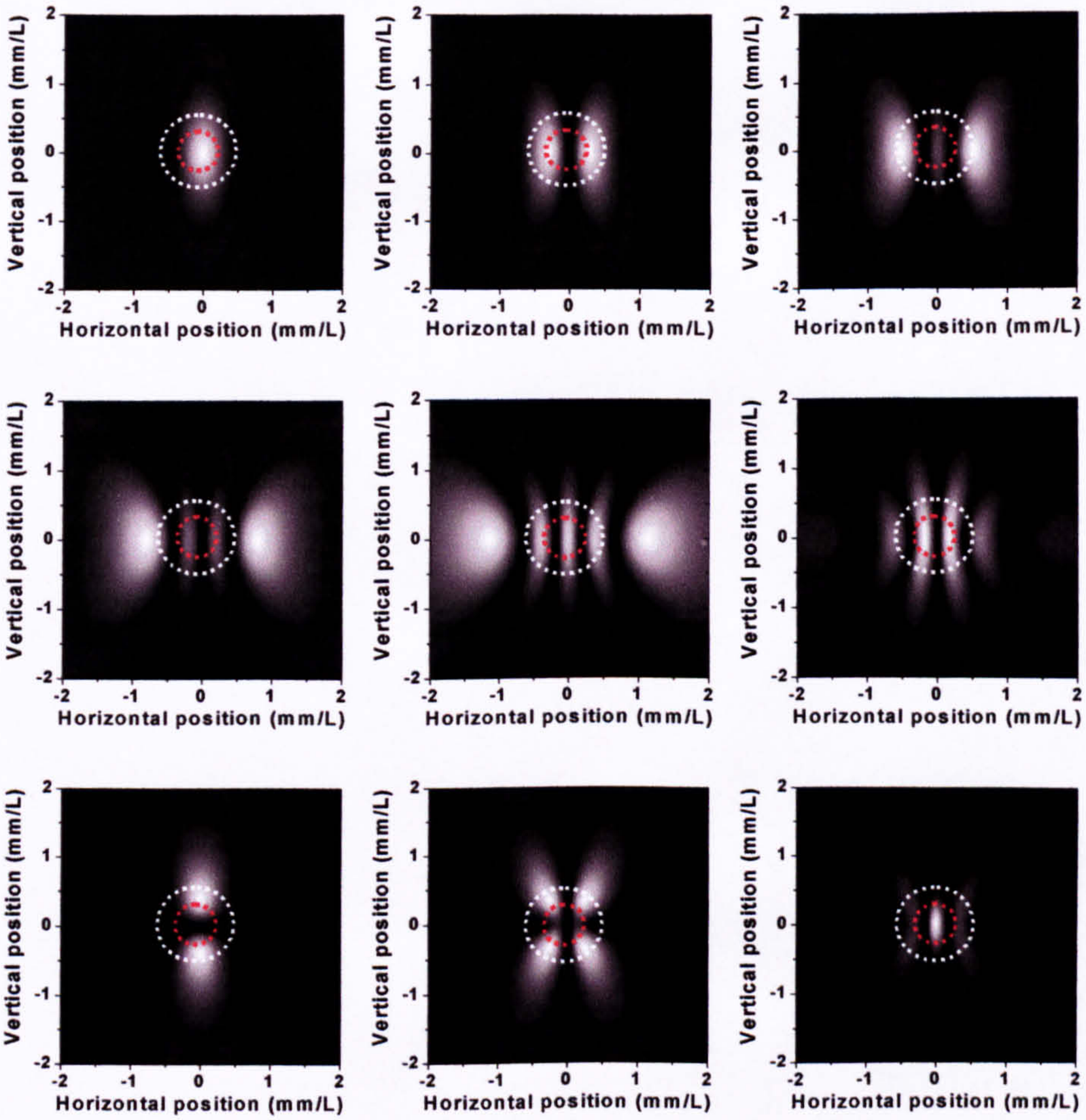

Figure 65 3D intensity plots of the far-field distributions for the TM modes numbered 0 to 7 in Table 31. The white dotted circle represents an f/0.8 cryostat window and the red dotted circle f/1.7 parabolic collection.

The fundamental mode (mode 0) had a FWHM divergence of ~ 25 degrees in the horizontal and ~ 72 degrees in the vertical direction.

4.4.2.11 Mesa-etched QC laser with vertical sidewalls, λ = 5.3 μm, width = 15 μm, T = 300 K, n_e = 1×10^{18} cm^{-3} substrate doping

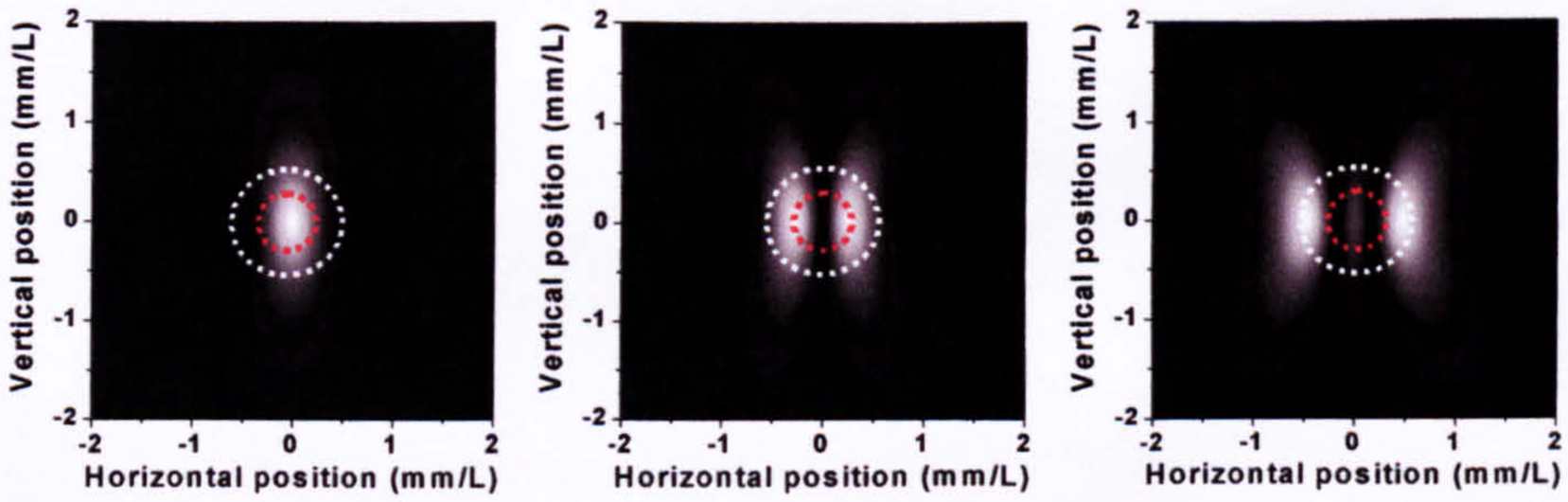

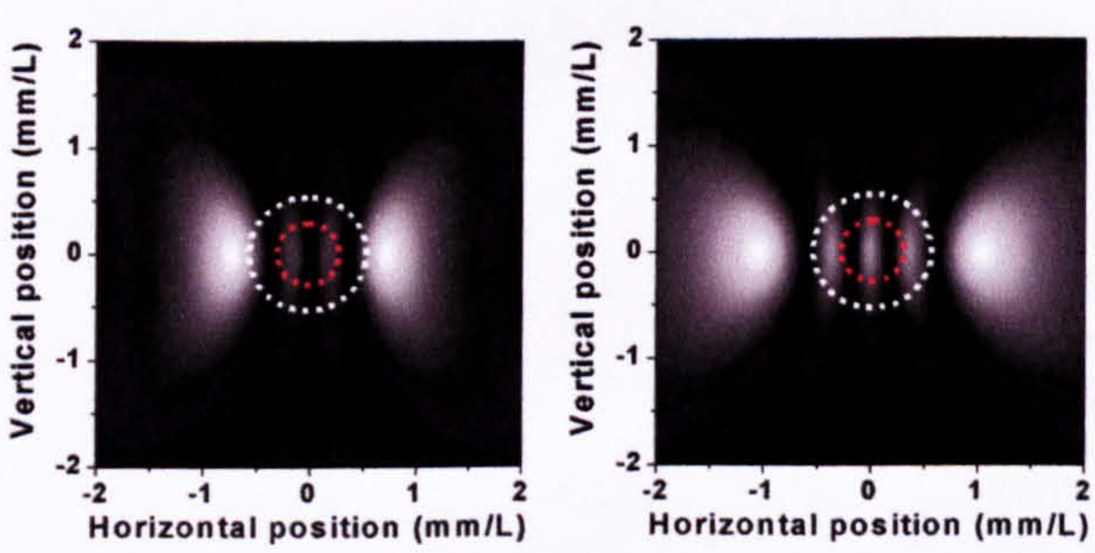

Figure 66 3D intensity plots of the far-field distributions for the TM modes numbered 0 to 4 in Table 33. The white dotted circle represents an f/0.8 cryostat window and the red dotted circle f/1.7 parabolic collection.

The fundamental mode (mode 0) had a FWHM divergence of ~ 26 degrees in the horizontal and ~ 66 degrees in the vertical direction.

4.5 Summary

Perhaps the most important findings were the prediction of the existence of higher order transverse modes, that these modes can have low values of g_{th} (comparable or better than that of the fundamental mode of the waveguide) and that the collection efficiency will vary dramatically from mode to mode (unless a collection optic is used with an extremely low f-number). These results were crucial in understanding the light-current curves of our QC lasers, which are presented in **Chapter 8**. We will see from the experimental results that the calculated order of increasing threshold gain and the calculated far-fields compared well with the experimentally acquired data. This also adds weight to the validity of the calculations of the refractive indices and loss coefficients of the semiconductors performed in the previous chapter.

It was also shown that the calculated performance of the QC lasers suffered greatly with an increase in the InP substrate doping level, even just from 1×10^{18} cm^{-3} to 3×10^{18} cm^{-3}. With the doping level of the InP substrate used in the fabrication of our QC lasers having being somewhere in the range from 4×10^{18} cm^{-3} to 8×10^{18} cm^{-3} it is safe to say that this error was the main culprit for poor performance of our QC lasers compared to that reported by other groups.

Beyond this, another interesting result was that these calculations showed that, in our typical mesa-etched QCLs with sloping sidewalls, the fundamental mode was not the mode with the lowest threshold gain; one of the higher order transverse modes held this position. The reason for this was that higher order modes preferentially experienced higher Γ and lower α_w because of the shape of the sidewalls. It is re-emphasised

though, that although the lossy silica insulation layer has been included in these calculations, the metal layers and sidewall roughness/imperfections have not. These effects may preferentially enhance the loss of higher order transverse modes, leading to a increase in their gain threshold. However, the far-field measurements presented in Chapter 8 confirmed the presence of higher order modes at low threshold currents, even for narrow (10 μm-wide) QCLs.

In general, the presence of the higher order transverse modes is likely to be a problem for many practical applications and the use of collection optics capable of gathering light at greater emission angles would not be a proper solution. The problem really needs to be tackled at its source either by suppressing the higher order modes or by eliminating them completely. The author makes several suggestions below on how to achieve these aims in the future.

The suppression of the higher order modes could perhaps be achieved by the use of a high loss coating on the sidewalls (e.g. metal) which would deliberately increase the loss for them over that of the fundamental mode. Alternatively, taking advantage of the greater divergence of the higher order modes, an external mirror and 'pin-hole' could be used to selectively enhance the gain of the fundamental mode. Using an anti-reflection coating on the laser facet would further enhance this technique.

Eliminating the higher order modes would require either a reduction in the waveguide width or in the refractive index contrast in the horizontal plane, or both. We would soon run into practical problems if we tried to further reduce the width of the current mesa-etched QCLs. If it were possible, it is likely that there would be a large increase in the waveguide losses associated with the increased interaction of the optical mode with the metal-coated sidewalls, as well as a large increase of the horizontal beam divergence. The attempts thus far to reduce the index contrast in the horizontal direction (e.g. the shallow-etched mesa and PSWOX QCLs) have worked well optically, but were plagued by poor electrical confinement, and so are not ideal.

Fresh approaches are required which involve new waveguide geometries and fabrication processes. Two major contenders in this area must be the buried heterostructure (a QC laser version of which has been demonstrated recently by Beck *et al.*)[11] and the buried native-oxide aperture waveguide configurations. Both of these could perhaps provide the combination of a narrow, low loss waveguide geometry with weak optical confinement, to produce a higher performance, single mode (transverse) QC laser with low output beam divergence (at least in the horizontal plane). In addition, if designed properly these structures should also provide excellent carrier confinement and heatsinking (see thermal modelling in Section **5.3.7**).

Future work on the optical waveguide modelling itself could include the modelling of structures with metallic layers on the sidewalls and the modelling of surface-plasmon modes and the coupling between them and the optical mode(s). Beyond that, modelling of DFB and DBR structures would be useful.

4.6 References

[1] J. Faist, A. Tredicucci, F. Capasso, C. Sirtori, D. L. Sivco, J. N. Baillargeon, A. L. Hutchison, A. Y. Cho, 'High-Power Continuous-Wave Quantum Cascade Lasers', *IEEE J. Quantum Electron.*, 34 (2) 336, February 1998.

[2] C. Gmachl, F. Capasso, A. Tredicucci, D. L. Sivco, R. Kohler, A. L. Hutchison, A. Y. Cho, 'Dependence of the Device Performance on the Number of Stages in Quantum-Cascade Lasers', *IEEE J. Selected Topics in Quantum Electron.*, **5** (3) 808, May/June 1999.

[3] A. S. Sudbo, "Film mode matching: a versatile numerical method for vector mode field calculations in dielectric waveguides", Pure and Applied Optics, **2** pp. 211-233, 1993.

[4] A. S. Sudbo, "Numerically stable formulation of the transverse resonance method for vector mode field calculations in dielectric waveguides", *IEEE Phot. Tech. Lett.*, **5** pp. 342-345, 1993.

[5] C. Sirtori, F. Capasso, J. Faist, D. Sivco, A. L. Hutchinson, A. Y. Cho, 'Quantum cascade unipolar intersubband light emitting diodes in the 8-13 μm wavelength range', *Appl. Phys. Lett.* **66** (1), 2 January 1995.

[6] *FIMMWAVE Version 3.3 Manual*, Photon Design (Europe) Ltd., 1996-99.

[7] C. Sirtori, J. Faist, F. Capasso, D. Sivco, A. L. Hutchinson, A. Y. Cho, 'Quantum cascade laser with plasmon-enhanced waveguide operating at 8.4 μm wavelength', *Appl. Phys. Lett.* **66** (24), 12 June 1995.

[8] L. A. Coldren, S. W. Corzine, *Diode Lasers and Photonic Integrated Circuits*, John Wiley & Sons, Inc., New York, 1995.

[9] C. Gmachl, F. Capasso, J. Faist, A.L. Hutchinson, A. Tredicucci, D.L. Sivco, J.N. Baillargeon, S.G. Chu, A.Y.Cho, 'Continuous-wave and high-power pulsed operation of index-coupled distributed feedback quantum cascade laser at $\lambda \approx 8.5$ μm', *Appl. Phys. Lett.* **72** (12), 23 March 1998.

[10] S. Slivken, A. Matlis, A. Rybaltowski, and M. Razeghi, 'Low-threshold 7.3 μm quantum cascade lasers grown by gas-source molecular beam epitaxy', *Appl. Phys. Lett.* 74 (19) 2758, 10 May 1999.

[11] M. Beck, J. Faist, A. Muller, U. Oesterle, M. Ilegems, E. Gini, H. Melchior, "High-Performance ($\lambda \approx 10.4$ μm) buried heterostructure quantum cascade lasers", Conference on Lasers and Electro-Optics Europe - Technical Digest, p.265, 2000.

Chapter 5 Thermal design and modelling

Although quantum cascade lasers have undergone a steady development and diversification on many fronts, one aspect of their performance, the maximum temperature of continuous wave (CW) operation, has remained relatively static. The best value of the maximum temperature of CW operation of an intersubband QC laser with emission wavelength at $\lambda \approx 5$ μm has been around 110 to 140 K.[1, 2] This is below the temperature range which would permit the use of thermoelectric (TE) coolers ($T > 200$ K). Raising the maximum temperature of CW operation into the range of TE coolers is desirable as this would significantly reduce the cost and size of the cooling system and open up many applications where portability and high average powers are needed e.g. trace gas sensing, military countermeasures. This chapter first briefly discusses the factors limiting CW operation and what efforts (including those of this author) have been made to combat them thus far. Then the remainder of the chapter concentrates on the use of a commercially available finite element modelling package for solving partial different equations (PDEase/2 version 2.5.3, SPDE, Inc.). This package was used to investigate the temperature distribution of a series of waveguide designs in order to determine their effectiveness at heat dissipation.

5.1 Factors limiting QCL performance in CW mode

The root of the problem limiting CW operation lies mainly in the intrinsically fast non-radiative decay of electrons from the upper lasing level ($n = 3$) by emission of longitudinal optical phonons ($\tau_3 \sim 1.3$ ps), and in the exponential nature of the increase of the threshold current density with temperature (see Section 2.3.1). Together they lead ultimately to high threshold current densities and to device heating which limit high temperature operation ($T > 140$ K) to pulsed mode operation. Heat dissipation has been highlighted as being of prime importance in QC lasers, owing to the high electrical power required for operation and the dependence of performance on the non-equilibrium phonon population.[3] The large power dissipation required to reach lasing threshold, in combination with the finite thermal resistance of the device, results in the actual temperature T_{act} of the active waveguide core being significantly higher than that of the heat sink, particularly in CW mode.

To compound this, there exists a positive feedback loop between the waveguide core temperature and the threshold current density which further degrades the performance of the laser, eventually so much so that lasing threshold cannot be achieved in CW mode even at relatively low heatsink temperatures.[10] To elaborate, with the temperature elevation of the core under operation comes an increase in both the threshold current density required to reach threshold and in the thermal resistance of the semiconductor materials (when in the phonon-phonon scattering-limited temperature range), which in turn feed back into higher core temperatures, and so on. To add to this, as we will see from the results of the thermal modelling given in this chapter, the existence of a large temperature gradient across the active waveguide core is evident. This is expected to exert further detrimental effects on the laser performance which are discussed below.

Under the temperature gradient each of the QC stages contained within the active waveguide core will be forced to operate under different conditions. Since the threshold current density and the linewidth, magnitude and peak position of the gain spectrum all change with temperature, they will exhibit a spread of values across the waveguide core. The expected ramifications follow:

1. Some periods of the active waveguide core may become too hot to reach or maintain threshold which effectively reduces the overall confinement factor of the optical mode and would lead to an increase in the threshold current density and a reduction in slope efficiency.

2. Any period below threshold will further elevate in temperature, since virtually all of the electrical power supplied to that period will be converted into phonons.

3. The peak of the gain spectrum will differ for each active period, leading to an effective broadening of the collective gain spectrum and therefore an increase in threshold current density once again. Evidence supporting this effect has been reported by Gmachl *et al.* in their studies of the QCL performance versus the number of cascade periods N_p.[4] They observed a greatly enhanced temperature-dependence of the FWHM of the subthreshold electroluminescence emission spectrum, $2\gamma_{32}$, for devices with a large N_p. The presence of a thermal gradient across the active waveguide core was offered as a likely explanation.

These effects in addition to the previous ones, will all contribute to the positive feedback loop leading to a 'thermal runaway' of the threshold current density under CW operation at high temperatures. Any means of reducing this temperature gradient, as well as the peak temperature, should be sought.

5.2 Waveguide designs and heat dissipation

Much of the previous efforts by other groups to improve the CW performance focused on optimising the quantum design of the intersubband transitions in the QC active region (as outlined in Section 2.1) in an attempt to reduce the amount of heat produced by the active cascade. Relatively little development has been devoted, perhaps until very recently, on just improving the removal of heat produced e.g. by the consideration of the thermal design of the waveguide, laser diode packaging and mounting. The general waveguide designs used and developments in this area of the field of QC lasers are covered briefly below. Note that not all of the waveguide designs outlined below have been fabricated in this work, but all of them (except the rib mesa structures) have been thermally modelled, as the results are interesting for possible future work. Details of the waveguide design and fabrication of mesa-etched, rib waveguide, and PSWOX QC lasers can be found in Chapter 6. Results from fabricated mesa-etched, rib waveguide, PSWOX, and PSWOX array QC lasers can be found in Chapter 8.

5.2.1 Mesa-etched or 'Deep-etched' QC Lasers

These have been the 'standard' type of waveguide used in the fabrication of QC lasers. The long wavelength of QCLs mediates against good confinement of the optical mode to the waveguide core and so the thick, 'plasma-enhanced' waveguide[1] is normally used. One disadvantage of this waveguide is that mesa-etching usually needs to be used in order to achieved good electrical confinement; otherwise, there is extensive lateral current spreading.[4] Mesa-etching removes the material adjacent to the waveguide so that any lateral heat extraction from the core is inevitably reduced.

In this chapter we will see the results of thermal modelling used to calculate the temperature distributions in mesa-etched QCLs mounted epilayer-up and epilayer-down (the results are given in Section 5.3.3). The effects of varying the waveguide width and input power density are investigated.

5.2.2 Rib waveguide or 'Shallow-etched' QC Lasers

A rib waveguide or 'shallow-etched' structure was reported by Gmachl *et al.* to have advantages in terms of temperature performance and output power in QC Fabry-Perot and QC DFB lasers.[5] It was reported that by etching down to just above the active region, rather than etching completely through it, it was possible to increase the T_0 from to 135 K to 206 K in one case.[5] This was attributed to the improved active region heatsinking introduced by the rib geometry. However, poor electrical confinement to the rib was evident as the threshold current of the device was approximately tripled due to lateral current spreading.

5.2.3 Planar Selectively Thermal Wet Oxidised (PSWOX) QC Laser

Taking this idea one step further, this author demonstrated planar selectively wet oxidised (PSWOX) QC lasers in which, rather than removing the upper cladding layer, it was converted to a native oxide by wet thermal oxidation.[6] This process formed an electrically insulating native oxide of low refractive index. The hope was that since there were areas of improved thermal conductivity adjacent to the region of heat generation, the thermal dissipation would be improved. Indeed, like the rib waveguides, these devices did exhibit an improved T_0 over their mesa-etched counterparts which could perhaps be attributed to an improved lateral heat flow. Thermal modelling of these PSWOX QC lasers mounted either epilayer-up or epilayer-down was carried out in this work and the results are given in Section 5.3.4.

5.2.4 Mesa-etched and PSWOX QC Array lasers

To achieve high average optical output powers, a QCL must be driven with high bias or high duty cycles. However, as we have discussed, this will cause heating of the active waveguide core which will deteriorate the laser performance. The motivation for investigating laser arrays was to provide a higher total optical power output while spreading the thermal power generated over a larger area, and so reducing localised temperature elevation of the waveguide core. The thermal modelling was used to investigate the laser temperature for a number of values of inter-device spacing to find the optimal spacing and to gauge the level of improvement over a single, broad laser operating under the same total power (and power density). Results are given in Section 5.3.5 for mesa-etched QC array lasers and in Section 5.3.6 for PSWOX QC array lasers.

5.2.5 QC Lasers with an InP Upper Cladding

5.2.5.1 Mounted epilayer-up

Growing an InP binary compound semiconductor rather than the usual $In_{0.52}Al_{0.48}As$ ternary compound semiconductor for the upper cladding layer was an early attempt to improve thermal dissipation.[1] Due to alloy scattering, the thermal conductivity of the ternary is ~ 20 times lower than the binary semiconductor.[2] This was initially reported by Faist *et al.* to have increased the maximum temperature of CW operation for epilayer-up mounted QCLs from $T \approx 121$K ($In_{0.52}Al_{0.48}As$ upper cladding) to 140 K (InP upper cladding),[1] although this author is not completely convinced that other factors may not have contributed to this improvement. This suspicion is supported by a subsequent paper by Faist *et al.* which concentrated more on the CW operation of the same design and came up with a lower value of ~ 110 K as the maximum temperature of CW operation.[2] Although it seems that the CW operation was not convincingly improved for these epilayer-up mounted InP-clad QCLs, the pulsed operation of the device at temperatures above $T \approx 200$ K was clearly enhanced compared to their $In_{0.52}Al_{0.48}As$-clad counterparts.

Although the resources were not available for this author to fabricate these devices, thermal modelling of the InP-clad QCL was still carried out. The results (see Section 5.3.7) are used to explain the behaviour observed by Faist *et al.* for these devices.

5.2.5.2 Mounted Epilayer-down

Since they possess an upper cladding of relatively high thermal conductivity, significant improvements in thermal dissipation are intuitively expected when these devices are mounted epilayer-down. Gmachl *et al.* demonstrated improved CW operation of a $\lambda \approx 8$ μm QCL by using epilayer-down heat-sinking in combination with high reflectivity (HR) facet coating. This was reported to have raised the maximum temperature of CW operation by ~ 20 K, but this was not as far as expected by their own finite element solution of a 2D non-linear differential equation for heat flow in that device.

Our $\lambda \approx 5$ μm QCL design using an InP upper cladding layer and mounted in an epilayer-down configuration was investigated using the thermal modelling and the results can be found in Section 5.3.7.

5.2.6 Buried heterostructure QC Lasers

Finally, buried heterostructures (BH) QCLs were demonstrated by Beck, Faist *et al.* very recently which exhibited evidence of improved heat dissipation.[7] In general, the buried heterostructure waveguide configurations are well known for their excellent heat dissipation as well as their good electrical and optical confinement to the waveguide. [8, 9] On the other hand, they are a more complex and expensive structure to produce. Formation of a BH laser involves mesa-etching and then regrowth of semiconductor material to replace that removed by the previous etching step. The regrown semiconductor provides electrical and optical confinement, as well as lateral heat extraction. The BH QCLs reported by Beck *et al.* employed InP as the upper cladding and regrowth material. Mounted epilayer-up on a Peltier cooled submount they still only operated in pulsed mode at room temperature, but the improved heat dissipation permitted the use of a higher duty cycle (5%) thereby allowing a higher average optical output power (5 mW).

In this work BH QCL structures have been modelled both epilayer-up and epilayer-down (see Section 5.3.7) to gauge whether the magnitude of the improvement in the heat dissipation might justify the extra complexity and cost of fabrication involved in their production.

5.3 Thermal Modelling of QCLs using Non-linear Finite Element Analysis

In the forthcoming sections, we look at thermal modelling which was used to investigate the magnitude and distribution of the temperature rise in quantum cascade lasers operating under conditions similar to high-power continuous-wave (CW) operation at a heatsink temperature of $T = 77$ K. Several waveguide geometries were investigated and compared including:

- mesa-etched QC lasers with an $In_{0.52}Al_{0.48}As$ upper cladding,
- PSWOX QC laser (must have an $In_{0.52}Al_{0.48}As$ upper cladding),
- mesa-etched QC array lasers with an $In_{0.52}Al_{0.48}As$ upper cladding,
- PSWOX QC array lasers (must have an $In_{0.52}Al_{0.48}As$ upper cladding),

- mesa-etched QC laser with an InP upper cladding,
- and buried heterostructure QC laser with InP upper cladding and regrowth.

As will become clear, the calculated temperature distributions were steady-state temperatures i.e. there is no information on the transient temperatures which would occur in pulsed mode operation of the lasers.

5.3.1 Mathematical Description of Problem

Non-linear finite element analysis was used to solve the thermal diffusion equation,

$$\frac{\partial}{\partial x}\left(K_x \frac{\partial T}{\partial x}\right)+\frac{\partial}{\partial y}\left(K_y \frac{\partial T}{\partial y}\right)+\frac{\partial}{\partial z}\left(K_z \frac{\partial T}{\partial z}\right)+S=\rho C_p \frac{\partial T}{\partial t}, \qquad (5\text{-}1)$$

where, T is the temperature in Kelvin (or ℃, if desired), K_x , K_y, and K_z (W m^{-1} K^{-1}) are the thermal conductivities in the x, y and z directions respectively, S is the value of the heat source (W m^{-3}) in any heated regions; the active regions of the QCL in this case, elsewhere it is zero. C_p (J kg^{-1} K^{-1}) and ρ (kg m^{-3}) are the specific heat and density of the material, the product of which gives the heat capacity (J m^{-3} K^{-1}).

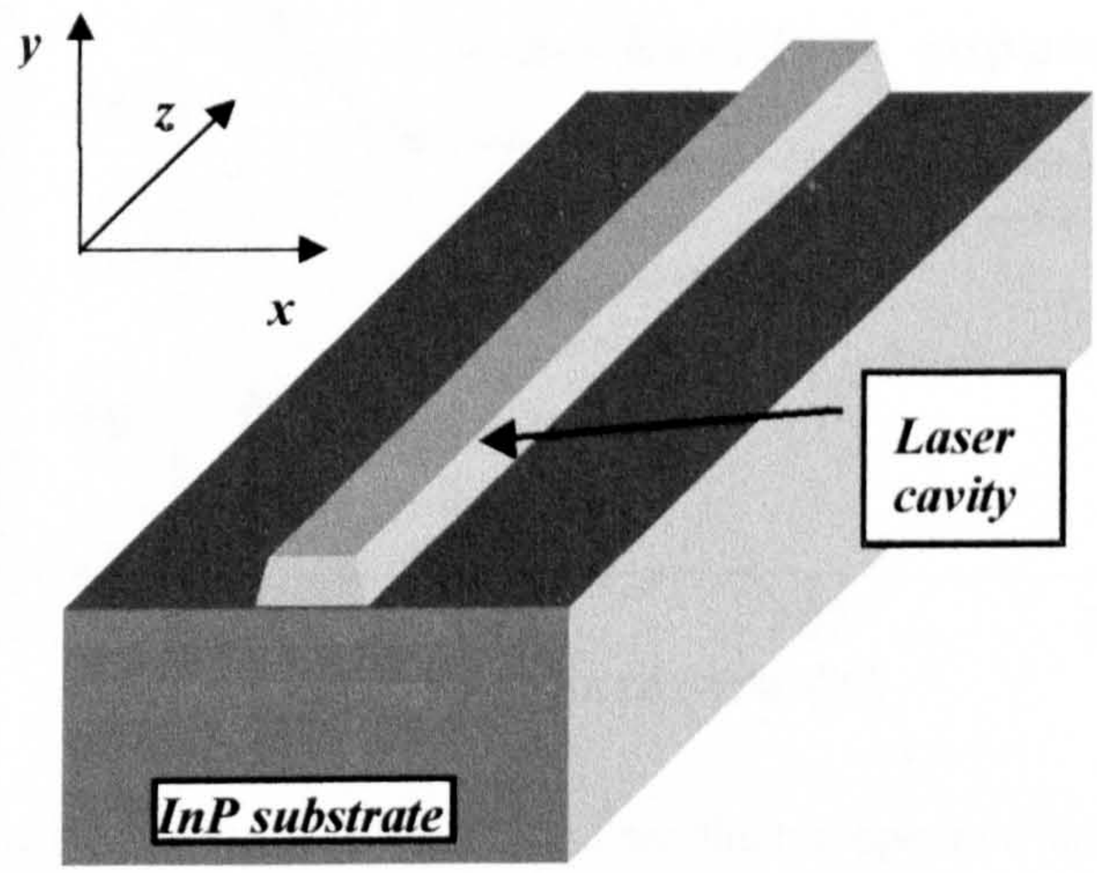

Figure 67 Simplified schematic drawing of the semiconductor laser diode and chosen co-ordinate system.

Referring to Figure 67, the x-axis was designated as the direction parallel to the semiconductor layers (or the 'lateral' direction). The y-axis was designated as the direction perpendicular to the semiconductor layers, but perpendicular to the longitudinal cavity of the laser. The z-axis lay parallel to the longitudinal laser cavity i.e. orthogonal to the x and y axes.

Assuming there is no net flow of heat along the laser cavity (in the z-direction), $\delta T/\delta z = 0$. The problem then becomes a two-dimensional one and the equation simplifies to,

$$\frac{\partial}{\partial x}\left(K_x \frac{\partial T}{\partial x}\right)+\frac{\partial}{\partial y}\left(K_y \frac{\partial T}{\partial y}\right)=\rho C_p \frac{\partial T}{\partial t}. \qquad (5\text{-}2)$$

This can be solved using a finite element analysis program for solving partial differential equations. Further simplifications were made by assuming that the thermal conductivities of the materials involved were isotropic, i.e. $K_x = K_y = K$. Also, it was possible to solve the time-dependant equation which would have allowed us to calculate the evolution of the temperature over time, but here we investigated the equilibrium

temperature reached, so the time-dependant version was not used. For steady state conditions, $\delta T/\delta t = 0$, so the right-hand-side may be set to zero and the equation then becomes,

$$\frac{\partial}{\partial x}\left(K\frac{\partial T}{\partial x}\right)+\frac{\partial}{\partial y}\left(K\frac{\partial T}{\partial y}\right)+S=0. \qquad (5\text{-}3)$$

The thermal conductivity of semiconductor (or metal) is temperature-dependant. The value of K at any given point (x, y) will be determined by the material and the temperature of the material at that point (x, y). This makes the problem non-linear, since calculating the temperature distribution requires a previous knowledge of the thermal conductivity distribution, which is itself temperature-dependant. The finite element analysis package employed an iterative process to solve the non-linear, partial differential equation,

$$\frac{\partial}{\partial x}\left(K(T)\frac{\partial T}{\partial x}\right)+\frac{\partial}{\partial y}\left(K(T)\frac{\partial T}{\partial y}\right)+S=0. \qquad (5\text{-}4)$$

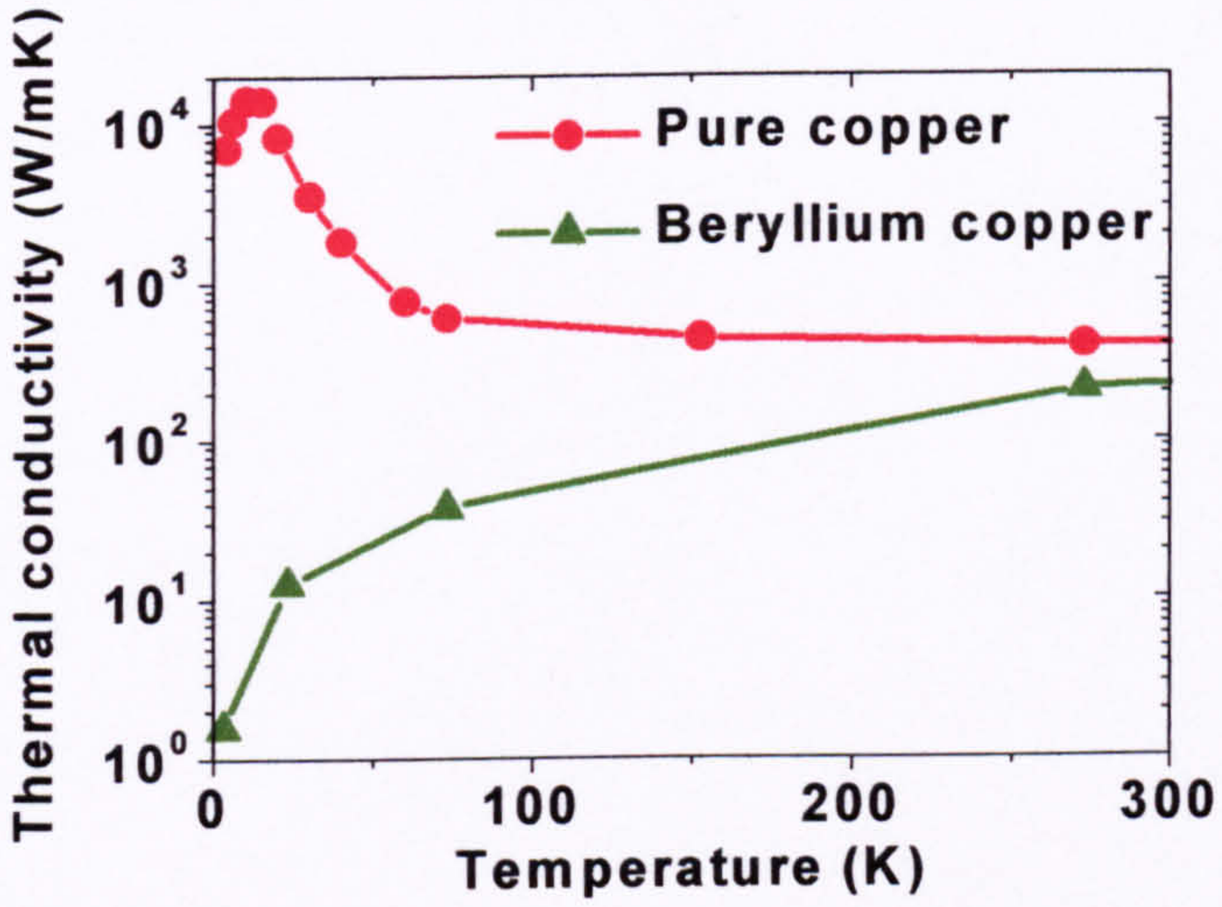

Figure 68 Thermal conductivity of pure copper and beryllium copper as a function of temperature.[11]

Material	Thermal Conductivity (W m^{-1} K^{-1})
InP	$406 - 2 * T + 2.88\ E^{-3} * T^2$, [10]
$In_{0.52}Al_{0.48}As$	$29 - (1.39E^{-1} * T) + (1.98\ E^{-4} * T^2)$, [10]
$In_{0.53}Ga_{0.47}As$	$29 - (1.39E^{-1} * T) + (1.98\ E^{-4} * T^2)$, [10]
Alumina	3 [11]
Copper	398 [11]
Indium	87 [10]
Helium gas	$1.63E^{-2} + (6.12E^{-4} * T) - (5.49E^{-7} * T^2)$,[11]

Table 36. Thermal conductivity values used in the calculations

In the calculations performed the following assumptions and approximations were made:

1. The temperature-dependence of the values of thermal conductivity of InP, $In_{0.53}Ga_{0.47}As$, $In_{0.52}Al_{0.48}As$, and He gas were approximated using polynomials given in Table 36. The ternary semiconductor compounds $In_{0.52}Al_{0.48}As$ and $In_{0.53}Ga_{0.47}As$ were described by polynomial equations. The values of thermal conductivities used for indium and copper were those reported for pure materials at room-temperature and were assumed to be constant with temperature. As one can see from Figure 68, the thermal conductivity of copper is a function of temperature and it sensitive to the presence of impurities. However, in the temperature region of interest (i.e. $T \geq 77$ K), the thermal conductivity is more or less

constant. The same was assumed for indium. In any case, the values of thermal conductivity of these layers are not as vital as those for the semiconductor layers. The results are much more dependant on the layers which limit heat flow such as the semiconductor layers.

2. The active region comprises of nearly 500 very thin (ranging between 0.9 to 5 nanometers in thickness) epitaxial layers; a superlattice of alternating $In_{0.52}Al_{0.48}As$ and $In_{0.53}Ga_{0.47}As$ layers. These were much too thin to be modelled as individual layers (layers with dimensions no less than 500 nm were permitted in this model), and so were grouped together and approximated as a single layer.

3. The active region was assigned a thermal conductivity of bulk ternary material. This simplification ignores the reflection of phonons (heat) at each $In_{0.52}Al_{0.48}As$ / $In_{0.53}Ga_{0.47}As$ interface in the superlattice. In practice this phenomenon would make the effective thermal conductivity of the superlattice anisotropic. It is believed that the value of K_y, the thermal conductivity perpendicular to the semiconductor layers, would be reduced with respect to K_x.

4. The values of thermal conductivities used were those reported for undoped layers; values for doped semiconductors may be significantly lower. The modelling was performed on what was effectively an undoped semiconductor laser, whereas doping levels in a quantum cascade laser can be high (7×10^{18} cm^{-3}) and vary throughout the epilayer (see Table 37). Addition of doping atoms to the crystal lattice creates crystalline imperfections upon which phonons can scatter, decreasing the thermal conductivity.[12] Towards room-temperature, the dependence of the thermal conductivity on doping level is weaker,[13] since at high temperatures phonon-phonon scattering dominates. At low temperature, where phonon-phonon scattering is reduced, the phonon-impurity scattering will dominate, and the value of K will drop with increasing doping levels. The values of temperature calculated by the modelling, should therefore be more accurate towards room-temperature. The temperatures calculated should always be an underestimate of the actual temperature since the thermal conductivity is over estimated at low temperatures.

Material	Layer Thickness (nm)	Doping Level ($cm^{-3}/10^{16}$)
Ternary ($In_{0.52}Al_{0.48}As$)	1200	700
Ternary ($In_{0.52}Al_{0.48}As$)	700	30
Ternary ($In_{0.52}Al_{0.48}As$)	600	20
Ternary ($In_{0.53}Ga_{0.47}As$)	300	10
Active region ($In_{0.53}Ga_{0.47}As$ \ $In_{0.52}Al_{0.48}As$)	1143	2.6 (average)
Ternary ($In_{0.53}Ga_{0.47}As$)	300	10
Binary (InP)	15000	100

Table 37 Summary of major semiconductor layers of the QCL in reverse order of growth.

5. There is no net heat flow along the laser cavity (*z*-direction).

6. Cooling due to convection was neglected.

7. Cooling due to radiation of heat was neglected. This is a reasonable assumption as long as the temperature difference, ΔT, between the heated surface and its surroundings is not too high. The value of cooling via radiation can be expressed by, $c_{rad} = \sigma.(\Delta T)^3$, where c_{rad} is the cooling by radiation (W m^{-2} K^{-1}), σ = 5.67E-8 W m^{-2} K^{-4} is the Stefan-Boltzmann constant. For c_{rad} = 1 W m^{-2} K^{-1}, ΔT = 260 K. Temperature differentials obtained in these calculations are lower than 150K, so that cooling by radiation of heat can be neglected.

5.3.2 Geometric Description of Problem

Reference should be made to the QC laser fabrication section for an understanding of the general QCL construction and geometry. The insulation and contact layers were not included in the modelling; these layers were very thin ~300nm, and as such could not be entered into the program as it could resolve layers whose x or y dimension was 1/2000th of the entire dimension of the problem. The model described a QC laser mounted with indium onto a copper heatsink and placed in a cryostat at $T = 77$ K. The sequence of layers (in order for epilayer-up mounting) included in the model were as follows: helium, upper cladding layer, active region, lower cladding layer, InP substrate, indium, and copper. Regions of helium, alumina (Al_2O_3), or InP were used to replace areas of the upper cladding, active region and lower cladding layers in order to emulate etched moats for 'Mesa-etched QCLs', alumina moats for 'PSWOX QCLs' (see Appendix 1 for a description of the PSWOX QCL), or InP regrowth for buried-heterostructure QCLs, respectively.

The program required that boundary conditions be set at the outer boundaries of the modelled geometrical space. To best reconstruct conditions in a cryostat, the boundaries were placed relatively far away from the laser chip and the temperature of the entire boundary was set to $T = 77$ K i.e. the bottom and sides of the copper block and the outer edges of helium gas were set to $T = 77$ K. The maximum distance of these boundaries from the chip was limited by the finite element analysis program used. Reiterating, the maximum dimensions of the entire geometric space could not exceed ~2000 times the minimum feature size in the geometric description.

The problem was described geometrically using the parameters listed in Table 38 (please refer to Figure 69, Figure 70, Figure 71, and Figure 72 where many of the parameters are described diagrammatically). The parameters in Table 39 were applied solely to the modelling of the array QC lasers.

Parameter in diagrams	**Parameter in code**	**Value\Description**
W_{wg}	MesaTopWidth (m)	Variable
W_{moat}	MoatBaseWidth (m)	Constant = 10 μm for single mesa and array mesa
		Constant = 60 μm for PSWOX mesa
H_{moat}	MoatDepth (m)	Constant = 4363 nm for single mesa and array mesa
		Constant = 2500 nm for PSWOX mesa
-	LowerCladdingThickness	Constant = 330 nm
-	ActiveThickness	Constant = 1143 nm
-	UpperCladdingThickness	Constant = 2890 nm
ϕ	MesaSidewallAngleDeg	Constant = 55 degrees
H_{air}	AirThickness	1 mm
H_{Cu}	HeatsinkThickness	1 mm
W_{Cu}	HeatSinkWidth	2 mm
H_{In}	InThickness	5 μm
H_{Sub}	SubstrateThickness	150 μm
W_{Sub}	SubstrateWidth	500 μm

Table 38 Parameters used to geometrically describe the QCL chip for the thermal model.

Parameter in diagrams	**Parameter in code**	**Value\Description**
D_{array} (μm)	MesaSpacing	Variable (distance between mesa in the array)
-	NoMesaInArray	Constant = 3 (number of mesa in the array)

Table 39 Parameters used to geometrically describe the QCL array chip for the thermal model.

It should be noted that the value of waveguide width W_{wg} in the model actually corresponds to an average active region width of W_{wg} + 2(3.46/tan ϕ) owing to the sidewall angle ϕ being less than 90°. A 'waveguide width' W_{wg} =5μm in the model therefore corresponds to an active region width of 5 + 4.85 ≈ 10μm. Values of W_{wg} = 10 μm and 15 μm correspond to an active region width of ~15μm and ~20 μm respectively. The reason for selecting the top of the mesa as the point of measurement was to prevent the selection of a mesa width which has a plateau width = 0 i.e. the two sloping sidewalls meet at the top, leaving no contact layer on top of the mesa.

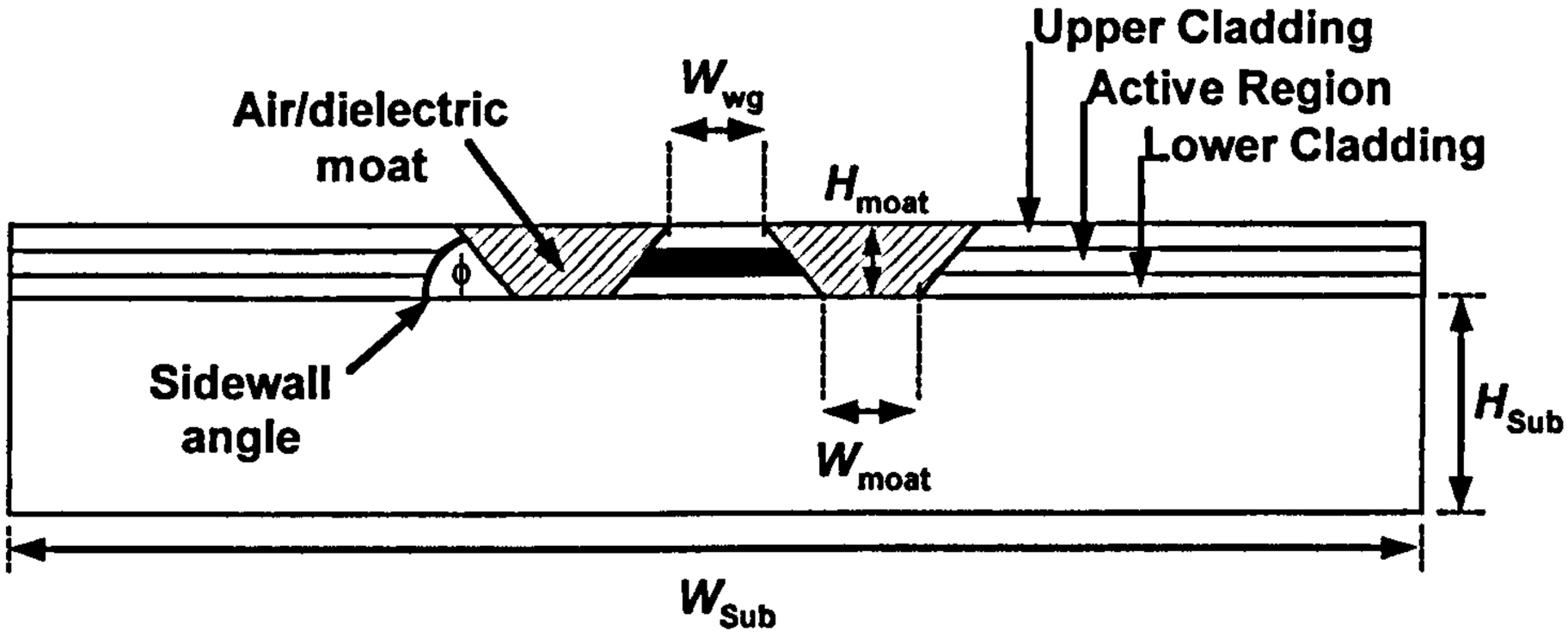

Figure 69 Geometric representation of the QCL mesa used by the finite element analysis, showing the mesa sidewall angle ϕ, the width of the waveguide plateau W_{wg}, the width of the moat base W_{moat}, the thickness/depth of the moat H_{moat}, the thickness of the substrate H_{Sub}, the width of the substrate W_{Sub}, and the position of the upper cladding, active region and lower cladding layers. The area of the active region in solid black represents where the heat is generated.

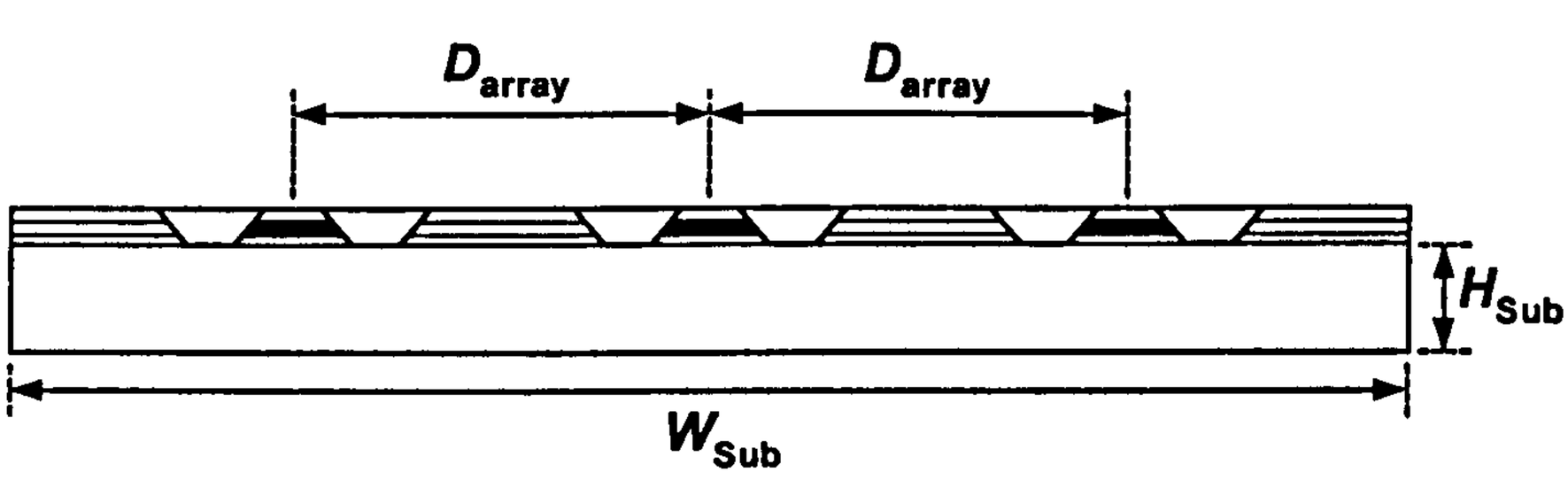

Figure 70 Geometric representation of the QC array laser used by the finite element analysis, showing the thickness of the substrate H_{Sub}, the width of the substrate W_{Sub}, and the distance D_{array} between individual mesa in the array. The areas of the active region in solid black represent where the heat is generated.

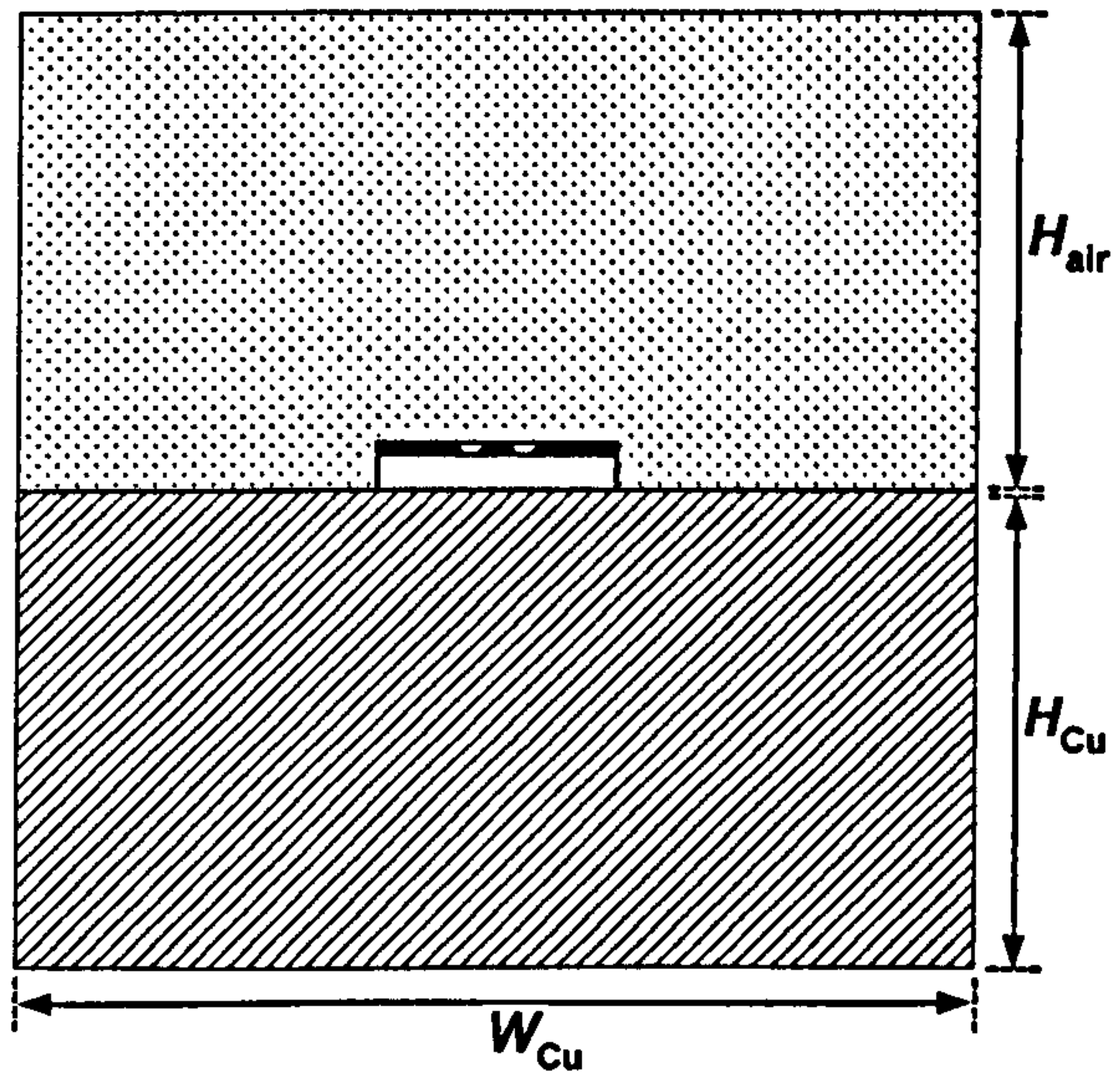

Figure 71 Geometric representation of the QC laser chip mounted epilayer-up onto a copper heatsink of width W_{Cu} and thickness H_{Cu}. The area, W_{Cu} by H_{air}, above the copper mount and laser chip is filled with 'air' (helium in our case).

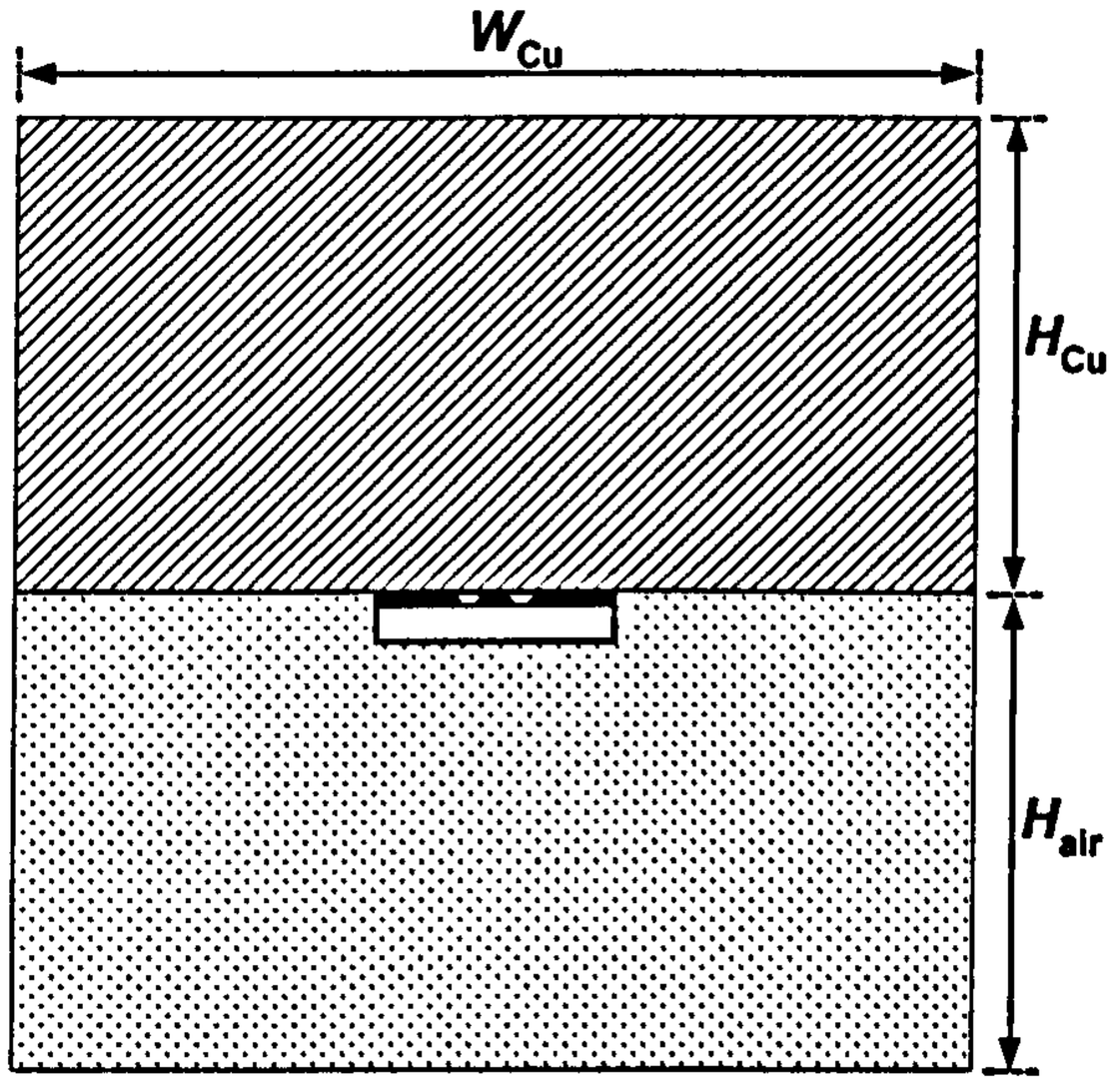

Figure 72. Geometric representation of the QC laser chip mounted epilayer-down onto a copper heatsink of width W_{Cu} and thickness H_{Cu}. The area, W_{Cu} by H_{air}, above the copper mount and laser chip is filled with 'air' (helium in our case).

5.3.3 Simulation results for QC Mesa Lasers

5.3.3.1 Epilayer-up mounted

First of all, the effect of reducing the waveguide width while maintaining a constant input power density into the active region was modelled by using the combinations of W_{wg} and power given in Table 40. This simulated reducing the laser width so as to produce a low threshold current laser (desirable). Note however, this may come at the expense of a low optical output power device (undesirable). Results of the simulation in the form of vertical and lateral temperature profiles are given in Figure 73 and in Figure 74, and the peak temperatures exhibited in each case are listed in Table 40. The results show that when the power density is held constant the laser temperature drops with decreasing W_{wg}. This is a result of there being a lower total thermal power to dissipate and a greater surface area to volume in a narrow mesa.

W_{wg} (μm)	P (W)	T_{peak} (K)
15	20	167
10	13.33	140
5	6.66	112

Table 40 The calculated peak temperature obtained for several values of W_{wg} and a constant power density.

Next, the effect of reducing the waveguide width while maintaining a constant generation of heat in the active region was modelled using a power of P = 20 W, and waveguide widths W_{wg} of 5, 10, and 15 μm (remembering that the parameter W_{wg} was defined as the width of the top of the mesa, and that the average width of the waveguide at the core was ~ 5 μm greater in each case). Results from these simulations are given in Figure 75 and in Figure 76, and the peak temperatures exhibited in each case are listed in Table 41.

The purpose of this set of simulations was to emulate driving a narrow laser with a high input current (high power) in an attempt to achieve higher optical output powers. It can be seen that such an attempt results in a large temperature elevation of the laser active region which will, in turn, reduce the laser efficiency so that rather than increasing the optical output power, a decrease in performance is more likely.

Note that although a combination of P = 6.66 W and W_{wg} = 15μm, gave the lowest temperature rise, this combination might not be practical for a real laser, as the threshold current (power) required to achieve lasing scales with the laser width.

W_{wg} (μm)	P (W)	T_{peak} (K)
15	20	167
10	20	185
5	20	217

Table 41 The calculated peak temperature obtained for several values of W_{wg} and a constant total power.

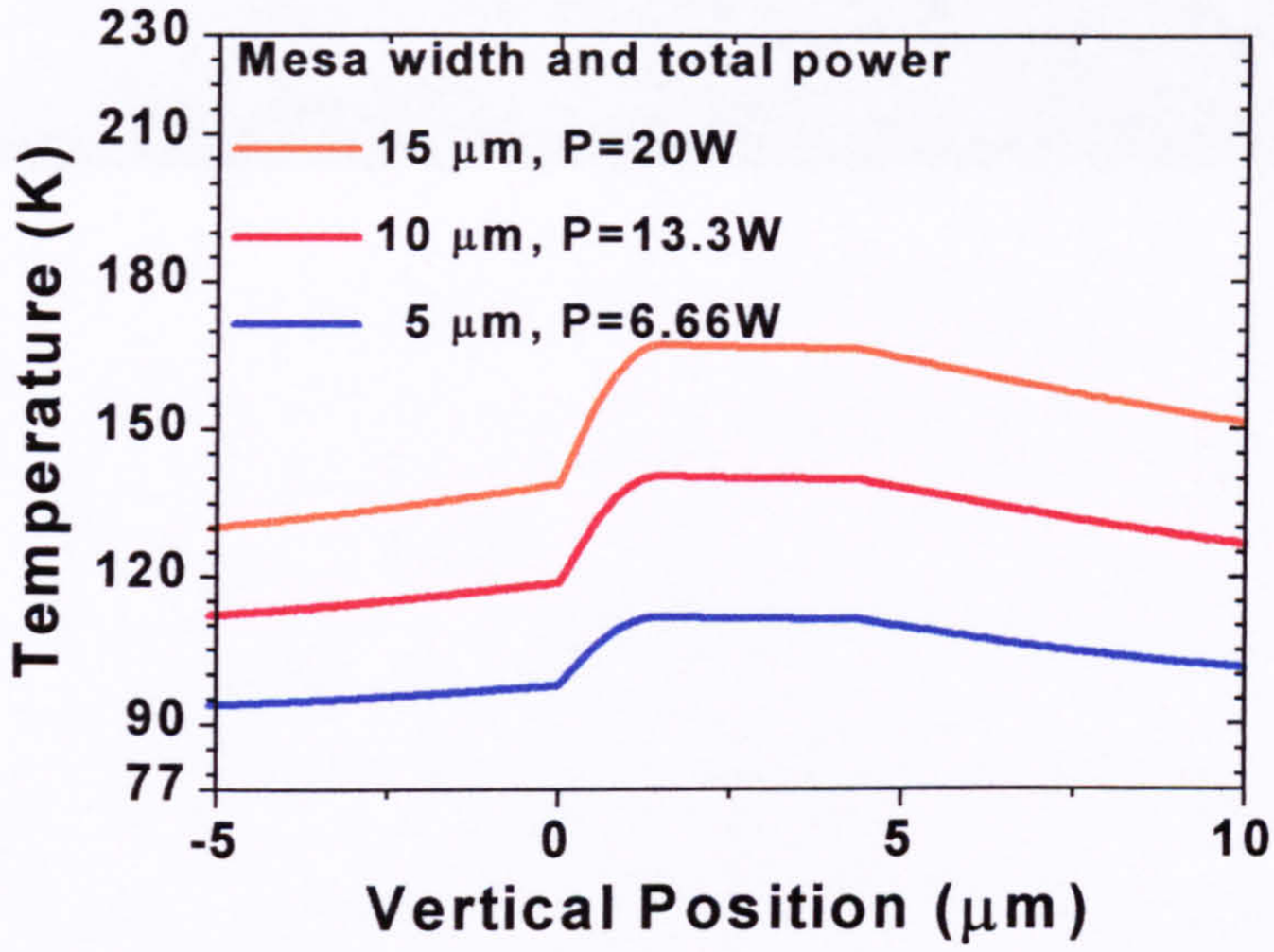

Figure 73 Temperature profile through a vertical cross-section (down through the centre of mesa) of the QCL mesa mounted epilayer-up on a heatsink set to T = 77 K. The calculation is shown for different values of waveguide width W_{wg}, keeping the input thermal power density in the 'Active Region' constant in each case. Position = 0 μm represents the InP substrate/epilayer interface. Position < 0 lies within the 'InP substrate', 0 < Position < 4.36μm contains the 'epilayer', and Position > 4.36μm represents 'air'. The 'Active Region' of the QCL lies 0.33μm < Position < 1.47μm.

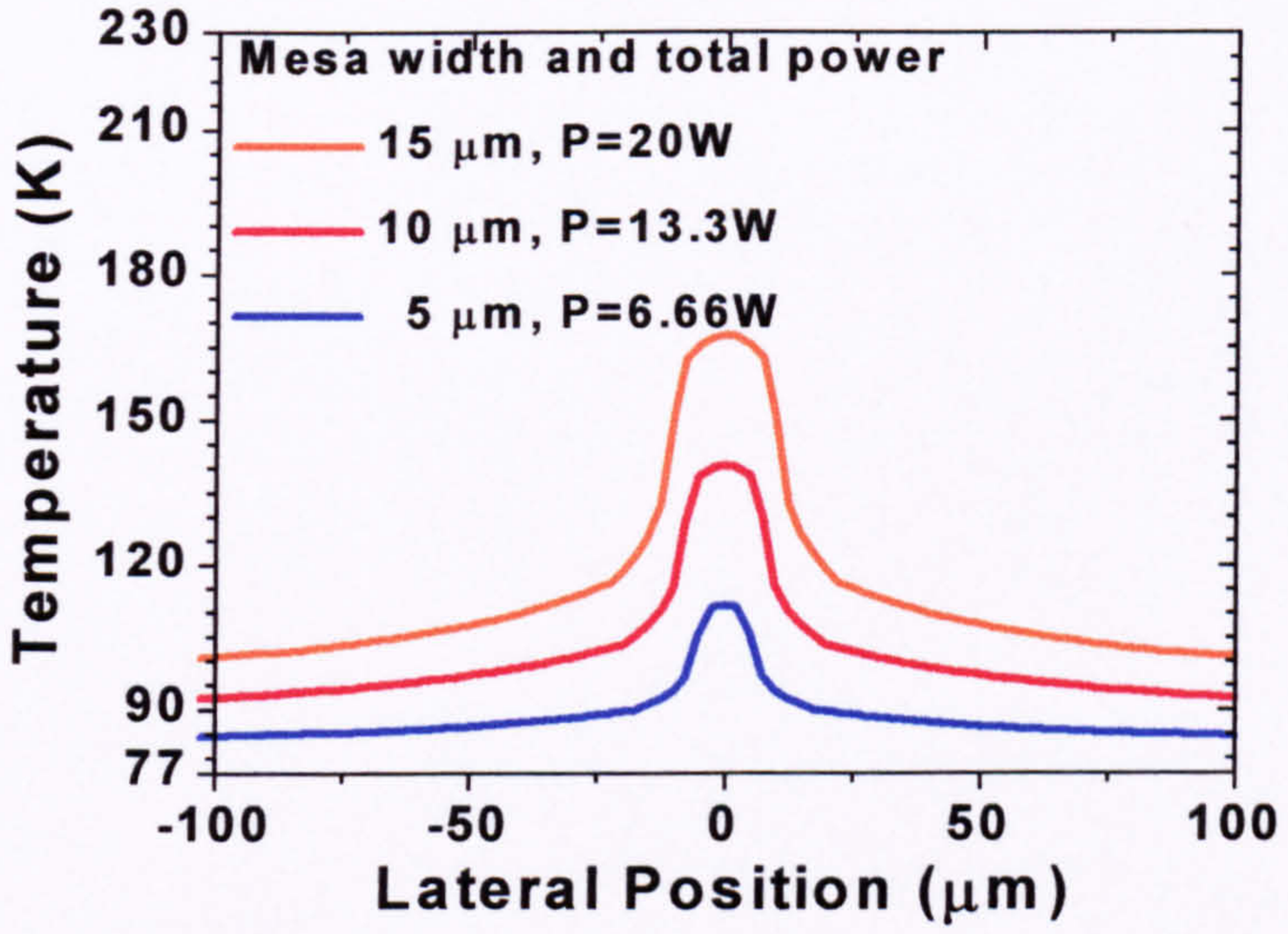

Figure 74 Temperature profile through a lateral cross-section (along active region/upper cladding interface) of the QCL mesa mounted epilayer-up on heatsink set to T = 77 K. Position = 0 μm represents the centre of the mesa. The calculation is shown for different values of waveguide width W_{wg}, keeping the input thermal power density in the 'Active Region' constant in each case.

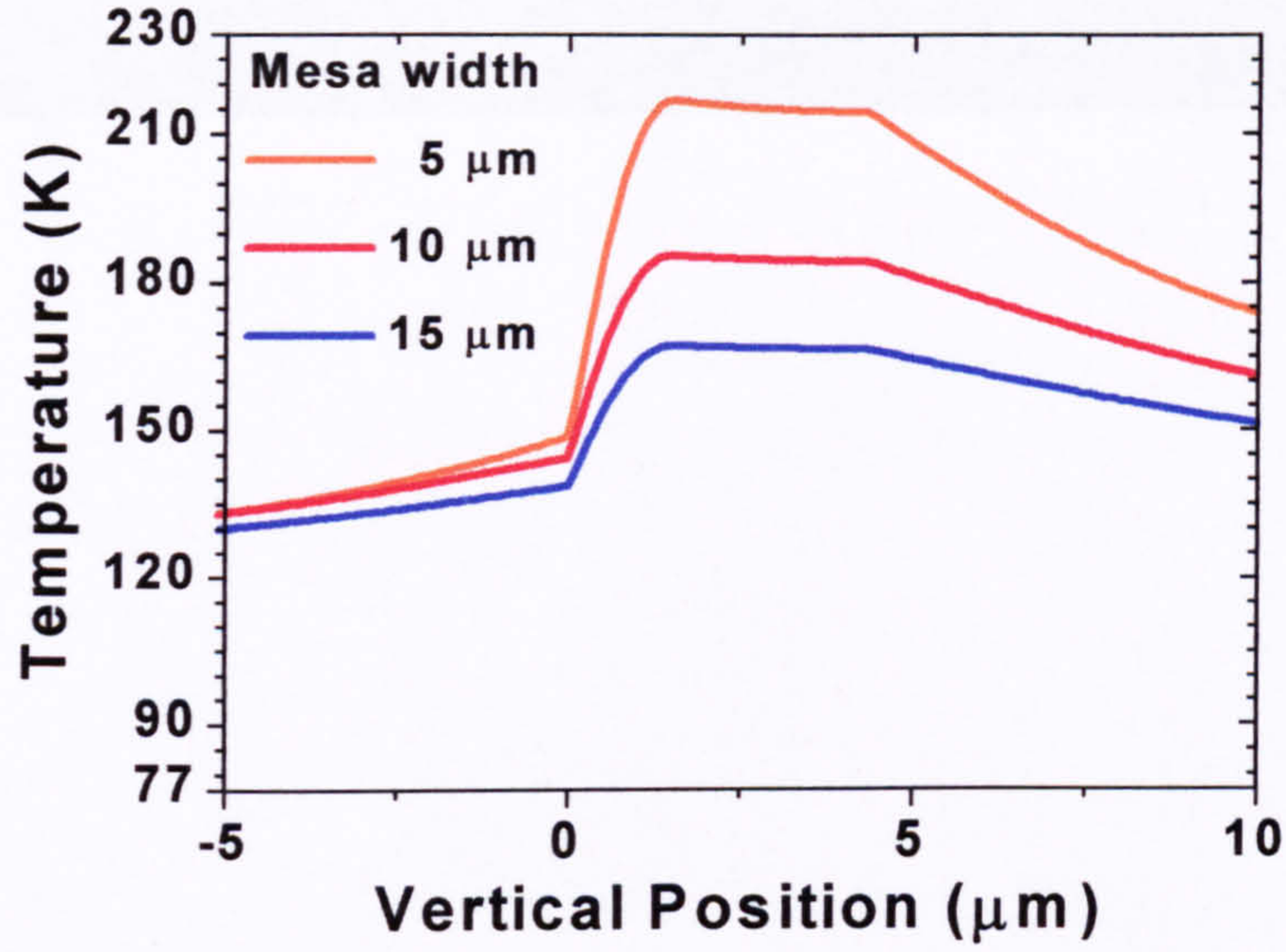

Figure 75 Vertical temperature profile through the QCL mesa mounted epilayer-up. The calculation is shown for different values of waveguide width W_{wg}, keeping the input thermal power in the 'Active Region' constant in each case, P =20 W.

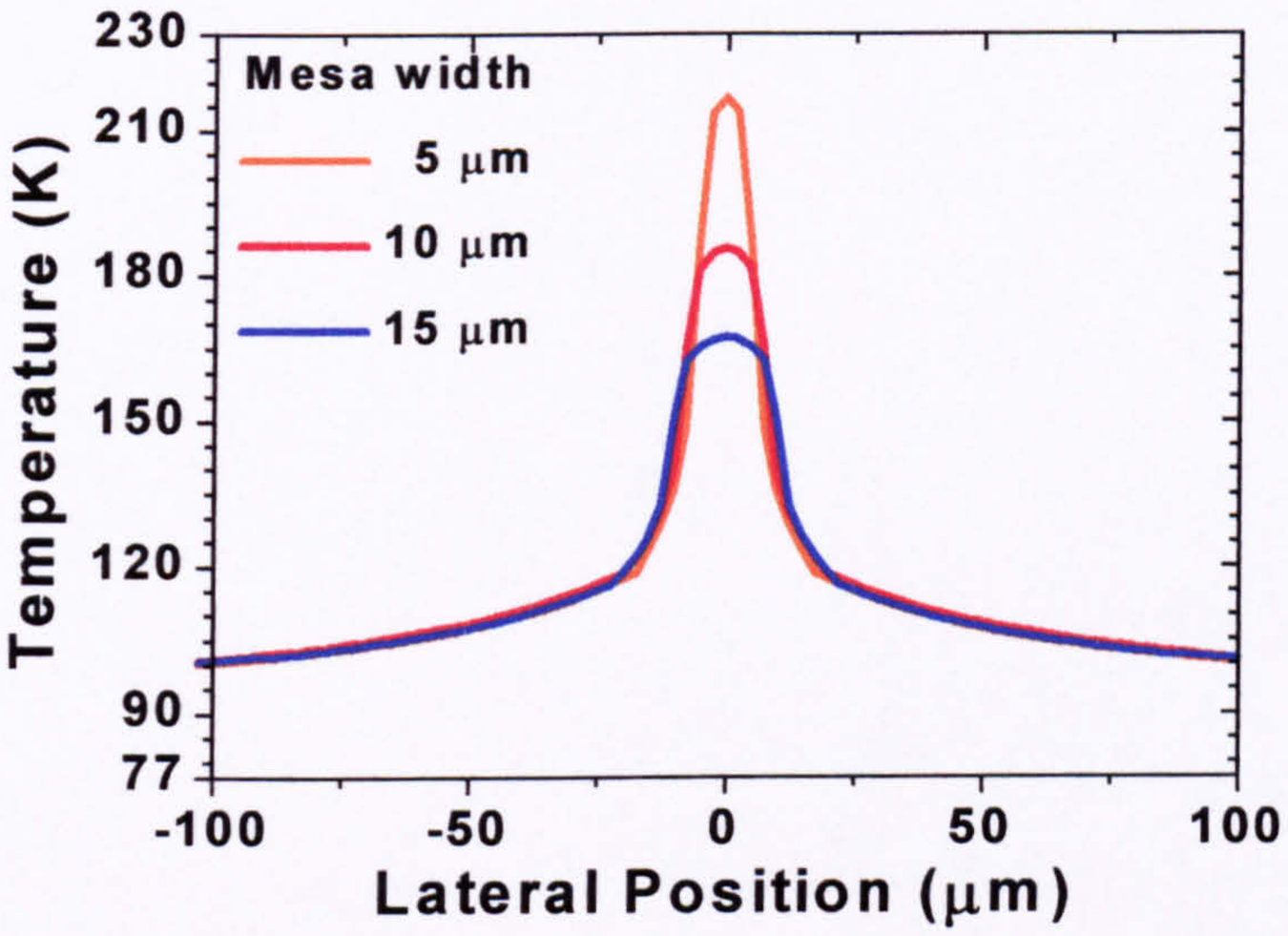

Figure 76 Lateral temperature profile of the QCL mesa mounted epilayer-up. The calculation is shown for different values of waveguide width W_{wg}, keeping the input thermal power in the 'Active Region' constant in each case, P =20 W.

Another important feature revealed by the vertical temperature profile (Figure 75) is the presence of a large temperature gradient across the active waveguide core (as much as 70 K in one case). As was discussed at the beginning of this chapter, the presence of this gradient will be detrimental to the QC laser performance and should be minimised.

The direction and magnitude of heat flow (heat vectors) can be seen in Figure 77 (case of W_{wg} = 5 μm, P = 20 W, epilayer-up). Long arrows indicate directions of fast heat flow. One can see that the vast majority of the heat extraction was performed by the InP substrate, as expected since it has a relatively high thermal conductivity and is in contact with the heatsink and the active waveguide core. There is only a small amount of heat loss into the helium from the sides and top of the mesa.

The conclusion which can be made from these first two sets of calculations is that narrow mesa are key to improving CW operation since they should be capable of producing laser emission without incurring extreme temperature elevations in the active waveguide core. However, often for some applications we might require a much greater optical output power than that attainable from a single narrow mesa. In order to obtain a high optical output power an array of narrow mesa could be investigated. Operating a number of narrow mesa in parallel, i.e. a QC array laser, may have the potential to increase the output power while retaining the benefits of the narrow mesa. This configuration is investigated thermally in Section 5.3.5.

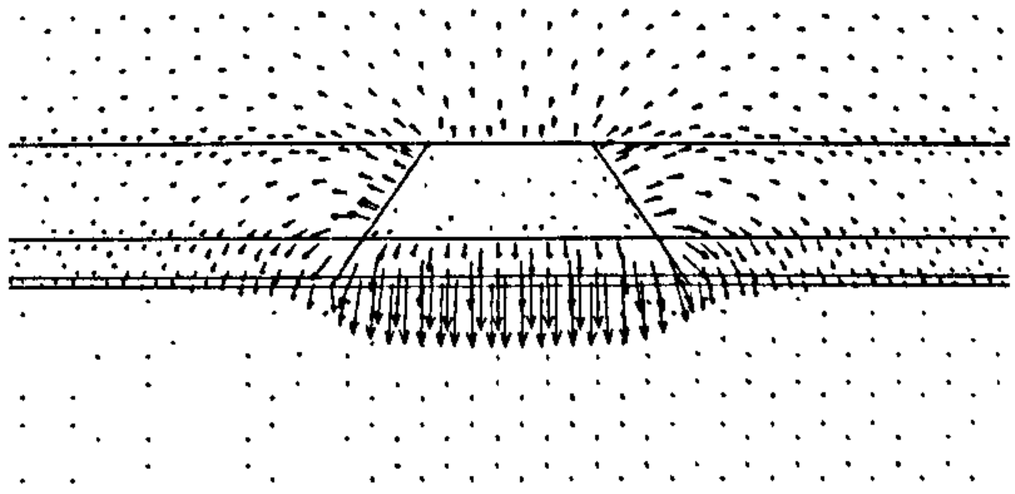

Figure 77 Calculated heat flow vectors for the case of QCL mesa W_{wg} = 5 μm, P = 20 W, mounted epilayer-up. The mesa is in the centre with the InP substrate below and helium gas above and in the moats.

5.3.3.2 Epilayer-down mounted

Epilayer-down mounting is commonly employed to improve the performance of semiconductor lasers, and has recently been used to improve the performance of QC lasers which had an InP upper cladding.[10] An identical set of thermal simulations were carried out, but this time based on the geometrical layout depicted in Figure 72, which represents an $In_{0.52}Al_{0.48}As$-clad QC laser mounted epilayer-down on a copper heatsink using indium bonding. Results from the simulations are given in graphical form in Figure 79 to Figure 82, and the peak temperatures exhibited in each case are listed in Table 42.

Comparing the results to the epilayer-up mounted case, there was a calculated reduction in the peak temperature of the chip when mounted epilayer-down. A drop of between 11 and 54 K was calculated depending on the combination of W_{wg} and P. Another important improvement was that the magnitude of the thermal gradient across the active region was reduced by a factor of ~2 in the epilayer-down mounted devices. This could help improve the overall performance of the laser by avoiding some of the positive feedback loops which lead to thermal runaway of the threshold current density.

W_{wg} (μm)	P (W)	T_{peak} (K)
15	20	134
10	13.33	119
5	6.66	101
15	20	134
10	20	143
5	20	163

Table 42 Combinations of W_{wg} and power and the resultant value of peak temperature calculated.

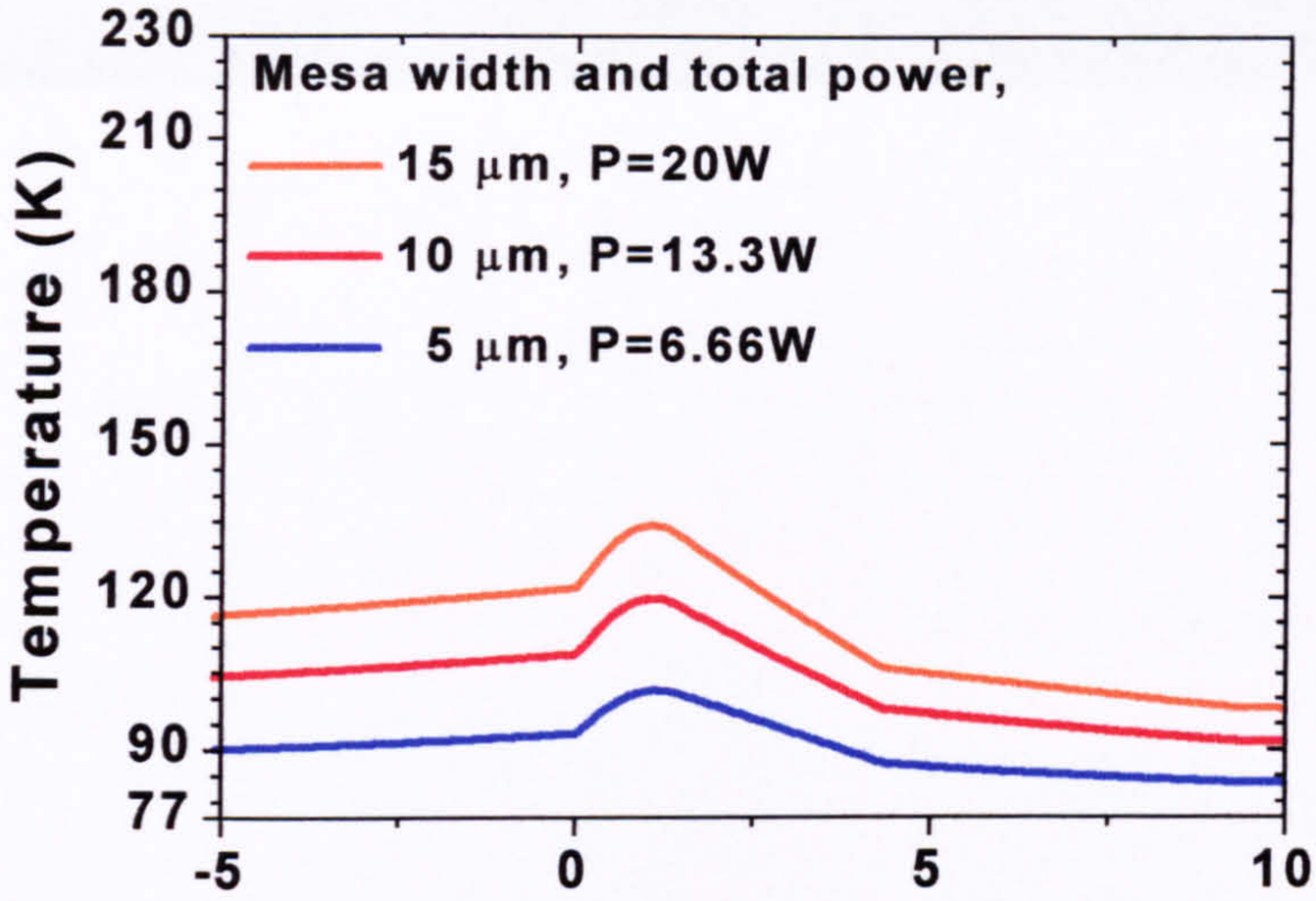

Figure 78 Vertical temperature profile of the QCL mesa mounted epilayer-down. The calculation is shown for different values of waveguide width W_{wg}, keeping the input thermal power density in the 'Active Region' constant in each case.

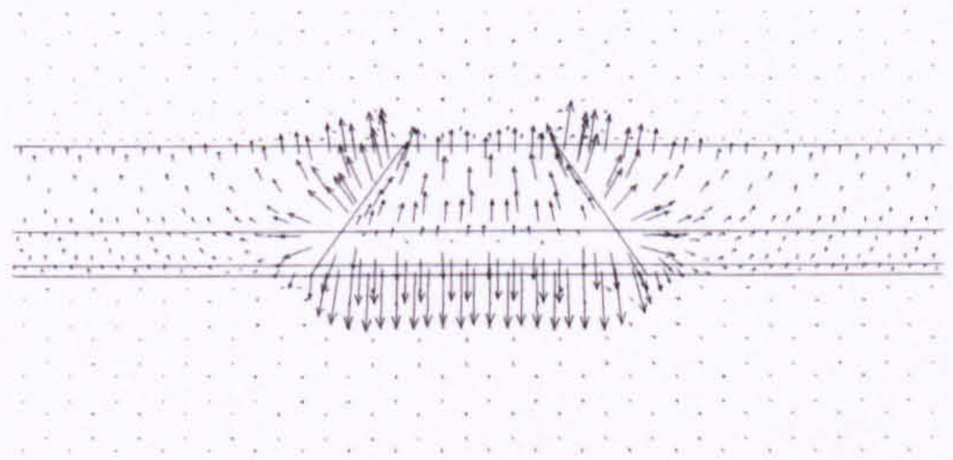

Figure 79 Calculated heat flow vectors for the case of QCL mesa W_{wg} = 5 μm, P = 20 W, mounted epilayer-down. The mesa is in the centre with the InP substrate below, the indium bonding layer above, and helium gas in the moats.

One can see from Figure 79 that, even though the device is mounted epilayer-down, there is still a large flow of heat into the InP substrate. This is the consequence of the poorer thermal conductivity of the $In_{0.52}Al_{0.48}As$ upper cladding layer which limits the effectiveness epilayer-down bonding. The use of an InP upper cladding layer would help alleviate this problem, improving the flow of heat directly to the heatsink. Although these devices were not fabricated in this work (owing to the inability to grow InP by MBE), the thermal profiles were calculated and the results are discussed in Section 5.3.7.

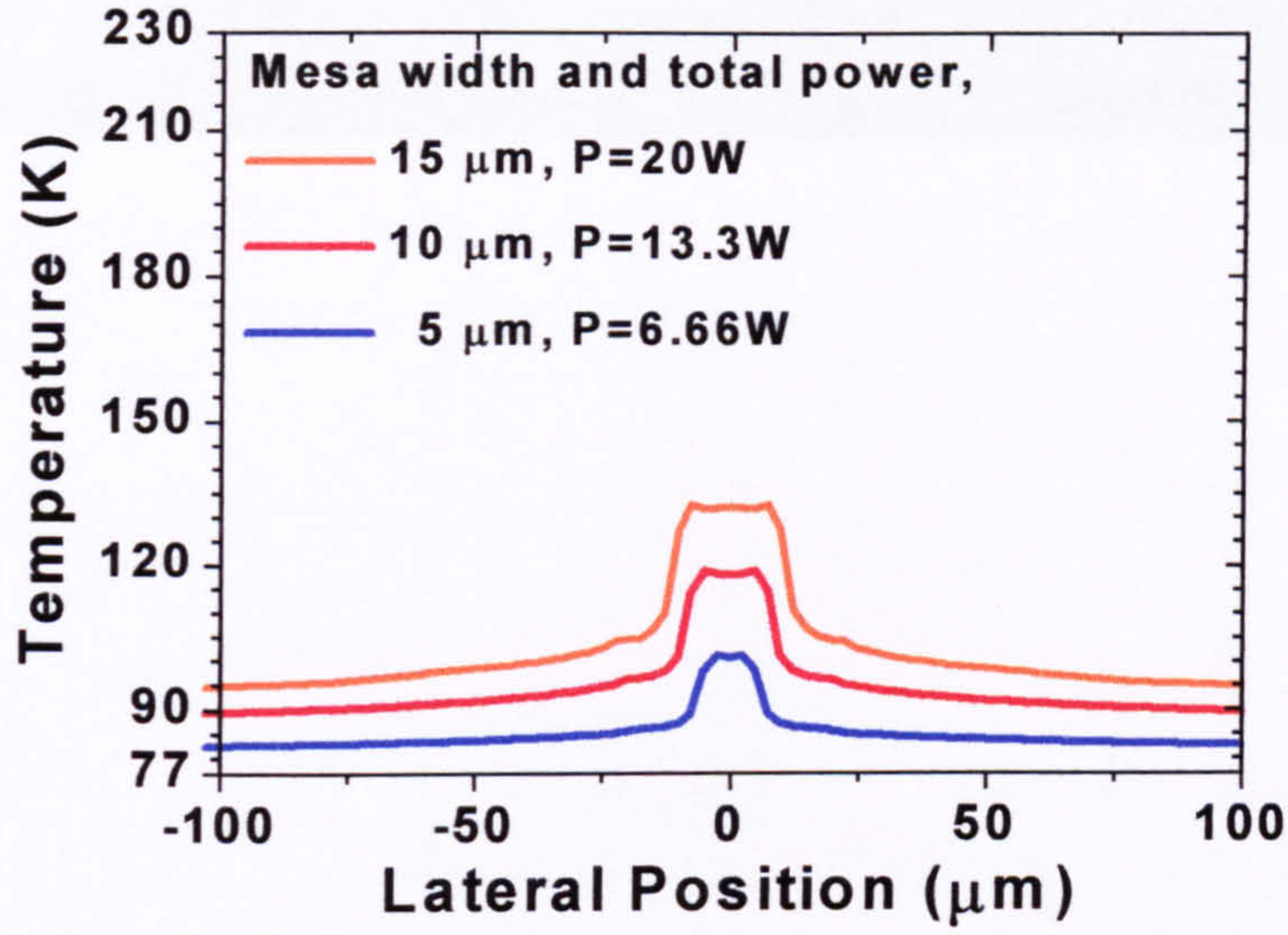

Figure 80 Lateral temperature profile of the QCL mounted epilayer-down. The calculation is shown for different values of waveguide width W_{wg}, keeping the input thermal power density in the 'Active Region' constant in each case.

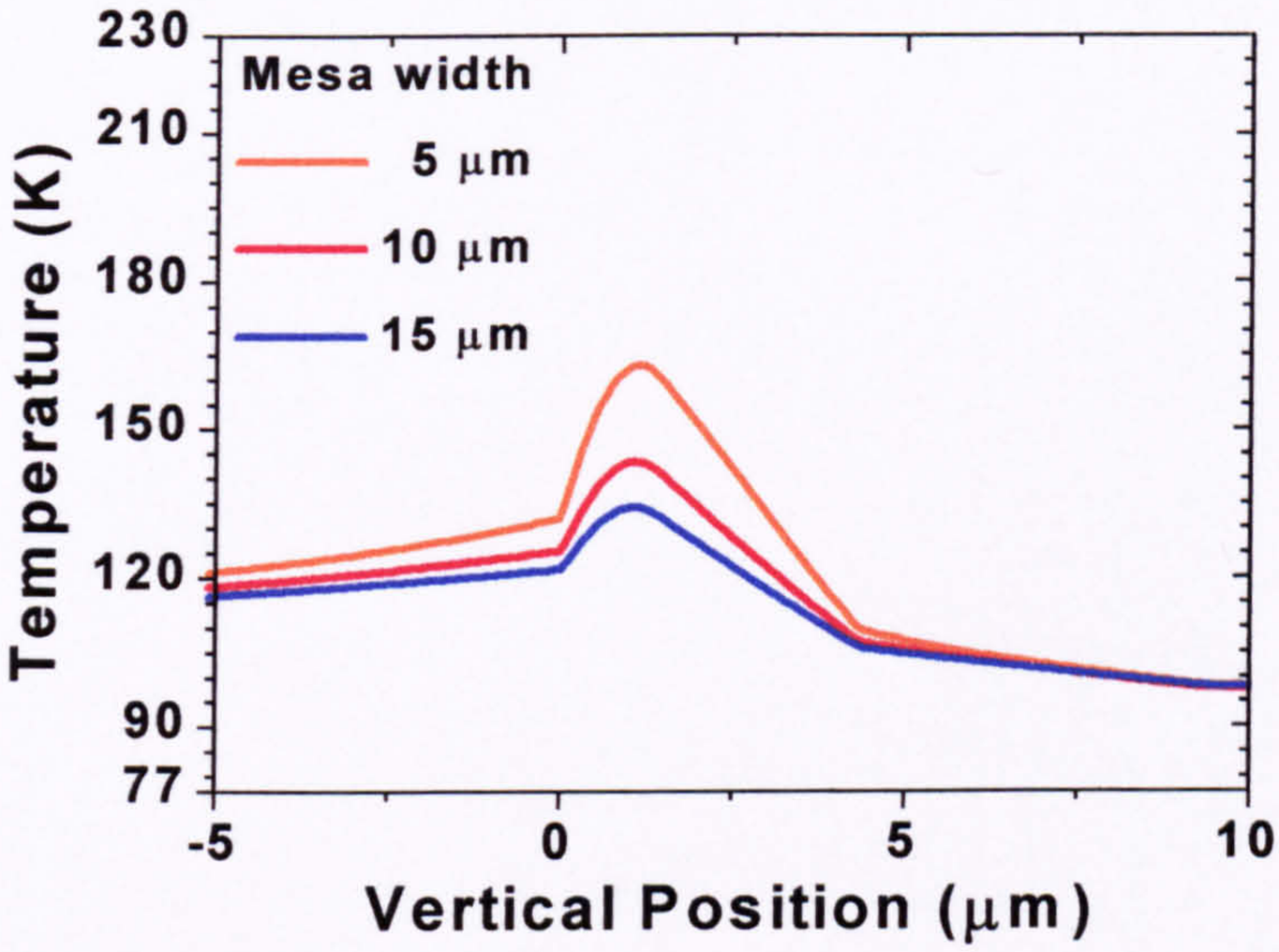

Figure 81 Vertical temperature profile through a QCL mesa mounted epilayer-down. The calculation is shown for different values of waveguide width W_{wg}, keeping the input thermal power in the 'Active Region' constant in each case, P =20 W.

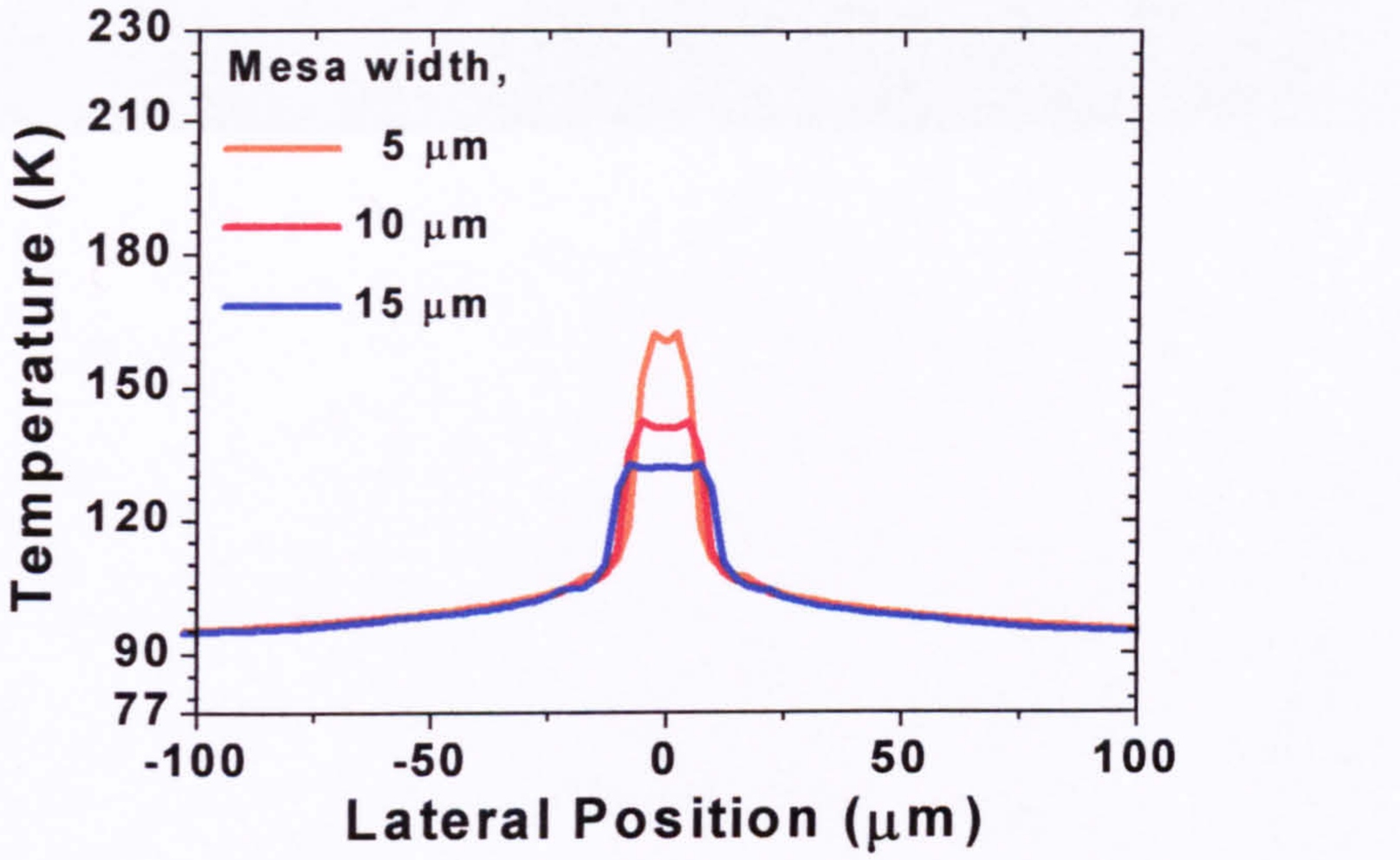

Figure 82 Lateral temperature profile through a QCL mesa mounted epilayer-down. The calculation is shown for different values of waveguide width W_{wg}, keeping the input thermal power in the 'Active Region' constant in each case, P =20 W.

5.3.4 Simulation results for PSWOX QC Lasers

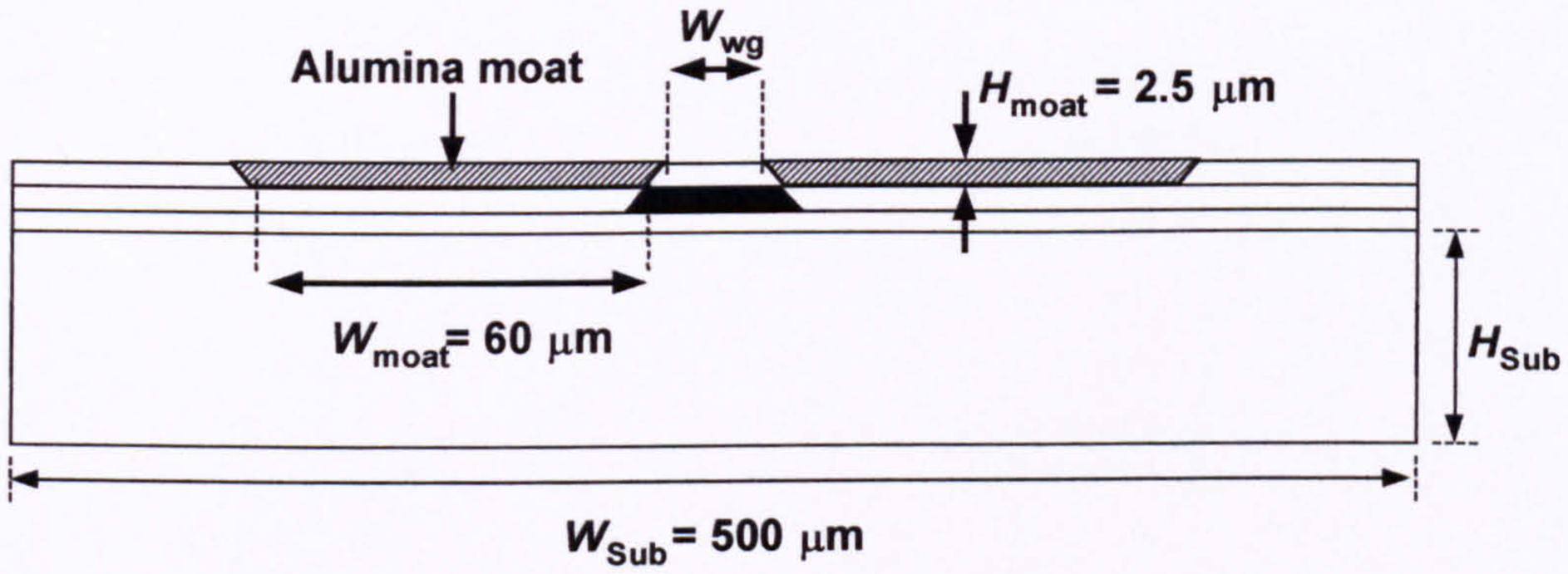

Figure 83 Geometric representation of the PSWOX QCL used by the finite element analysis. The area of the active region in solid black represents where the heat is generated.

Unlike in the mesa-etched QC lasers, the moats in the PSWOX QCLs consisted of alumina and only extended down through the upper cladding layer. The hope was that, since there were areas of improved thermal conductivity adjacent to the region of heat generation, the thermal dissipation would be improved. For the simulation of the PSWOX QCLs, geometrical changes were made (see Figure 83 and Table 38) and the thermal constants of the moat were changed from those for air to those assumed for alumina (see Table 38).

5.3.4.1 Epilayer-up mounted

Results from the simulations are again given in graphical form in Figure 84 to Figure 88, and the peak temperatures exhibited in each case are listed in Table 43.

W_{wg} (μm)	P (W)	T_{peak} (K)
15	20	168
10	13.33	140
5	6.66	112
15	20	168
10	20	177
5	20	211

Table 43 Combinations of W_{wg} and power and the resultant value of peak temperature calculated.

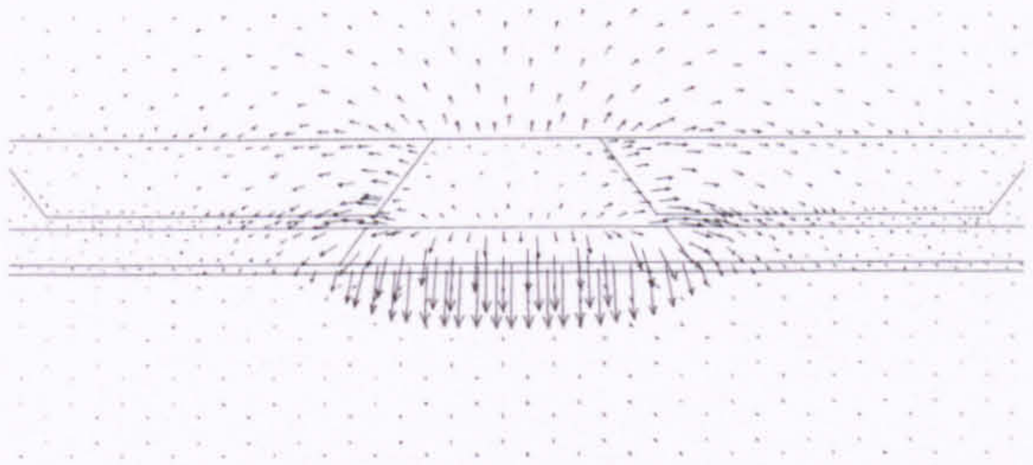

Figure 84 Calculated heat flow vectors for the case of PSWOX QCL W_{wg} = 5 μm, P = 20 W, mounted epilayer-up. The laser waveguide is in the centre with the InP substrate below it and helium gas above. On either side of the laser the upper cladding has been replaced with alumina and the waveguide core layer is passive (no heat generated).

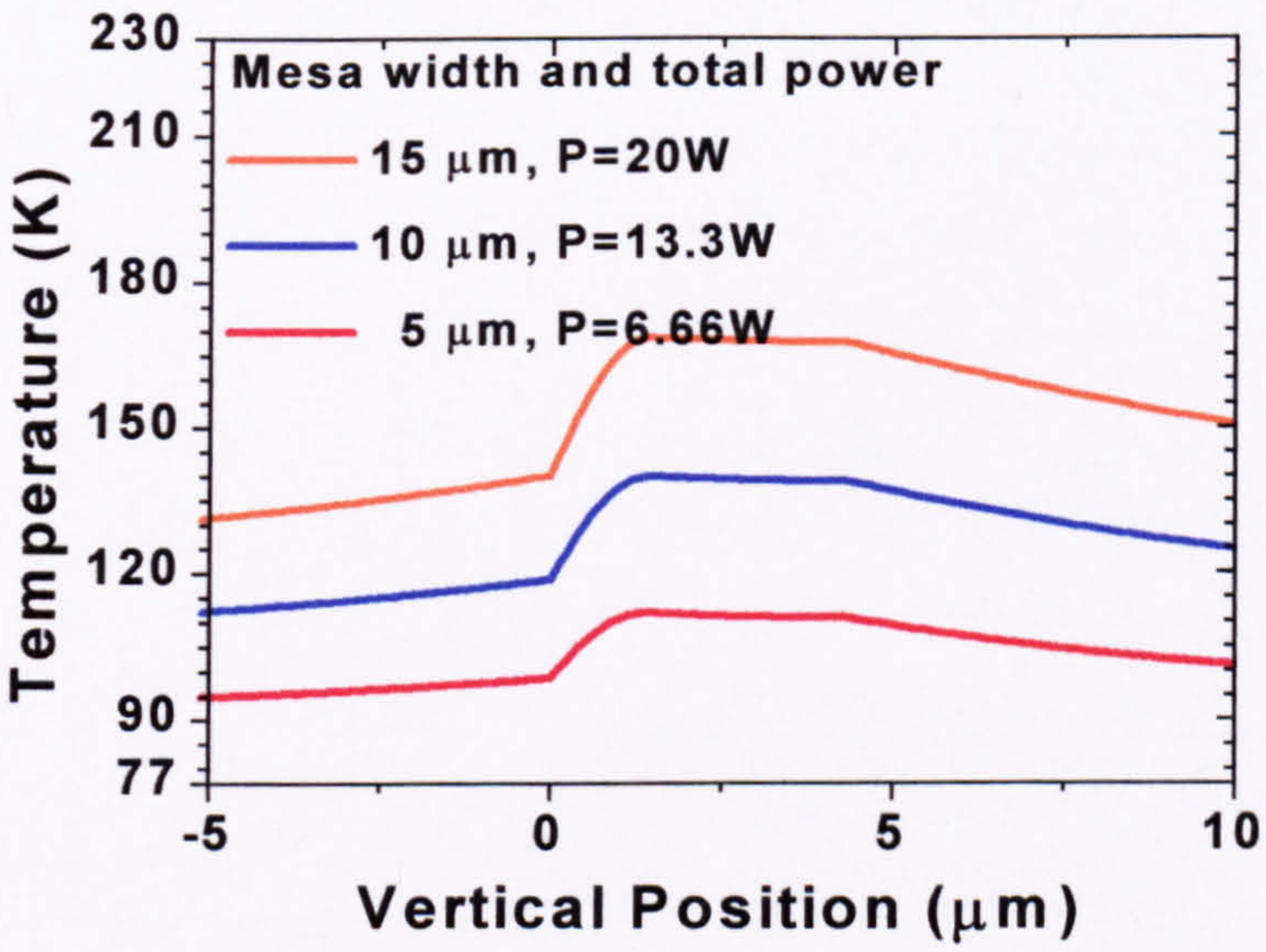

Figure 85 Vertical temperature profile of the PSWOX QCL mounted epilayer-up. The calculation is shown for different values of waveguide width W_{wg}, keeping the input thermal power density in the 'Active Region' constant in each case.

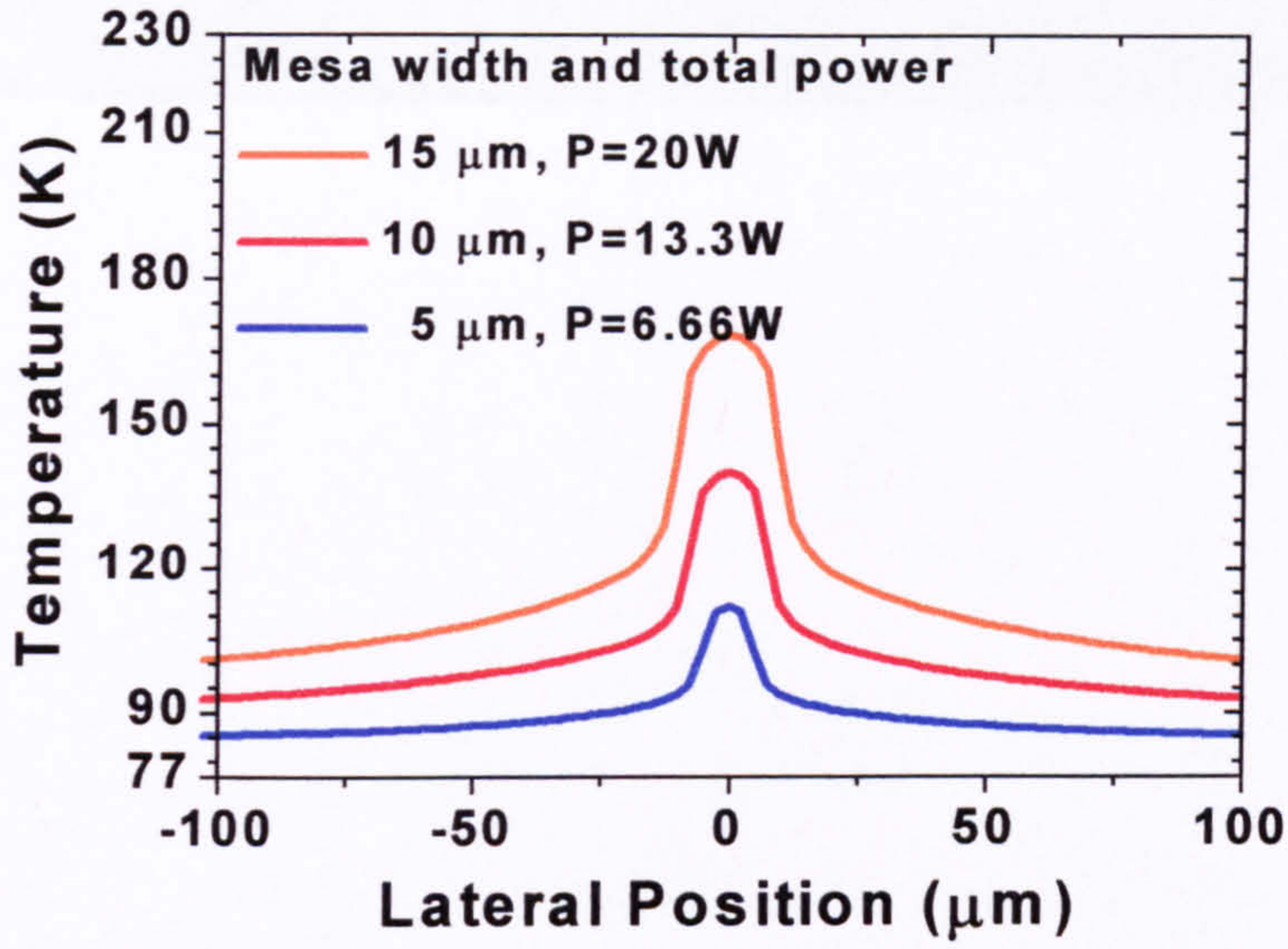

Figure 86 Lateral temperature profile of the PSWOX QCL mounted epilayer-up. The calculation is shown for different values of waveguide width W_{wg}, keeping the input thermal power density in the 'Active Region' constant in each case.

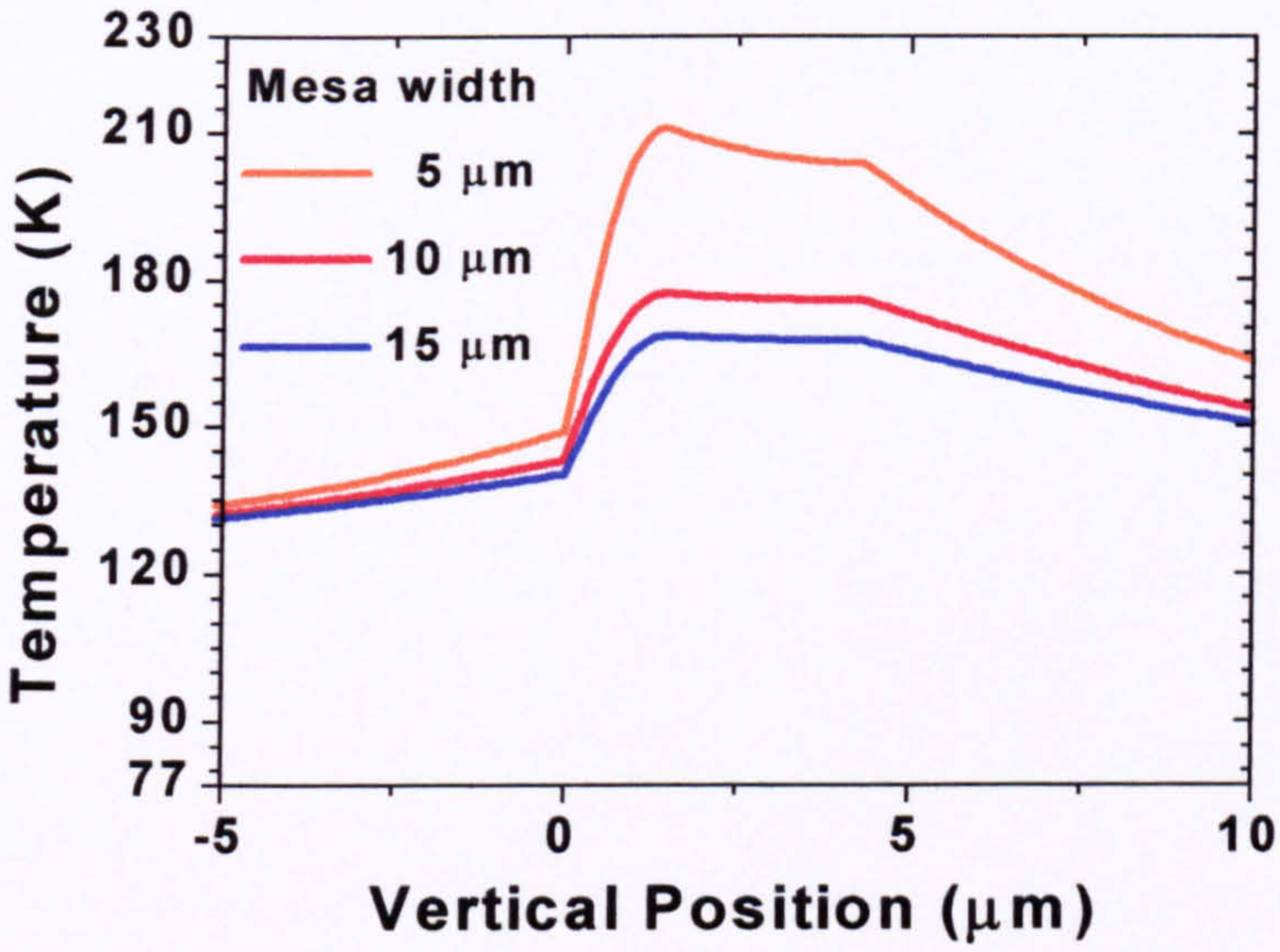

Figure 87 Vertical temperature profile through the PSWOX QCL mounted epilayer-up. The calculation is shown for different values of waveguide width W_{wg}, keeping the input thermal power in the 'Active Region' constant in each case, P =20 W.

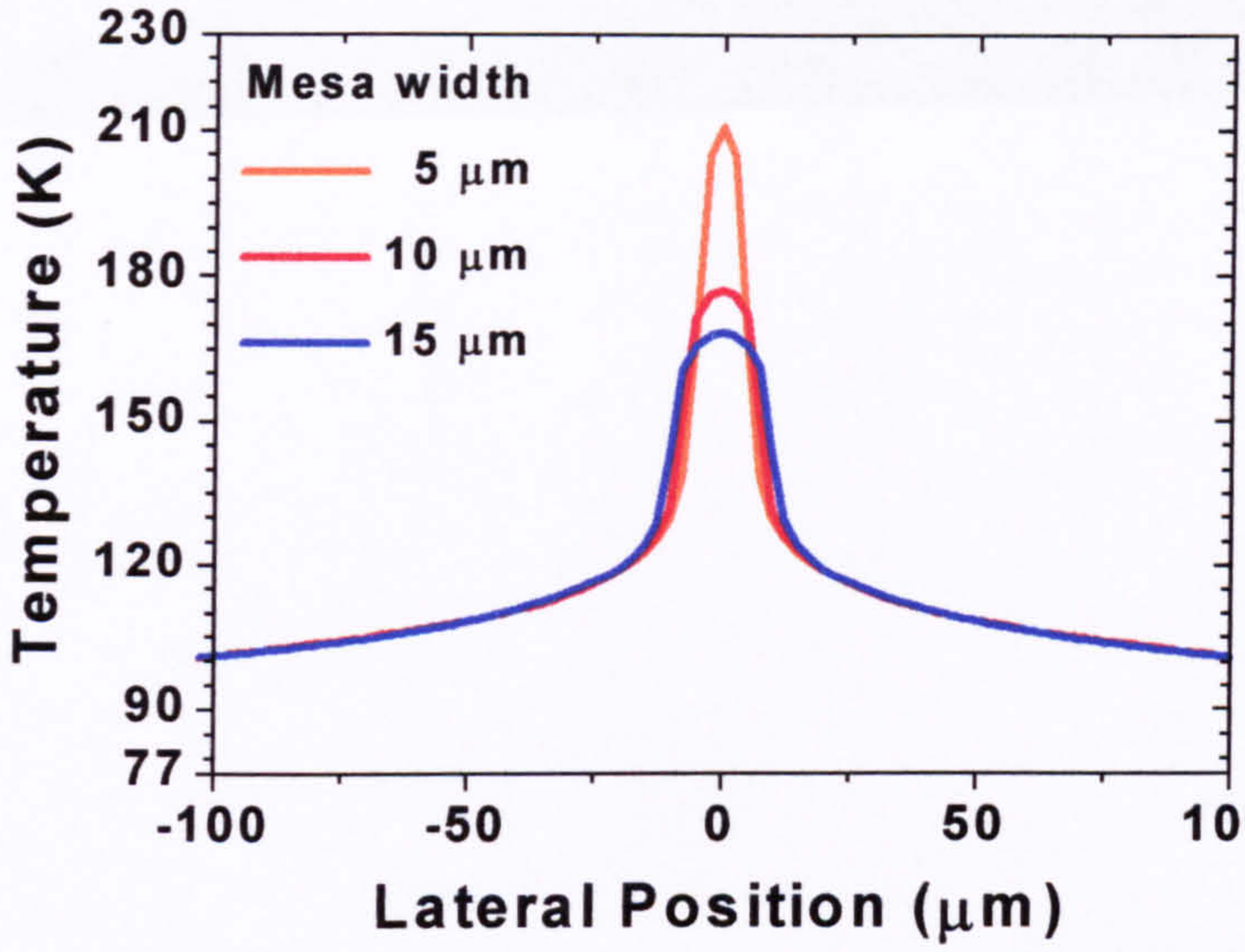

Figure 88 Lateral temperature profile through a PSWOX QCL mounted epilayer-up. The calculation is shown for different values of waveguide width W_{wg}, keeping the input thermal power in the 'Active Region' constant in each case, P =20 W.

From the heat flow diagram Figure 84 and the peak temperatures listed in Table 43, it can be seen that the simulation indicated that there was only a minor reduction (~ 8 K) in the peak temperatures of the epilayer-up mounted PSWOX QCLs compared to the epilayer-up mounted QCL mesa. The reduction was only for narrow geometries operating under high powers. This does not concur with the experimental evidence found for the mesa-etched and PSWOX QCLs fabricated in this work. Actual PSWOX QCLs exhibited improved T_0 over their mesa-etched counterparts. Possible explanations for this will be discussed in the conclusions at the end of this chapter.

5.3.4.2 Epilayer-down mounted

Results from the simulations for epilayer-down mounted PSWOX QCLs are given in graphical form in Figure 90, Figure 91, Figure 92, and Figure 93, and the peak temperatures exhibited in each case are listed in Table 44.

W_{wg} (μm)	P (W)	T_{peak} (K)
15	20	133
10	13.33	115
5	6.66	99
15	20	133
10	20	140
5	20	159

Table 44 Combinations of W_{wg} and power and the resultant value of peak temperature calculated.

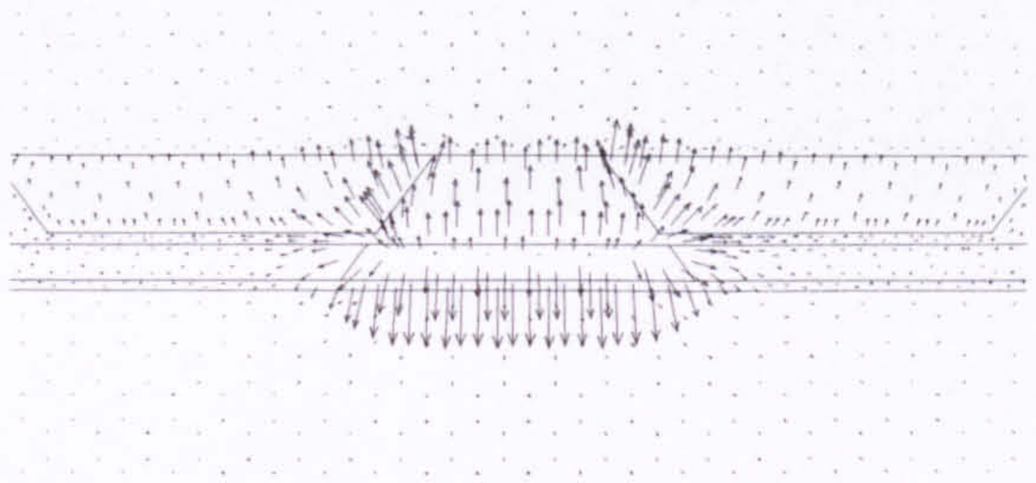

Figure 89 Calculated heat flow vectors for the case of a PSWOX QCL W_{wg} = 5 μm, P = 20 W, mounted epilayer-down. The y-axis gives the vertical position and the x-axis gives the lateral position.

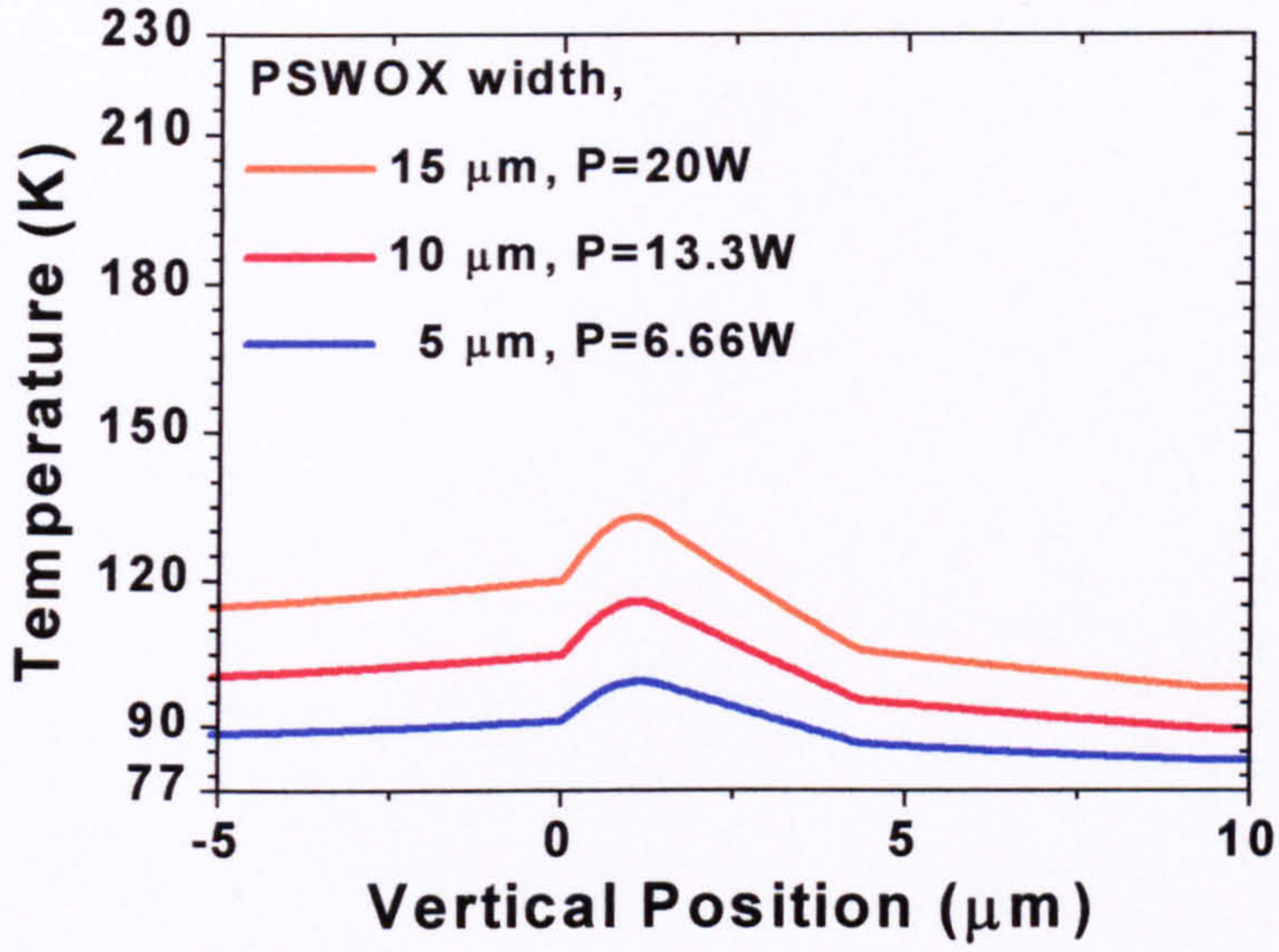

Figure 90 Vertical temperature profile of the PSWOX QCL mounted epilayer-down. The calculation is shown for different values of waveguide width W_{wg}, keeping the input thermal power density in the 'Active Region' constant in each case.

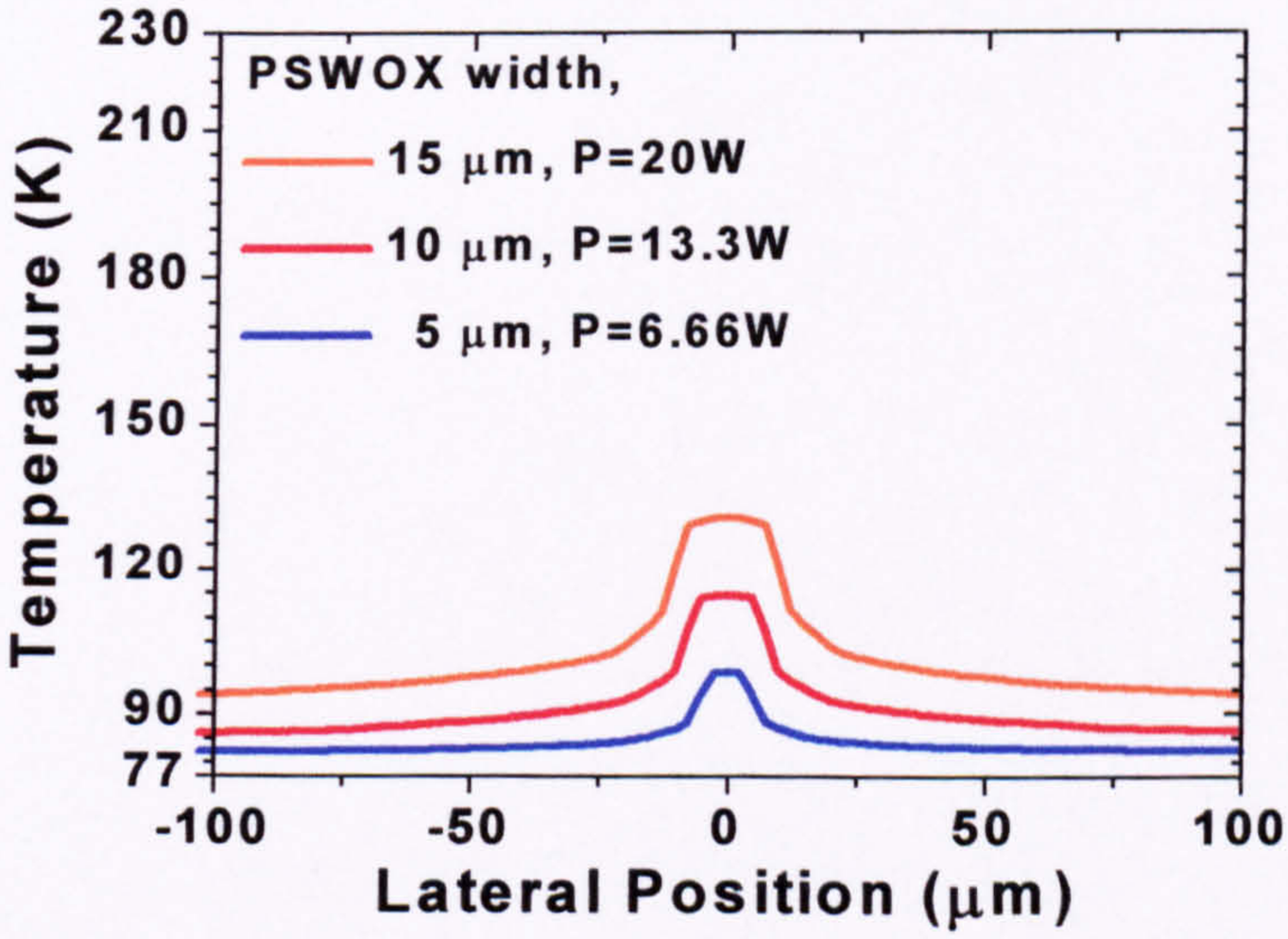

Figure 91 Lateral temperature profile of the PSWOX QCL mounted epilayer-down. The calculation is shown for different values of waveguide width W_{wg}, keeping the input thermal power density in the 'Active Region' constant in each case.

Figure 92 Vertical temperature profile through the PSWOX QCL mounted epilayer-down. The calculation is shown for different values of waveguide width W_{wg}, keeping the input thermal power in the 'Active Region' constant in each case, P =20 W.

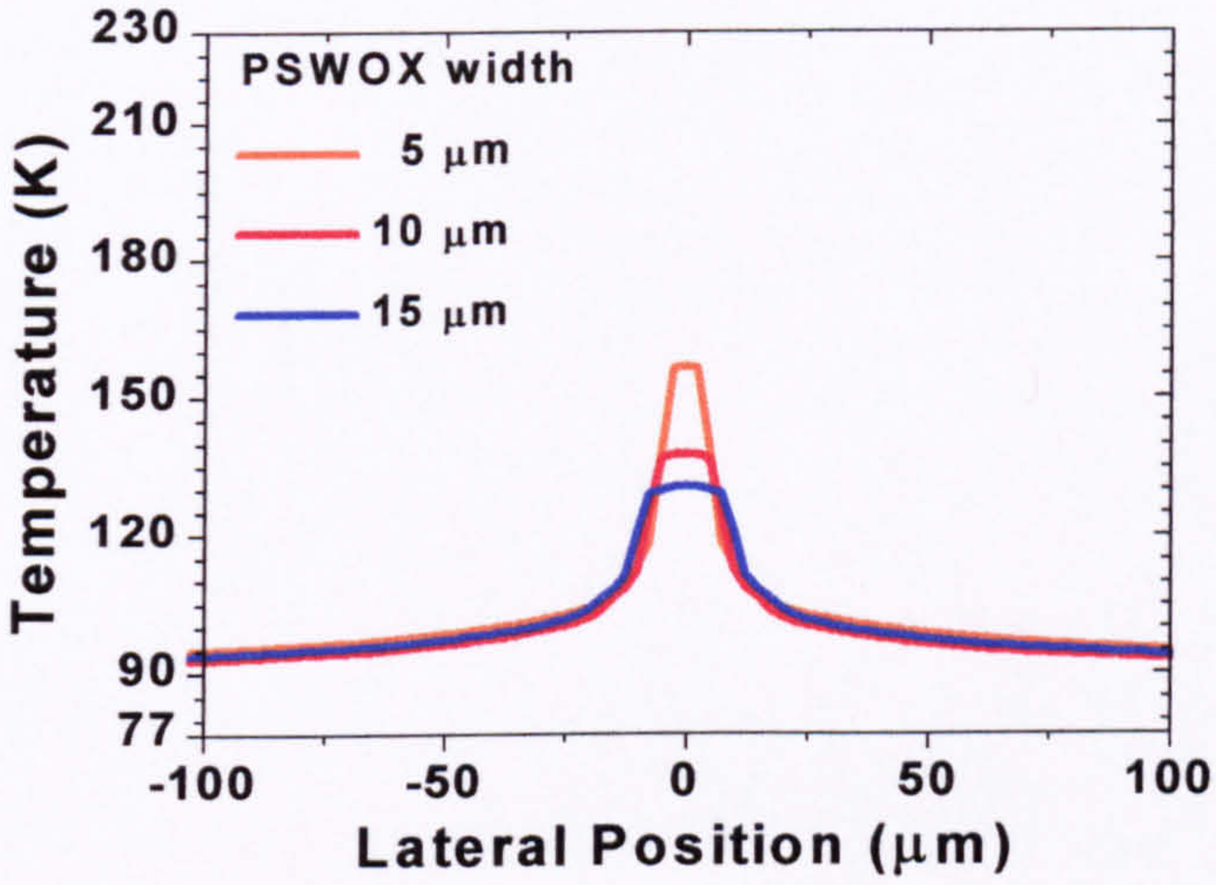

Figure 93 Lateral temperature profile through a PSWOX QCL mounted epilayer-down. The calculation is shown for different values of waveguide width W_{wg}, keeping the input thermal power in the 'Active Region' constant in each case, P =20 W.

Comparing the peak temperatures obtained for the epilayer-down mounted PSWOX QCLs and QCL mesa, again there was only a very slight reduction (~ 4 K) for the PSWOX configuration.

5.3.5 Simulation results for Mesa-etched QC Array Lasers

To achieve high average optical output powers, a QCL must be driven with a high bias or at high duty cycles. However, as we have seen this produces heat in the active region which will rapidly deteriorate the laser performance. Having confirmed that narrow mesa operating under low bias conditions were more favourable in terms of keeping the laser cool, the motivation for investigating arrays was to provide a higher total optical power output while retaining thermal advantages of the single devices. A number of narrow, spatially separated QCLs working in parallel on the same chip (i.e. a QCL array) would effectively spread the heat generated over a larger area, delocalising the heating. For a given optical output power, the active region temperature of each QCL in the array should be lower than it would be for single device emitting the same

optical power. The total heat generated (and therefore the heatsink temperature) should remain the same, but the heat should be more delocalised in the laser chip.

The spacing between the individual members of the array should be such that the thermal cross-talk is minimised. Intuitively, it was suspected that this distance would be equal to or greater than the substrate thickness, however, we will discuss the matter more methodically below.

The InP substrate conducts the heat away from each laser towards the copper heatsink. Unfortunately, the thermal resistance of the InP is relatively high ($K < 68$ W m^{-1} K^{-1} at $T = 300$ K) compared to that of the copper ($K \approx 400$ W m^{-1} K^{-1} at T = 300 K) and it therefore acts as a barrier to heat dissipation. In order to reduce thermal resistance between each laser waveguide and the copper heatsink (and to facilitate cleaving) the InP substrate is normally thinned to ~150 μm. Now, the InP in close proximity to the copper will be at a temperature close to that of the copper itself i.e. $T \approx 77$ K. However, the temperature of the InP adjacent the active region of each laser will be elevated by the heat generated there. This situation results in a thermal gradient across the InP between the copper heatsink and each device. If the distance between the active region and the copper heatsink is short (i.e. the InP substrate is thin), this thermal gradient will be very steep. Under these conditions the phonons will preferentially diffuse towards the heatsink, rather than laterally towards its neighbouring waveguides in the array. It is reasonable then that if the substrate is thinned to 150 μm, then a separation of 150 μm between the each waveguide should be sufficient to prevent localisation of heat. A value of 150 μm is also considered to be practical when considering that if the array is to include a large number of devices, the total width of the array chip width must not be excessive.

The thermal modelling was used to investigate the laser temperature for a number of values of inter-device spacing to find the optimal spacing and to gauge the level of improvement over a single, wide laser operating under the same total power (and power density).

5.3.5.1 Mounted epilayer-up

Thermal modelling was carried out for arrays of three 5 μm-wide ($W_{wg} = 5$ μm) mesa, spaced D_{array} apart on a 500 μm-wide chip (refer to Figure 70). Again, the temperatures of the outer boundaries of the geometrical representation were set to $T = 77$ K to imitate a heatsink held at liquid nitrogen temperature. The total power of $P = 20$ W was divided equally between the three mesa in the array so that each mesa was 'supplied' with 6.66 W of thermal power. The simulation was performed for a range of values of D_{array} which are listed in Table 45 along with the peak temperatures calculated for each member of the array. The values of temperature were taken from the lateral thermal profile across the chip (that is the temperature calculated along the lateral cross-section at the active region/upper cladding interface), shown in Figure 94. The profile of a single 15 μm-wide mesa being operated under the same conditions is also displayed for comparison.

	Peak Temperature, T_{peak} (K)		
D_{array} (μm)	Left-hand Mesa	Centre Mesa	Right-hand Mesa
5	-	167	-
30	133	137	133
50	133	135	133
75	131	134	131
100	130	129	130
150	**128**	**129**	**128**
200	129	127	129

Table 45 Values of peak temperature calculated for a range of array spacing for the epilayer-up mounting configuration.

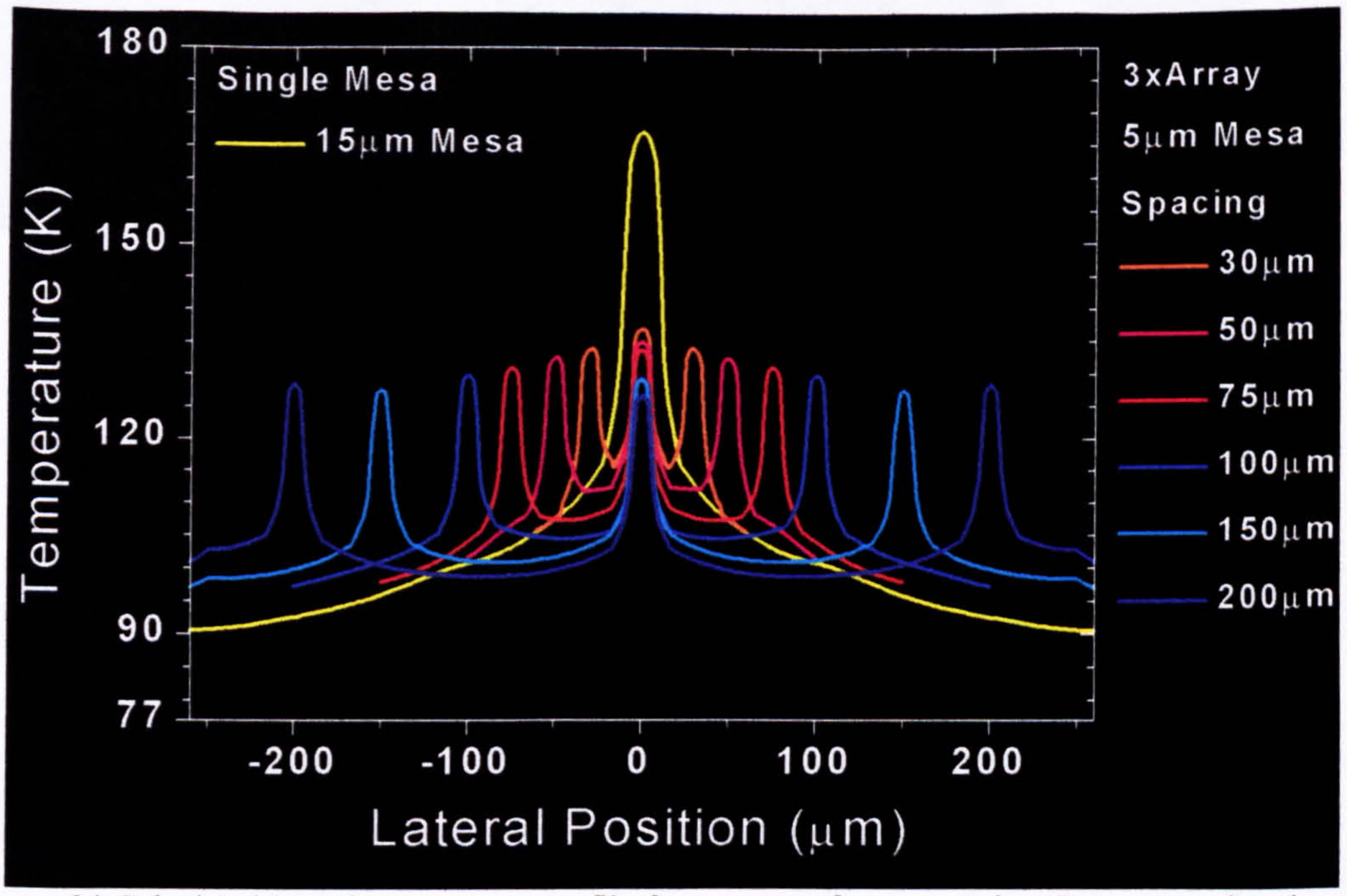

Figure 94 Calculated lateral temperature profile for a range of mesa spacing D_{array} separating three 5 μm-wide mesa. The chip was in the epilayer-up configuration and the total input thermal power in the 'Active Region' was the same in each case, P =20 W. The temperature profile for a single mesa combined from the 3 single mesa is also shown.

The temperature elevations for all values of D_{array} tried were significantly lower (there was a maximum peak temperature difference of 40 K) than the equivalent single mesa obtained when the three components of the array merge into one. The variation in the peak temperature between the arrays of different D_{array} was lower, with a maximum difference in peak values of ~10 K. From the profiles in Figure 94, the trend as the D_{array} increases was that the heat generated was spread out such that the temperature rise was more uniform across the laser chip.

Doubling the spacing from 50 μm to 100 μm, decreased the temperature of the central mesa by 5.6 K, whereas doubling the spacing from 100 μm to 200 μm only resulted in a further decrease of just 2.6 K. Therefore, for a laser chip with a substrate thickness of H_{sub} = 150 μm, a spacing D_{array} ~ 150 μm would indeed appear to be appropriate.

5.3.5.2 Mounted epilayer-down

	Peak Temperature, T_{peak} (K)		
D_{array} (μm)	**Left-hand Mesa**	**Centre Mesa**	**Right-hand Mesa**
5	-	132	-
30	119	120	119
50	117	118	117
75	115	116	115
100	114	115	114
150	**113**	**114**	**113**
200	112	113	112

Table 46 Values of peak temperature calculated for a range of array spacing for the epilayer-down mounting configuration.

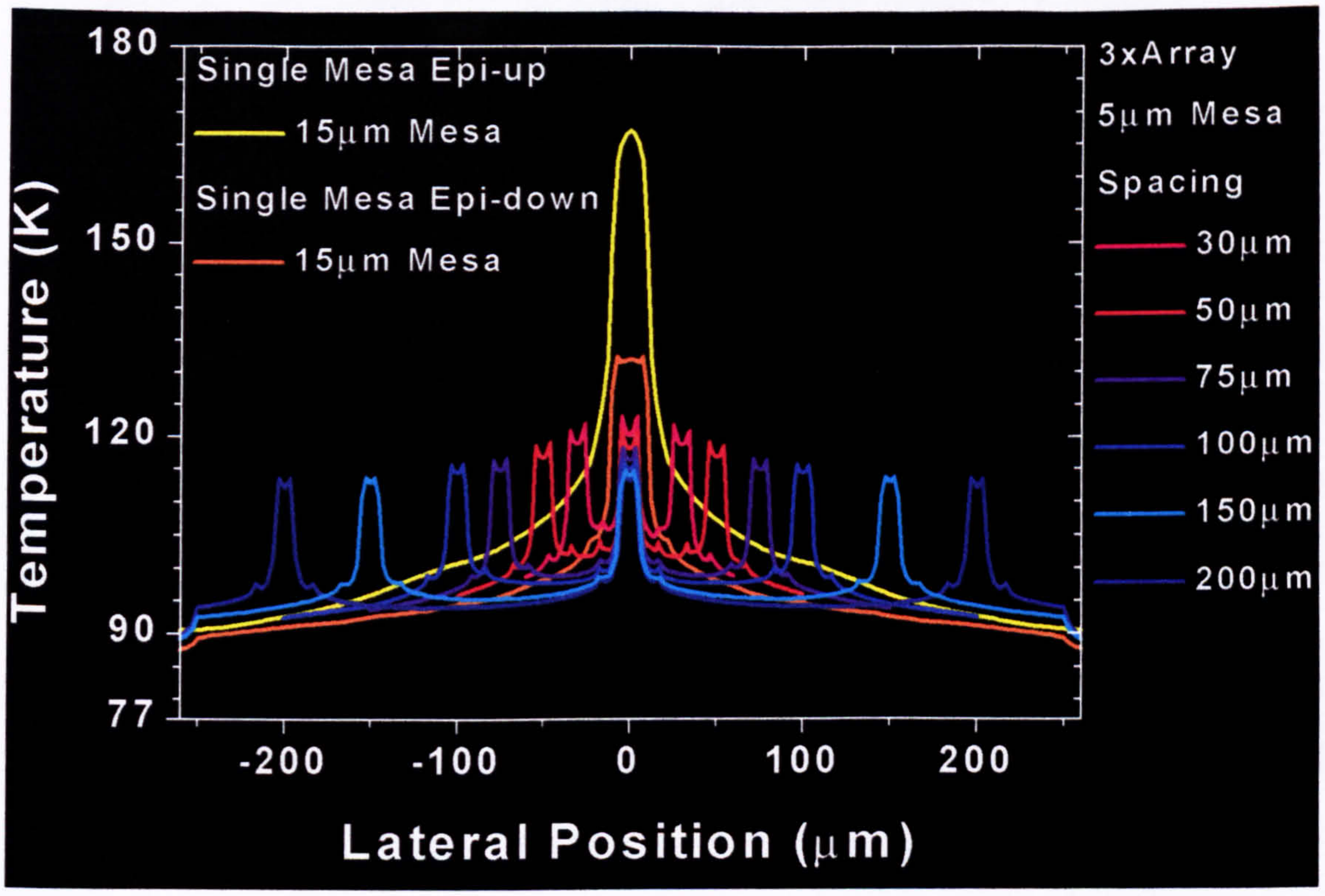

Figure 95. Calculated lateral temperature profile of the QCL mesa array mounted epilayer-down. The total input thermal power in the 'Active Region' was the same in each case, P =20 W.

An identical set of simulations were carried out on an array mounted epilayer-down on a copper heatsink using indium bonding. The simulation was performed for a the same range of values of D_{array} which are listed in Table 46 along with the peak temperatures calculated for each member of the array. The lateral temperature profile across the chip is shown in Figure 95. The profiles of a single 15 μm-wide mesa mounted epilayer-up and epilayer-down and being operated under the same conditions is also displayed for comparison.

As expected, mounting the arrays epilayer-down led to further improvements with the maximum reduction in T_{peak} being 44 K over a single, broad mesa mounted epilayer-up. The improvement over a single, broad mesa mounted epilayer-down was still 19 K.

5.3.6 Simulation results for PSWOX QC Array Lasers

The PSWOX lasers only exhibited marginally better thermal performance when operated at high powers. When operated in an array with low powers we can therefore expect that there will not be any great improvement over the QCL mesa array. The structures were modelled in any case for completeness.

Simulations were carried out for an array of three 5 μm-wide (W_{wg} = 5μm) PSWOX QCLs, spaced D_{array} = 150 μm apart on a 500 μm-wide chip (refer to Figure 70). Again, the total power of P = 20 W was divided equally between the three devices in the array and the simulation was performed for both epilayer-up and epilayer-down geometries. Listed in Table 47 are the peak temperatures calculated for each member of the array in each case. The vertical and lateral temperature profiles are given in Figure 96 and Figure 97, respectively. For comparison, the profiles of a single 15 μm-wide mesa being operated under the same power density are also displayed in these figures for both the epilayer-up and epilayer-down mounted cases.

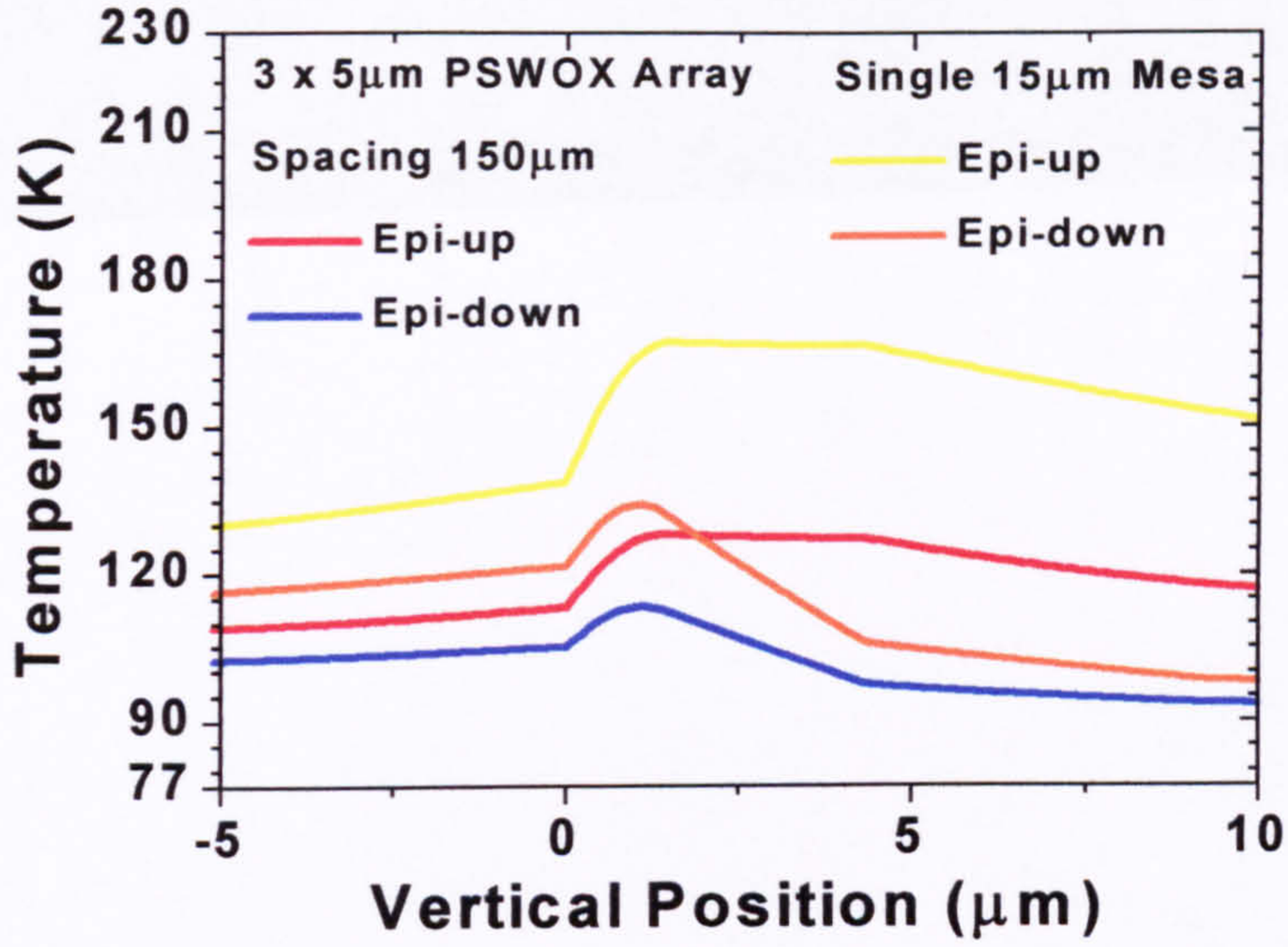

Figure 96 Vertical temperature profiles of central device of the PSWOX array QCL when mounted either the epilayer-up or epilayer-down configurations. Simulation results for a single 15 μm-wide mesa are included for comparison.

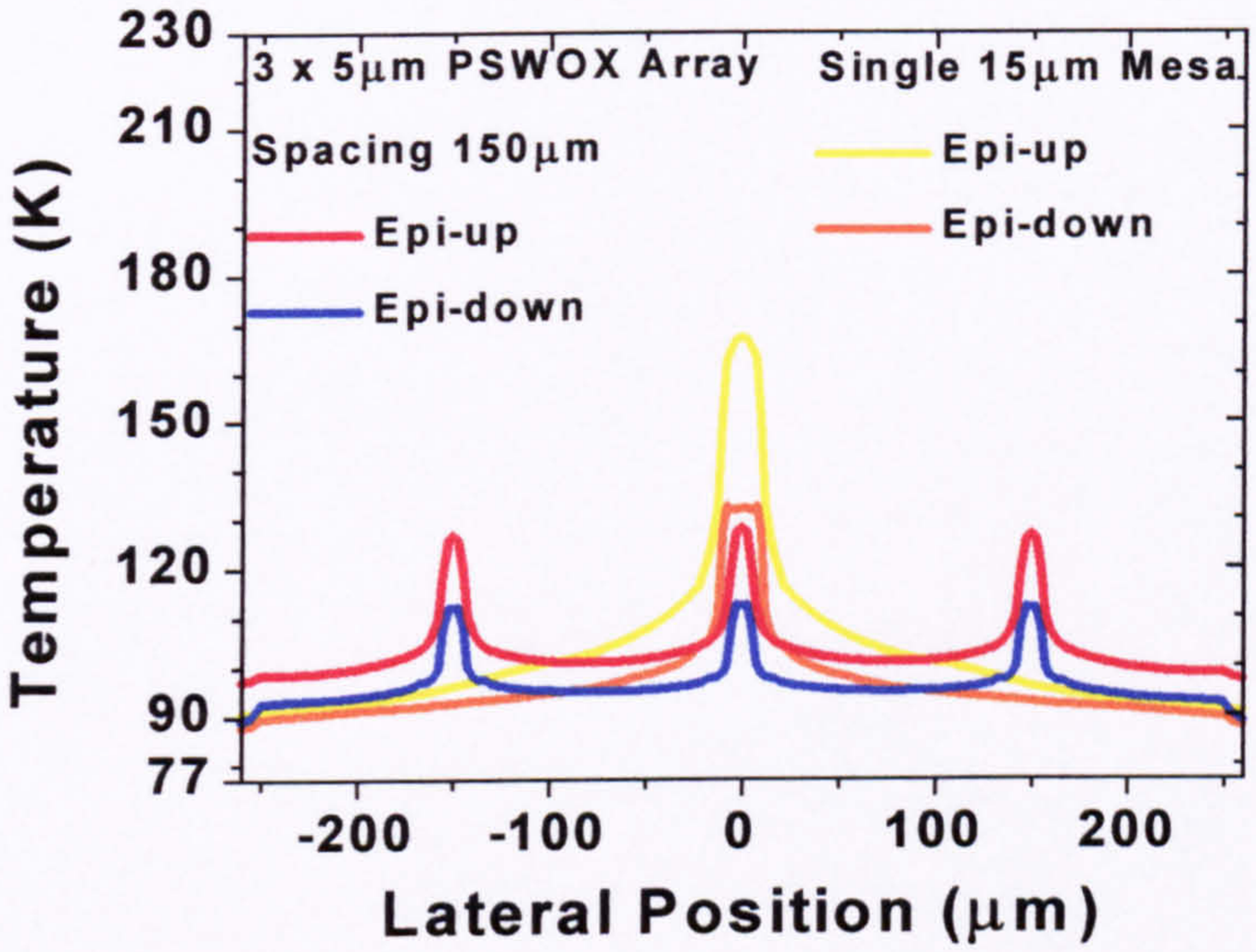

Figure 97 Lateral temperature profiles of the PSWOX array QCL when mounted either epilayer-up or epilayer-down. Simulation results for a single 15 μm-wide mesa are included for comparison.

	Peak Temperature - T (K)		
Mounting	**Left-hand Mesa**	**Centre Mesa**	**Right-hand Mesa**
Epi-up	126	127	126
Epi-down	112	112	112

Table 47 Values of peak temperature for each laser in the PSWOX Array QCL. The array spacing was D_{array} = 150 μm and contained 3 PSWOX lasers, each dissipating P = 6.66 W of thermal power.

The simulations indicate that further substantial improvements may be obtained if the lasers are mounted epi-layer down. According to these simulations, the best performance was obtained using the PSWOX QCL array mounted epilayer-down, although the improvement over the mesa-etched QCL array mounted epilayer-down was very slight (a couple of degrees Kelvin).

5.3.7 Simulation of Mesa-etched and Buried Heterostructure QC lasers with an InP upper cladding

The superior pulsed-mode performance of QC lasers employing an InP upper cladding has been well reported, but the improvements to CW-mode operation has not been so convincing.[1, 2, 14] Thermal modelling of an InP-clad QC laser was published very recently by Gmachl *et al.*.[10] That work also solved the two-dimensional non-linear differential heat-flow equation using a finite element modelling package, but on a $\lambda \approx 8$ μm QCL design and at different heatsink temperatures, $T = 145$ or 165 K.

Structures using an InP upper cladding layer could not be investigated experimentally by this author, owing to the limitation of our MBE growth facility. Nevertheless, modelling was still carried out to determine whether the ability to use an InP upper cladding was useful for CW-mode operation. Four structures were modelled in which the thermal constants of the upper cladding layer were replaced with those for InP. Again $W_{wg} = 5$ μm and $P = 20$ W, and all other parameters remained as they were in the previous simulations. Four permutations were investigated based on whether using epilayer-up or epilayer-down mounting, and air-filled moats (i.e. a mesa-etched QCL) or InP-filled moats (i.e. a buried heterostructure QCL). The vertical temperature profile is given in Figure 98 for the four cases.

	Air moat	**InP moat**
Epi-up	215 K	154 K
Epi-down	136 K	126 K

Table 48 Values of the peak temperature in the active waveguide core for the four different configurations of QCL mesa employing an InP upper cladding.

The results indicated that in the case of an epilayer-up mounted mesa-etched QC laser, the presence of the InP upper cladding did not reduce the temperature of the device at all. This is consistent with the CW measurements performed by Faist *et al.* as was outlined in Section 5.2.5.1. The performance of InP-clad QCL mesa mounted epilayer-up have been reported to have improved performance over $In_{0.52}Al_{0.48}As$-clad devices when operated in pulsed mode only. We must remember that our simulations calculated the *steady-state* temperature, i.e. CW operation. The steady state solutions give no information on the transient temperatures.

For instance, imagine this structure when the CW power supply has just been switched on. At the start, the InP upper cladding layer, like the core, is cool. Once the pulse starts, the active waveguide core generates heat, which is removed by both the InP substrate and InP upper cladding. The InP substrate has a large volume and is in good thermal contact with the heatsink. As such, it is kept cool by transferring the heat to the heatsink. In contrast, the InP upper cladding has a low volume and cannot loose the heat it has removed from the core, as it is not well connected (thermally) to the heatsink. As time progresses, the heat builds up in the InP-upper cladding rendering it ineffective in terms of heatsinking. Hence, in the steady state the structure, as it was modelled, offered no advantages. This scenario is supported by the heat-flow diagram of the structure given in Figure 99, which indicated that virtually all of the heat flowed downwards into the substrate in the steady-state.

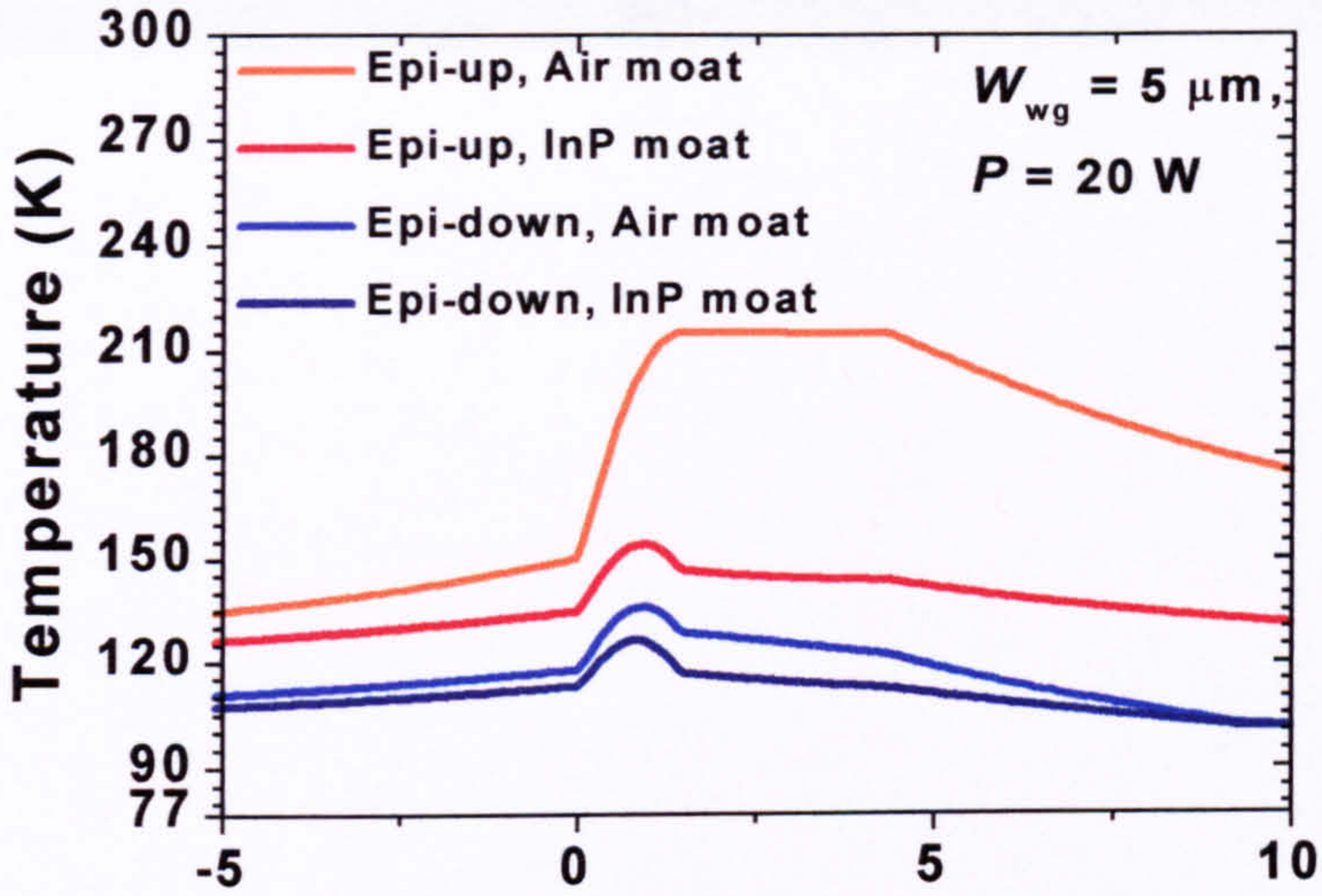

Figure 98 Vertical temperature profile calculated for the four InP-clad QCL designs.

In their paper reporting the CW operation of this structure, Faist *et al.* compared the threshold current obtained in pulsed operation with that observed in CW mode, and thereby deduced the effective thermal resistance R_{th} of their device to be ~ 6.6 K/W. The expression they used to do this follows:

$$T_{act} = T_{sub} + R_{th}P\,, \tag{5-5}$$

where T_{sub} was the temperature of the heatsink/substrate, T_{act} was the actual temperature in active waveguide core, and P was the electrical power dissipated in the laser.

We can use this equation to find a value of R_{th} for our very similar structure to test the accuracy of our simulation. Taking T_{act} = 200.5 K from the average temperature of the active waveguide core (as calculated from the vertical temperature profile in Figure 98), along with P = 20 W, and T_{sub} = 77 K, and substituting these values into a rearrangement of Eq. (5-5), we calculate a value of R_{th} = 6.2 K/W, in very good agreement with the data of Faist *et al.*.

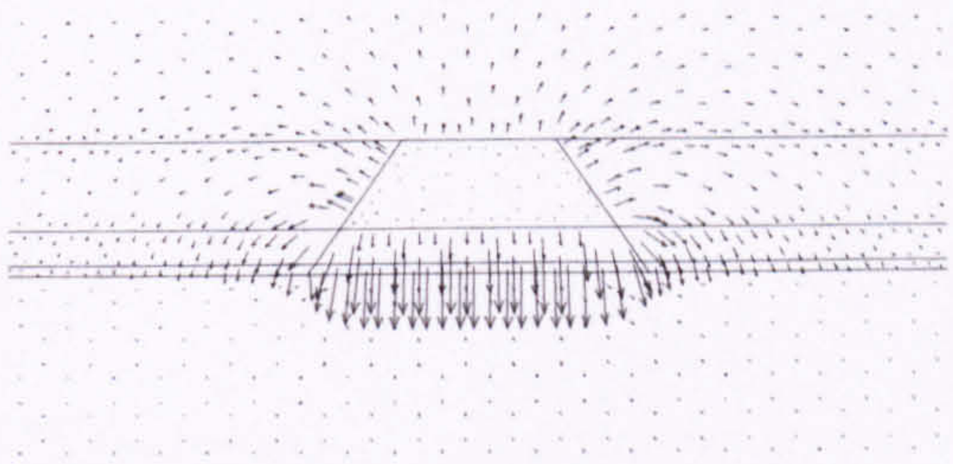

Figure 99 Calculated heat flow vectors for the epilayer-up mounted, mesa-etched QCL with an InP upper cladding, W_{wg} = 5 μm and P = 20 W. The mesa is in the centre with the InP substrate below and helium gas above and in the moats.

In an attempt to provide better heatsinking in the epilayer-up configuration, the simulation was repeated, but this time the moat composition was changed from air (helium) to InP. This should allow improved lateral heat flow and will make a thermal connection between the InP upper cladding and the InP substrate. The thermal connection provides an 'overflow' for phonons which gather in the upper cladding, allowing them to diffuse down into the substrate and finally to the heatsink, rather than being trapped in the isolated upper cladding layer. This structure would be similar to a buried heterostructure (BH) QCL, such as that demonstrated very recently by Beck *et al.*.[7]

Referring to Table 48 and Figure 98 this alteration resulted in a large drop (~59 K) in the calculated temperature of the active waveguide core and in the temperature gradient across it. From the heat-flow diagram in Figure 100, we can see that there is indeed a greater flow into the InP upper cladding layer than before. The flow is not quite equal in both directions (upwards and downwards), but there is a great improvement.

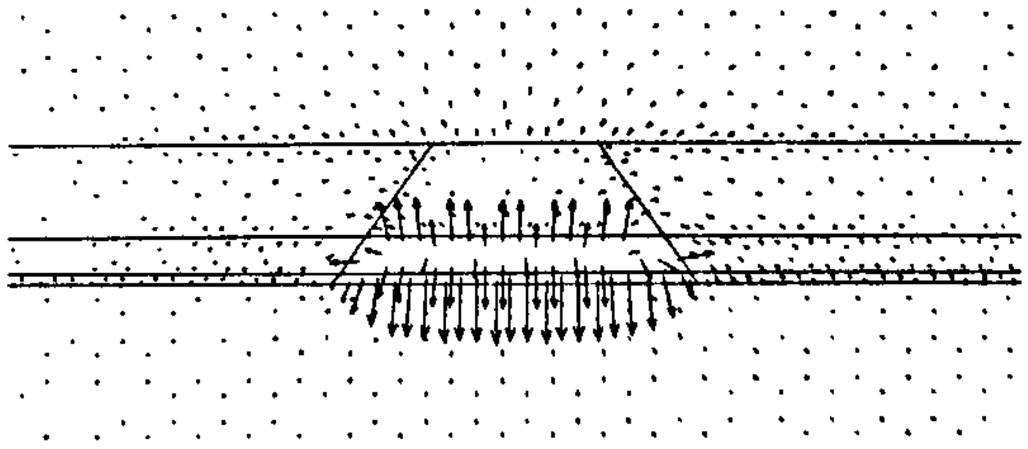

Figure 100 Calculated heat flow vectors for the case of the BH QCL mounted epilayer-up. It had InP upper cladding and moats, $W_{wg} = 5$ μm, and $P = 20$ W. The mesa is in the centre with the InP substrate below and helium gas above.

In the simulations in Section 5.3.3.2 of QCL mesa with a ternary upper cladding layer, a reasonable improvement came from the epilayer-down mounting. Since the thermal conductivity of InP is superior to that of $In_{0.52}Al_{0.48}As$, QCLs with an InP upper cladding layer should be in a better position to benefit from epilayer-down mounting. Both the InP-clad mesa-etched QCL and the InP-clad BH configurations were thermally modelled epilayer-down to determine what magnitude of enhancement could be expected.

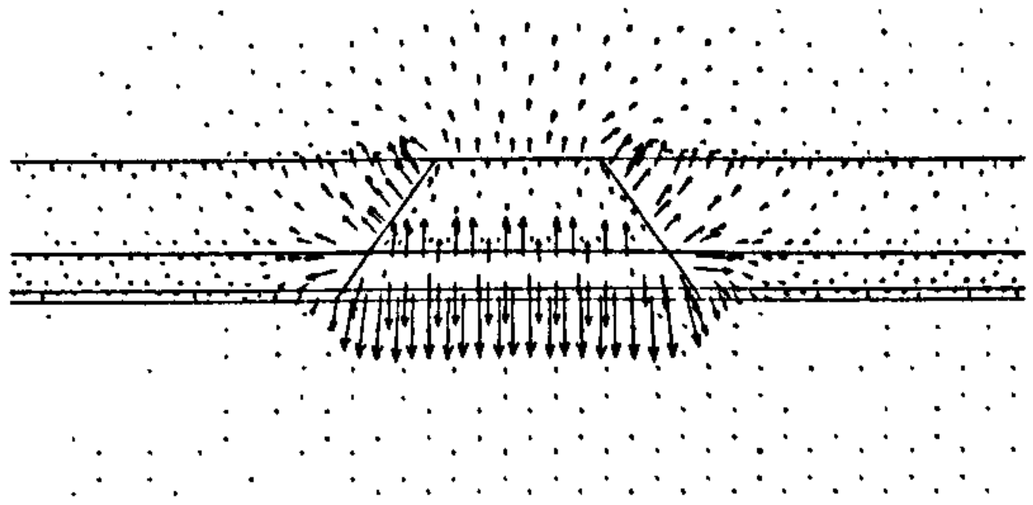

Figure 101 Calculated heat flow vectors for the epilayer-down mounted, mesa-etched QCL with an InP upper cladding, $W_{wg} = 5$ μm and $P = 20$ W. The mesa is in the centre with the InP substrate below, the indium bonding layer above, and helium gas in the moats.

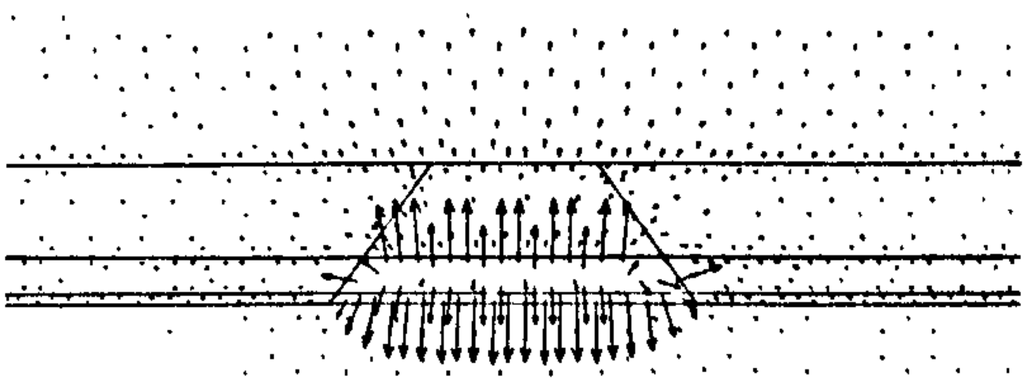

Figure 102 Calculated heat flow vectors for the epilayer-down mounted BH QCL with an InP upper cladding, $W_{wg} = 5$ μm and $P = 20$ W. The mesa is in the centre with the InP substrate below, the indium bonding layer above.

First of all, from the heat-flow diagram (Figure 101) for the mesa-etched QCL with an InP upper cladding we can see that the epilayer-down mounting permitted the upper cladding to extract heat from the active region. The heat flowing into the upper cladding could now escape almost directly to the heatsink so that the flow could be maintained in the steady state. Note however that even though the sample was mounted junction

down, the majority of the heat still flowed from the active waveguide core into the InP substrate. It was only in the case of the BH QCL mounted epilayer-down (see Figure 102) that the heat flow appeared to split evenly into the upper and lower cladding layers, maximising the dissipation of heat.

Although both of these epilayer-down mounted configurations showed a reduction in T_{peak}, the improvement for the mesa-etched (i.e. air moats) case was much more dramatic than for the BH; a drop in T_{peak} of 79 K for the mesa-etched versus 28 K for the BH QCL. Very interestingly, this meant that the epilayer-down mounted mesa-etched InP-clad QCL structure actually outperformed the epilayer-up mounted BH QCL structure by as much as 18 K. Further, mounting the BH QCL epilayer-down only reduced T_{peak} by a further 10K over the epilayer-down mounted mesa-etched counterpart. This is significant since BH fabrication is, in general, much more difficult (and expensive) than a simpler mesa-etched geometry. The extra effort to make a BH QCL might not be worth the meagre returns if epilayer-down mounting was used; this may be a case of diminishing returns.

However, it is also important to note that several of the assumptions made in the modelling (such as the omission of the dielectric layer for the mesa-etched structures, and the adverse effect of doping on the thermal conductivity of the semiconductor layers) may have lead to an underestimation of the temperature rise, and more so in the mesa-etched case. In that case the gap in performance between the two structures (mesa-etched and BH) would actually be larger than predicted and perhaps the BH QCL would be well worth the added effort and cost.

5.4 Summary

The modelling indicated that a large temperature increase of the active waveguide core would exist under CW (or quasi-CW) operation. The thermal resistance derived using the thermal modelling agreed very well with that calculated by Faist *et al.* from experimental data. The presence of a temperature gradient across the active waveguide core was also revealed, which was especially pronounced in devices mounted epilayer-up (except in the BH QCL structure). This is expected to be detrimental to the QC laser performance for the reasons already detailed in Section 5.1. The magnitude of the gradient was reduced by using epilayer-down mounting or a BH QC laser design, making these configurations favourable.

		Mesa-etched		PSWOX		Mesa array 3 × 5 μm		PSWOX array 3 × 5 μm	
		Epi-up	Epi-down	Epi-up	Epi-down	Epi-up	Epi-down	Epi-up	Epi-down
W_{wg} (μm)	P (W)	T_{peak} (K)	T_{peak} (K)	T_{peak} (K)	T_{peak} (K)	T_{peak} (K)	T_{peak} (K)	T_{peak} (K)	T_{peak} (K)
15	20	167	134	168	133	129	114	127	112
5	20	217	163	211	159				

Table 49 Comparison of peak temperatures calculated for each device configuration using an $In_{0.52}Al_{0.48}As$ upper cladding.

		Mesa-etched InP-clad		BH QCL InP-clad	
		Epi-up	Epi-down	Epi-up	Epi-down
W_{wg} (μm)	P (W)	T_{peak} (K)	T_{peak} (K)	T_{peak} (K)	T_{peak} (K)
5	20	215	136	154	126

Table 50 Values of the peak temperature in the active waveguide core for the four different configurations of QCL mesa employing an InP upper cladding.

It is important to limit localised heating to avoid the non-linear increases in temperature and threshold current density. Keeping the input power density constant, the magnitude of the heating decreased with the waveguide width, so that narrow mesas were found to be more appropriate for CW operation on a purely thermal basis. The modelling told us that it was advantageous to split a broad laser operating under power P_{total} into a number N_{mesa} of narrower spatially separated lasers each operating under power P_{total}/N_{mesa}. The narrower geometry of each component of the array allowed better heat dissipation and the spatial separation between them spread the generated heat across the chip, lowering localised heating. The optimum spacing between the devices of the array was found to be ~ 150 μm for a substrate thickness of 150 μm.

In terms of CW temperature elevation of mesa-etched QC lasers, the use of an InP upper cladding layer was shown to have no advantages over an $In_{0.52}Al_{0.48}As$ one unless the lasers were mounted epilayer-down, in keeping with experimental data by Faist et al..[1, 2] Mounting of an InP-clad mesa-etched QC laser epilayer-down led to a large drop in the calculated core temperature, and so should permit CW operation to higher heatsink temperatures. It even outperformed an epilayer-up mounted BH QC laser in these calculations, suggesting that a BH structure was not worth the effort unless it was also mounted epilayer-down. When mounted epilayer-down, the BH QC laser showed the lowest temperature elevation and gradient in the active waveguide core of all the single-mesa devices. Under the same power injection, the best performance of all modelled configurations came from the QC array lasers, with even the *epilayer-up* mounted array being comparable to the *epilayer-down* mounted BH QC laser.

Care must be taken here, however, since the modelling neglects the effects of doping on the thermal conductivity and the fact that the active waveguide core is actually a superlattice consisting of ~500 individual layers.

The values of thermal conductivities used were those reported for undoped layers; values for doped semiconductors may be significantly lower. The modelling was performed on what was effectively an undoped structure, whereas doping levels in a QC laser can be high and vary throughout the epilayer. Addition of doping atoms to the crystal lattice creates crystalline imperfections upon which phonons will scatter, decreasing the thermal conductivity. Towards room temperature, the dependence of the thermal conductivity on doping level is weak, since at high temperatures phonon-phonon scattering dominates. At low temperature, where phonon-phonon scattering is weak, the phonon-impurity scattering dominates, and the value of K drops with increasing doping levels. The values of temperature calculated by the modelling should therefore be more accurate towards room temperature and the temperatures calculated should always be an underestimate of the actual temperature.

As mentioned, the active region was a superlattice, but in the modelling it was assigned a thermal conductivity of bulk ternary material. This simplification ignored the reflection of heat at each InAlAs/InGaAs interface in the superlattice. In practice, we would expect this would make the effective thermal conductivity of the superlattice anisotropic; the value of K_y, the thermal conductivity perpendicular to the semiconductor layers, would be reduced with respect to K_x.

Both of the above phenomenon would lower the thermal conductivity in the vertical direction, making lateral heat flow more important. The discrepancy would be particularly noticeable when the devices are mounted epilayer-down, since the main flow of heat in that case would be through the upper cladding layers, which are quite highly doped, in fact. Such a discrepancy between laser temperature predicted by 2D non-linear finite element analysis and the temperature indicated by the performance of actual QCL devices mounted epilayer-down, was reported by Gmachl *et al.*[10] They believed that the difference was perhaps due to a combination of

the simplifications made, such as (3) and (5) listed previously in the assumptions/simplifications in Section 5.3.1.

Another interesting consequence of the increased importance of lateral heat flow would be that, the PSWOX QC laser would show a better temperature performance than that of the mesa-etched QC lasers, as they provide material adjacent to the mesa which may assist the lateral flow of heat. This may account for the improved temperature performance observed in practice (see Chapter 8).

To complement the thermal modelling, it would be productive to measure the temperature distribution of an operating QC laser, perhaps using techniques such as microRaman.[15]

5.5 References

[1] J. Faist, F. Capasso, C. Sirtori, D.L. Sivco, J.N. Baillargeon, A.L. Hutchinson, S.G. Chu, A. Y. Cho, 'High power mid-infrared (λ~5 μm) quantum cascade lasers operating above room temperature', *Appl. Phys. Lett.* **68** (26), 24 June 1996.

[2] J. Faist, A. Tredicucci, F. Capasso, C. Sirtori, D. L. Sivco, J. N. Baillargeon, A. L. Hutchison, A. Y. Cho, 'High-Power Continuous-Wave Quantum Cascade Lasers', *IEEE J. Quantum Electron.*, **34** (2) 336, February 1998.

[3] M. Razeghi, "Kinetics of quantum states in quantum cascade lasers: device design principles and fabrication", *Microelectronics Journal.* **30** 1019-1029, 1999.

[4] C. Gmachl, F. Capasso, J. Faist, A. L. Hutchinson, A. Tredicucci, D. L. Sivco, J. N. Baillargeon, S. G. Chu, A. Y. Cho, 'Continuous-wave and high-power pulsed operation of index-coupled distributed feedback quantum cascade laser at λ ≈ 8.5 μm', *Appl. Phys. Lett.* **72** (12), 23 March 1998.

[5] F. Capasso, C. Gmachl, A. L. Hutchinson, A. Tredicucci, J. Faist, D. L. Sivco, J. N. Baillargeon, A. Y. Cho 'High-performance, widely tuneable, single-mode, mid-infrared distributed feedback quantum cascade lasers', *CLEO'98*, CThD4, pp. 341-342, 1998.

[6] C. D. Farmer, P. T. Keightley, C. N. Ironside, C. R. Stanley, L. R. Wilson, J. W. Cockburn, 'A quantum cascade laser fabricated using planar native-oxide layers', *Appl. Phys. Lett.* **77** (1), 3 July 2000.

[7] M. Beck, J. Faist, A. Muller, U. Oesterle, M. Ilegems, E. Gini, H. Melchior, "High-Performance (λ ≈ 10.4 μm) buried heterostructure quantum cascade lasers", Conference on Lasers and Electro-Optics Europe - Technical Digest, p.265, 2000.

[8] H. C. Casey, Jr., M. B. Panish, *Heterostructure Lasers Part B: Materials and Operating Characteristics*, Academic Press Inc., New York, 1978.

[9] J. Gowar, *Optical Communication Systems,* Second Edition, p. 397, Prentice Hall International (UK) Ltd., 1993.

10 C. Gmachl, A. M. Sergent, A. Tredicucci, F. Capasso, A. L. Hutchinson, D. L. Sivco, J. N. Baillargeon, S. N. G. Chu and A. Y. Cho, "Improved CW operation of Quantum Cascade Lasers with Epitaxial side Heat Sinking", IEEE Photonics Tech. Letts. **11** (11), pp.1369-1371 (1999).

11 A. L. Edwards, 'For Computer Heat-Conduction Calculations A Compilation of Thermal Properties Data', UCRL-50589, February 1969.

[12] S. Adachi, *Physical Properties of III-V Semiconductor Compounds - InP, InAs, GaAs, GaP, InGaAs, and InGaAsP*, Wiley, New York, 1992.

[13] O. Madelung, Ed., *Semiconductors: Group IV Elements and III-V Compounds*, Springer-Verlag, Berlin Heidleberg, 1991.

[14] J. Faist, C. Sirtori, F. Capasso, D. L. Sivco, J. N. Baillargeon, A. L. Hutchinson, A. Y. Cho, "High-Power Long-Wavelength (λ ~11.5 μm) Quantum Cascade Lasers Operating Above Room Temperature", *IEEE Photon. Technol. Lett.*, **10** (8) 1100, August 1998.

15 W. C. Tang, H. J. Rosen, P. Vettiger and D. J. Webb, "Raman microprobe study of the time development of AlGaAs single quantum well laser facet temperature on route to catastrophic breakdown", *Appl. Phys. Letts.* **58** pp.557-559, 1991.

Chapter 6 Fabrication

One of the great advantages of QC lasers over the other mid-IR emitters, such as lead salt and Sb-based interband lasers, is that many of the standard fabrication processes used to make conventional semiconductor lasers can also be used to produce QC lasers. The reason for this is that, just like the vast majority of commercial interband laser diodes, the QC lasers are made using the same well-developed material systems i.e. they are InP- or GaAs-based. Owing to the very thin semiconductor layers required for the replication of QC active region and injector designs, the QC material must be grown by molecular beam epitaxy (MBE). MBE can grow atomically thin semiconductor layers of different composition with abrupt interfaces and is routinely used in the manufacture of a wide range of semiconductor devices.[1] Having said this, the QC laser does poses a challenge to the MBE growth as ~ 500 layers must be grown precisely, and the MBE machine (and grower!) must operate over a relatively long period to grow the thick epilayer required. A summary of the MBE wafers used in this work is discussed at the end of the next chapter in Section 8.8. This chapter is devoted to the fabrication procedures developed for all of the different kinds of devices produced, a general description of which follows. The detailed procedures are placed in Appendix B.

6.1 General fabrication issues

Having just pointed out the similarities between the fabrication of QC lasers and conventional interband lasers, we will now look at the few important differences. When designing the fabrication process for QC lasers one must take into consideration that they differ from conventional visible or near-infrared bipolar semiconductor lasers in a number of fundamental ways:

1. The QC laser is a unipolar device; all of the designs demonstrated thus far have been constructed entirely from a combination of *n*-type and undoped semiconductor layers.

2. In order to improve the optical confinement, the upper cladding layers are highly doped to enhance the contrast in the refractive index between them and the active waveguide core. Unfortunately, the low resistivity of the epilayer, along with its thickness means that strong lateral current spreading can take place if mesa-etching is not employed (see results in Chapter 8 or Ref. [^{2}], for example). Mesa etching is therefore usually used in order to obtain good electrical confinement. The PSWOX and shallow-etched waveguide geometries suffer from poor electrical confinement and hence higher threshold currents (again, see results in Chapter 8 or Ref. [2]).

3. The transverse dimensions of waveguide the modes are proportional to the effective wavelength ($\lambda=\lambda_0/n_{\text{eff}}$) of the light in the waveguide. The cross-section of the optical waveguide of a QC laser must therefore be relatively large in order to provide efficient optical confinement. Even with a plasma-enhanced waveguide, typical waveguide dimensions are height ≈ 4 μm and width ≈ 15 μm. This has knock on effects on photolithographical processes such the uniformity of resist coverage on spinning, resist exposure times, etc..

4. The dielectrics, silicon dioxide and silicon nitride, which are widely employed in the fabrication of conventional interband near-infrared lasers are so chosen for their high transparency in that spectral region as well as for their excellent electrical insulation properties and adhesion to semiconductors. However, they can possess strong absorption peaks in the mid- and far-IR spectral regions (see Section 3.7). Any overlap between an optical mode with a lossy dielectric-coated sidewall will lead to increased

waveguide losses, and a corresponding rise in J_{th} for that mode. Where practical, the dielectric material should be chosen to avoid these absorptions.

5. Whereas the operation voltages commonly needed in conventional interband lasers are only around 1-2 V, the voltages required in QC lasers are inherently much greater, around 6-10 V. The chosen dielectric and its thickness should be such that the maximum electric field it will experience under operation (including any transients on the current pulse) should be less than its dielectric strength (the electric field intensity at which the dielectric breaks down and becomes conductive). Otherwise, the electrical insulation layer will break down and a short circuit may form.

6. QC lasers operate under high currents as well as high voltages i.e. they consume a high electrical power. Much of this power is converted into heat in the active region which degrades the performance of the laser and limits CW operation to cryogenic temperatures (see Section 2.3.4 and Chapter 5). In order to reduce heating of the active region, the thermal resistance between it and the heatsink should be minimised.

With these points in mind, fabrication procedures were developed by the author specifically for the QC lasers.

6.2 Mesa-etched and Rib-mesa lasers

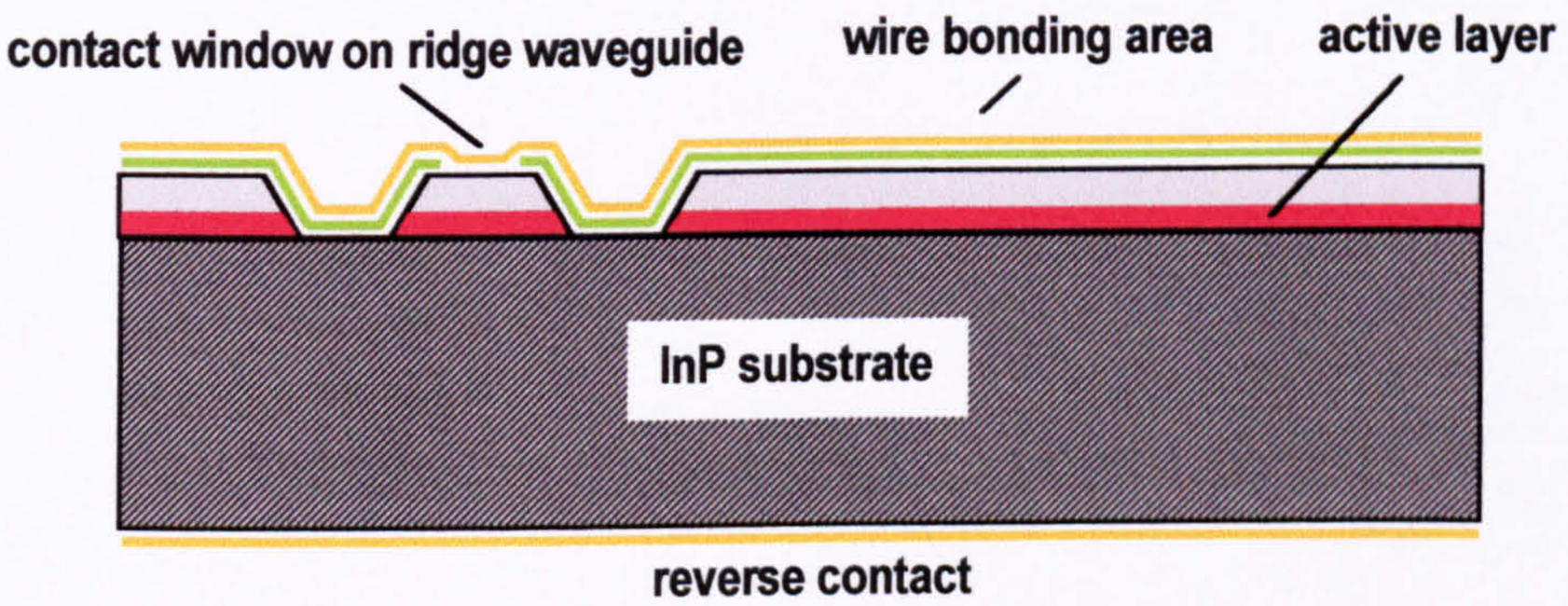

Figure 103 Schematic drawing of the mesa-etched QCL. The green layer represents the insulator, the gold layers represent the metal contact layers, and the red layer represents the active waveguide core sandwiched between the upper ($In_{0.52}Al_{0.48}As$) and lower (InP substrate) cladding layers.

The first stage in the fabrication of the QC lasers was to form the optical/electrical waveguide by photolithographical and wet etching steps. Parameters such as the waveguide height, width, and spacing were defined by these steps. The ridge height was determined by the vertical etch rate, etch time and the selectivity of etch to different layers. The ridge width was determined by the mask dimensions, and the horizontal etch rate (undercut) and sidewall profile. It was ensured that the waveguide pattern was parallel to the edge of the sample to permit the formation of mirrors normal to the laser cavity. These would be formed towards the end of the processing through cleaving. A crystallographic etch was used (H_3PO_4:H_2O_2:H_2O, 1:8:1), so that this edge had to be the appropriate crystal plane in order to produce the desired sidewall profile (undercut or overhang).

Since the waveguides were only 10 to 20 μm in width, it was not practical to wire bond directly to them and hence a broad contact area was incorporated in the design. The individual waveguides were spaced by D_{array} =

500 μm, which was chosen to facilitate cleaving into single laser bars and to provide sufficient room for the wire bonds.

Electrical current was only to be injected in through the cap layer of the waveguide and so a dielectric layer was needed elsewhere to provide electrical insulation between the semiconductor and metal contact layer. The operational voltages required in QC lasers are around 6-10 V and as QCLs are often driven with short (~50 ns) pulses, supply voltage overshoots should also be taken into consideration in the voltage rating. Since the dielectric strength of silica is ~30×10^6 Vm^{-1},[1,3] at least 400 nm of silica should be used, which can, in theory, support a maximum of 12V.

After the deposition of the dielectric layer, a contact window was opened through the insulation layer on the top of the waveguide by a photolithographical and dry etch step. Deposition of metals made an electrical connection to the top of each ridge waveguide through the window in the silica layer, and provided a broad, flat region adjacent to each waveguide to which wire bonds were eventually attached. Discussion of the metal contact layers used, the laser cleaving, mounting and electrical connections follow after a quick overview of the PSWOX QCL fabrication.

6.3 PSWOX lasers

In general, the fabrication of the PSWOX lasers was quite simple and involved the following stages:

1. Deposition, and then patterning of silica mask by one photolithographical sequence and two short wet etch steps.

2. Planar selective thermal wet oxidation (PSWOX).

   Planar selective thermal wet oxidation was used to convert (or partially convert) the exposed areas of $In_{0.52}Al_{0.48}As$ into an electrically insulating low refractive index native-oxide. By forming two 10 μm or 60 μm-wide stripes of native-oxide, say 20μm apart, a 20 μm-wide laser stripe could be formed with both optical and electrical confinement.

3. Formation of contact window through silica mask on the waveguide by one photolithographical sequence and one dry wet etch step. The planar geometry was advantageous as more uniform layers of photoresist were obtained. This made the photolithographical stage involved in the formation of the contact window both easier and more reliable than in the case of the mesa-etched lasers.

   One problem that was encountered after a thermal wet oxidation run was that the silica in close proximity to the native oxide stripes was found to be much more resistant to dry etching than usual (and virtually impervious to wet etching). It was postulated that this might have been due to diffusion of In or As species out of the native oxide and into the silica during the thermal wet oxidation. Inspection under an optical microscope showed that the silica close to the native oxide stripes had changed in colour slightly, perhaps indicating a change in refractive index due to such contaminants. Under the standard conditions used with our dry etch machine (C_2F_6 plasma), 200 nm of PECVD SiO_2 would normally have been removed within 6 minutes. In contrast, it was found that ~ 14 minutes was necessary to open the contact window on the PSWOX devices. Note that only the SiO_2 in close proximity (~ 10μm) to the regions of native oxide had exhibited an increased resistance to etching; the SiO_2 elsewhere on the same sample etched as normal.

4. Evaporation of the upper metal contact layer was followed by thinning of the InP substrate and then deposition of the lower metal contact layer onto the polished substrate. Finally, cleaving, mounting and wire bonding were performed.

6.4 Choice of metal contact layers

Being a unipolar device, the QC laser has only n-type semiconductor contact layers. The InP substrate is n-type doped $1x10^{18}$ cm^{-3} and the final epilayer is a very heavily n-type doped $2x10^{19}$ cm^{-3} $In_{0.53}Ga_{0.47}As$ contact layer. It would follow then that both the upper (epilayer) and reverse (substrate) metal contacts employed should be those designed for n-type semiconductors in order to provide low resistance, ohmic contacts. However, this was not the case for reasons, which are outlined below.

Since ultrasonic wire bonding was used to access individual devices, it was essential that the metal contact adhered strongly to the dielectric layer. On the contrary, it was discovered that the adhesion of the n-type contact (Au/Ge/Au/Ni/Au) to the dielectric was very poor and it often detached during the wire bonding process. In contrast, the Ti/Pd/Au contact was found to have much better adhesion, and so was preferable. Alloying of these contacts is common practise in order to lower the contact resistance. This was inadvisable in the case of QC lasers as the semiconductor layers adjacent to the upper contact play a vital role in preventing coupling of the optical mode to the lossy surface-plasmon mode present at the semiconductor/metal interface.[4] Alloying would alter the surface-plasmon mode, and perhaps increase the losses associated with it.

If the semiconductor surface is very heavily doped, a nominally rectifying metal-semiconductor junction can become an ohmic contact. This is because the depletion region is made so thin that the electrons can tunnel through the barrier rather than requiring the energy to surmount it.[5, 6] Since our cap layer was very heavily doped, a nonalloyed Ti/Pd/Au contact could be used. A series of transmission line measurements (TLM) were performed to compare the contact resistance of p-type and n-type contacts on a heavily doped (2×10^{19} cm^{-3}) $In_{0.53}Ga_{0.47}As$ layer.

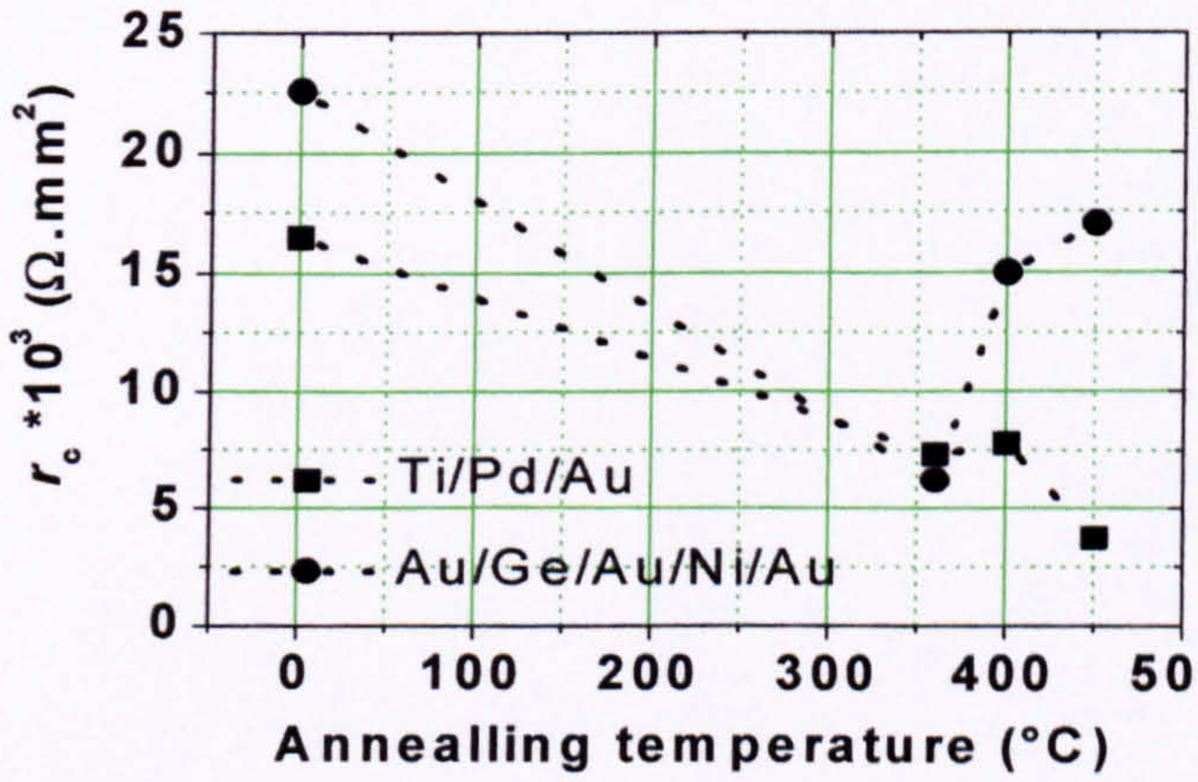

Figure 104 Contact resistance of the p-type and n-type metal contacts on n-type doped 2×10^{19} cm^{-3} InGaAs for various annealing temperatures.

A highly n-type (Si) doped 2×10^{19} cm^{-3} InGaAs sample was patterned with a transmission line measurement (TLM) pattern by a lift-off technique and standard p-type (Ti/Pd/Au) and n-type (Au/Ge/Au/Ni/Au) were evaporated. After lift-off the samples were annealed using a rapid thermal annealer for 60 seconds at

temperatures of either 360, 400 and 450 °C and then four-probe TLMs were performed on each sample using the an HP semiconductor parameter analyser.

The contact resistances were extracted from the TLM data and are shown graphically in Figure 104. Before annealing, the specific contact resistance of the n-contact ($r_c = 2.3\times10^{-4}$ Ωcm^2) was actually slightly higher than that of the p-contact ($r_c = 1.7\times10^{-4}$ Ωcm^2). Annealing the contacts at 360 °C led to a decrease in the contact resistance for both contacts, so that after annealing they both had practically the same resistance ($r_c = 7\times10^{-5}$ Ω cm^2 for the p-contact and $r_c = 6\times10^{-5}$ Ω cm^2 for the n-contact).

The TLM measurements therefore confirmed that, in the case of a QCL with a very heavily doped n-type semiconductor layer, a p-type metal contact could be used instead of an n-type one for the upper contact layer. In fact, for non-alloyed contacts the Ti/Pd/Au contact had lower specific contact resistance. Further, alloying only reduced r_c by a factor of ~2 so that there was not a huge penalty for using non-alloyed contacts in this case. The Ti/Pd/Au was therefore adopted as the standard upper contact for the QC laser for its good adhesion and lower contact resistance.

It is noted, however, that a value of $r_c = 1.7\times10^{-4}$ Ωcm^2 is quite high and will lead to large series resistance in the device. For a typical $A = 2\text{mm} \times 3\mu\text{m}$ contact area, the resistance would be $R = r_c/A = 2.8$ Ω. Considering the high operational current, this will lead to a significant heating in the device.

6.5 Laser cleaving, mounting and electrical connections

The sample would now be ready to be cleaved up into individual lasers. In this stage, the laser cavity mirrors were formed and the length of the laser cavity was defined. The final fabrication stage is to mount the laser bar onto a metal heatsink. This forms an electrical, thermal and mechanical bond to the laser diode. The heatsink is made of copper due to its excellent electrical and thermal conductivity (K ≈ 400 Wm^{-1}K^{-1} for pure copper)[7]. Ideally, for maximum heat dissipation, the substrate or epilayer of the laser would be in direct contact with the copper and both surfaces would be completely flat to maximise the contact area. However, the surfaces are far from being perfectly flat and intermediate bonding layers are required in order to improve the contact area, and to form a mechanical bond that must also be electrically and thermally conductive. Unless the bonding material has a better thermal conductivity than copper, its thickness should be low in order to minimise the additional thermal resistance from diode to the copper. Indium has been found to work well for this purpose as it has a fairly good thermal (~23 Wm^{-1}K^{-1}) and electrical conductivity, a low melting point (~157°C), and is very ductile.[7] The ductility is an especially important property of indium for cryogenic temperature laser operation as it can accommodate the strain at the solder joint arising from the different coefficients of thermal expansion of the metal and semiconductor.[8]

As smooth a surface as possible was obtained on the copper mount by using mechanical polishing, finishing with 3 μm aluminium oxide polishing grit. The mounts were cleaned thoroughly with Opticlear, Acetone, Methanol, IPA, and deoxidised in a hot N_2/H_2 atmosphere before the ~200 nm of gold was sputtered onto the polished copper surface. The de-oxidation stage was carried out immediately before gold deposition. The gold coating helped prevent surface oxidation and greatly improved the wetting of the indium to the heatsink surface. The indium bond was formed between the gold layer on the heatsink and the gold contact layer of the laser diode. Soldering flux was used during the bonding process to deoxidise and clean the gold and indium surfaces to further facilitate wetting.

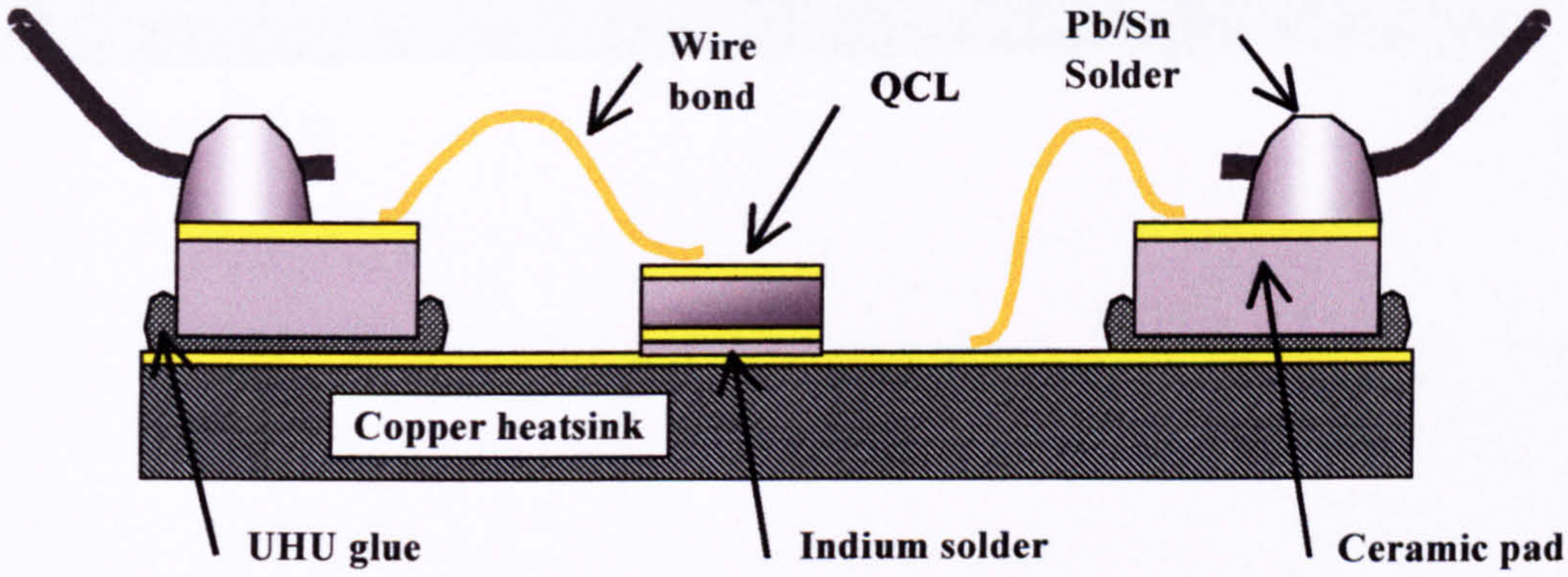

Figure 105 Illustration of a QC laser mounted using the procedures describe in the text.

Next, positive and negative electrical connections were made to the diode. In general for QC lasers, the epilayer should be made negative w.r.t. the substrate (but this depends upon the order in which the epitaxial layers are grown). Any connection to the metal heatsink provided an electrical connection to the underside of the laser bar. Ceramic pads with a thick gold coating on the upper surface were bonded to the gold heatsink using UHU glue. They served as electrically conductive platforms, electrically isolated from the heatsink. UHU glue was used as it remained flexible after curing, preventing detachment at cryogenic temperatures which can occur due to differences in thermal coefficient of expansion for the ceramic, glue, and copper heatsink. The glue was also soluble in acetone, so that it could be thinned down for easier application, and removed at a later date to recycle the mount. Ultrasonic gold-wire bonding was performed to make a connection from the contact layer on top of the laser bar to a ceramic pad. The ceramic pad provided an interface between the thin gold wires from the diode to the thick wires from outside world.

6.6 Summary

The procedures used to fabricate the different QC lasers used in this work have been detailed. This will allow quick replication of the work if so required. Fortunately, there is no great difficulty in fabricating the QC lasers in this work, and they could be processed much like any other semiconductor laser, as long as a few basic practical considerations are kept in mind, such as the high voltages dropped across the insulation layer.

The only major concern was the potentially high contact resistance, which could degrade performance, especially in CW mode. Care should be exercised not to damage the semiconductor contact layer before deposition of the metal contact.

Future developments could address the contact resistance issues and improve the heatsink design to make it more reliable and effective.

6.7 References

[1] A. Y. Cho, "Advances in molecular beam epitaxy (MBE)", *J. Crystal Growth*, **111** 1, 1991.

[2] C. Gmachl, F. Capasso, J. Faist, A.L. Hutchinson, A. Tredicucci, D.L. Sivco, J.N. Baillargeon, S.G. Chu, A.Y.Cho, 'Continuous-wave and high-power pulsed operation of index-coupled distributed feedback quantum cascade laser at $\lambda \approx 8.5$ μm', *Appl. Phys. Lett.* **72** (12), 23 March 1998.

[3] D. K. Cheng., *Field and Wave Electromagnetics*, Second Edition, Addison-Wesley Publishing Company, Inc, Reading, 1989.

[4] C. Sirtori, J. Faist, F. Capasso, D. L. Sivco, A. L. Hutchinson, A. Y. Cho, 'Quantum cascade laser with plasmon-enhanced waveguide operating at 8.4 μm wavelength', *Appl. Phys. Lett.* **66** (24), 12 June 1995.

[5]G. Stareev, H. Kunzel "Tunneling behaviour of extremely low resistance nonalloyed Ti/Pt/Au contacts to n(p)-In0.53Ga0.47As and n-InAs/InGaAs", *J. Appl, Phys.*, **74** (12), pp. 7592-7595, 15 Dec. 1993.

[6]G. Stareev, H. Kunzel, G. Dortmann "A controllable mechanism of forming extremely low-resistance nonalloyed ohmic contacts to III-V compound semiconductors", *J. Appl, Phys.*, **74** (12), pp. 7344-7356, 15 Dec. 1993.

[7] A. L. Edwards, 'For Computer Heat-Conduction Calculations A Compilation of Thermal Properties Data', UCRL-50589, February 1969.

[8] H. H. Manko, *Solders and Soldering*, Third Edition, McGraw-Hill, Inc., New York, 1992.

Chapter 7 Characterisation

Characterisation of the fabricated lasers was essential in order to have feedback on the quality of the MBE growth and the fabrication procedures used, and on the relative performance of the waveguide designs. This chapter discusses how the characterisation of the QC lasers was performed through a collaboration with the Department of Physics and Astronomy at the University of Sheffield. The collaboration is briefly discussed before outlining the techniques and the equipment used to characterise the QC lasers. In some cases, the equipment adversely affected the results and so an understanding of the set-up was necessary in order to interpret some of the data. Difficulties with the calibrations and their influence on the work are also discussed.

7.1 Overview

A prerequisite for entry into the field of QC laser development is access to an optical characterisation system including:

- a cryostat with a mid-IR transparent window for optical access and co-axial cable feedthroughs for electrical access to the laser diode,
- a pulsed laser diode driver capable of producing short current pulses (<100 ns) of large amplitude (greater than several amperes) into 50 ohms,
- a lock-in amplifier or boxcar averager,
- mid-IR optics (e.g. gold-coated parabolic mirrors, or calcium fluoride or zinc selenide lenses),
- mid-IR detector (e.g. HgCdTe, thermopile, or quantum-well infrared photodetector (QWIP)),
- and a mid-IR spectrometer. Ideally, the mid-IR spectrometer should be a step-scan Fourier transform infrared spectrometer which can produce reasonably high-resolution spectra (easily down to 0.01 cm^{-1}) of mid-IR light sources which are emitting low average powers.

The existing laser diode characterisation systems which were available in-house were designed for room-temperature operation of visible and near-infrared laser diodes, and as such were not appropriate for this work. The high cost of the characterisation system needed necessitated the application for outside funding. Unfortunately, the attempts in the 1st and 2nd years of this PhD to secure support from the EPSRC New Generation Laser Diode (NGLD) initiative were both unsuccessful. Consequently, the development of QC lasers and achievement of the original project objectives (including gas sensing) were adversely affected. Funding was finally secured in the final 10 months of the PhD allowing a characterisation system to be designed constructed by the author. Proper measurements using this new system could not be performed within the timescale of the PhD and so the system constructed is not discussed.

The circumstances of the PhD therefore dictated that measurements needed to be carried out in collaboration with Dr. John Cockburn's Quantum Cascade Laser Group in the Department of Physics and Astronomy at the University of Sheffield. From 1991-1996 their group had developed considerable expertise in techniques such as PL, EL and step-scan lock-in FTIR spectroscopy to provide quantitative information in vertical transport in semiconductor tunnelling structures. They began developing QC lasers in the GaAs/AlGaAs material system in 1996. An informal collaboration with Dr. Cockburn's group began in September 1997 (the beginning of the 2nd year of this work) when they very kindly agreed to optically characterise our QC LED

structures. Although QC LEDs had been fabricated within the first 6 months, all efforts to detect the weak QC emission in-house had been unsuccessful, simply down to a lack of appropriate equipment. When the same devices were sent to Dr. Cockburn's group, QC electroluminescence was rapidly confirmed. A QC laser followed close behind in Feb 1998, which constituted the very first lasing QC structure produced in the UK.

Until the closing phases of the PhD, the collaboration with Dr. Cockburn's group was informal. Consequently, the author of this work had little control over the measurements. Although our collaborators possessed considerable expertise in the measurement of intersubband PL and EL, there was an inevitable learning curve in the crossover between the measurement of weak, multidirectional spontaneous emission and QC laser diode characterisation. This meant that there was a gradual evolution of characterisation set-up over time, involving changes in equipment and power calibrations. Obviously, it would have been ideal for all devices to have been measured under identical conditions and to have had a set program of characterisation e.g. every device had an IV, LI, and spectral measurement. However, this was not the case under the circumstances of the PhD. It is acknowledged, therefore, that the measurements were not comprehensive. Despite this, the measurements played a critical role in determining the source of the problems in our QC lasers.

Until close to the end of the work, the main measurements performed were pulsed-mode light-current (LI) curves and spectral analysis of laser emission. Current-voltage curves (IV) were available, but only using CW currents up to $I \approx 0.7$ A at $T = 77$ K. Towards the end of the practical work simultaneous pulsed LI and IV up to ~ 6A were developed by our collaborators which revealed valuable information on the performance of our devices. The ability to perform far-field profiles was also developed by our collaborators at the very end of the PhD, and the few results obtained served a vital role in confirming the cause of the anomalous LI curves which will be presented in the following chapter.

7.2 Description of characterisation system

Figure 106 illustrates the measurement system which was used to characterise the QC lasers at the University of Sheffield. The system may be categorised into five sub-systems:

- the cryogenic system,
- the laser diode supply and monitoring electronics,
- the optical collection and processing,
- the optical signal detection and processing electronics,
- and the computer controlled data acquisition, data processing, and instrument control via GPIB (general purpose interface bus).

The entire system served two purposes, namely computer-controlled light-current curve acquisition, and computer-controlled spectral analysis. Both measurements could be carried out at controlled heatsink temperatures ranging between 10-300 K, with QCL diode supply currents of 0-7 A, 50-100 ns pulses duration and 0-5 kHz repetition rates. Unless otherwise stated the measurements were performed using 50-100 ns pulses at a repetition rate of 5 kHz.

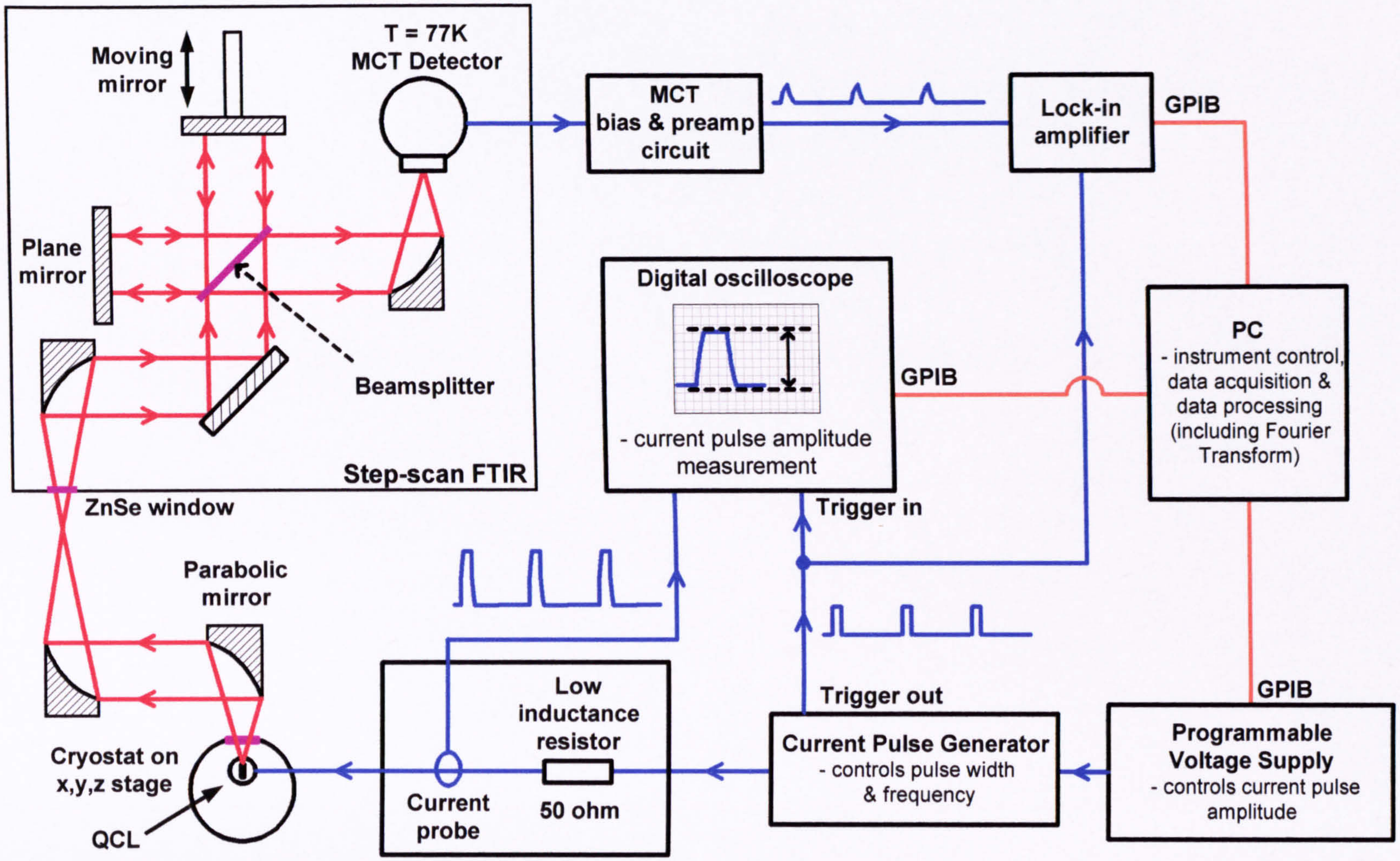

Figure 106 Schematic drawing of the characterisation set-up at the University of Sheffield.

7.2.1 Cryogenic system

Control of the laser diode heatsink temperature was performed by placing the heatsink-mounted QCL on the cold head of an Oxford Instruments closed-cycle helium-flow CCC1104 vacuum loading cryostat. The heatsink temperature was controlled manually by using the accompanying cryostat temperature controller, which measured the temperature of the cold head using a calibrated rhodium-iron thermocouple. Coaxial cable feedthroughs and ZnSe windows provided electrical and optical access to the sample space.

7.2.2 Laser diode supply and monitoring electronics

An Avtech AVL-2-C-EA-PN voltage pulse generator was used which was capable of supplying V = 0-350 V pulses into 50 ohms (therefore I = 0 to 7 A), with pulses duration of 50-100 ns, rise times of 2 ns and repetition rates of 0-5 kHz. The pulse generator also had a 0-10 V input for zero - full-scale control of the output pulse amplitude. This input was connected to the output of an external programmable voltage supply, which was itself controlled remotely by a PC via GPIB.

The Avtech voltage pulse generator was configured to emulate a constant-current source by placing a 50 ohm resistor in series with the QCL. The resistance of the QC laser diode above threshold was ~ 1 ohm, so that current was limited mainly by the 50 ohm series resistor. This resistor also provided the necessary load impedance to roughly match to the output impedance of the pulse generator. The actual resistor used was a Meggitt CGS high-power thick-film, low inductance resistor, chosen so as to minimise inductive kicks which would be obtained if a standard wire-wound resistor had been used. Coaxial cable feedthroughs were installed on the cryostat and 50 ohm coaxial cable was used wherever possible to carry the current pulses to the QCL, including inside the cryostat. All connections were kept as short as was practically possible.

The magnitude of the current pulses produced were measured using a calibrated, broadband current probe (711S current probe, American Laser Systems, Inc.) in conjunction with a computer-controlled (via GPIB) digital oscilloscope.

7.2.3 Optical collection and processing

The discussion of the optical system begins with the positioning of QCL within the cryostat. For the most part QCLs had to be mounted onto TO-5 headers (CIE P/N 4ML012 version A from Kemtron International Ltd.) in order to be compatible with the system in use by our collaborators. Having worked primarily in the field of spontaneous intersubband emission, these mounts had been adopted by them since they were suitable for that application, were readily available commercially, and because mounting devices on them was quick and reliable. Although they were extensively used throughout this work for the reasons above, they were not so appropriate for edge-emitting laser diodes, as will be explained below.

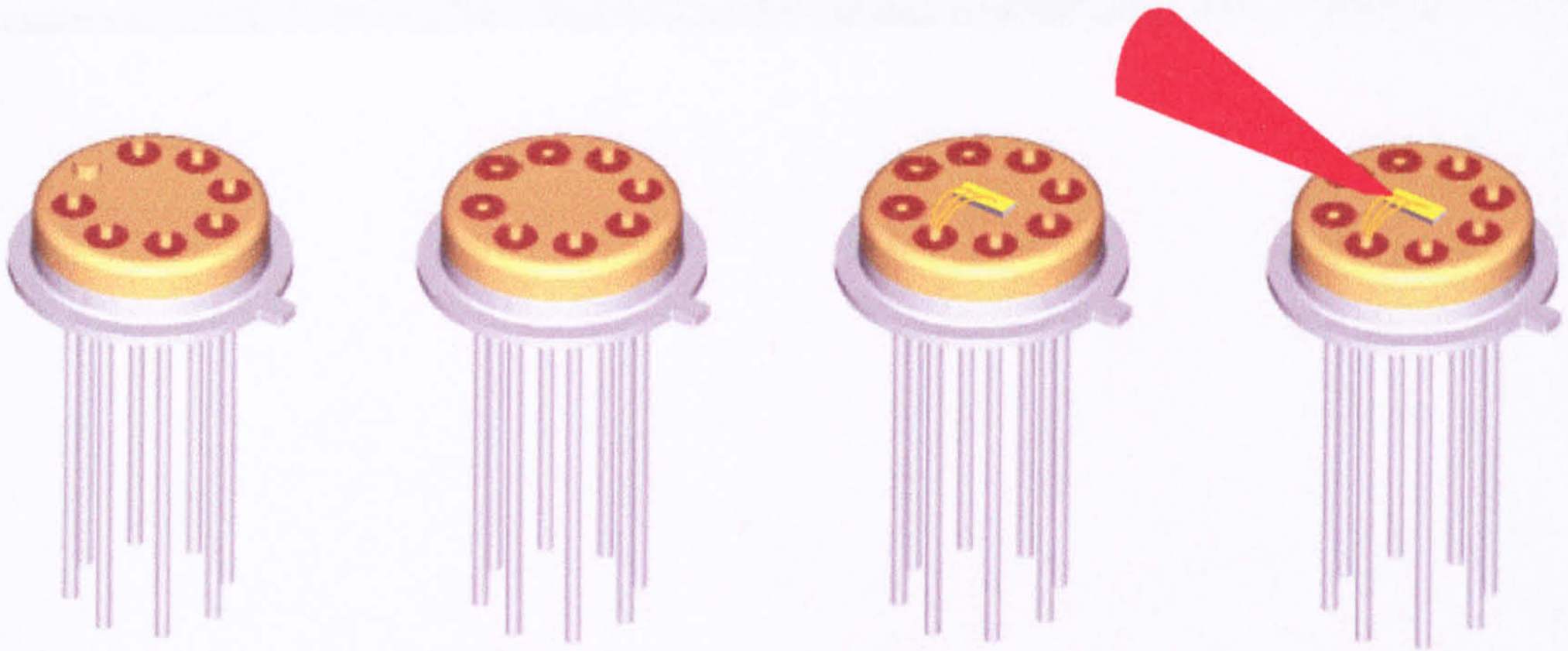

Figure 107 Illustration of the use of a TO-5 header as a QCL mount. Shown is (a) a TO-5 similar to the ones used, (b) the same header after filing down the heads of the pins in front of the facet, (c) the header with a QCL mounted and wire bonded, and (d) the direction of emission from the mounted QCL (emission from rear facet not shown). The metal tab on the rim of the TO-5 can be used for alignment purposes.

An illustration of a TO-5 header similar to the ones used is shown in Figure 107. As depicted in Figure 108, these mounts were undesirable on an optical basis. As with many conventional semiconductor lasers, the beam divergence in the plane normal to the epitaxial layers is large in QC lasers (roughly ± 35 degrees). To avoid obstruction/reflection of the output beam, the laser must be located close to the edge of the mount. This was not the case when employing the TO-5 headers.

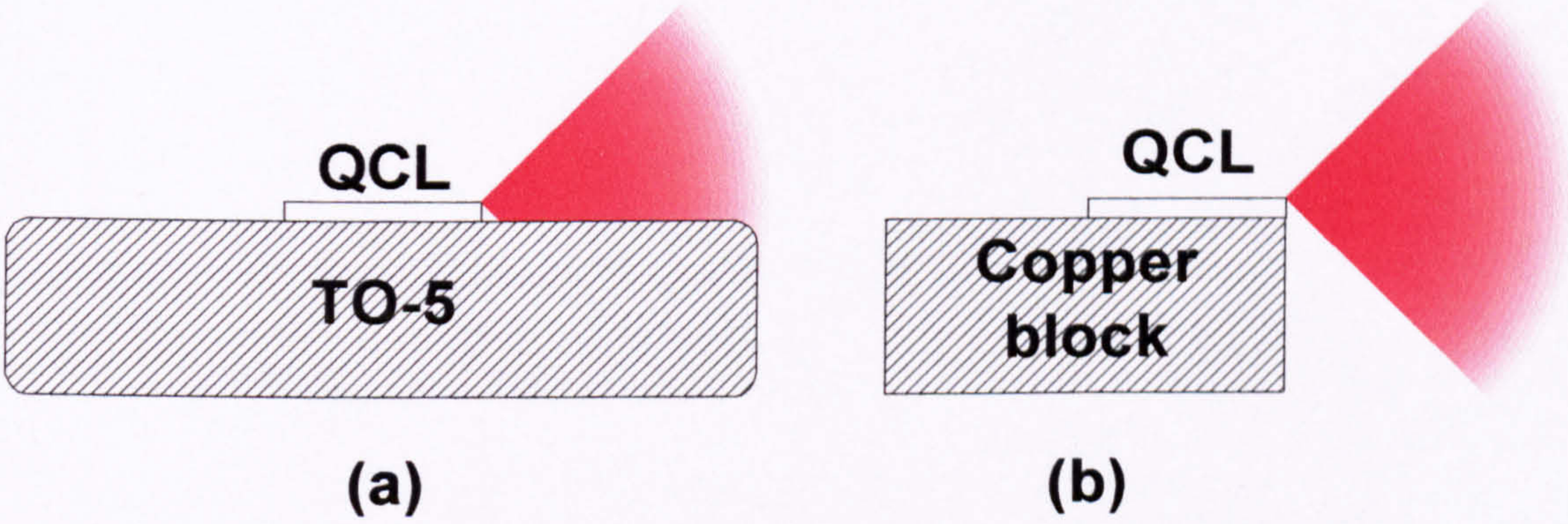

Figure 108 Schematic drawing of (a) the obstruction of the laser output beam (red) when mounted on a TO-5 header, and (b) the unobstructed beam when mounted in the more generally accepted mounting position for an edge-emitting laser diode.

Although far superior optically, the use of the copper blocks for edge-mounting did have its disadvantages. A commercial supplier was not located, and the mounts had therefore to be manufactured in-house. The polished copper mounts took quite some time to produce and varied in surface quality. Once polished they required cleaning, deoxidising and gold-coating to prevent oxidation of the copper surface and provide a surface to which indium would easily wet. Unlike the TO-5 headers, there were no in-built means of making an isolated (from the copper mount) electrical connection to the upper laser contact, and so gold-plated ceramic bonding pads had to be used. These too were made in-house by evaporating gold onto a large

ceramic sheet, before dicing it into many tiny pads. The quality and adhesion of the gold to the ceramic varied greatly, and became the source of many reliability problems. Another reliability problem came in the securing of the ceramic pads to the copper mounts. A general-purpose glue manufactured by UHU was finally found to be the most reliable, but pads still detached from time to time after cryogenic cycling.

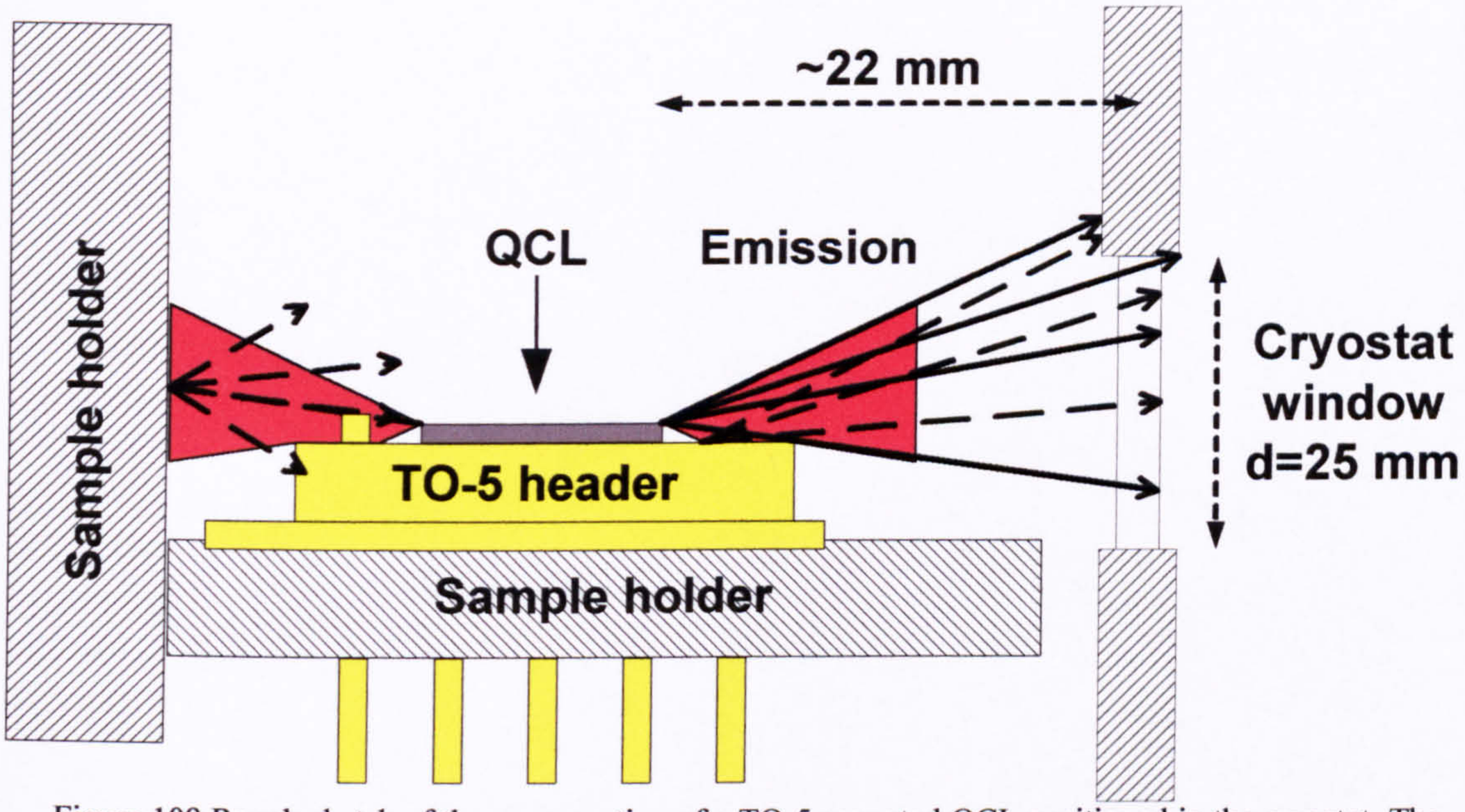

Figure 109 Rough sketch of the cross-section of a TO-5-mounted QCL positioned in the cryostat. The diagram is not to scale. Examples of direct (as opposed to scattered/reflected) rays are shown as solid arrows. Examples of scattered/reflected rays of light are drawn as arrows with long-dotted lines.

Next, we expand our view of the optical system to the cryostat sample space with the TO-5 header mounted inside, as illustrated in Figure 109. When interpreting the optical measurement results we should keep in mind the following complications that were introduced by this set-up:

1. The TO-5 header will have obstructed light emitted from the forward-facing facet, chopping off part of the beam. Only the upper half of the elliptical beam will have travelled unobstructed towards the cryostat window.

2. The light which was obstructed by the TO-5 header will have been reflected and scattered off the rough TO-5 header surface. Some of the reflected/scattered light will have mixed with the unobstructed beam, corrupting far-field pattern of the unobstructed beam.

3. Light emitted from the rear-facing facet may also have reflected/scattered off of the metal sample holder at the rear of the device, then travelled forwards and out of the cryostat window corrupting the far-field originating from of the forward-facing facet.

4. Reflection, refraction, and some absorption of the light will have occurred at the ZnSe cryostat window (not depicted in Figure 109), so that a percentage of the light will not be transmitted through the window.

5. Lastly, the limited diameter of the cryostat window restricted the cone of light accessible. Scattered and direct light will have been obstructed if it was incident beyond the area of the cryostat window. Given a cryostat window diameter of 25 mm and a distance of 22 mm between it and the laser facet, only the light emitted within cone of $\pm$ 29.6 degrees was able to exit the cryostat and be measured.

The remainder of the optical system, comprising of the gold-coated parabolic collection mirrors and a step-scan Fourier transform infrared (FTIR) spectrometer with a mercury cadmium telluride (MCT) detector, is

shown schematically in Figure 106. The cryostat was suspended on a x, y, z positioning stage so that the QCL facet could be positioned at the focal point of the first parabolic mirror (facing cryostat window). This mirror (focal length $f = 69$ mm, diameter $d = 40$ mm, so it was an $f/1.7$ optic) only collected and collimated light within a cone of acceptance of ± 16 degrees. The light was then directed by a second parabolic mirror into the step-scan FTIR.

Inside the FTIR the light passed through a Michelson interferometer with one fixed and one moving mirror, before being focused onto a liquid nitrogen-cooled mercury cadmium telluride (MCT) detector. The FTIR may be operated in one of two modes; linear-scanning or step-scanning. In the linear-scanning (also known as rapid-scanning) mode, one full spectral scan is performed by sweeping the unfixed mirror by a predetermined distance (related to the resolution of the spectra) in one single motion. The time-evolution of the electrical signal from the detector, called an interferogram, is sampled and sent to a computer where it is recorded and stored in the memory. Once the scan is complete, the computer software uses an algorithm to calculate the Fourier transform of the interferogram which reveals the spectral content light source. A number of scans can be made and the data averaged (spectra coaddition) to improve the signal to noise level.

To investigate optical signals of very low intensity, or low average powers such as QC lasers, step-scanning mode is more appropriate. In this mode, the unfixed mirror is moved in equal steps. At each step the mirror is stopped and held very still while averaging of the signal is performed using a lock-in or boxcar amplifier referenced to the QCL current pulse repetition frequency. Not only does this improve the S/N ratio, but it also means that the interferogram will only contain spectral information at the modulated frequency; the background spectral content is ignored. Step-scan lock-in FTIR spectroscopy was the technique used for the measurements in this work. For a review of the characterisation of QC lasers using step-scan FTIR spectroscopy the reader is referred to Ref. [1].

7.3 Light-current curves and calibrations

Calibrated measurements of the current and voltage pulse magnitudes, and the emitted optical power were performed by our collaborators. The current was measured using a calibrated current probe which was a reliable means of making the measurement. However, our collaborators experienced a problem with the current calibration which went undetected for a long period. The problem led to the measured current being approximately 37 % lower than it really was. The measurements have since been adjusted by this factor to compensate. In this way, the results presented are still valid, but the incorrect data did have an adverse effect on our efforts to understand the relatively poor performance of our lasers.

A fixed collection efficiency of 15% was assumed, and the collected light was attenuated when necessary to avoid saturation effects on the MCT detector. Independent checks on the system calibration by another quantum cascade laser group agreed with the laser power calibration to within 16% for the device tested. However, in assuming a fixed collection efficiency this calibration also assumed that all devices measured had identical output beam profiles, and that these beam profiles did not change significantly with drive current. In contrast, the results of the far-field profile calculations in Chapter 4 and the far-field profile measurements presented in Chapter 8 indicate that neither of these assumptions were strictly valid. Where optical powers are given, they should only be regarded as being approximate.

The sensitivity of the collection efficiency to changes in output beam divergence was heightened by the relatively high *f*-number (with respect to the divergence of the higher order transverse waveguide modes) collection mirror used (*f*/1.7 ≡ ± 16 degrees). Given a collection optic with a much lower *f*-number, such as the *f*/0.8 (± 32 degrees) optics used by other QC groups,[2] the sensitivity should reduce. More of the light from higher order transverse modes would be within the cone of collection and differences from device to device could be better accommodated. Our collaborators recently indicated that using a *f*/0.8 collection optic did reduce the fluctuations seen in the LI curves. However, it is acknowledged that this tries merely to compensate for the poor transverse mode control of the lasers and does not address the root of the problem, which lies in the our waveguide design and fabrication. Recommendations for suppressing/eliminating higher order transverse modes in the QC laser were given in Section 4.5.

7.4 Far-field profiling

As mentioned previously, the opportunity to measure the far-field profiles of the lasers came towards the end of this work. This was timely since it had been realised that the existence and detection of higher order transverse modes might resolve the origin of the perplexing power fluctuations observed in the LI curves. Figure 110 shows a sketch of an almost 'ideal' far-field measurement on an 'ideal' output beam from the fundamental mode of the laser. The MCT detector element, which measured 1×1 mm in size, was stepped in the lateral and vertical directions at 1 mm intervals to build up a 2D intensity profile (with a spatial resolution of 1mm) of the far-field of the laser. Our collaborators automated the measurement by using computer-controlled stepper motors to perform a raster scan over the output beam.

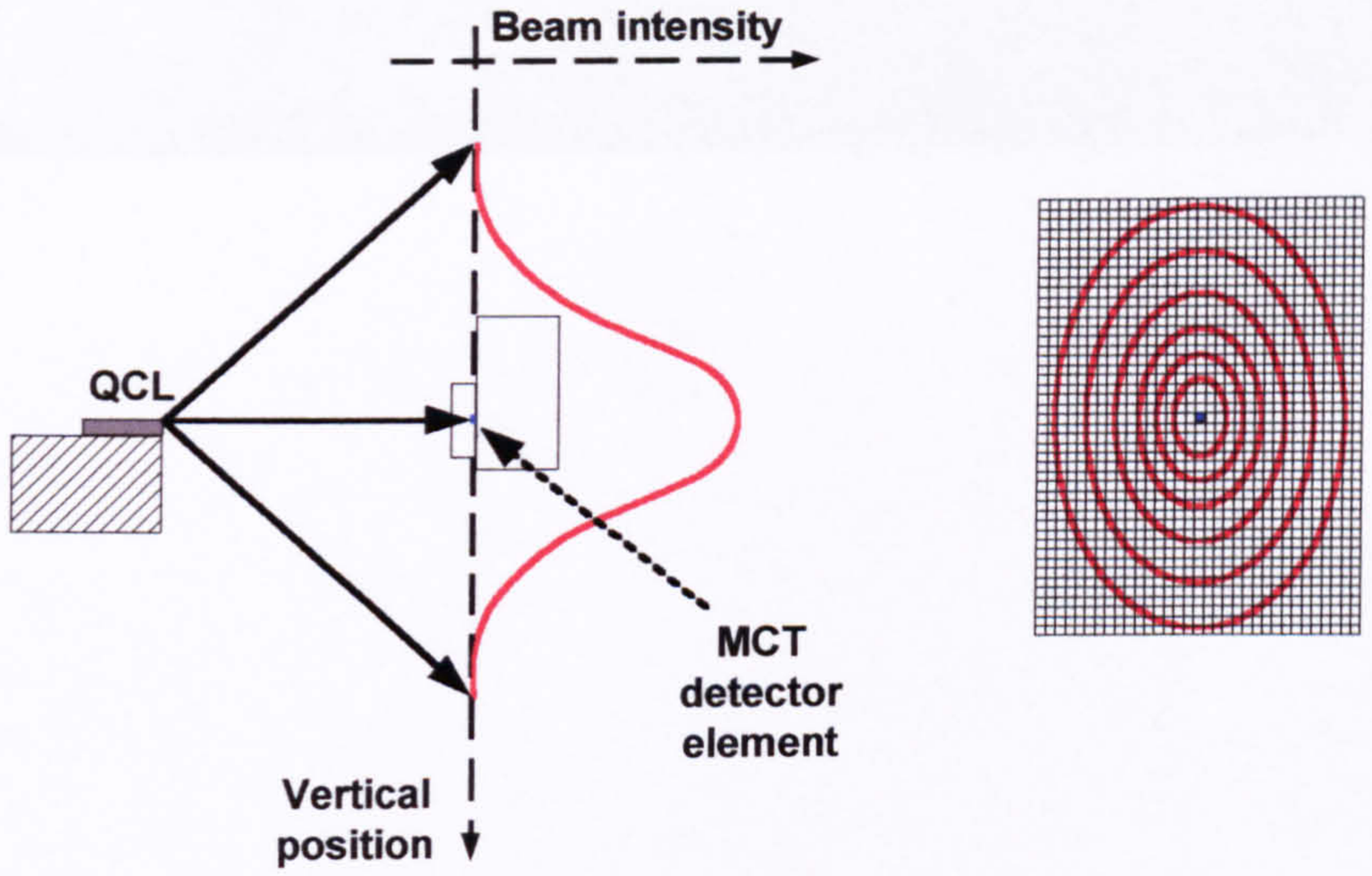

(a) (b)

Figure 110 Illustration of the far-field measurement. The side-on view in (a) depicts the vertical intensity profile (red) of the output beam of the fundamental mode of the laser taken at distance of several centimetres from the laser facet. Also shown is the 1 mm × 1 mm MCT detector element (blue) positioned at the peak of the intensity profile. The face-on view in (b) shows a contour plot (red lines) representing the intensity profile of the fundamental optical mode in 2D. The superimposed grid of 1 mm x 1 mm squares represents the detector element positions as the detector is scanned in 2D to map the far-field profile. With reference to (a), the blue-filled grid element at the centre shows the corresponding position of the detector element.

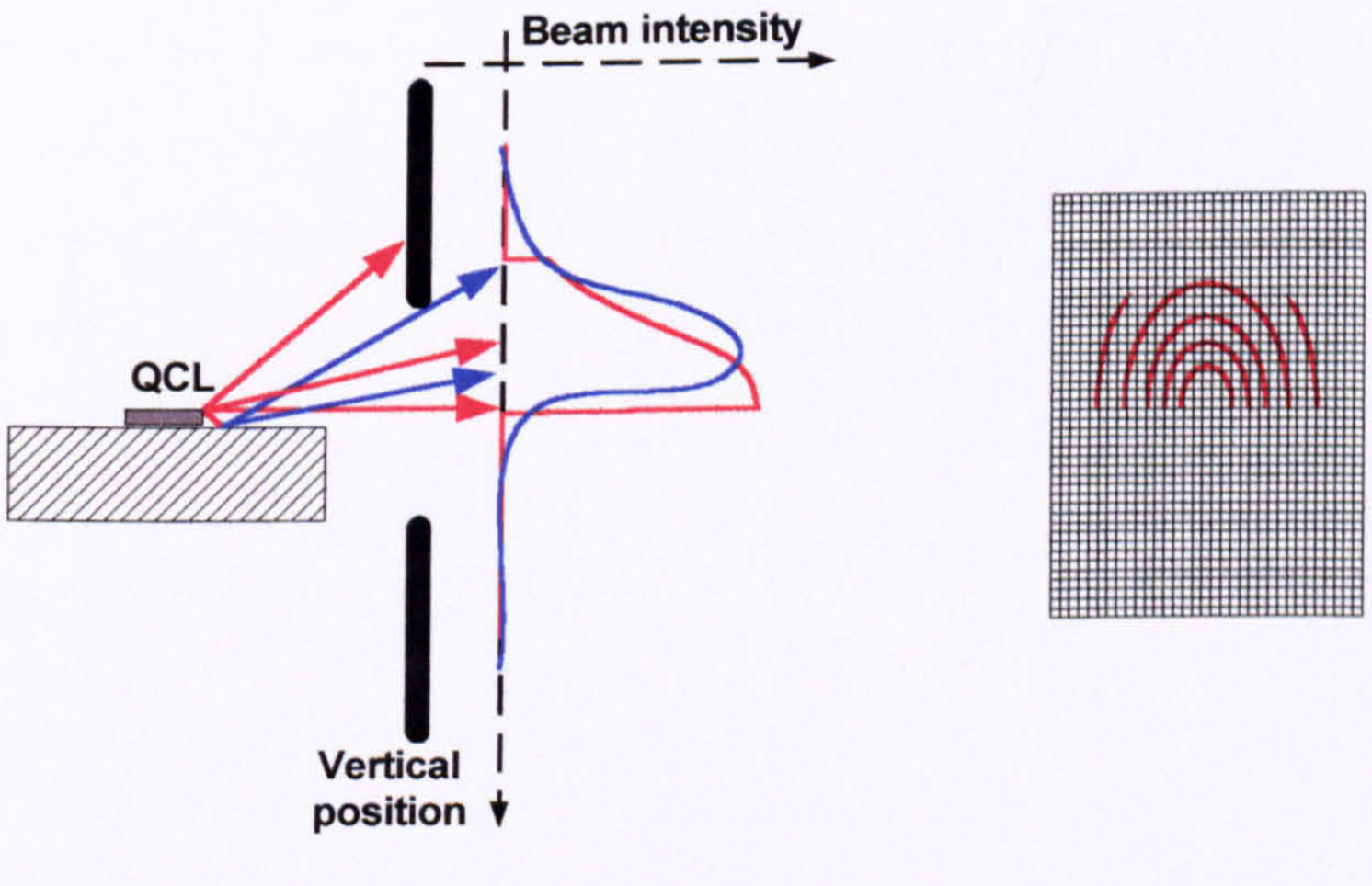

(a) (b)

Figure 111 Illustration of the actual far-field measurement. The side-on view in (a) depicts the vertical intensity profile (red) of the unobstructed output beam and the reflected/scattered light (blue). The face-on view in (b) shows a contour plot (red lines) representing the intensity profile of the unobstructed rays, but cropped by the finite diameter of the cryostat window (scattered/reflected profile not included).

The actual far-field measurements deviated from the 'ideal' measurement described above owing to the optical complications imposed by the TO-5 header and cryostat as listed in Section 7.2.3. Considering these factors, a more realistic illustration of the far-field measurements is shown in Figure 111. This illustration still does not show the undesirable reflections off the TO-5 header which would further complicate things. Once these problems had been realised, efforts were made to mount more devices onto copper blocks and accommodate these in the cryostat. Only points 3 to 5 applied if a copper block was used in place of a TO-5 header. Time limitations meant that not many far-field measurements could be performed before the end of this work, but those which were measured were instrumental in proving that the higher order transverse modes were lasing (see Chapter 8Chapter 8) and that the far-field changed with increasing current.

7.5 Summary

Critical to this work was access to a laser characterisation set-up capable of cooling the devices to cryogenic temperatures, supplying them with nanosecond pulses of known current and voltage, collecting the mid-IR emission and measuring its power, spectral content, and far-field distributions. These measurements were essential in order to have feedback on the quality of the MBE growth and fabrication procedures, and on the relative performances of the waveguide designs. Very fortunately, much of this was achieved through a collaboration with the Department of Physics and Astronomy at the University of Sheffield.

Alas, the characterisation was not all plain sailing and some problems were encountered with the current calibration which resulted in misleadingly normal values of J_{th} for our QCLs. The results have since been corrected for this, but the misleading feedback did inhibit progress somewhat.

The calibration of the optical power measurements assumed a fixed collection efficiency which implied that all devices measured had the same output beam profiles and that these beam profiles did not change significantly with drive current. In contrast, the results of the far-field profile calculations in Chapter 4 and the far-field profile measurements presented in Chapter 8 indicate that neither of these assumptions were strictly valid, especially when using a collection optic of high *f*-number. Where optical powers are given in the results, they should only be regarded as being approximate.

Mounting of QCLs on TO-5 headers compounded problems and moving to edge-mounting of the lasers onto copper blocks (or a similar heatsink) as the standard practice is highly recommended in the future. Consideration of the influence of the TO-5 header, especially on the presented far-field measurements in Chapter 8 should be kept in mind, as should the restricted optical access to the QCL when mounted in the cryostat.

On that subject, it is suggested that the optical access to the QC lasers be improved by mounting the lasers closer to the cryostat window. According to the calculated and measured far-field distributions, much of the far-field profile was obscured by the cryostat. Mounting the lasers closer to the cryostat window would allow measurement of much more of the far-field, making it possible to identify the modes more easily. Further, by summing the power measured at each point in the far-field, the total power of the entire emission could be obtained. In the short-term it would be advisable to use low *f*-number collection optics or non-imaging optics (such as a metal cone) to reduce the sensitivity of the collection efficiency to changes in the far-field distribution. In the long run, the design of single transverse mode waveguides should be pursued in order to eliminate the problem at its source.

7.6 References

[1] R. Hapanowicz, "FT-IR spectrometers profile optoelectronic emitters", *Laser Focus World*, July 1996.

[2] J. Faist, F. Capasso, C. Sirtori, D.L. Sivco, J.N. Baillargeon, A.L. Hutchinson, S.G. Chu, A.Y.Cho, 'High power mid-infrared (λ~5 μm) quantum cascade lasers operating above room temperature', *Appl. Phys. Lett.* **68** (26), 24 June 1996.

Chapter 8 Results of the QC laser characterisation

Characterisation of the fabricated lasers was essential in order to have feedback on the quality of the MBE growth and the fabrication procedures, and on the relative performances of the waveguide designs. This chapter presents the measurements made on the following devices:

- narrow (10 μm-wide), normal (15 μm-wide) and broad (112 μm-wide) mesa-etched QCLs,
- a shallow-etched QCL,
- a mesa-etched QCL array,
- and PSWOX QCLs.

Details of the fabrication processes used to make these devices were presented back in Chapter 6, and the techniques, equipment and conditions under which the forthcoming measurements were carried out were covered in the last chapter (Chapter 7). In this chapter, the results of light-current (LI), current-voltage (IV), spectral and far-field measurements on actual devices are presented and explained with the assistance of the optical and thermal modelling results already given in Chapter 4 and Chapter 5, respectively. A discussion of the wafers used in the fabrication will be made at the end of this chapter in Section 8.8.

In the following text, each device has an identification label, such as A1376.2.1. This first part tells us from which wafer the device was fabricated; wafer A1376 in this case. As was described in Chapter 6, the lasers were not made individually; rather, a batch of 'identical' devices were made together on a small sample of wafer and the second part of the label refers to this batch number. Finally, the last part of the label distinguishes between individual devices cleaved from the same batch.

Using Eq. (2-2) along with the length L_{cav} and width W of the laser, the values of J_{th} for each heatsink temperature were calculated from the corresponding I_{th} in the LI curves. L_{cav} was set at the time of cleaving and was accurate to ± 50 μm. The width of the laser at the mid-point of the active waveguide core was measured using a scanning electron microscope calibrated in the horizontal direction so that the measured width was accurate to ± 1 μm. A plot (not shown here) of $\mathrm{Ln}(J_{th})$ (or $\mathrm{Ln}(I_{th})$ in the case of the PSWOX and shallow-etched mesa) as a function of T was made and a linear fit of the slope at high temperature yielded the value of the characteristic temperature of the laser T_0. The plot of J_{th} (or I_{th} in the case of the PSWOX and shallow-etched mesa) as a function T is given for each laser, and on it a the straight red line indicates the data points (or temperature range) which were used to deduce the T_0.

Where high resolution spectra were taken which resolved the longitudinal modes, the average spacing between the modes was measured and used to calculate the effective index of the lasing mode using the formula,

$$n_{eff} = \frac{c}{2\Delta f\, L_{cav}} = \frac{5}{\Delta\omega\, L_{cav}}, \qquad (8\text{-}1)$$

where L_{cav} was the length of the cavity (mm) and $\Delta\omega$ was the longitudinal mode spacing (cm^{-1}). The uncertainty in the cavity length (± 50 μm) has been included as this can lead to a large error in the calculated value of n_{eff}.

8.1 Mesa-etched $\lambda \approx 5\ \mu m$ QC lasers of width = 15 μm

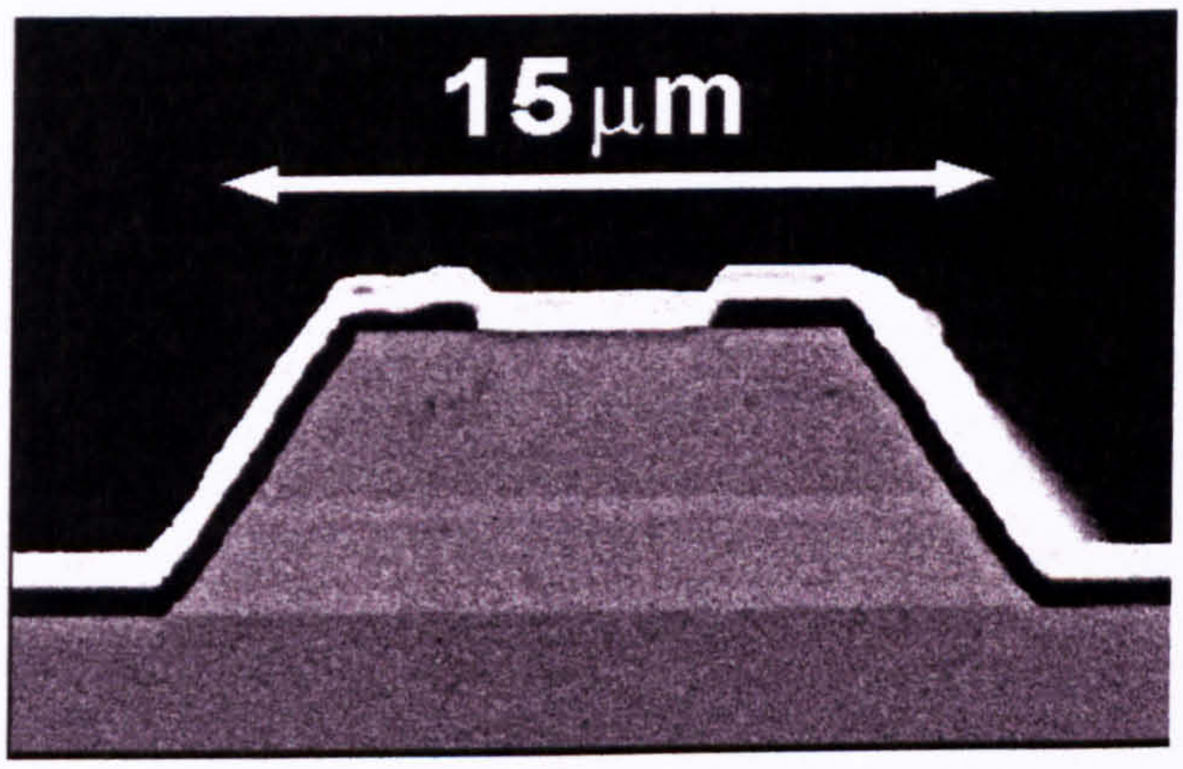

Figure 112 Scanning electron micrograph of the cleaved laser facet of one of the mesa-etched QCLs. Moving on a line from the centre-bottom of the micrograph to the centre-top, the dark grey layer was the InP substrate, followed by the waveguide core comprising 0.3 μm-thick $In_{0.53}Ga_{0.47}As$ layer, 25 repeats of the QC stage (total of ~1.1 μm), then 0.3 μm-thick $In_{0.53}Ga_{0.47}As$ layer. Above that lay the ~2.5 μm-thick $In_{0.52}Al_{0.48}As$ upper cladding layer and 10 nm-thick $In_{0.53}Ga_{0.47}As$ contact layer. The metal layer (the very bright layer in micrograph) injected current through the window in the insulation layer (the black-looking layer between the semiconductor and the metal on the sidewalls). The measured width was $W = 15$ μm at the midpoint of the active waveguide core.

8.1.1 QCL A1376.2.3, L_{cav} = 2 mm, SiO_2 dielectric, T0-5 header

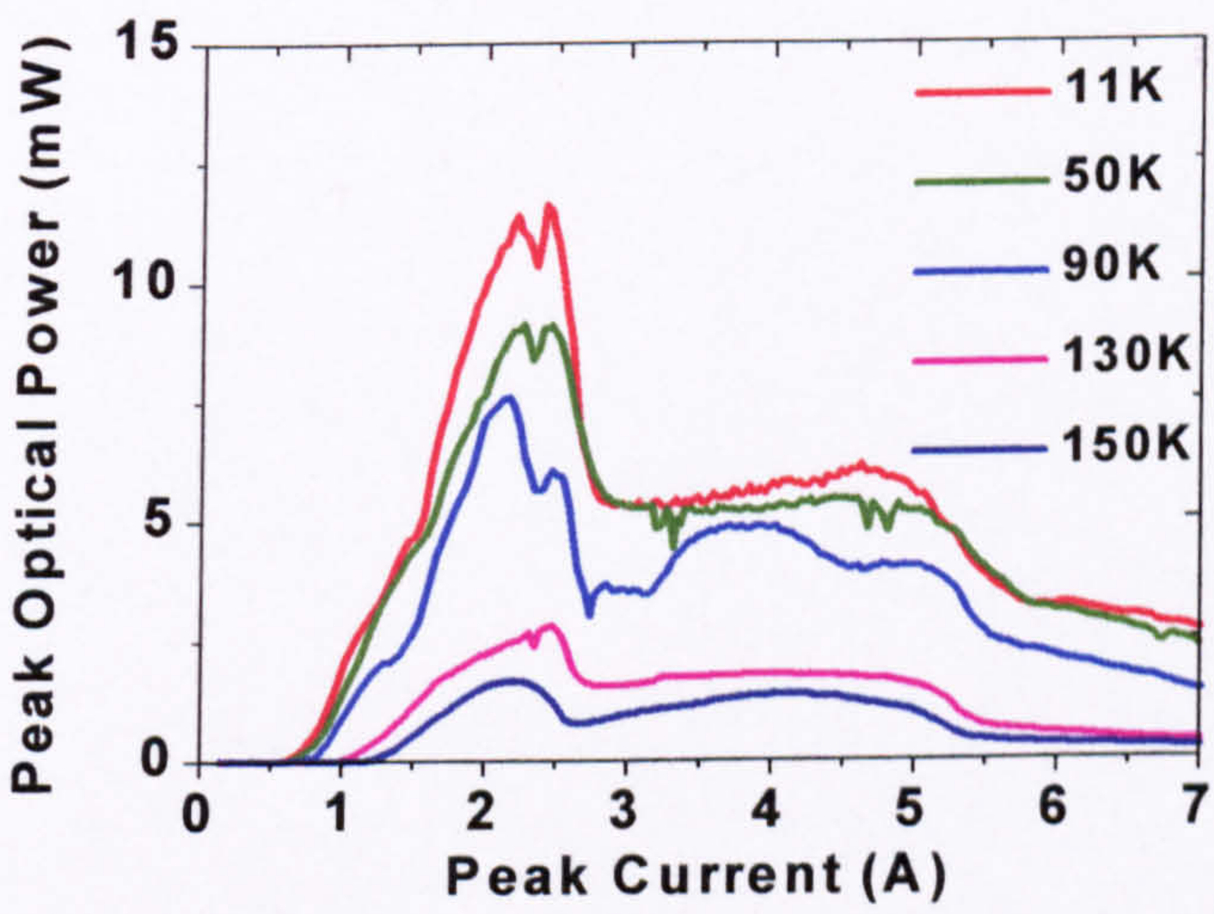

Figure 113 Measured LI curves of device A1376.2.3 at a series of heatsink temperatures.

The LI curves obtained (see Figure 113) were not very typical of those reported in the literature, [1, 8, 11] neither in shape nor in the best peak optical power obtained. The initial slope efficiency was only ~ 0.007 W/A, and then the collected output power dropped dramatically at around $J_{th} \approx 8$ kA\cm^2 , then again at 16 kA/cm^2. Note that the general shape was constant with temperature, with only the threshold current increasing and output power decreasing. Lasing was only observed up to ~ 150 K.

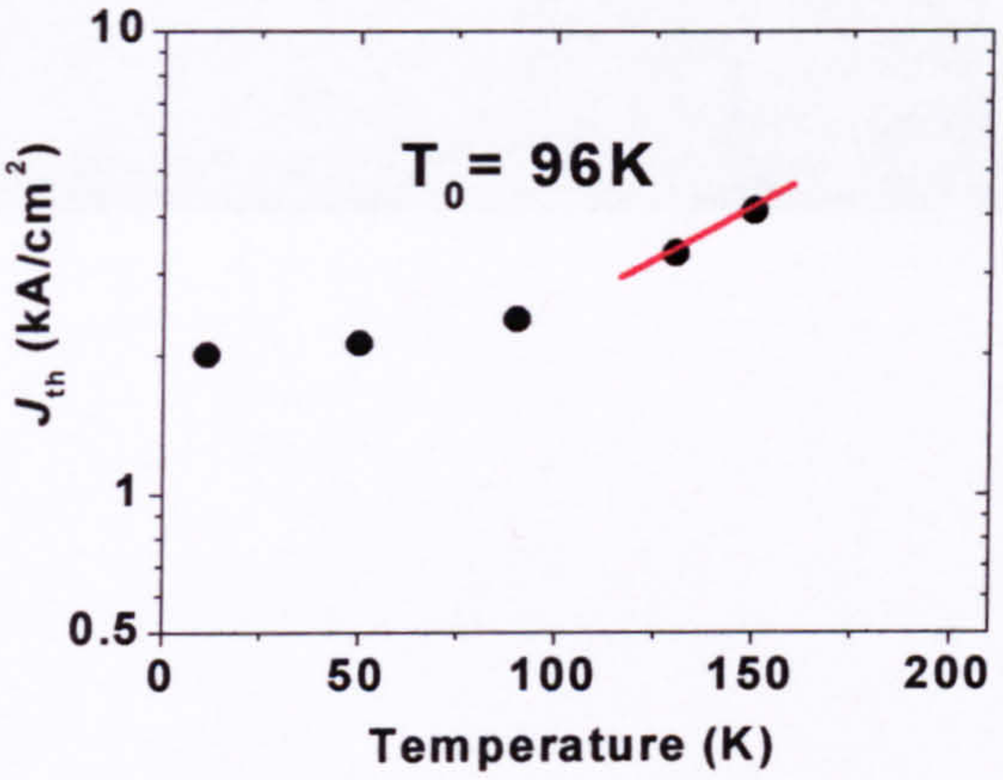

Figure 114 Measured temperature-dependence of J_{th} of device A1376.2.3. The value of T_0 was deduced from the same data from the best fit (linear) slope at high temperature of a plot of T as a function of Ln(J_{th}).

Referring to Figure 114, the T_0 for the device was not too unusual at T_0 = 96 K, but very importantly the minimum J_{th} was approximately *twice* that reported for this design by Faist *et al.* (see Table 2).[8]

Parameter	**Value**
W (μm)	15
L_{cav} (mm)	2
J_{th} (kA/cm^2) at $T \approx 10$ K	~ 2.0
P (W) per facet max. at $T \approx 10$ K	0.012
$\partial P/\partial I$ (W/A) at $T \approx 10$ K	0.007
T (K) maximum	150
T_0 (K)	96 $(130 < T < 150)$

Table 51 Key parameters measured for laser A1376.2.3.

8.1.2 QCL A1376.2.1, L_{cav} = 3 mm, SiO_2 dielectric, T0-5 header

8.1.2.1 LI curve measurement

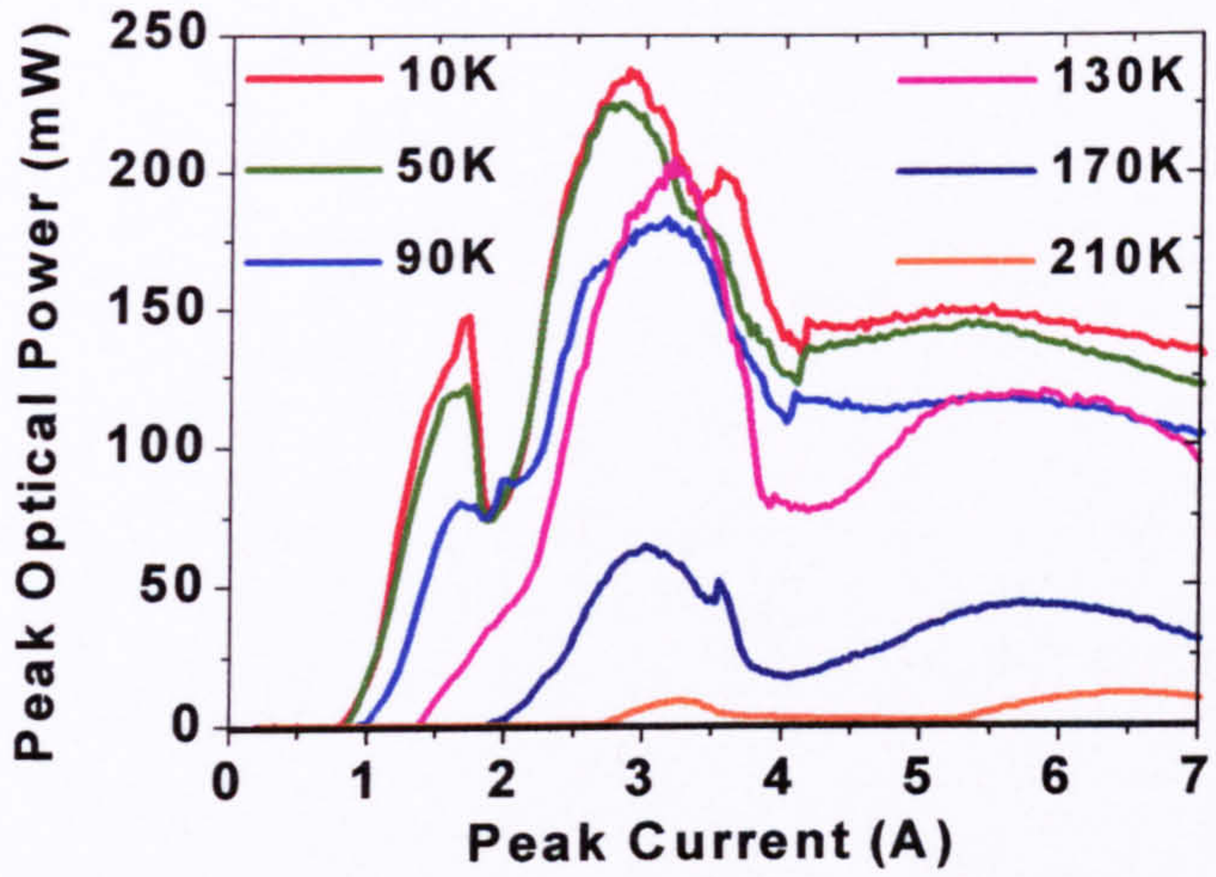

Figure 115 Measured LI curves of device A1376.2.1 at a series of heatsink temperatures.

The maximum output power $P \approx 235$ mW, maximum operating temperature $T \approx 210$ K, slope efficiency $\partial P/\partial I \approx 280$ mW/A, and $T_0 = 110$ K of the 3 mm-long laser A1376.2.1 were much better than the 2 mm-long A1376.2.3 device. The shape of LI curve of A1376.2.1 was similar to that of A1376.2.3, but in the longer device the initial slope no longer increased monotonically; it dropped abruptly at $J_{th} \approx 4$ kA/cm^2, then recovered and increased again until a second peak at $J_{th} \approx 6.7$ kA/cm^2. Note that the presence of this temporary drop in power became less pronounced with temperature. Looking back at the initial slope on device A1376.2.3, we can see that there was a less pronounced kink in the LI at approximately the same point.

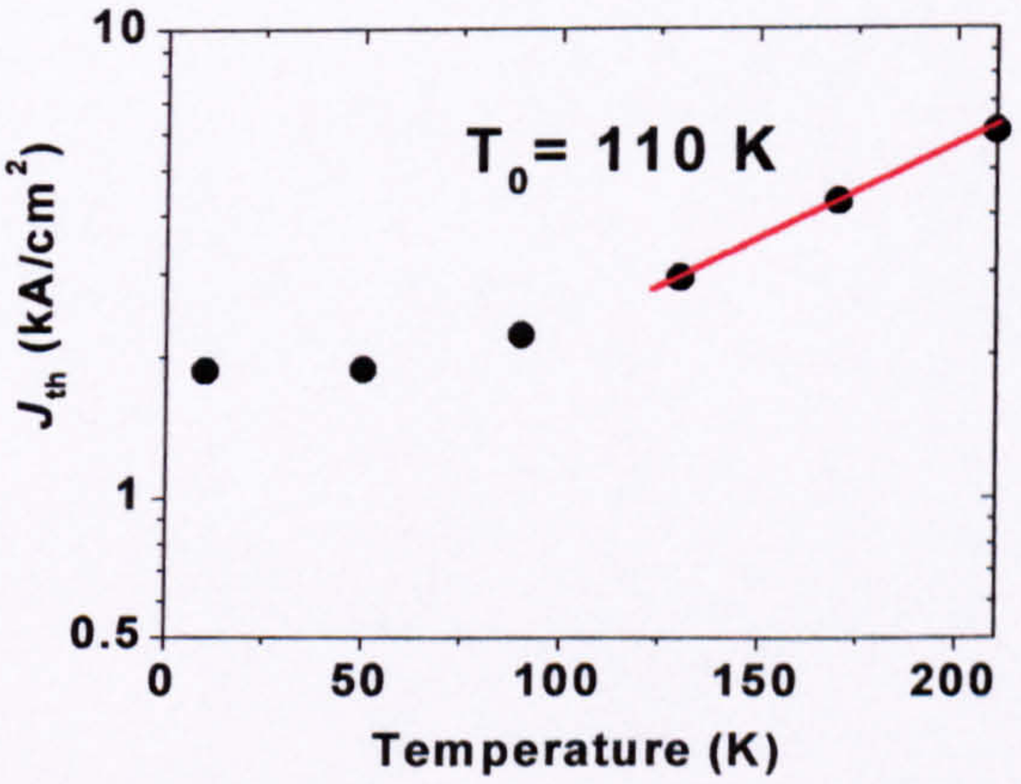

Figure 116 Measured temperature-dependence of J_{th} of device A1376.2.1.

The $T_0 \approx 110$ K of this device compared very well with that reported by Faist *et al.* for mesa-etched devices using the same active region design ($T_0 \approx 109$ K),[1] which was another good indication of that the observed performance problems were not related to the quality of the active waveguide core of wafer A1376.

Parameter	Value
W (μm)	15
L_{cav} (mm)	3 ± 0.05 mm
J_{th} (kA/cm^2) at $T \approx 10$ K	~ 1.9
P (W) per facet max. at $T \approx 10$ K	0.24
$\partial P/\partial I$ (W/A) at $T \approx 10$ K	0.28
T (K) maximum	210
T_0 (K)	110 $(130 < T < 210)$

Table 52 Key parameters measured for laser A1376.2.1.

By comparison with the expected values of $\partial P/\partial I \approx 0.6$ W/A and $J_{th} = 0.93$ from Table 2, we can see that the measured $\partial P/\partial I$ was ~ half that expected and J_{th} was ~ double. Using $J_{th} \approx 2$ kA/cm^2 and assuming $\Gamma = 0.5$ we calculate $\alpha_w \approx 30$ cm^{-1} with the aid of Eq. **(2-3)**. Taking this new value of α_w and using it in Eq. **(2-12)** yields $\partial P/\partial I \approx 0.3$, which agrees well with the measured value. These findings indicated that the source of the poor performance was the optical waveguide. The optical modelling gave $\alpha_w \approx 13$ cm^{-1} and $\alpha_w \approx 21$ cm^{-1} for InP substrate doping levels of 1×10^{18} cm^{-3} and 3×10^{18} cm^{-3}, so that the measurements indicated that InP substrate doping level was greater than 3×10^{18} cm^{-3}.

8.1.2.2 Spectral analysis

Figure 117 presents laser emission spectra taken at a series of drive currents and compared to the LI curve. As we can see, the spectra of the collected emission varied with the drive current. A broadening of the emission spectrum and its shift to lower energy with increasing current is expected, owing to the increase in the core temperature and the possible thermal gradient across it, and to the increasing quasi-Fermi level in the $n = 3$ state. Note that what we are seeing in these spectra is the envelope of the collection of many lasing longitudinal modes of the laser. The resolution of these particular spectra was not high enough to resolve the individual longitudinal modes of approximate spacing $\Delta\omega \approx 0.5$ cm^{-1}.

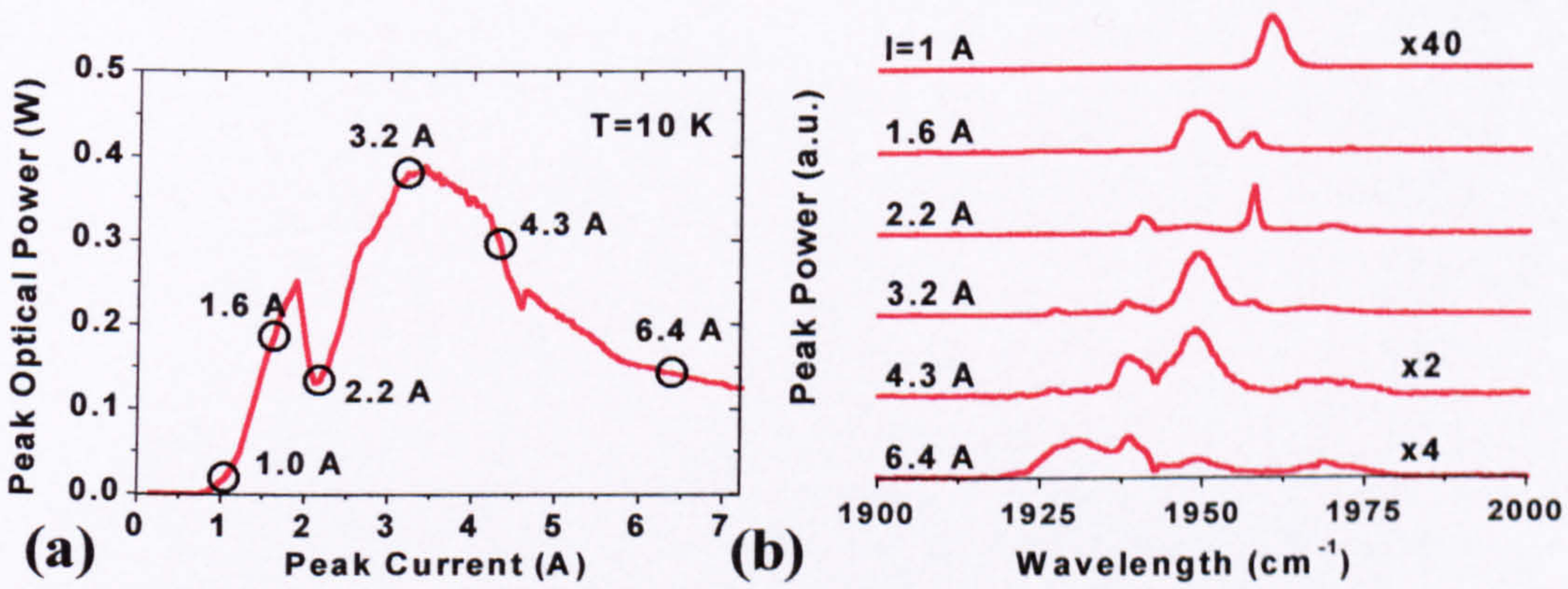

Figure 117 Comparison of 9A (a) the LI curve and (b) the emission spectra at various drive currents for device A1376.2.1 at $T \approx 10$ K. The spectrometer resolution was set too low to resolve the longitudinal modes of the laser ($\Delta\omega \approx 0.5$ cm^{-1}). Note that where the power axis scale of the spectra has been multiplied, the multiplication factor has been shown to the right of the spectrum.

8.1.3 QCL A1376.2.2, L_{cav} = 3 mm, SiO_2 dielectric, T0-5 header

8.1.3.1 Spectral analysis

It is interesting to show the spectra as a function of drive current of a second QC laser of the same length L_{cav} = 3 mm and from the same batch as A1376.2.1.

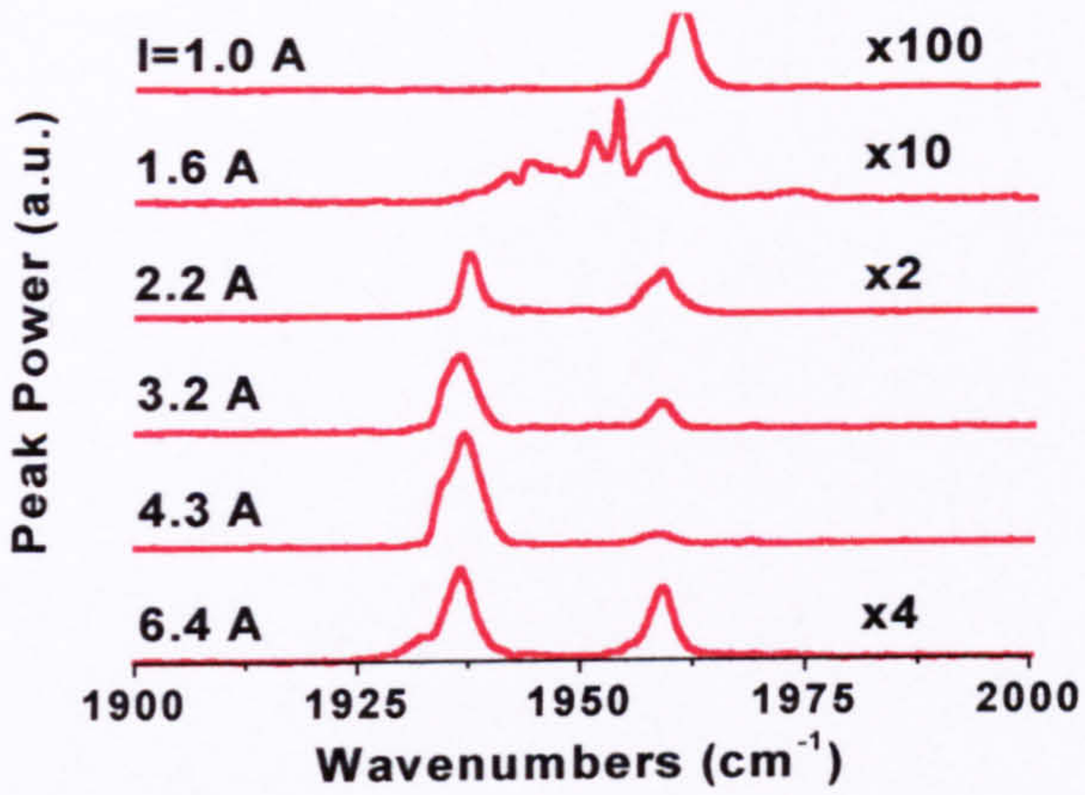

Figure 118 Measured emission spectra of device A1376.2.2 at a series of drive currents. Note that where the power axis scale of the spectra has been multiplied, the multiplication factor has been shown to the right of the spectrum.

8.1.3.2 Far-field measurements

The LI curve given in Figure 119 was taken in a slightly different manner to that normally performed. In order to identify specific currents of interest for far-field measurements, a LI curve was measured without collection optics. The MCT detector was placed as close to the cryostat window as possible and the detector element positioned on axis with the laser facet. Since the detector element was small (1 × 1 mm), this essentially made the angle of collection ~ 0 degrees and consequently the collection efficiency became very sensitive to any changes in beam divergence, as was desired in this case.

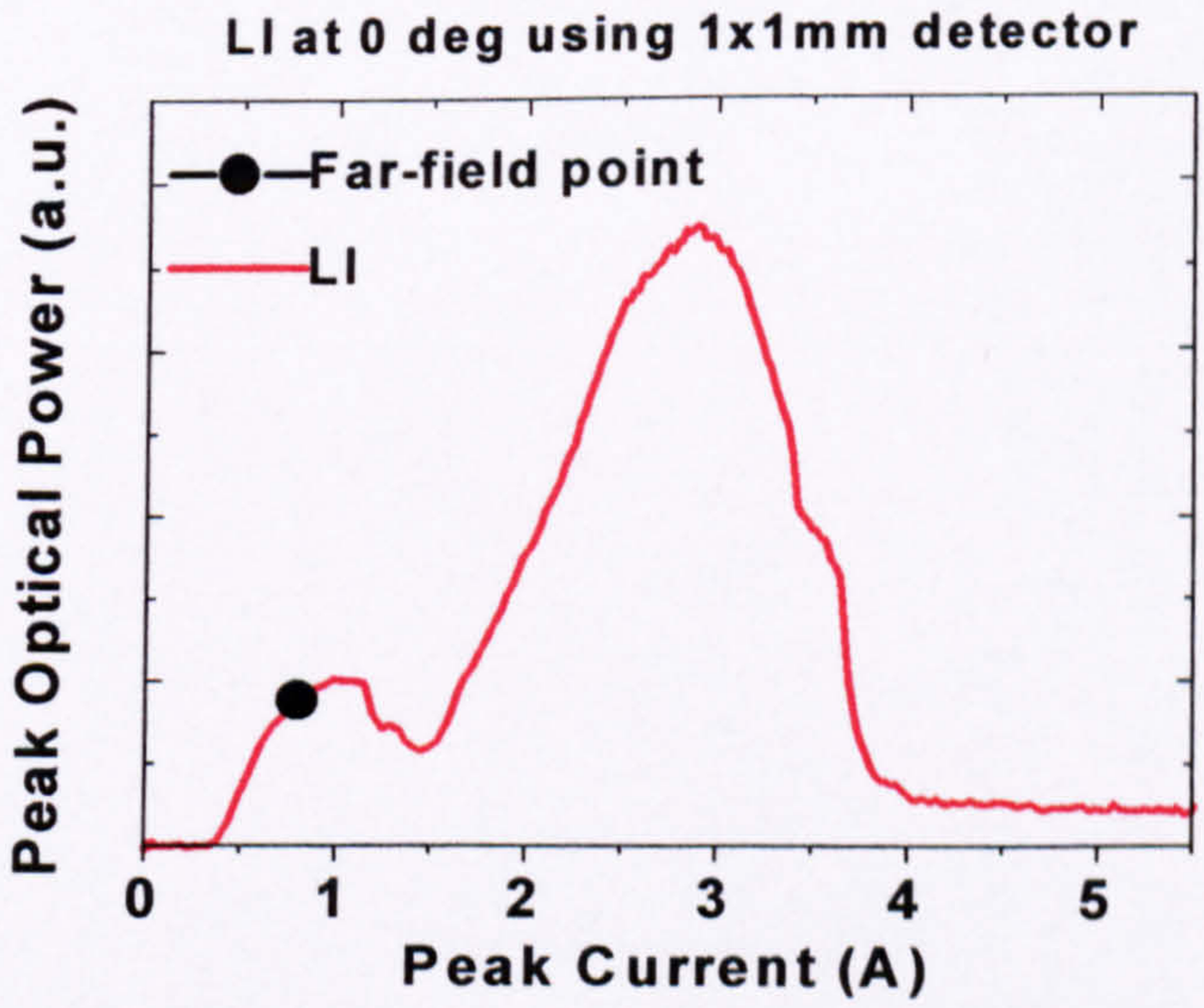

Figure 119 LI curve of device A1376.2.2 measured at $T \approx 11$ K and without collection optics. The black dot marks the point at which the far-field measurement shown Figure 120 was taken.

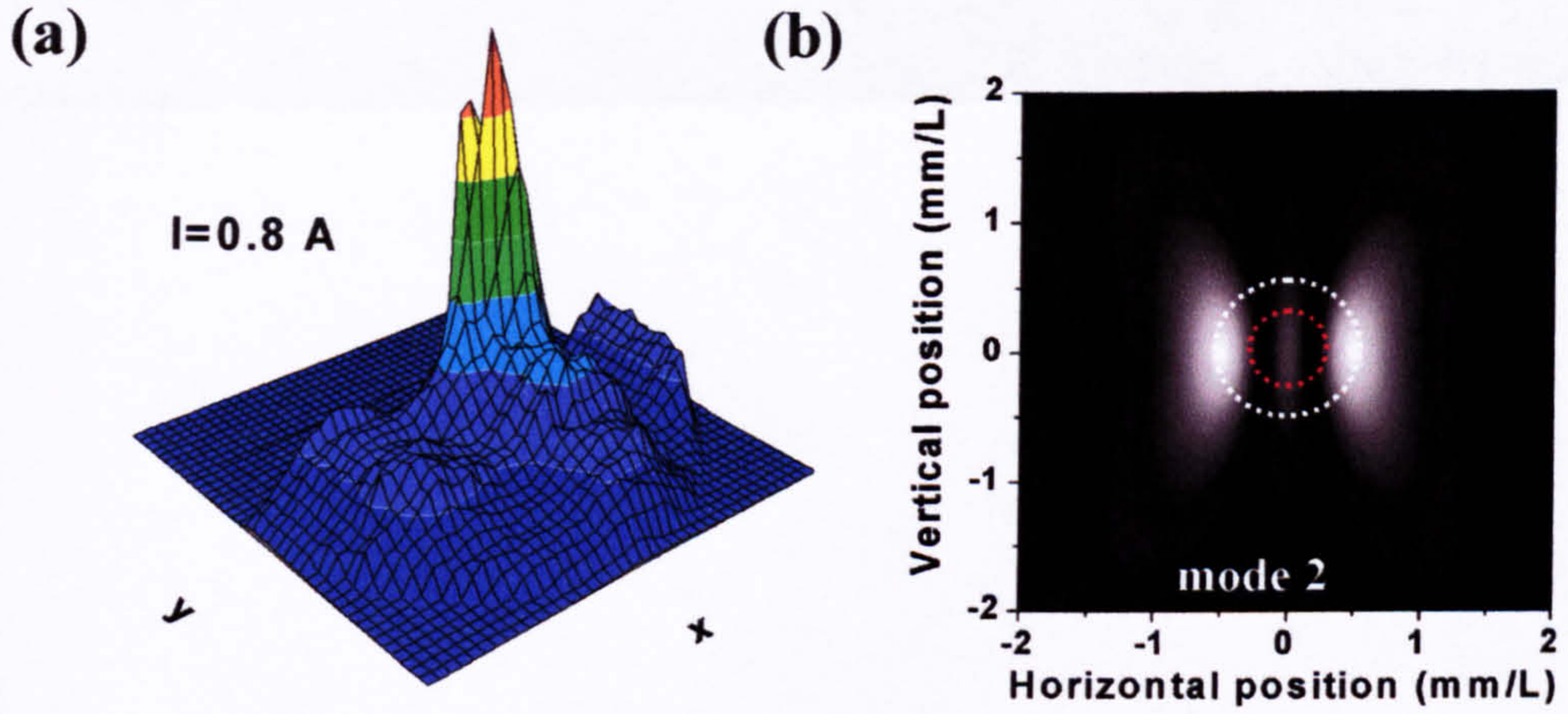

Figure 120 (a) 3D intensity plot of the measured far-field profile at a distance of $L \approx 42$ mm from the laser facet for device A1376.2.2 at $I = 0.8$ A (marked on the LI curve in Figure 119). The x-axis represented the horizontal direction (a.u.) which was parallel to the epitaxial layers, the y-axis the vertical direction (a.u.), and the z-axis the optical intensity (a.u.). (b) Intensity plot of the calculated far-field distribution of mode 2 from Table 15. The white dotted circle represented a $f/0.8$ cryostat window and the red dotted circle $f/1.7$ parabolic collection.

A far-field profile was performed at $I = 0.8$ A and the 3D intensity plot of the measured data is shown in Figure 120 (a). Note that this device was mounted on a T0-5 header, so that the considerations outlined in Section 7.4 should be kept in mind when interpreting the profile. For instance, one can immediately see that the rear of the profile was abruptly chopped off half way down the y-axis of the profile owing to obstruction of the beam by the TO-5 header. Additionally, the light emitted outside the area cryostat window was obstructed, as indicated by the abrupt circular drop in optical power on the periphery of the beam profile.

Despite this, we can still make out several interesting features. Not far above the threshold current at $I = 0.8$ A the measured profile showed a narrow (in the x-direction) peak in the centre and the beginnings of two other peaks at the periphery of the cryostat window aperture. Comparing this measured far-field profile to that was calculated in Section 4.4.2.2 for this device, we can see that the observed profile was much too narrow to be that of the fundamental mode of the waveguide, but matches very well with that of the 2nd order mode (given again in Figure 120 (b)). Furthermore, if we refer back to Section 4.4.1.2 the calculations of the g_{th} of the modes from the optical modelling indicated that the 2nd order mode was the mode with the lowest threshold current and so would be expected to be the first to lase. Unfortunately, no further drive currents were investigated. We therefore cannot say at this point that the profile, and therefore the collection efficiency, changed with drive current.

8.1.4 QCL A1376.4.2, L_{cav} = 3 mm, Si_3N_4 dielectric, TO-5 header

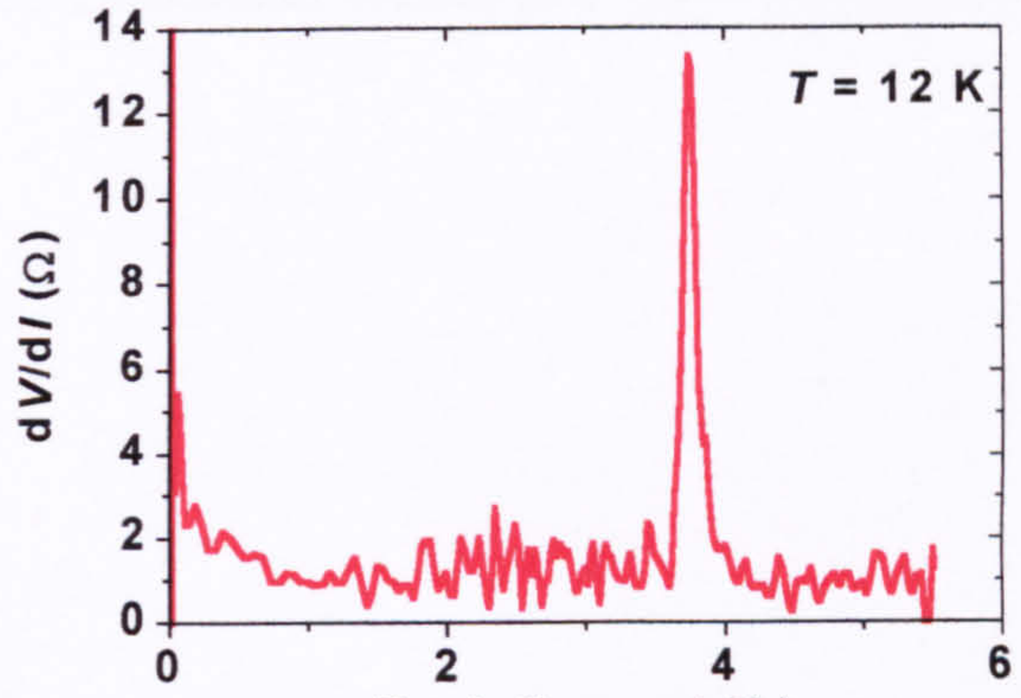

Figure 121 Differential resistance deduced from the IV curve in Figure 122. The sharp spike at $I \approx 3.8$ A indicated the loss of resonant tunnelling injection from the injector state g into the upper lasing state $n = 3$.

A comparison of the simultaneously measured IV and LI of device A1376.4.2 was another important indication that these fluctuations in the LI curves were related to changes in collection efficiency rather than changes in the QC active waveguide core characteristics. The loss of resonant tunneling of electrons from the injector ground state g into the upper lasing level $n = 3$ is accompanied by a temporary increase in the differential resistance of the device i.e. a kink in the IV curve.[2] We can see from the comparison of the LI and IV curves in Figure 122 and the plot of the differential resistance versus the drive current in Figure 121 that the loss of resonant tunnelling definitely occurred *after* the loss of optical power output. Following the dotted line we see that there was a steep drop in the output power at the point of the loss of resonance, but it could not have been responsible for the features at lower currents. This evidence further strengthens the argument that the observed fluctuations in the LI curves were a consequence of changes in collection efficiency or waveguide losses as a function of drive current, and were not related to the active waveguide core performance.

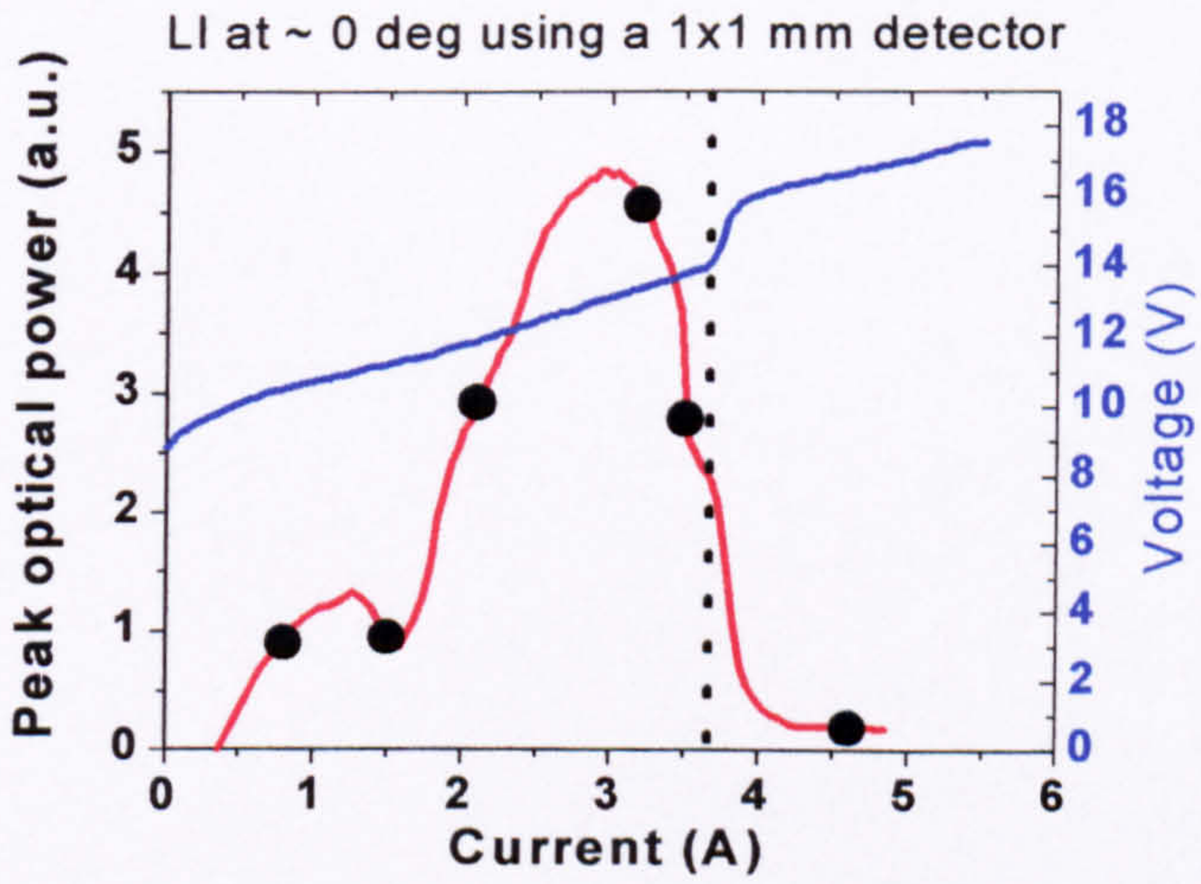

Figure 122 Simultaneously measured LI (red line, no collection optics) and IV (blue line) curves of device A1376.4.2. The black dots on the LI curve indicate at which currents the far-field measurements shown in Figure 124 were taken. The vertical dotted line is only a guide for the eye to compare the LI curve and IV curve at the point where resonant tunnelling injection from the injector state g into the upper lasing state $n = 3$ terminates.

The black dots on the LI curve in Figure 122 indicate the currents at which far-field measurements were performed for this device. These profiles are displayed in Figure 124 and show the far-field profile shape changing as a function of drive current. As the far-field was distorted owing to the influence of the TO-5 header and the limited optical access (see Section 7.4 for information), it was impossible to say for sure which transverse modes were present. From Section 4.4.1.2, the calculated order of the transverse modes from low to high g_{th} was: mode 2 (g_{th} = 43.5 cm^{-1}), 3 (g_{th} = 44.0 cm^{-1}), 1 (g_{th} = 44.7 cm^{-1}), 0 (g_{th} = 46.1 cm^{-1}), 4 (g_{th} = 48.8 cm^{-1}), and then 5 (g_{th} = 65.4 cm^{-1}). It does appear that the lasing began with the 2nd order transverse mode (mode 2), and then the broadening of the distribution at higher currents suggested the presence of other transverse modes, but their identity could not be ascertained here.

The crucial point though, was that the distribution changed spatially with drive current. This indicated that there were changes in the distribution of output power among the different transverse modes and that the collection efficiency was indeed changing as a function of the drive current. The measured far-field data for I = 0.8 A and I = 3.2 A has been plotted in a slightly differently in Figure 123 to show this more clearly. In the far-field profiles, the outer dotted circle represents the cryostat window aperture, and the inner dotted circle represents the parabolic mirror collection. It was obvious that the ratio of emission inside to outside the collection cone of the parabolic collection mirror was different at these two currents and so the assumption that the collection efficiency was constant with current was invalid. This explained the observed fluctuations in the collected optical output power and made the optical power calibrations unreliable.

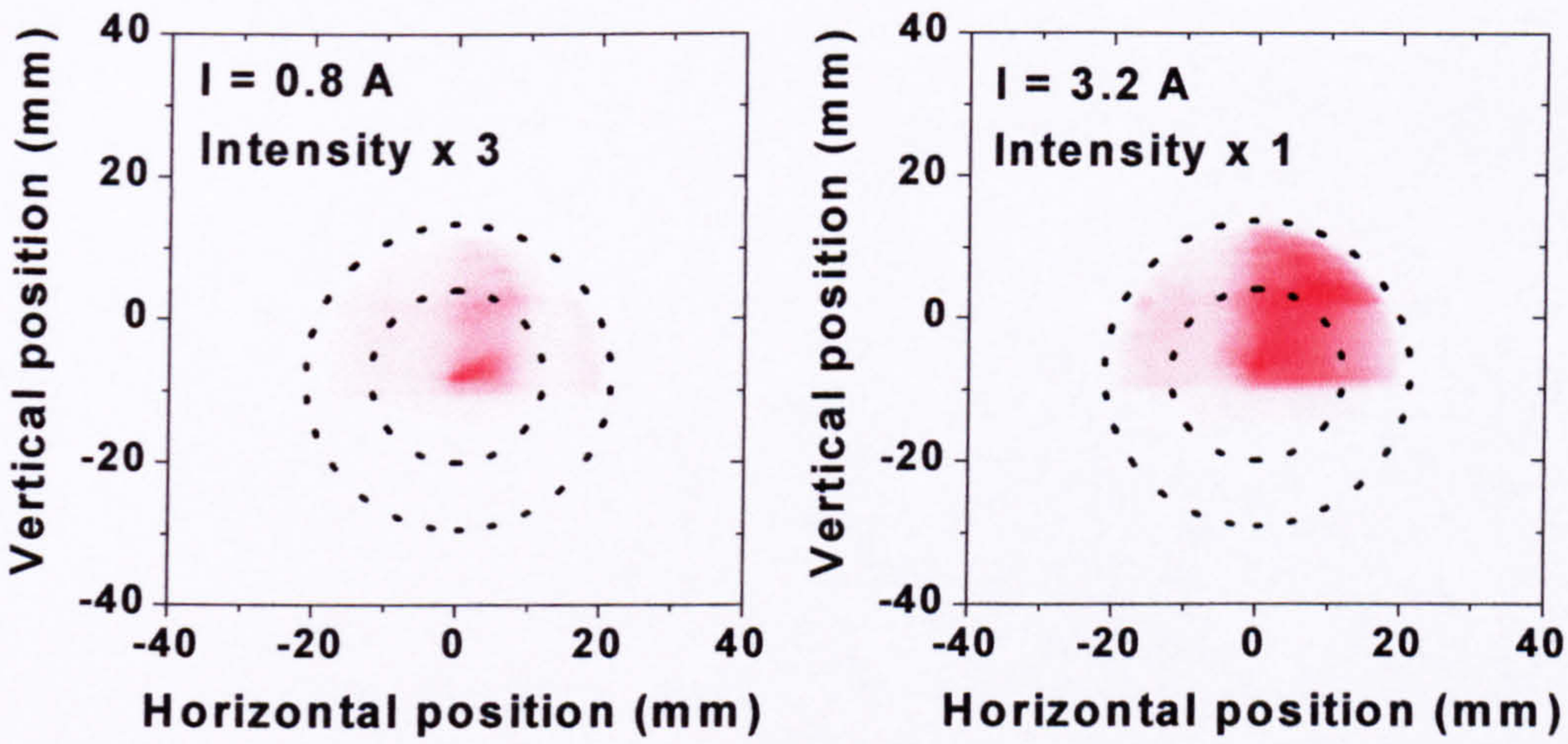

Figure 123 Density plots of the far-field profiles performed at I = 0.8 and 3.2 A. The colour indicates the measured optical intensity scaling from white to red for low to high intensity level. Light enclosed by the superimposed small dotted circle will be collected by the f/1.7 parabolic mirror. The large dotted circle represents the cryostat window aperture.

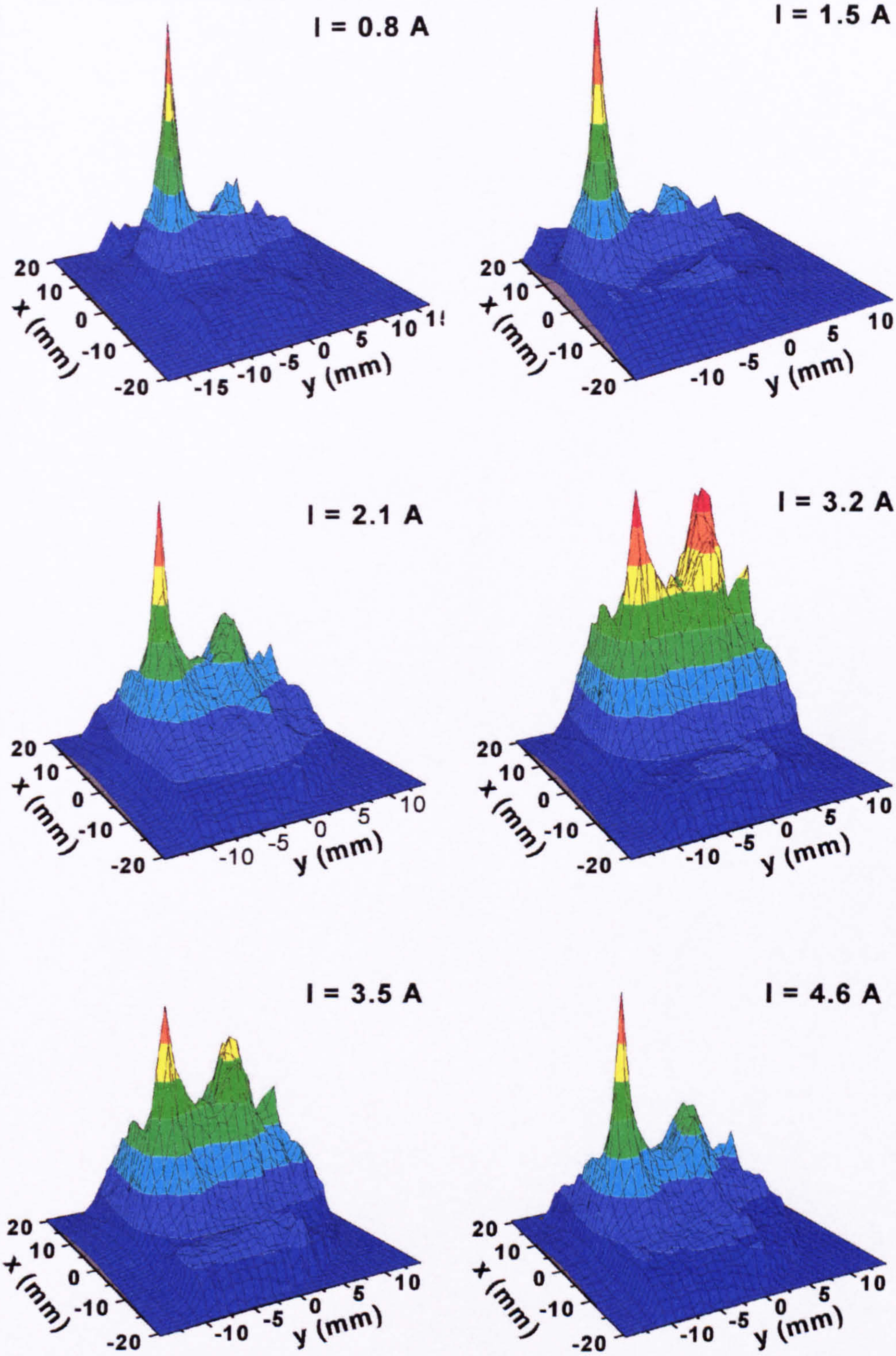

Figure 124 3D intensity plots of the measured far-field profiles at a distance of $L \approx 42$ mm from the laser facet. Profiles are shown for the six drive currents marked on the LI curve in Figure 122. The x-axis represents the horizontal direction in (mm) which was parallel to the epitaxial layers, the y-axis the vertical direction (mm), and the z-axis the normalised optical intensity (a.u.).

8.2 Narrow mesa-etched $\lambda = 5\ \mu m$ QCLs, width $\approx 10\ \mu m$

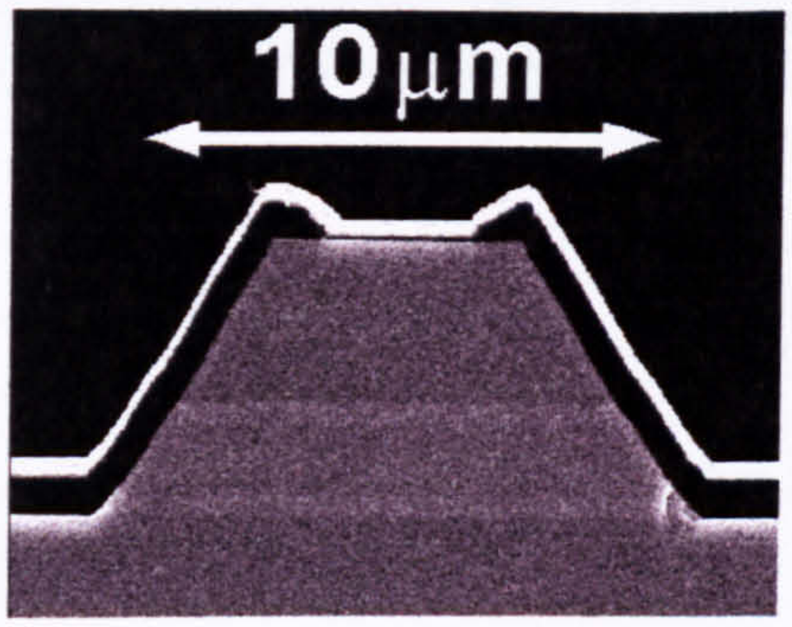

Figure 125 Scanning electron micrograph of the cleaved laser facet of one of the narrow mesa-etched QCLs. Please refer to the caption of Figure 112 for a description of the layers. The measured width was $W = 10\ \mu m$ at the midpoint of the active waveguide core.

8.2.1 QCL A1376.5.1, $L_{cav} = 2.15$ mm, Al_2O_3 dielectric

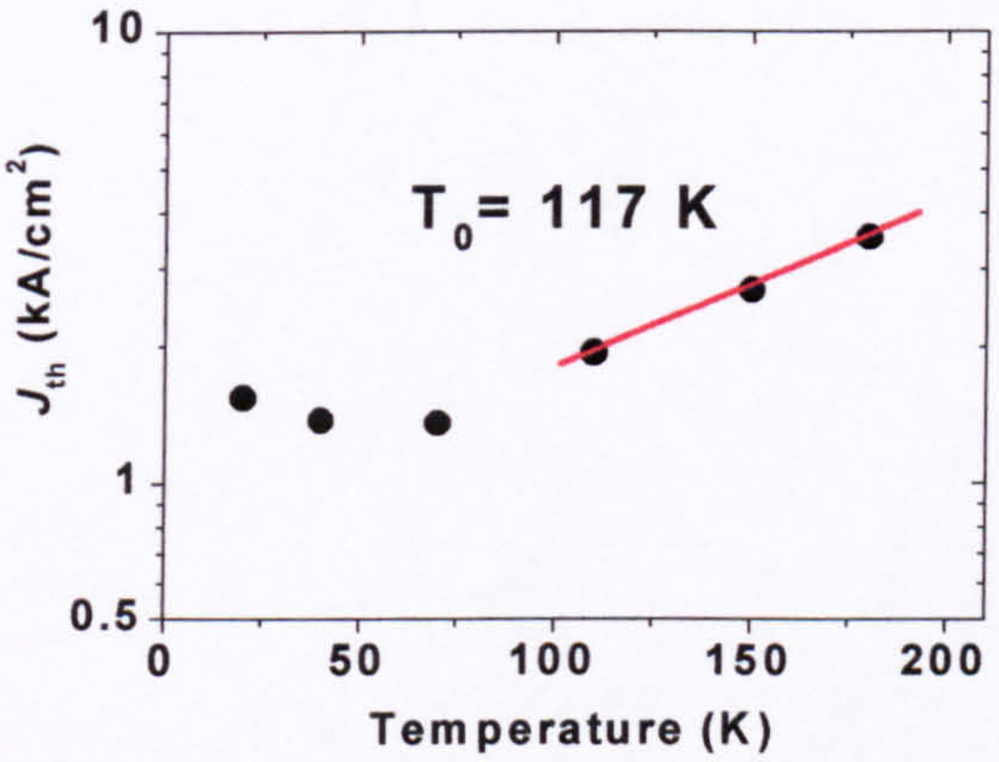

Figure 126 Measured temperature-dependence of the J_{th} of device A1376.5.1.

Parameter	Value
W (μm)	10
L_{cav} (mm)	2.15 ± 0.05 mm
J_{th} (kA/cm^2) at $T \approx 10$ K	~ 1.5
P (W) per facet max. at $T \approx 10$ K	0.06
$\partial P/\partial I$ (W/A) at $T \approx 10$ K	0.06
T (K) maximum	200
T_0 (K)	117 $(130 < T < 210)$

Table 53 Key parameters measured for laser A1376.5.1.

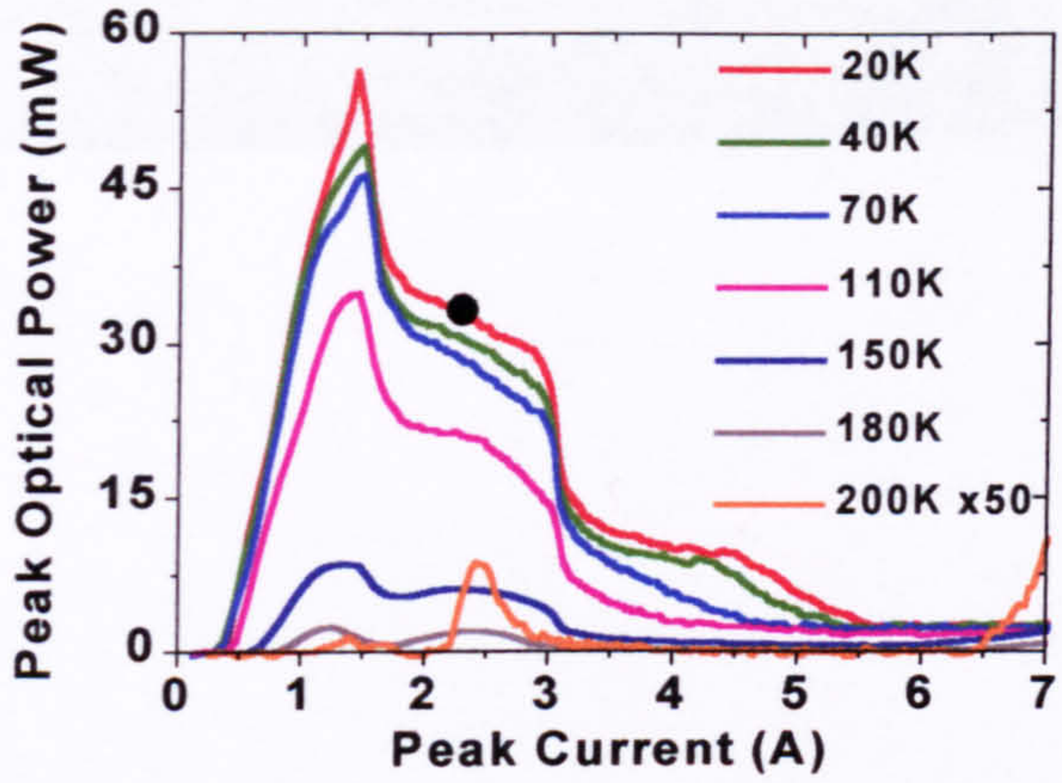

Figure 127 Measured LI curves of device A1376.5.1 at a series of heatsink temperatures. The black dot indicates the current at which the far-field measurement in Figure 128 was made.

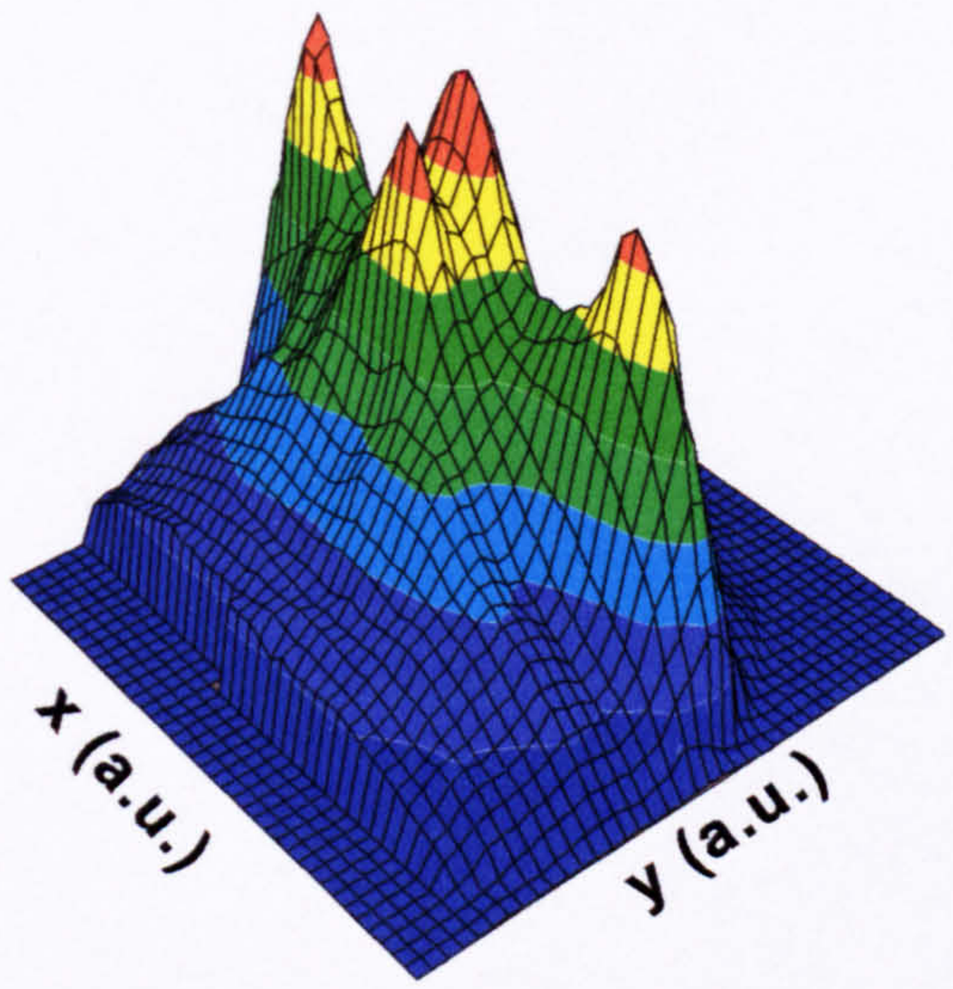

Figure 128 3D intensity plot of the measured far-field profile of device A1376.5.1 at a distance of $L \approx$ 42 mm from the laser facet. Profiles are shown for the six drive currents marked on the LI curve in Figure 122. The x-axis represents the horizontal direction in (mm) which was parallel to the epitaxial layers, the y-axis the vertical direction (mm), and the z-axis the normalised optical intensity (a.u.).

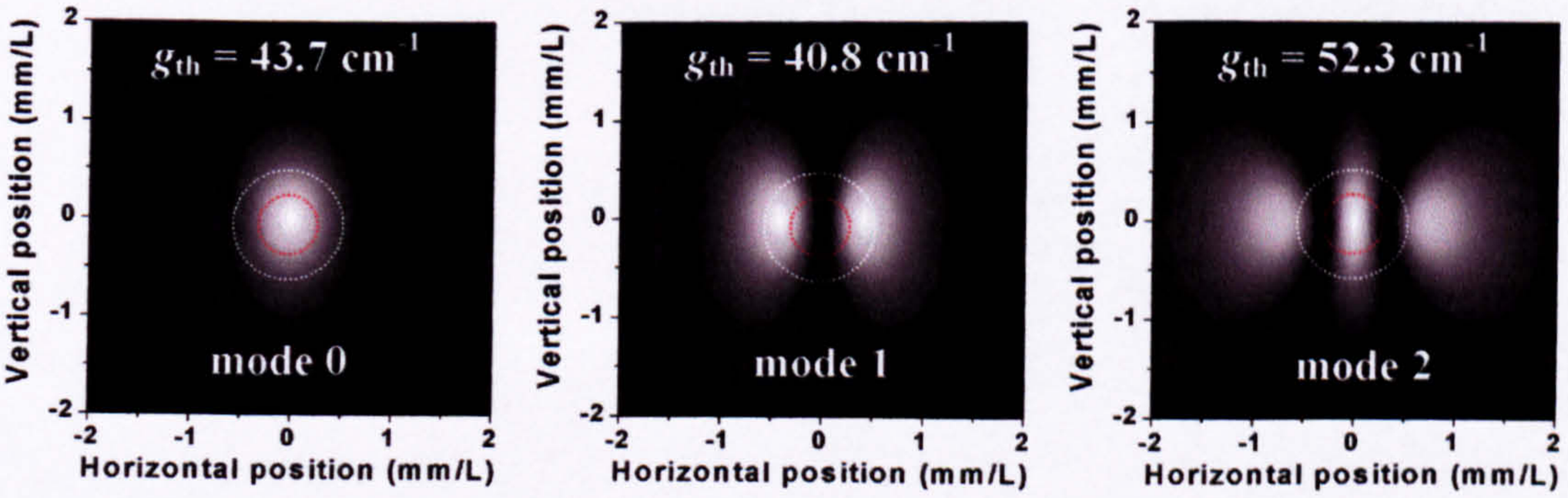

Figure 129 3D intensity plots of the calculated far-field distributions of modes numbered 0 to 2 in Table 20. The white dotted circle represents a *f*/0.8 cryostat window and the red dotted circle *f*/1.7 parabolic collection. The calculated threshold gain is quoted for each mode.

The LI curve (see Figure 127) of these narrow QC lasers had a well-defined shape exhibiting sharp drops in the collected optical power at $J_{th} \approx 6.7$ and 14 kA/cm^2 after an straight initial slope of $\partial P/\partial I \approx 60$ mW/A. The $T_0 = 117$ K (see Figure 126) was slightly improved over the 15 μm-wide devices. This is consistent with the lower temperature elevation of the core predicted by the thermal modelling for narrower waveguides (see 5.2.1). The far-field profile shown in Figure 128 was measured at a current of 2.4 A, which is marked on the LI curve in Figure 127. This device was edge-mounted on a copper block rather than on a TO-5 header, so that the distortion of the far-field profile by the set-up was much reduced. Referring back to Section 4.4.1.4, the calculated order in increasing g_{th} of the transverse modes was mode 1 ($g_{th} = 40.8$ cm^{-1}), mode 0 ($g_{th} = 43.7$ cm^{-1}), mode 2 ($g_{th} = 52.3$ cm^{-1}), mode 3 ($g_{th} = 118$ cm^{-1}), and then mode 4 ($g_{th} = 762$ cm^{-1}). Comparing the measured far-field profile with the calculated ones in Section 4.4.2.4, we see that the measured profile did not correspond to any single waveguide mode and therefore indicated the simultaneous lasing of two or more transverse modes, or hopping between them during the pulse. The combination of calculated profiles which are suggested as those best fitting the features of the measurement, modes 1 and 2, and perhaps mode 0, are displayed again for convenience in Figure 129.

8.3 Shallow-etched $\lambda \approx 5$ μm QCLs of rib width = 17 μm

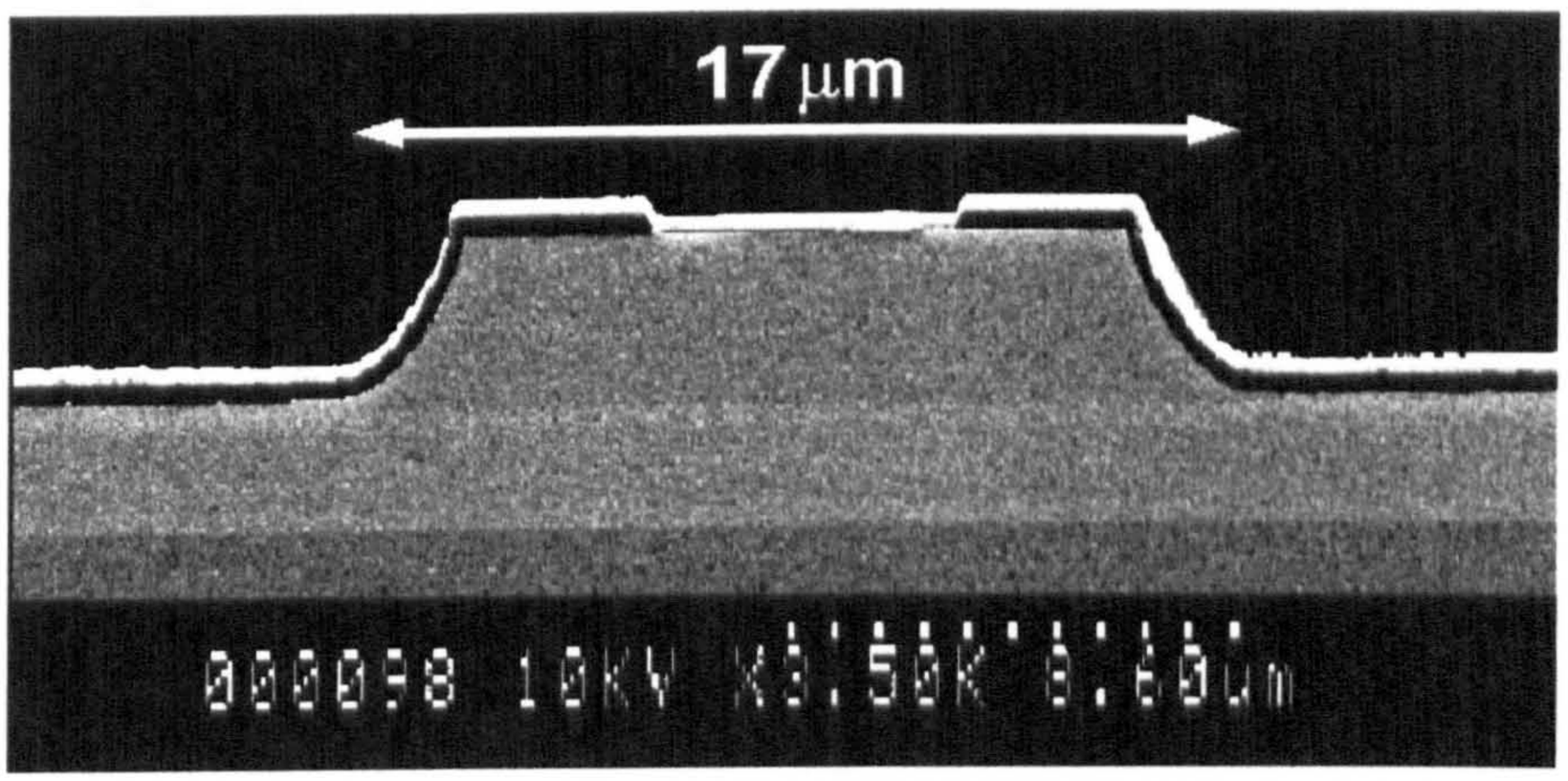

Figure 130 Scanning electron micrograph of the cleaved laser facet of one of the shallow-etched QCLs. Again, please refer to the caption of Figure 112 for a description of the layers. The measured rib width was $W = 17$ μm.

In the batch A1376.1, only the upper cladding was etched away on either side of the injection window. This left the active waveguide core intact to form a 'shallow-etched' QC laser, with a rib width of 17 μm in this case. These devices have been shown to be capable of very high values of T_0, but this comes at the expensive of a high threshold current owing to poor lateral electrical confinement.[3]

8.3.1 QCL A1376.1.1, L_{cav} = 2 mm, SiO_2 Dielectric

Unfortunately, only a single LI curve at $T = 10$ K was performed for this device so no value of T_0 could be obtained for this device (this was not owing to any limitation of the device). Note also that the output power was still increasing when the current pulse generator reached its maximum output, so output powers > 0.56 W may be expected with additional current injection above $I = 7$ A. The threshold current of the shallow-etched laser was ~ 3 times greater than that expected for a 17 μm-wide mesa-etched laser, which suggested an effective width of $W \approx 55$ μm at threshold. This signified a large lateral spreading of the current into the

unetched core beyond the central 17 μm-wide rib, in agreement with the results reported by Gmachl *et al.* for shallow-etched QCLs using a $\lambda \approx 8.5$ QC active region design.[3]

Referring to Figure 131, there was an upwards kink in the LI at $I \approx 5.8$ A, which perhaps indicated the appearance of another transverse mode with a higher collection efficiency. The slope efficiency increased from 0.09 to 0.2 W/A at that point. With reference to the calculated threshold gain and far-field profiles for this device (see Sections 4.4.1.6 and 4.4.2.6, receptively), we expect that lasing will commence mode 3 (g_{th} = 44.6 cm^{-1}). The modes in order of increasing g_{th} above mode 3 were: mode 4 (g_{th} = 44.7 cm^{-1}), mode 2 (g_{th} = 45.3 cm^{-1}), mode 1 (g_{th} = 45.7 cm^{-1}), and then mode 0 (g_{th} = 46.6 cm^{-1}). The lasing of one of these modes could have increased the collection efficiency (calculations of the collection for each mode have not been carried out yet).

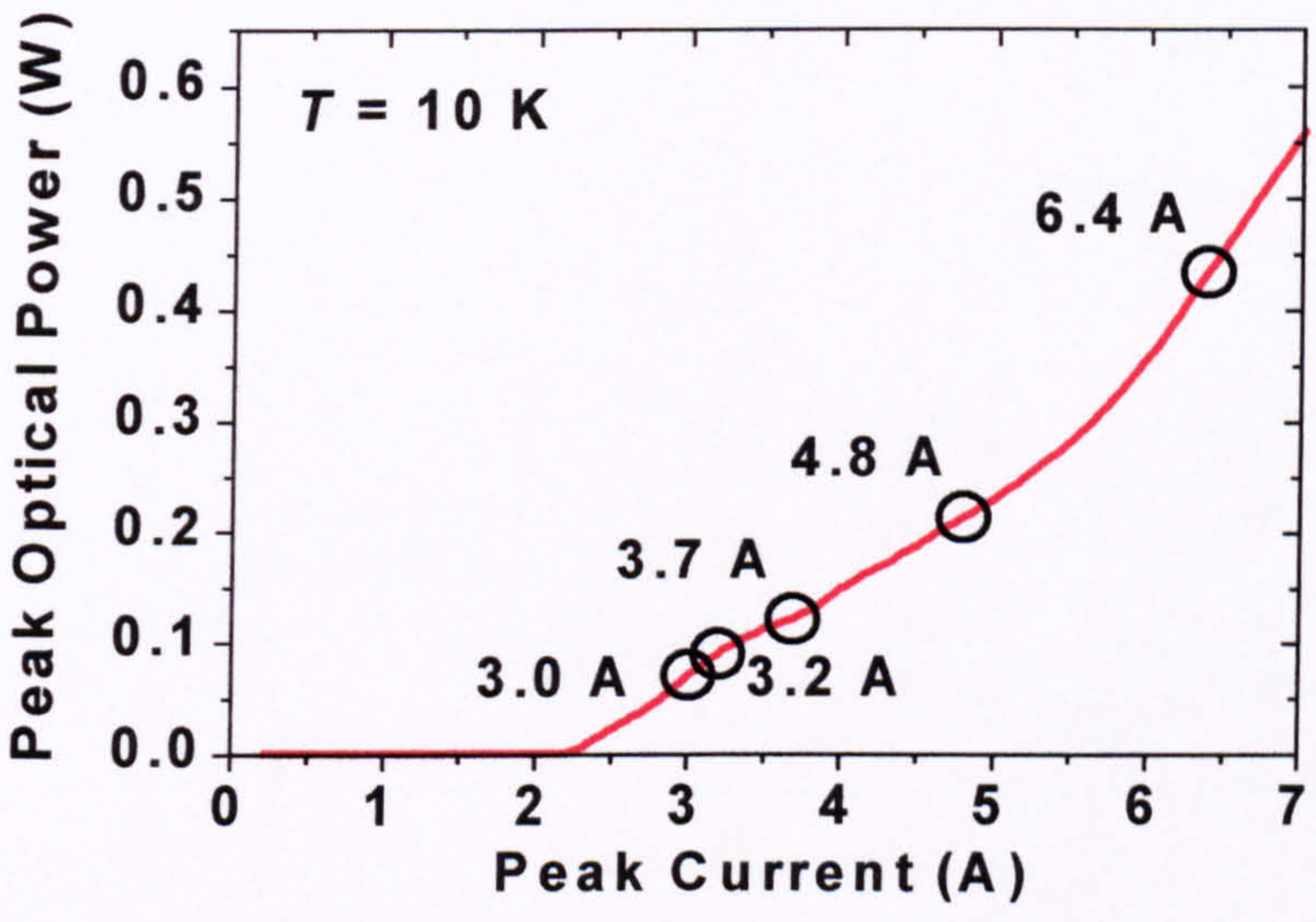

Figure 131 Measured LI curve of device A1376.1.1.

Parameter	Value
W (μm)	17
L_{cav} (mm)	2 ± 0.05 mm
J_{th} (kA/cm^2) at $T \approx 10$ K	6.5
P (W) per facet max. at $T \approx 10$ K	0.56
$\partial P/\partial I$ (W/A) at $T \approx 10$ K	first 0.09, then 0.2
T (K) maximum	-
T_0 (K)	-
$\Delta\omega$ (cm^{-1})	0.74
n_{eff}	3.30 to 3.47

Table 54 Key parameters measured for laser A1376.1.1. The J_{th} was calculated assuming W = 17 μm.

The spectra at different drive currents were measured, but in this case, the higher resolution capabilities of the FTIR spectrometer were put to better use so that the longitudinal modes were resolved to a higher degree. Over 60 longitudinal modes were counted in the spectrum at $I = 6.4$ A. The small dip at $\omega \approx 1942$ cm^{-1} could be attributed to an absorption line of water.[4]

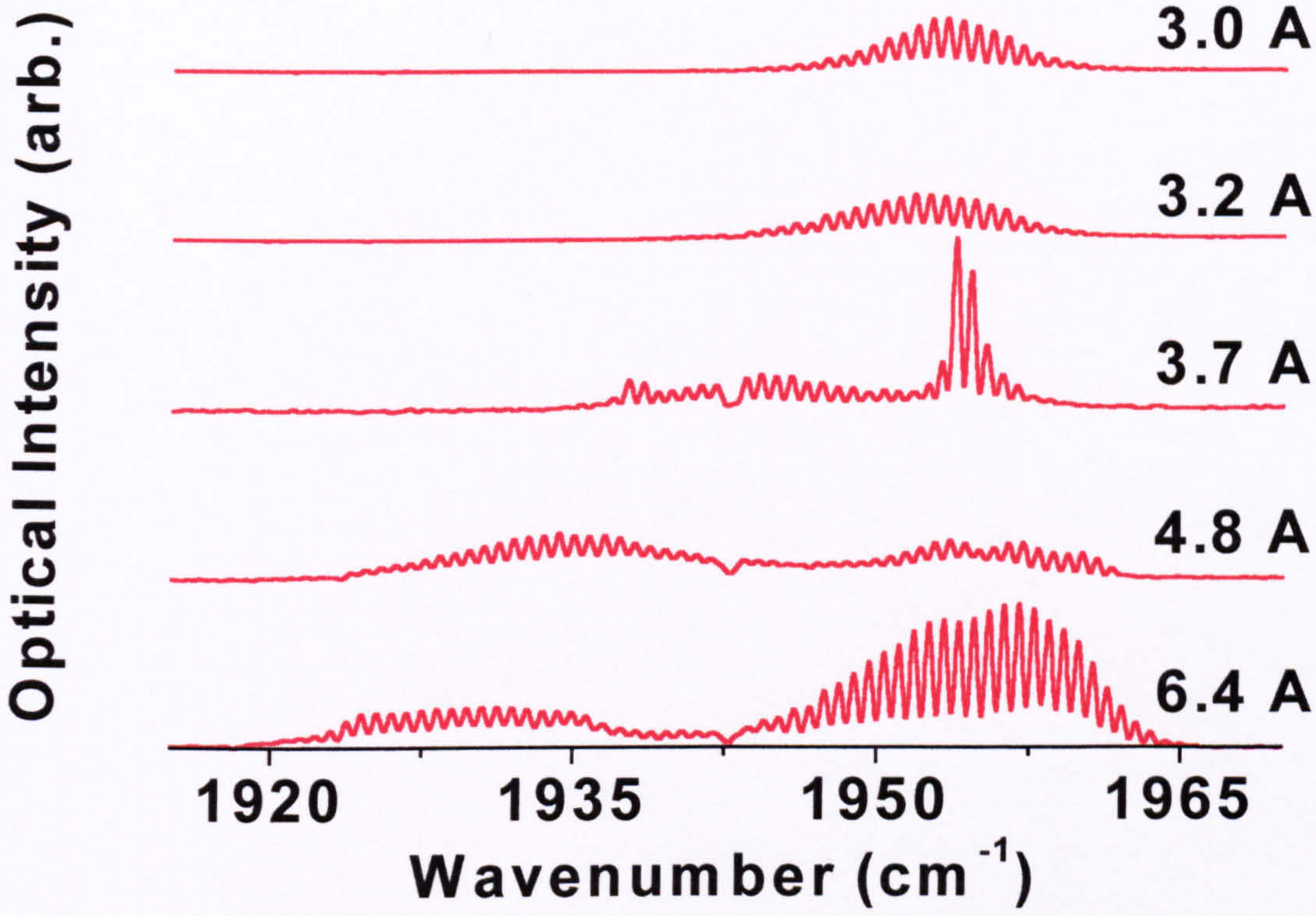

Figure 132 Measured emission spectra of device A1376.2.2 at a series of drive currents. Note that where the power axis scale of the spectra has been multiplied, the multiplication factor has been shown to the right of the spectrum.

8.4 Broad-area, mesa-etched $\lambda \approx 5\ \mu m$ QC lasers of width $\approx 112\ \mu m$

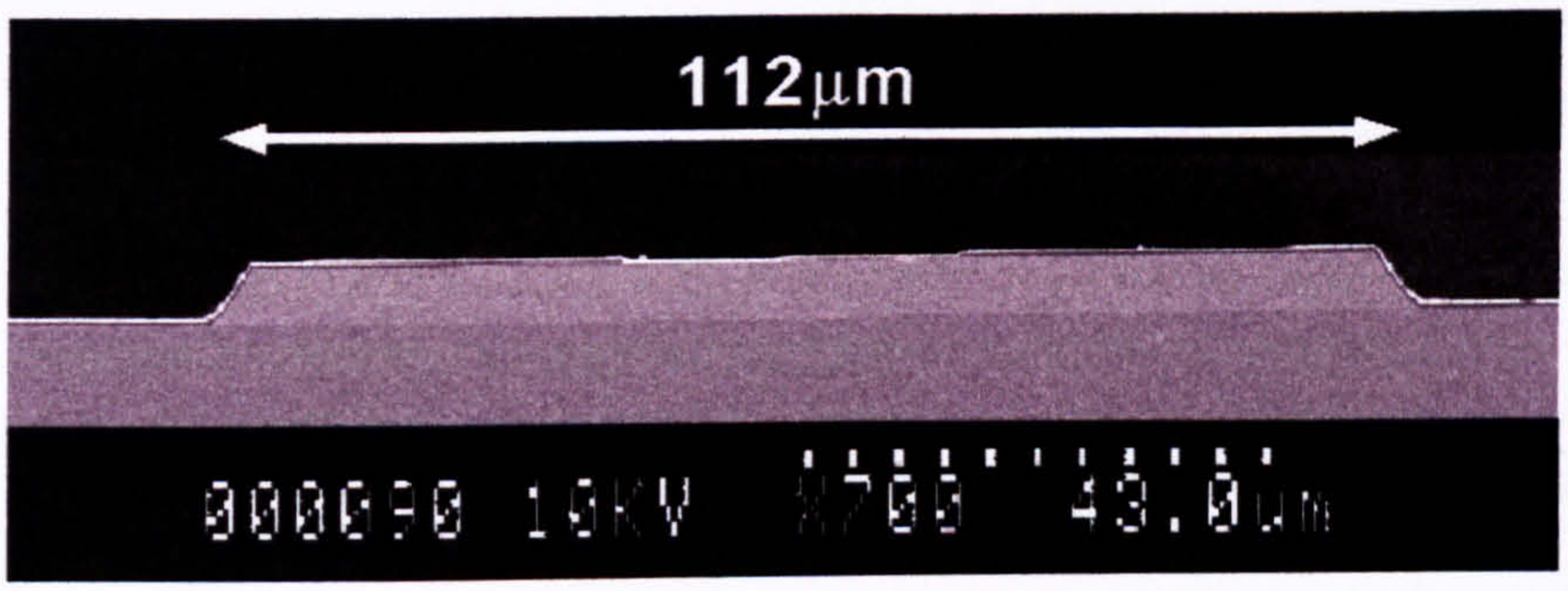

Figure 133 Scanning electron micrograph of the cleaved laser facet of one of the broad-area mesa-etched QCLs. The measured width was $W = 112\ \mu m$.

8.4.1 QCL A1376.3.3, L_{cav} = 1 mm, SiO_2 Dielectric

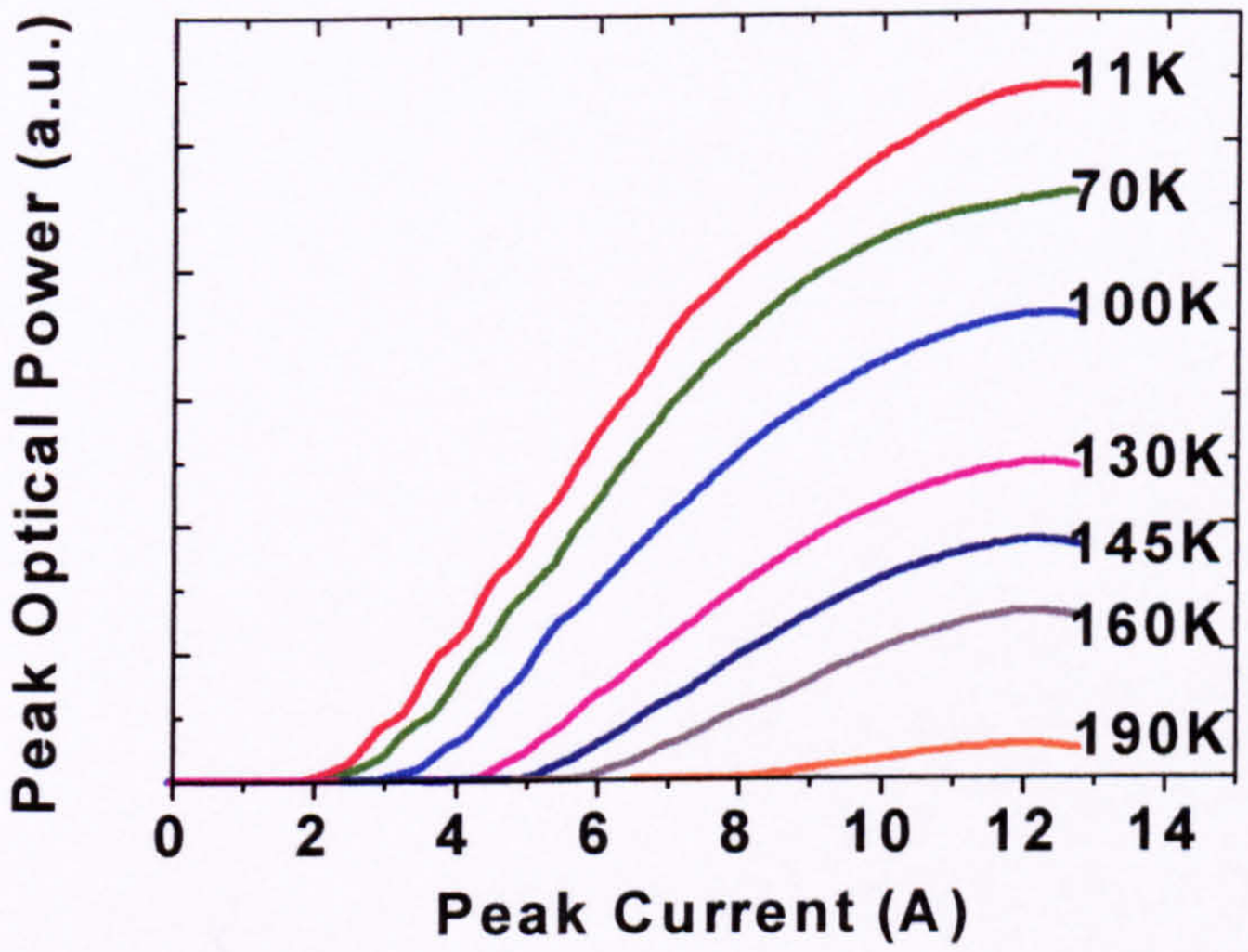

Figure 134 Measured LI curves of device A1376.3.3 at a series of heatsink temperatures.

Although we expect high output power from these broad-area devices, unfortunately the optical power was not calibrated owing to unavoidable equipment malfunctions. Further, our collaborators reported that there was a problem with the current calibration in this measurement too, so the currents shown are only a rough guide. We therefore present only the shape of the LI curve! In particular, attention is brought to the ripples on the LI curve at low temperature and current which were thought to be the caused by additional transverse modes reaching threshold with increasing drive current. This was consistent with the optical modelling of the waveguide modes, which indicated the existence of a large number of transverse modes with close values of threshold gain. The relatively straight nature of the LI curve can be explained by the low divergence of output beam and the weak dependence of the beam divergence on the transverse mode order.

8.5 Mesa-etched $\lambda \approx 5$ μm QCL Array with mesa width = 11 μm

8.5.1 A1376.8.1, L_{cav} = 2.6 mm, array of 3 waveguides spaced 150 μm apart, SiO_2 Dielectric

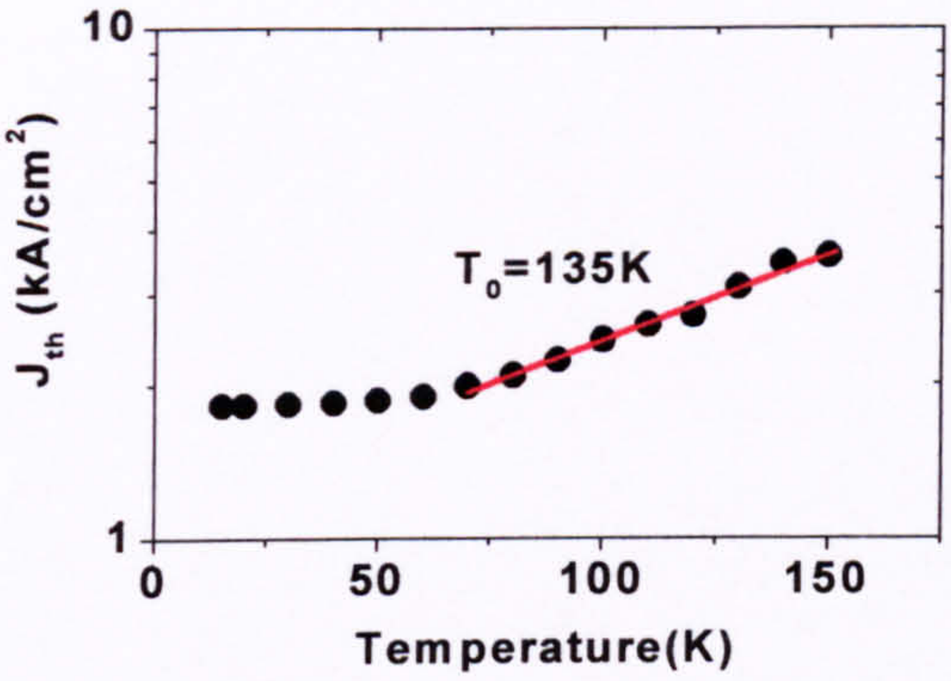

Figure 135 Measured temperature-dependence of J_{th} of the A1376.8.1 QC array laser.

The motivation for fabricating arrays of narrow mesa was to take advantage of the lower temperature elevation of the waveguide core in narrow mesa (see Section 5.3.3), while counteracting the lower output power available from them by using multiple lasers in parallel. Ultimately, the aim was essentially to obtain higher CW operating temperatures and average output powers, but this was not put to the test.

The array lasers were fabricated in the same way as the usual mesa-etched QC lasers, but the spacing between the laser waveguides was reduced to 150 μm. The results presented here were for an array of three 2.6 mm-long lasers spaced 150 μm apart. In contrast to previous measurements, these devices were tested using the characterisation system constructed by the author at the University of Glasgow. This system was very similar in many ways to that of our collaborators, using the same current probe model, a liquid nitrogen-cooled MCT detector, an *f*/1.4 gold-coated parabolic collection mirror, an Oxford Instruments closed-cycle continuous-flow cryostat, and a pulse generator capable of 100 ns pulses at a pulse repetition frequency of 5 kHz. For this measurement, the device was driven with 200 ns-long pulses at a pulse repetition frequency of 5 kHz.

The threshold density current was measured as a function of temperature and is displayed in Figure 135. The J_{th} was again high, consistent with the previous measurements and the improper doping of the InP substrate. The T_0 was significantly higher than in the previous devices, but this may have simply been a consequence of these measurements being performed in a different cryostat, perhaps with better heatsinking. In any case, the initial results were encouraging and the arrays warrant further investigation once material with the correct the correct substrate doping level is obtained since this limited their performance.

8.6 PSWOX $\lambda \approx 5\ \mu m$ QC lasers, oxide aperture = 20 μm

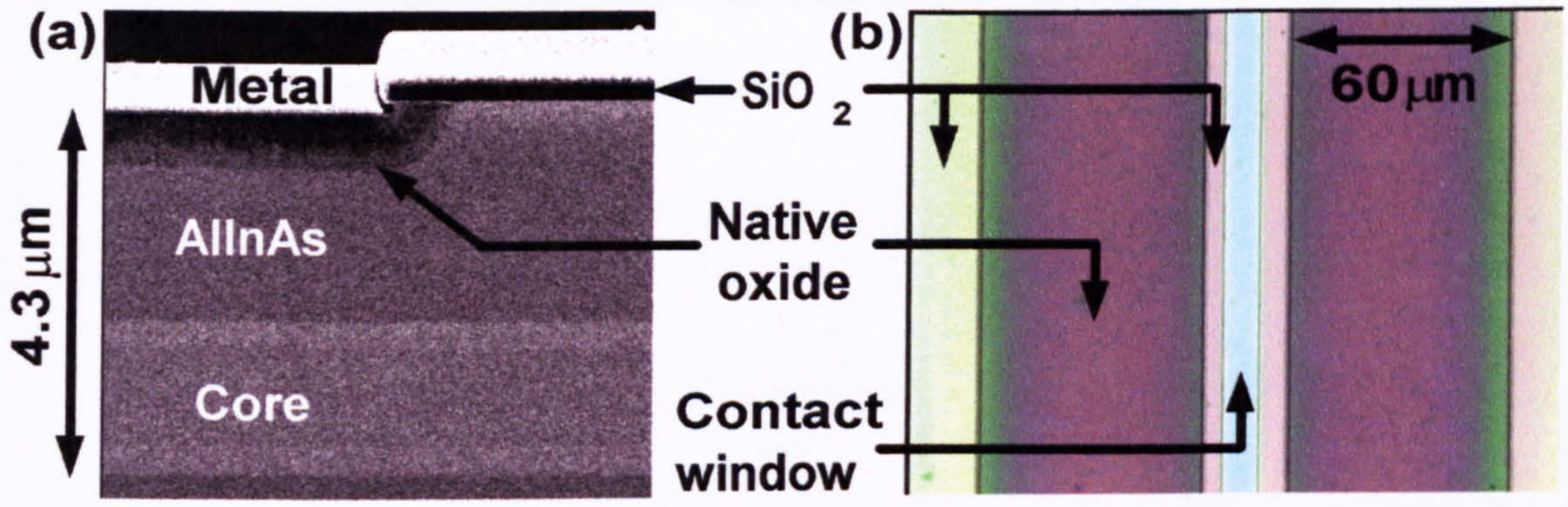

Figure 136 (a) scanning electron micrograph of the cross section of the PSWOX QC laser after metallisation and (b) a plan view micrograph of the same waveguide before metallisation using an optical microscope.

The motivation behind the investigation of the PSWOX QC lasers was outlined in Section 5.2.3 and their fabrication is covered in Sections 6.3 and B.1. Oxidation down through the entire 2.5 μm-thick $In_{0.52}Al_{0.48}As$ upper cladding was desirable, but was not achieved at the time. This was due to the infancy of the development of the process in our dept. and restrictions imposed by the equipment used.

Fig. 1(a) shows a scanning electron microscope (SEM) cross-section of the facet of a completed PSWOX QC laser at the edge of the waveguide. The micrograph shows a darkened region extending ~ 0.65 μm down from the upper surface of the $In_{0.52}Al_{0.48}As$ cladding. Here the semiconductor had been exposed to the steam and is labelled 'native oxide'. Below the $In_{0.52}Al_{0.48}As$ upper cladding lay the QC laser waveguide core. Fig. 1(b) shows a plan view image of a section of the laser before the final metallisation had been carried out. In the centre, running vertically, was the 20 μm-wide optical waveguide. The lighter bar in the centre of the waveguide corresponded to the region where the silica oxidation mask had been removed to form the 8 μm-wide contact window. The 60 μm-wide dark regions on either side of the waveguide were the native oxide layers. The subsequent metallisation step for current injection made contact to the waveguide through the 8 μm-wide contact window. In the lateral direction the spread of injected current was limited to some extent by the electrically insulating oxide regions, and the low refractive index of the oxide ($n \approx 1.67$ at $\lambda = 1.55\ \mu m$)[5] provided optical confinement. The limited depth of this oxide region implied that these lasers were similar to shallow-etched QC lasers, in that a large degree of current spreading could be expected.

8.6.1 QCL A1376 PSWOX.2.2, L_{cav} = 2 mm, on TO-5 header

The measured LI curves in Figure 137 indicated high output powers which would perhaps have continued to increase beyond the output current limitations of the equipment. Similarly, the maximum temperature of operation was limited by the maximum drive current of the pulse generator. The I_{th} rose beyond the upper limit of the equipment at $T \approx 130$ K. The slope efficiency at $T = 10$ K was measured as $\partial P/\partial I \approx 440$ mW/A. The curves were relatively straight, indicating that either there was no hopping between transverse modes or that the collection efficiency of the transverse modes was very similar. Indeed, the optical modelling of the PSWOX QCL had indicated that there should only be a single guided horizontal transverse mode (see Section 4.4.1.8). The $J_{th} \approx 9.5$ kA/cm^2 at $T = 10$ K, calculated using the measured $I_{th} = 3.8$A, $W = 20$ μm and $L_{cav} = 2$mm, was very high and suggested that a large lateral current spreading took place. Based on the J_{th} of

the mesa-etched QCLs, the effective width of device at threshold was ~100 μm rather than 20μm. The inferior electrical confinement compared to that of the shallow-etched QC laser could be explained by the presence of the highly doped $In_{0.52}Al_{0.48}As$ upper cladding which remained unconverted (to native oxide) between the native oxide layer and the core. Despite the large effective width of the laser and subsequent high threshold currents, an improved T_0 = 129 K was observed (see Figure 138). This at fulfilled one of the aims of the device.

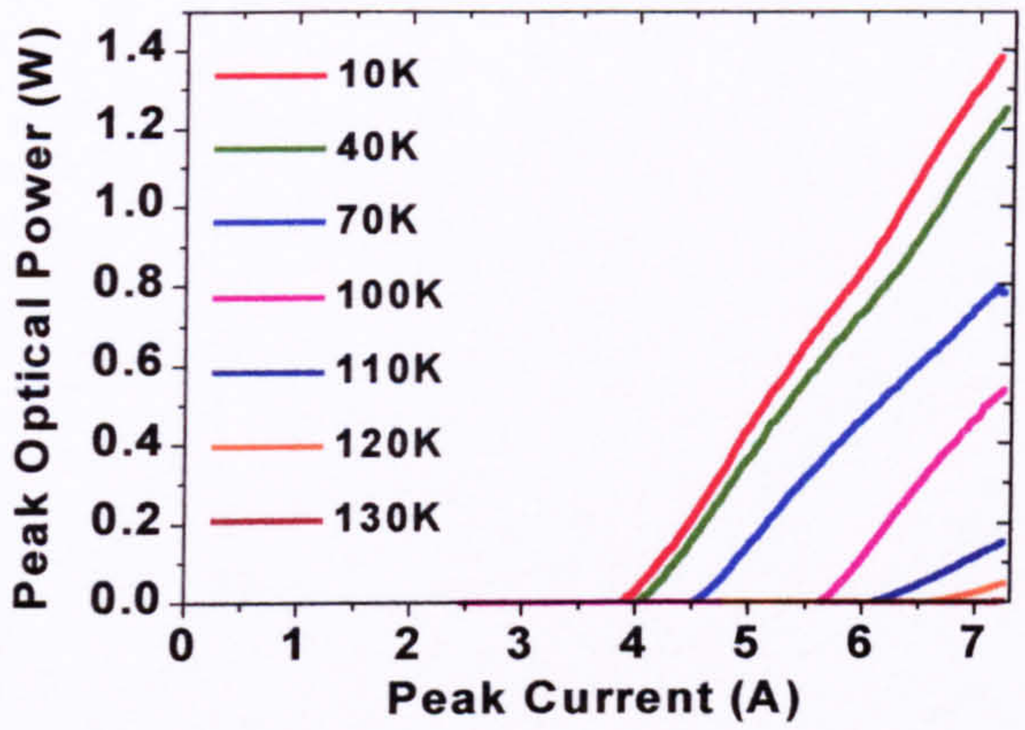

Figure 137 Measured LI curves of device A1376 PSWOX.2.2 at a series of heatsink temperatures.

As expected from the optical modelling, a comparison of vertical and horizontal cross sections of the measured far-field profile of a PSWOX QCL (see Figure 139) revealed a very narrow beam divergence in the horizontal plane compared to that in the vertical plane. In the horizontal plane the FWHM of the beam was ~6 times lower than in the vertical direction. The high divergence in the vertical direction was typical for the high level of optical confinement provided by the thin plasma-enhanced waveguide, with the beam waist at the facet being ~ 3 μm in the vertical direction. The equation below can be used to estimate the beam divergence, θ_{beam} in radians (the half-apex angle), given the wavelength of the light λ (m), and the radial FWHM size of the optical mode at the laser facet ω_0 (m), [6]

$$\theta_{beam}(rad) = \tan^{-1}\left(\frac{\lambda}{\pi\omega_0 n}\right) \approx \frac{\lambda}{\pi\omega_0 n}.$$

The far-field profile in the horizontal direction indicated a beam waste of ~ 6 × 3 = 18 μm. This indicated that stimulated emission was only being emitted from the active waveguide core situated immediately below the 20 μm-wide oxide aperture.

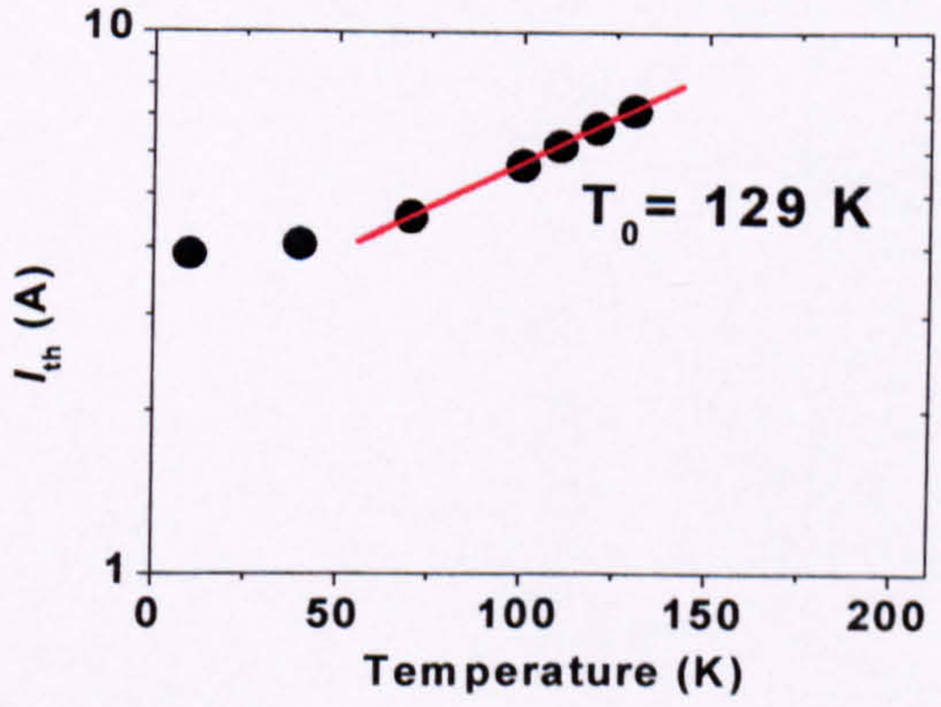

Figure 138 Measured temperature-dependence of J_{th} of device A1376 PSWOX.2.2.

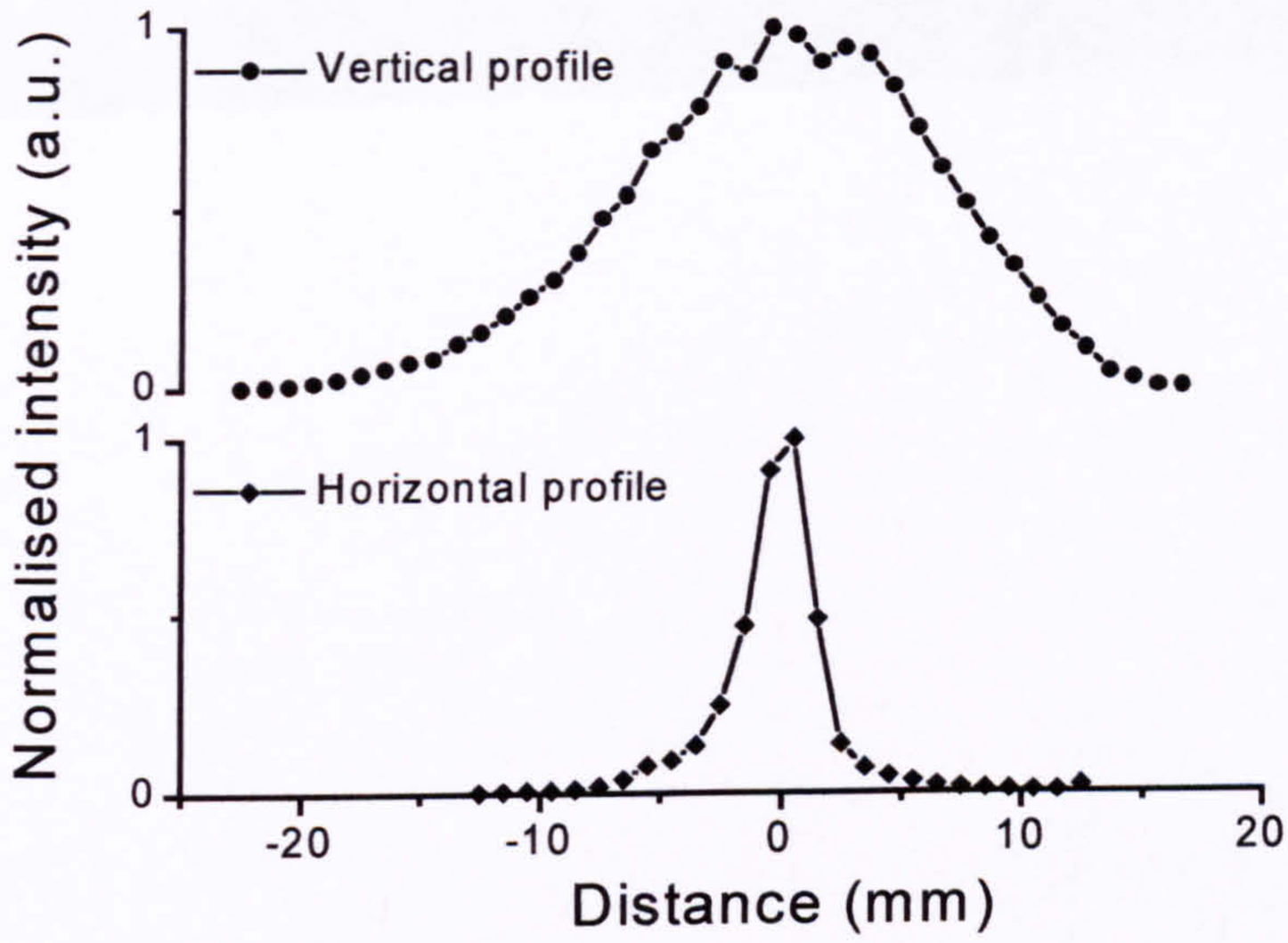

Figure 139 Normalised cross sections of the far-field emission patterns measured in the directions normal (vertical profile) and parallel (horizontal profile) to the epitaxial layers. The distance between the detector element and the laser facet was not measured.

Since it was shown that the light was only being generated in the ~ 20 μm region below the oxide aperture, this indicated that the current which spread laterally did not contribute to the emitted optical power. This current will only have generated phonons, and very few photons, as it traversed the waveguide core under the native oxide regions (owing to the poor radiative efficiency below threshold). In contrast, the high slope efficiency which was measured above threshold implied that virtually all additional current injected above threshold generated photons which contributed to the output power emitted from the 20 μm-wide region under the oxide aperture. It is suggested that this could be understood by a reduction in the differential resistance of the lasing active regions owing to the enhancement of the electron transport by stimulated emission. Sirtori *et al.* showed that the slope efficiency was related to differential resistance above threshold, and that a small value of dV/dI was necessary to obtain high slope efficiency.[2]

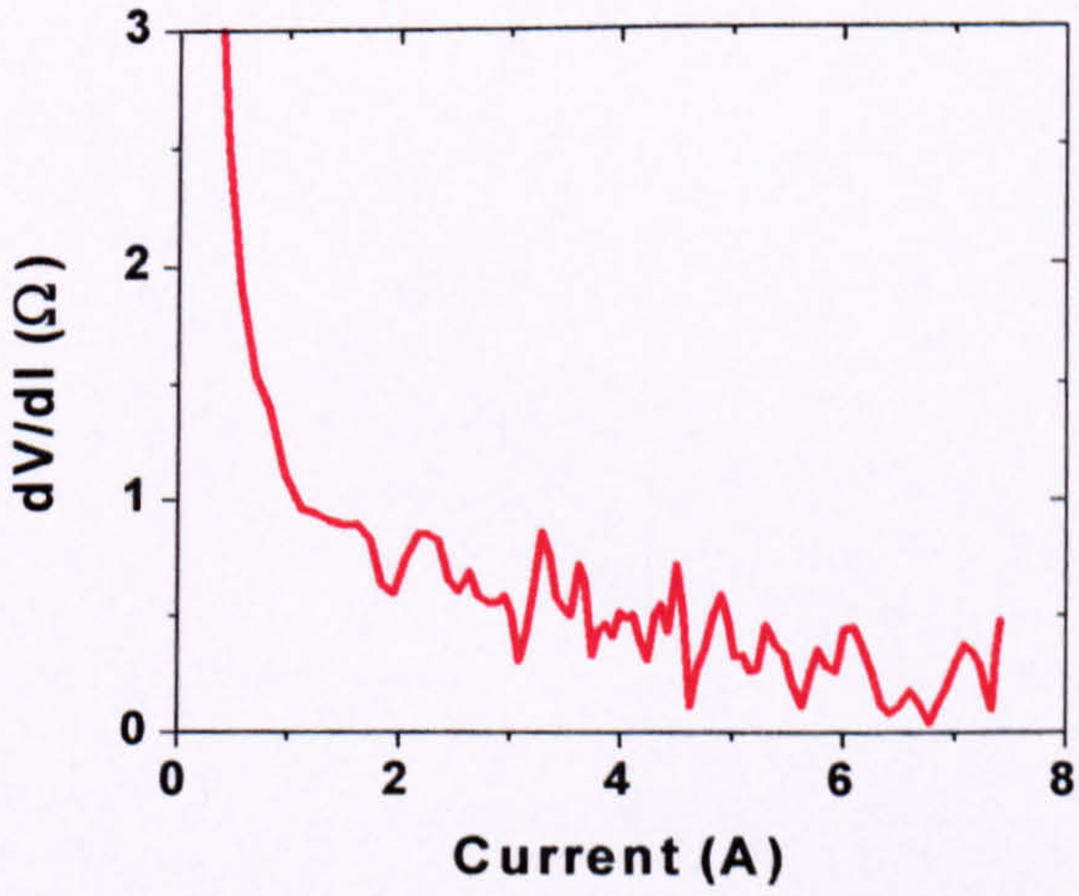

Figure 140 Differential resistance deduced from the IV curve of PSWOX.2.2.

From the measured IV curve, the differential resistance of the laser was plotted as a function of current in Figure 140. A low value was expected, limited by the series resistance the metal/semiconductor junctions, since the effective lateral width of the active waveguide core (~ 100 μm) was large compared to the contact

(~ 8 μm). Sure enough, the differential resistance followed downwards trend above the threshold current of $I \approx 4$ A, which does support the above argument. Further evidence pointing to these effects was found in a second PSWOX QC laser presented in Section 8.6.2.

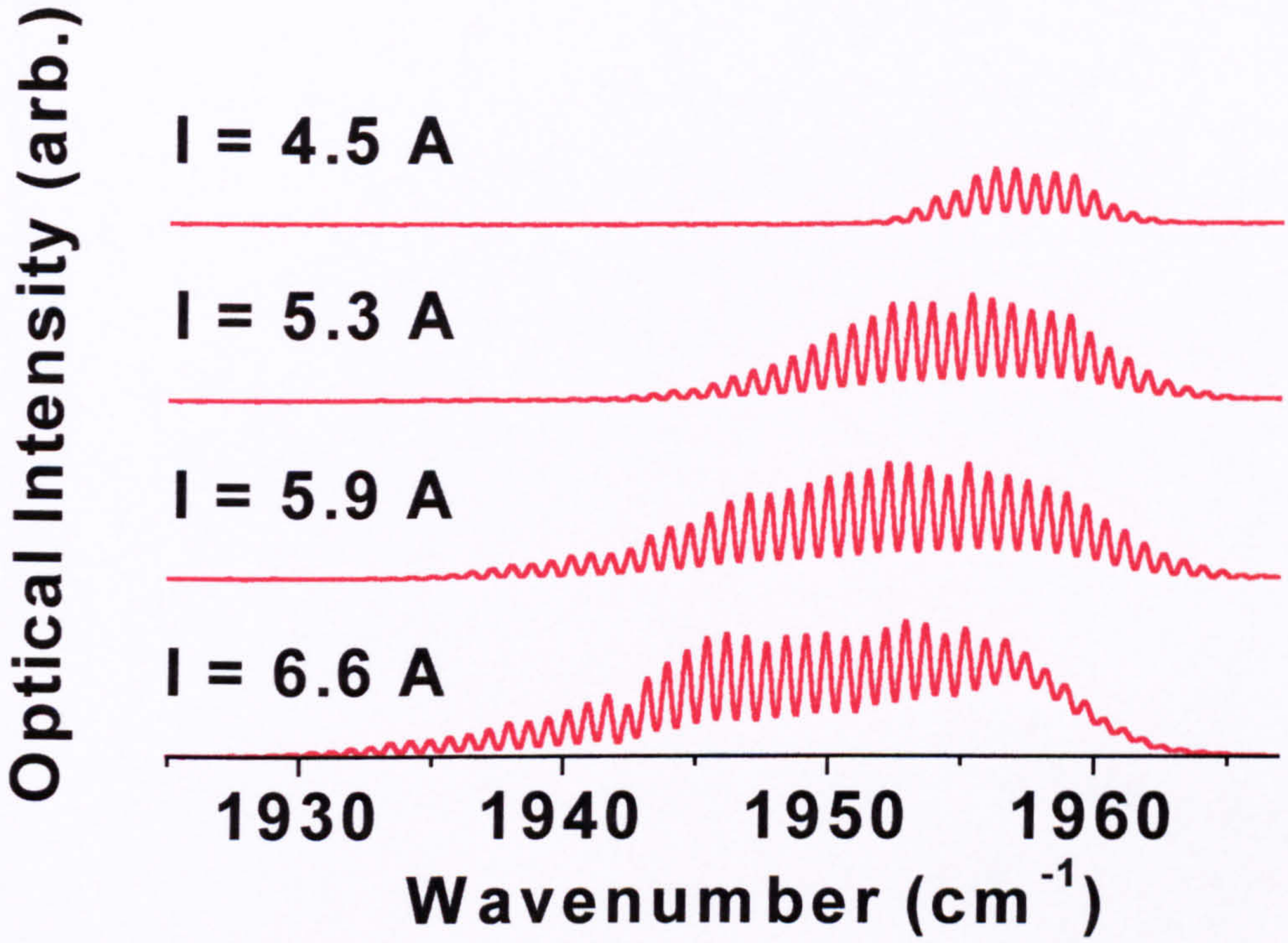

Figure 141 Measured emission spectra of device PSWOX.2.2 at a series of drive currents.

Spectra as a function of drive current were performed. The observed spectra broadened with current and shifted to lower energy. A slight modulation of the envelop of the spectrum at $I = 6.6$ A can be made out.

Parameter	**Value**
W (μm)	20
L_{cav} (mm)	2 ± 0.05 mm
J_{th} (kA/cm^2) at $T \approx 10$ K	9.5
P (W) per facet max. at $T \approx 10$ K	1.39
$\partial P/\partial I$ (W/A) at $T \approx 10$ K	0.44
T (K) maximum	130
T_0 (K)	129
$\Delta\omega$ (cm^{-1})	0.74
n_{eff}	3.30 to 3.47

Table 55 Key parameters measured for laser A1376 PSWOX.2.2b. The J_{th} was calculated assuming $W = 20$ μm.

8.6.2 QCL A1376 PSWOX.2.2b, L_{cav} = 2 mm, copper block

Results for a second PSWOX QCL from the same batch as A1376 PSWOX.2.2 are presented below. This device was mounted on a copper block rather than a TO-5 header.

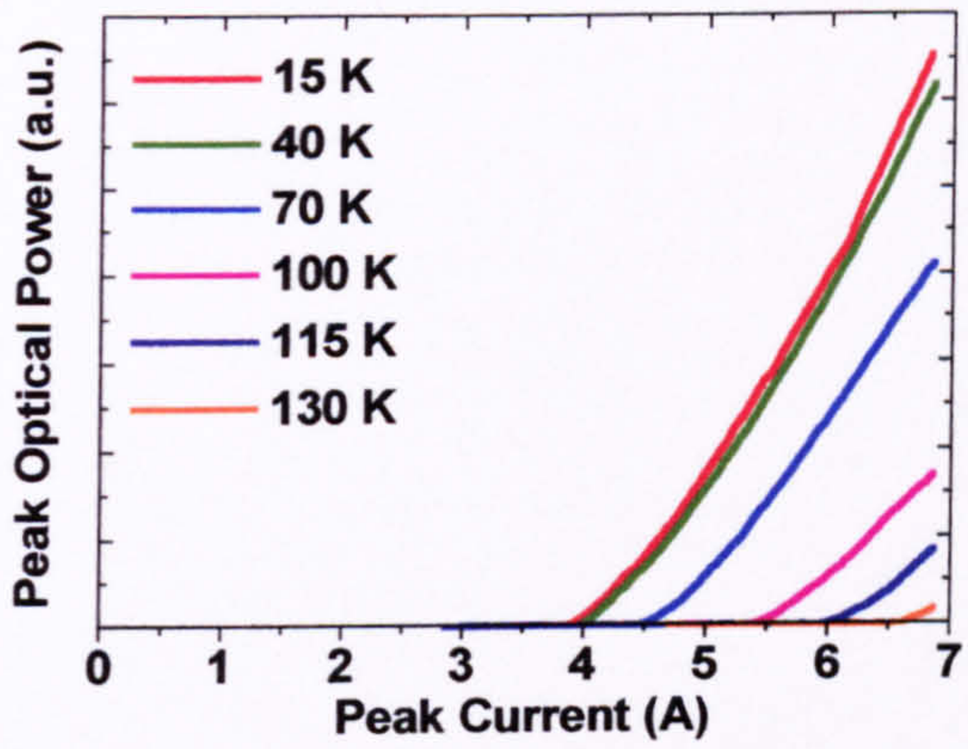

Figure 142 Measured LI curves of device A1376 PSWOX.2.2b at a series of heatsink temperatures.

The LI curves for this second device were similar in nature to those of PSWOX.2.2, except for two features. Firstly, the measured slope efficiency was approximately half that measured for the previous device PSWOX.2.2. Secondly, the LI curves exhibited an upwards curvature with current, indicating a gradually increasing collection or slope efficiency. The slope of the T = 15 K curve increased from ~ 0.1 W/A to 0.3 W/A from I = 4 to 7 A. An increase in collection efficiency as a function of current was not evident from the measured far-field profiles which will be given in Figure 146. An increase in the slope efficiency could be interpreted as an increase in the ratio of useful current to current lost via lateral spreading. This further supports the hypothesis that there may be a decrease in the differential resistance of the 20 μm-wide lasing region with increasing current/optical intensity.

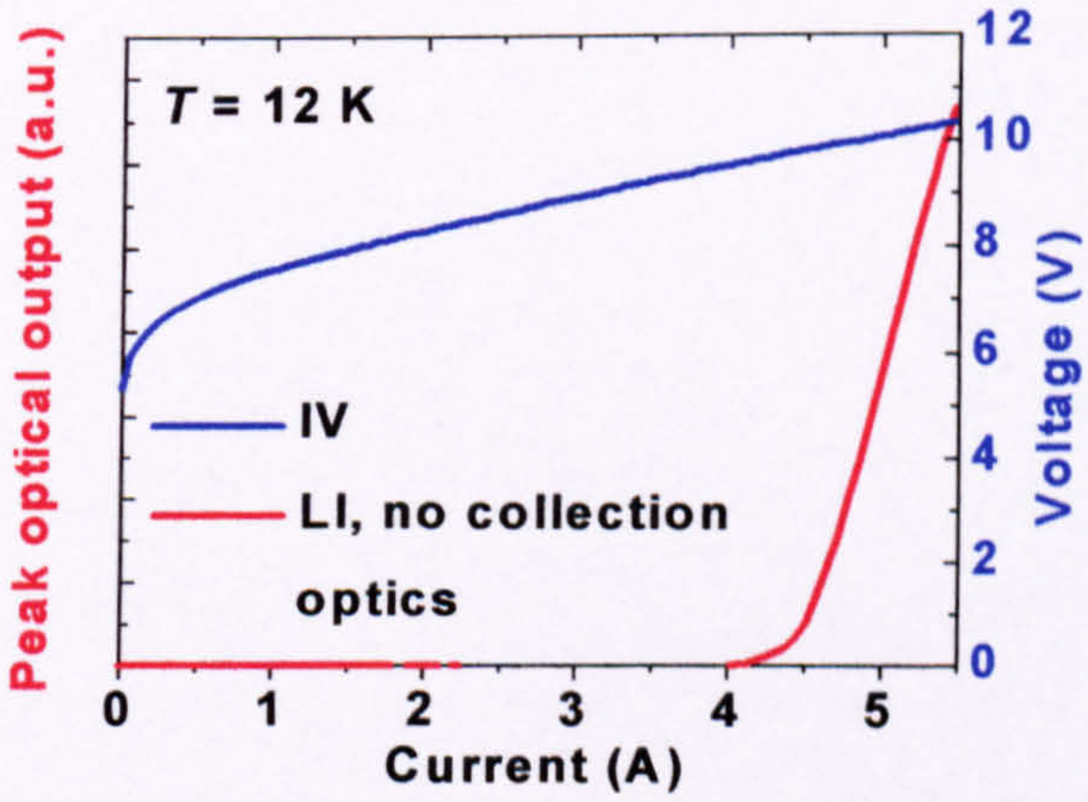

Figure 143 Simultaneously measured LI (red line) and IV (blue line) curves for device A1376 PSWOX.2.2a at T = 12 K.

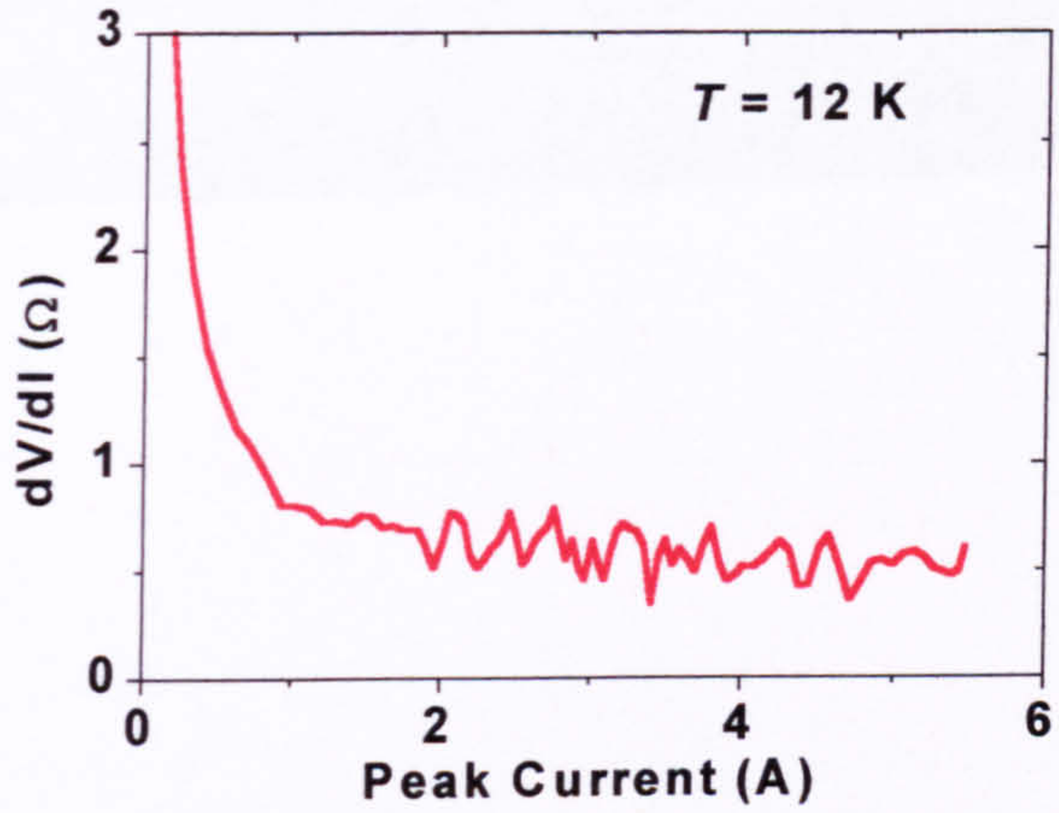

Figure 144 Differential resistance deduced from the IV curve in Figure 143.

From the measured IV curve, the differential resistance of this laser was plotted as a function of current in Figure 144. In this device, it would appear that the contribution of the contact resistance was much larger than in PSWOX.2.2, perhaps owing to damage to the semiconductor contact layer during the harsh fabrication. Gmachl *et al.* attributed 0.3 Ω of the differential resistance of their QC lasers to the metal contacts,[7] so this does not seem unreasonable. The differential resistance did continue a slight downwards trend with increasing current right to the end of the measured range, which again supports, if only very weakly, the possibility that their was a reduction in dV/dI associated with the stimulated emission enhancement of the electron transport through the active regions.

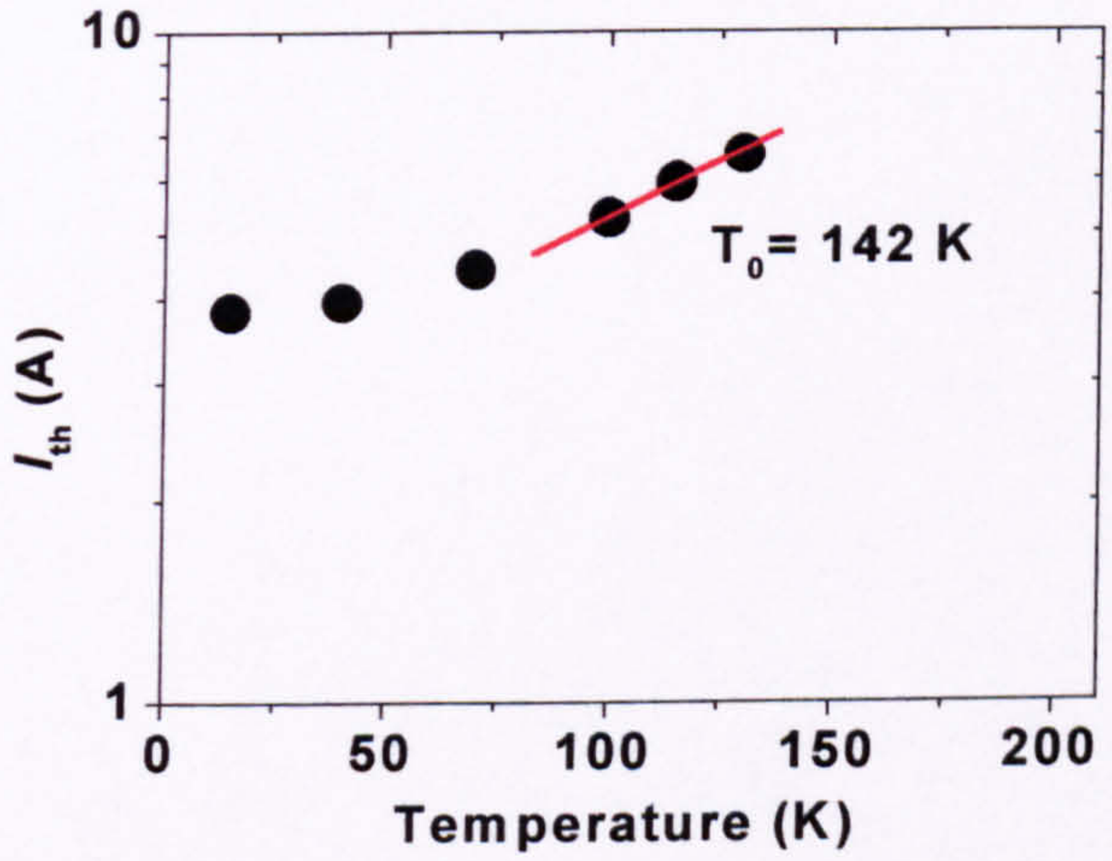

Figure 145 Measured temperature-dependence of J_{th} of device A1376 PSWOX.2.2b.

The T_0 = 142 K of the device mounted on the copper block was further improved over that on the TO-5 header (a third device mounted on a copper block also showed improved T_0 = 138 K). The T_0 of these PSWOX devices was at least 21 K higher than in mesa-etched QC lasers mounted on copper blocks for which the best value was T_0 = 117 K (see Section 8.2.1). The maximum temperature of operation was limited by the maximum drive current of the pulse generator.

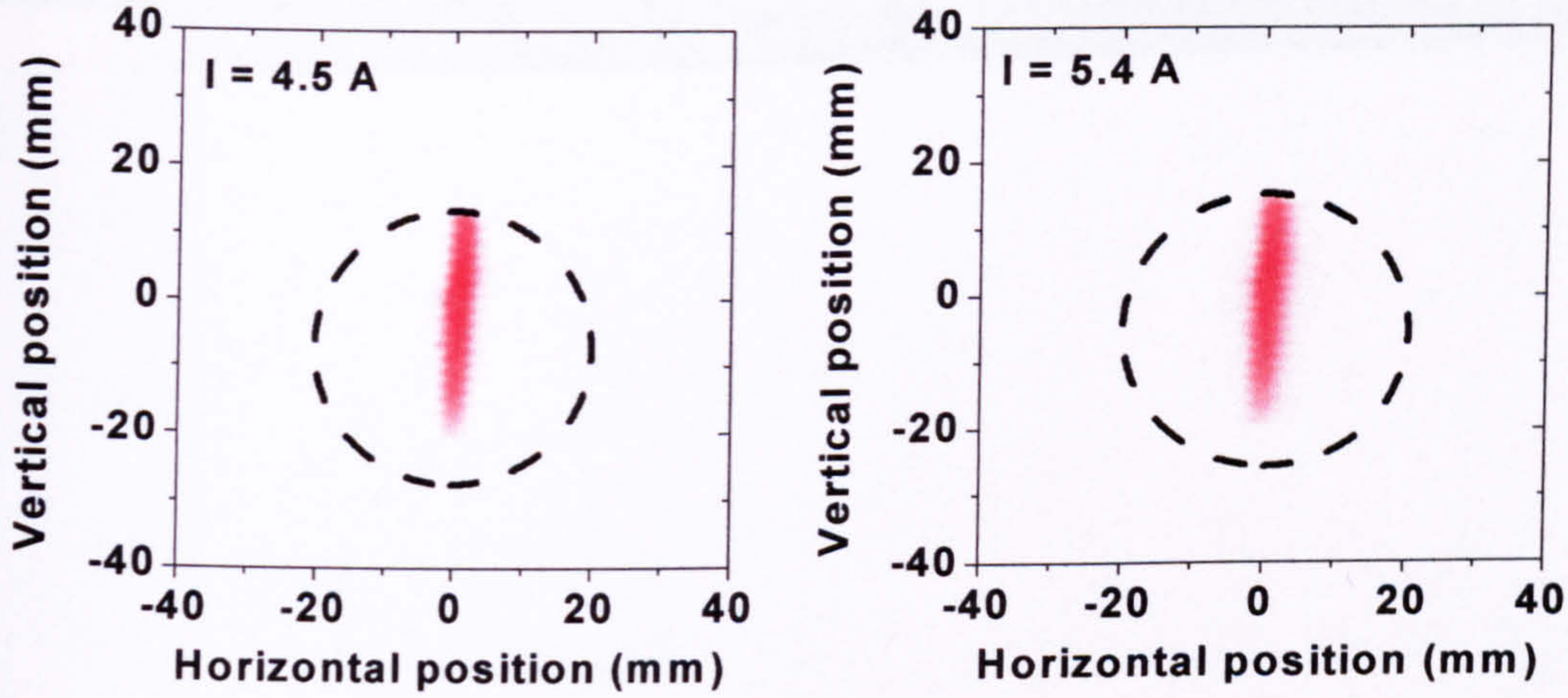

Figure 146 Measured far-field profiles of device A1376 PSWOX.2.2b at two drive currents. Note that the 'zigzag' on the profile was an artefact of the measurement.

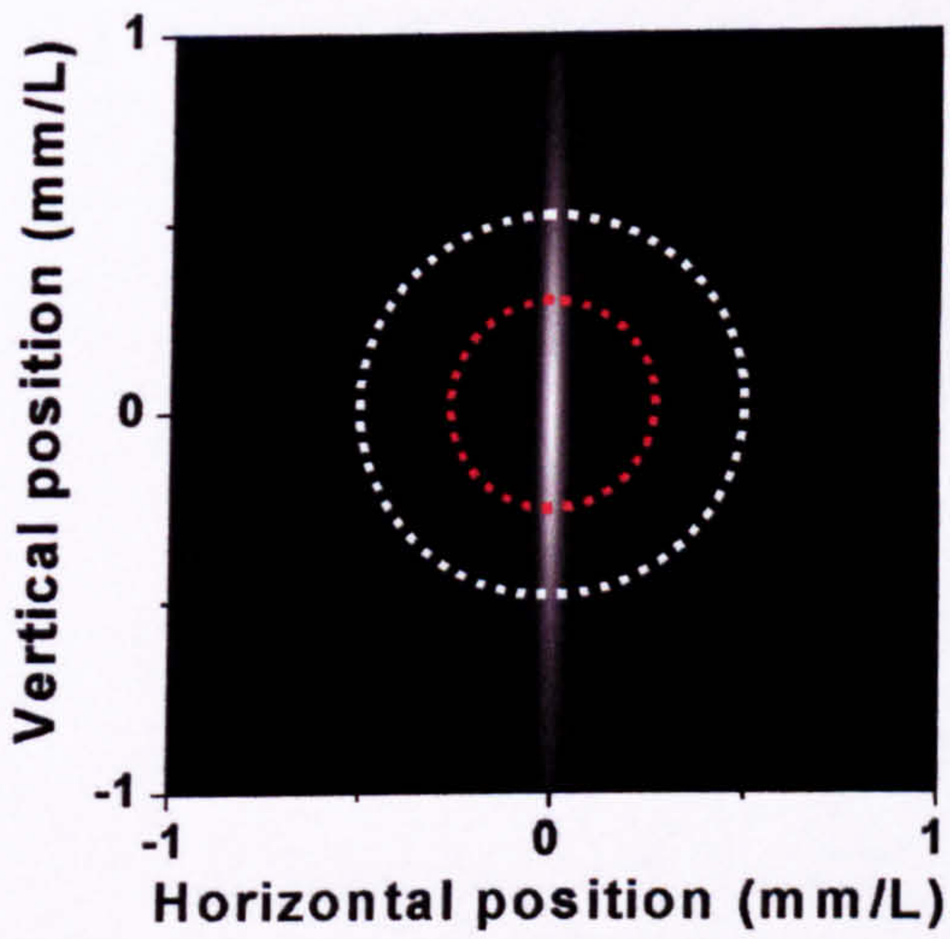

Figure 147 Calculated far-field profile of the PSWOX QCL (see Section 4.4.2.8). The white dotted circle represents a f/0.8 cryostat window and the red dotted circle f/1.7 parabolic collection.

The measured far-field profiles of device A1376 PSWOX.2.2b at $I = 4.5$ A and $I = 5.4$ A are given in Figure 146. The calculated far-field profile is displayed in Figure 147 for a quick comparison. First of all, in contrast to mesa-etched devices we saw no apparent change in the measured far-field with current, in agreement with the optical modelling. This accounted for the relatively straight LI curves of the PSWOX devices. The optical modelling also agreed well with the shape of the far-field beam, except that the calculated beam was narrower than the measured one. This can be explained by difficulties in accurately measuring the narrow beam. Looking closely, one can see a zigzag pattern on the measured far-field profile. The profile was generated by the performing a raster-like scan of the beam i.e. the detector element was stepped from left to right, step down, scan right to left, step down, scan left to right, etc. The zigzag suggests that that the detector was stepped too fast for the power measurement to respond before the next step. This resulted in a smearing the beam to produce the zigzag pattern and a broadening of the beam in the horizontal direction. Further, the width of the detector element (1 mm) was large compared to the calculated width of the beam (2 mm) so that the resolution of the measurement in the horizontal direction was low. Using a

smaller detector element or moving the detector further away from the laser would help (but would also reduce the signal to noise ratio).

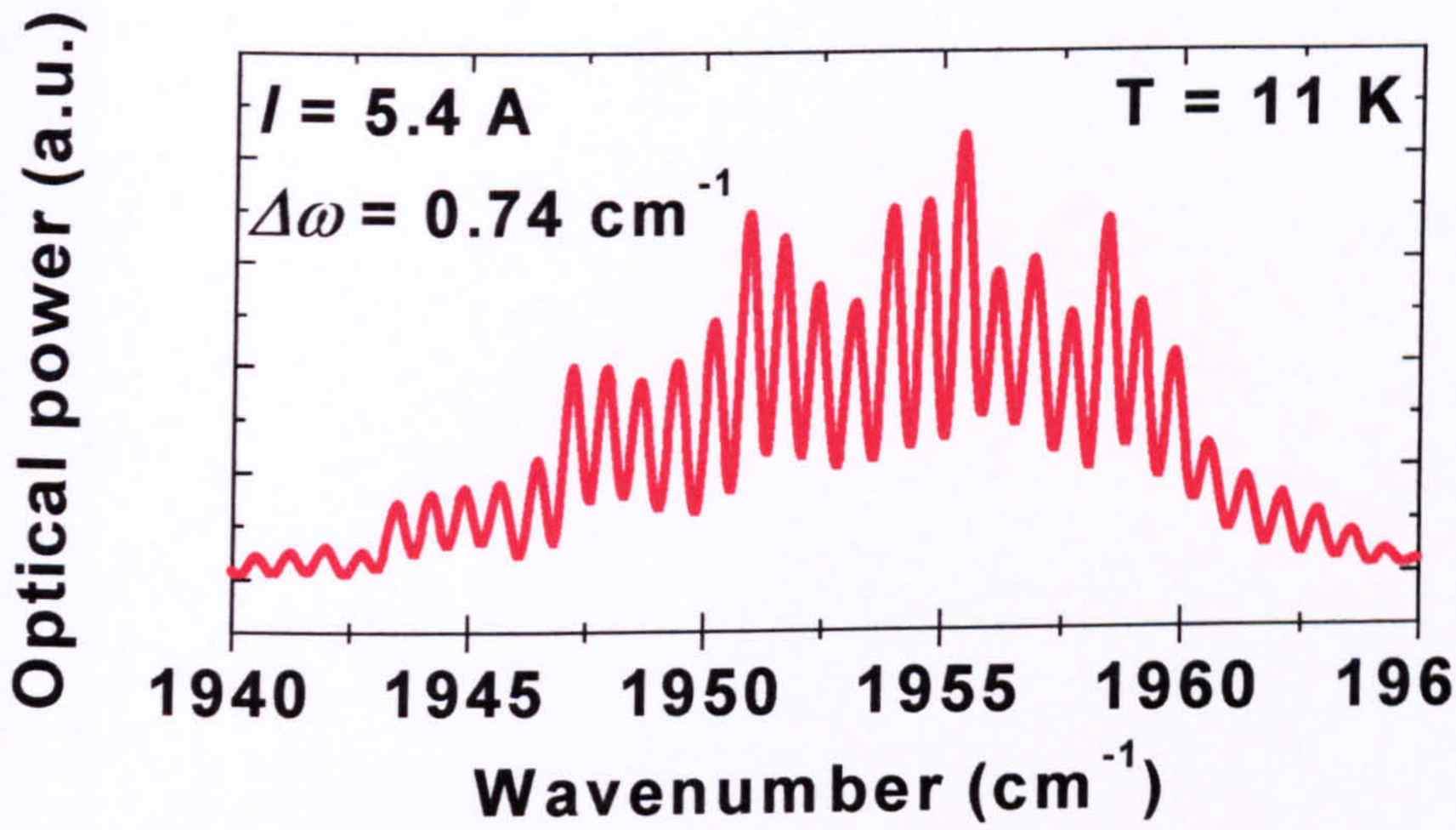

Figure 148 Measured emission spectra of device PSWOX.2.2b at $I = 5.4$ A and $T = 11$ K.

The emission spectrum of the laser at a drive current of $I = 5.4$ A $T = 11$ K is shown in Figure 148. The modulation of the envelope of the modes is noted, but as yet unexplained.

Parameter	**Value**
W (μm)	20
L_{cav} (mm)	2 ± 0.05 mm
J_{th} (kA/cm^2) at $T \approx 10$ K	9.5
P (W) per facet max. at $T \approx 10$ K	0.66
$\partial P/\partial I$ (W/A) at $T \approx 10$ K	0.1 to 0.3
T (K) maximum	130
T_0 (K)	142
$\Delta\omega$ (cm^{-1})	0.74
n_{eff}	3.30 to 3.47

Table 56 Key parameters measured for laser A1376 PSWOX.2.2b. The J_{th} was calculated assuming W = 20 μm.

8.6.3 QCL A1376 PSWOX.2.2c, L_{cav} = 0.9 mm, copper block

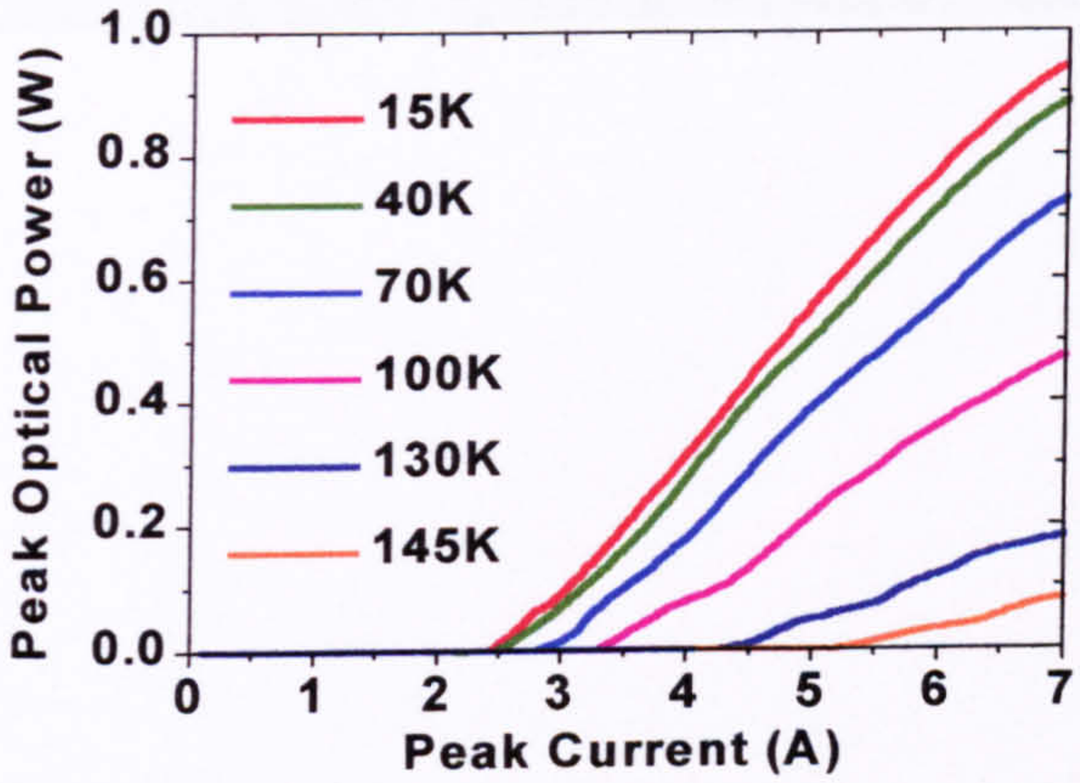

Figure 149 Measured LI curves of device A1376 PSWOX.2.2c at a series of heatsink temperatures.

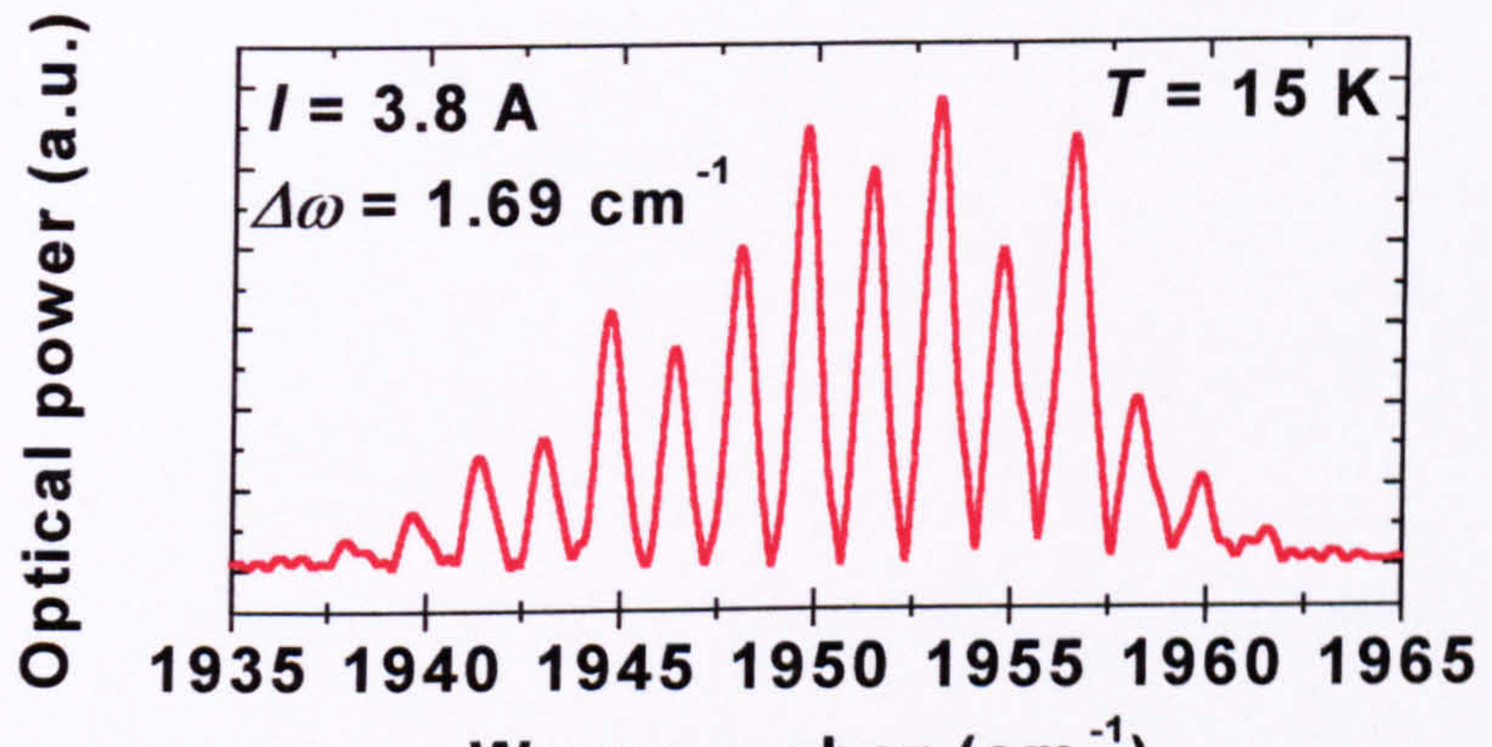

Figure 150 Measured emission spectra of device PSWOX.2.2c at I = 3.8 A, T = 15 K.

Results from one last PSWOX, which had a relatively short cavity length, L_{cav} = 0.9 mm, are presented. The use of short cavity allowed the mode spacing to be increased to $\Delta\omega$ = 1.69 cm^{-1} (see Figure 150). The motivation for this was that our collaborators at the University of Strathclyde, Glasgow required QC lasers for gas spectroscopy. A large mode spacing was useful to them so that they could use an external monochromator to select a single longitudinal mode.

Despite the short cavity length, the output power from this laser still managed to exceed 0.9 W per facet and the output power was still rising when the output current limit of the pulse generator was reached. The slope efficiency was more or less constant at 0.2 W/A over the full current range (T = 10 K). However, the T_0 = 76 K of this device was a very low, perhaps owing to a temperature elevation of the core above that of the heatsink as a result of the high threshold current density $J_{th} \approx 13.3$ (assuming W = 20 μm).

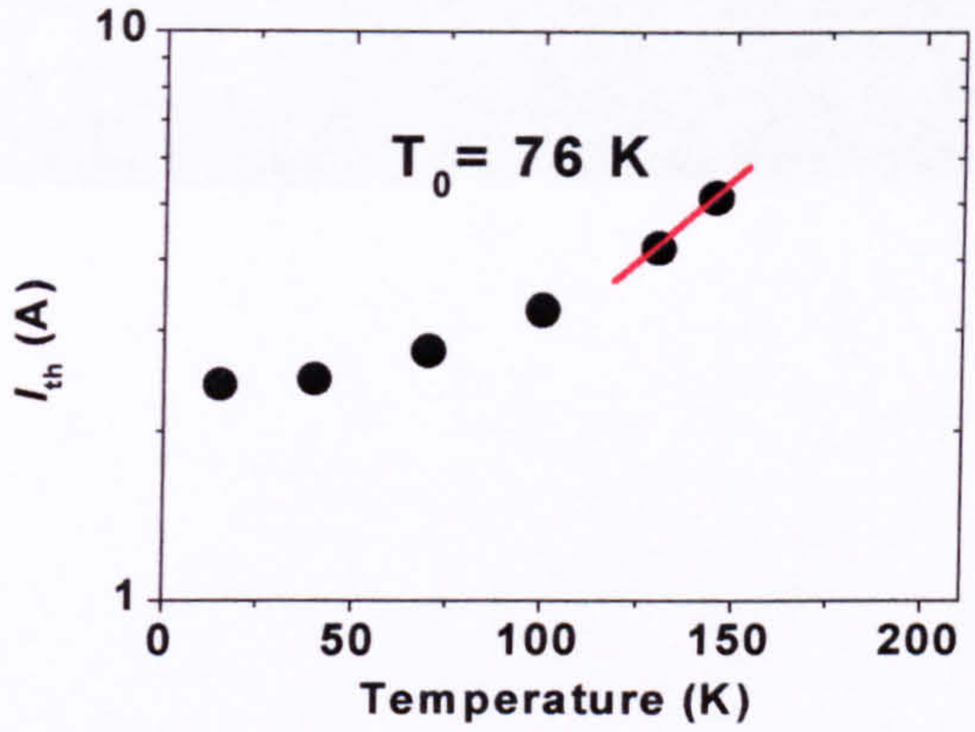

Figure 151 Measured temperature-dependence of J_{th} of device A1376 PSWOX.2.2c.

Parameter	Value
W (μm)	20
L_{cav} (mm)	0.9 ± 0.05 mm
J_{th} (kA/cm^2) at $T \approx 10$ K	13.3
P (W) per facet max. at $T \approx 10$ K	0.93
$\partial P/\partial I$ (W/A) at $T \approx 10$ K	0.2
T (K) maximum	150
T_0 (K)	76
$\Delta\omega$ (cm^{-1})	1.69
n_{eff}	3.11 to 3.48

Table 57 Key parameters measured for laser A1376 PSWOX.2.2c. The J_{th} was calculated assuming W = 20 μm.

8.7 Mesa-etched $\lambda \approx 8\mu m$ QCL width = 16 μm

8.7.1 M1746.1.1, L_{cav} = 2 mm, width = 16 μm, SiO_2 dielectric layer

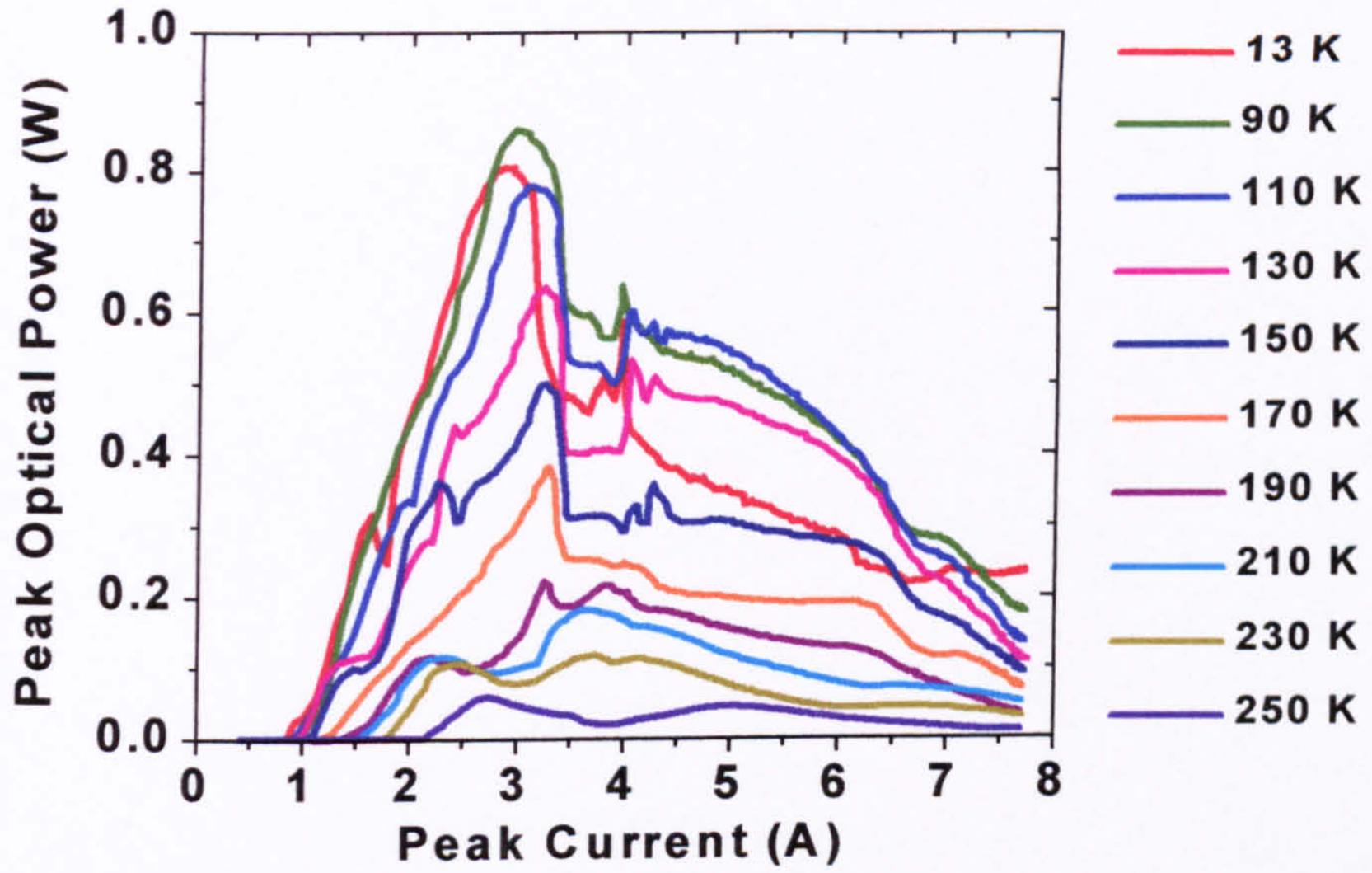

Figure 152 Measured LI curves of device M1746.1.1 at a series of heatsink temperatures.

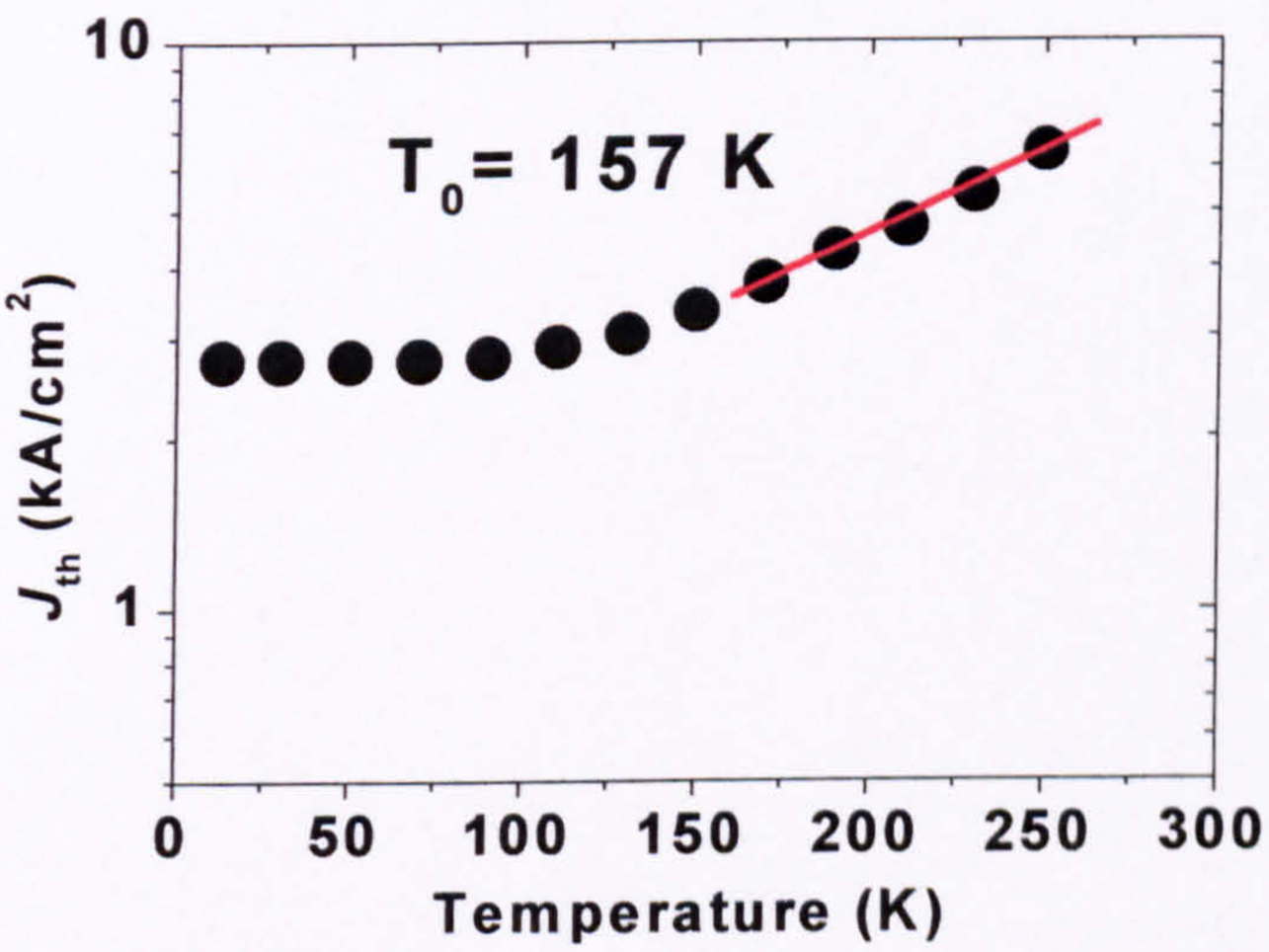

Figure 153 Measured temperature-dependence of J_{th} of device M1746.1.1.

Finally, results are presented for lasers fabricated from a wafer based on a $\lambda \approx 8$ μm QCL design with 'near optimum performance' by Gmachl *et al.*.[11] The circumstances surrounding the source of this wafer are revised in just a moment in Section 8.8. From the copy of the growth sheet of the wafer used, the growth of this wafer deviated from the design by Gmachl *et al.* in two ways. Rather than the 30 stage specified in the original design only 25 were grown. More drastically perhaps, rather than the 1×10^{17} cm^{-3} substrate doping level specified, a n^+ substrate (doping level in the 10^{18} cm^{-3} range) was used. Values of the calculated refractive index and loss in InP for the doping range 1×10^{18} cm^{-3} $< n_e <$ 10×10^{18} cm^{-3}, were approximately $2.8 < n < 1.5$ and 100 cm^{-1} $< \alpha <$ 3000 cm^{-1}. Given the strong dependence of the refractive index and loss of the InP on the doping level at $\lambda \approx 8$ μm we can expect a major impact on the device performance.

Parameter	Value
W (μm)	16
L_{cav} (mm)	2 ± 0.05 mm
J_{th} (kA/cm^2) at $T \approx 10$ K	~ 2.7
P (W) per facet max. at $T \approx 10$ K	0.8
$\partial P/\partial I$ (W/A) at $T \approx 10$ K	0.53
T (K) maximum	250
T_0 (K)	157

Table 58 Key parameters measured for laser M1746.1.1.

The threshold current density of $J_{th} \approx 2.7$ kA/cm^2 for our laser compared with $J_{th} \approx 1$ kA/cm^2 reported by Gmachl *et al.* signifies that there were enhanced waveguide losses owing to the improper doping of the substrate. The measured LI curves revealed a surprisingly good laser performance given the circumstances. The best peak output power at $T = 10$ K of 0.8 W compared very well to that of 0.7 W reported by Gmachl *et al.*, and the laser still exhibited a very high $T_0 = 157$ K. The value reported by Gmachl *et al.* was $T_0 = 130$ K for mesa-etched lasers of width between 11 and 17 μm, but this was for the temperature range $200 < T < 320$ K so that a proper comparison cannot be made here. The maximum heatsink temperature at which lasing was observed was $T = 250$ K, falling well short of the $T = 320$ K operation demonstrated by Gmachl *et al.* which was not surprising given the unusually high threshold current density of our device. Large improvements in performance are expected when a revised wafer can be grown.

8.8 Overview of MBE Wafers

The results presented in this chapter were measured from lasers fabricated in a variety of waveguide configurations, but only from two wafers: A1376 and M1746. These were not the only wafers from which devices were made and tested. At this point, we backtrack just a little to summarise the wafer growths.

The MBE material for the QC lasers fabricated during the work came from two sources. The MBE group in our own Department, led by Prof. Colin Stanley, was our first source of material. Referring to Table 59, they supplied three InP-based QC wafers in total, all of which followed the design by Faist *et al.*.[8] QC electroluminescence was observed from the first wafer B748, but with there having been an error in the active region growth sequence, lasing was never achieved using it. It was from the second of these wafers (B804) that that the first QC lasers in the UK were produced. However, as can be ascertained from Table 59, the lasers from wafer B804 still did not perform to anywhere near the level expected. Faist *et al.* had demonstrated a peak power as high as 25 mW at $T = 300$ K,[8] whereas our lasers fabricated from wafer B804 only produced this amount of power at $T \approx 11$ K, and lasing ceased at $T \geq 120$ K.

The second source of material was through a collaboration with Dr. Cockburn's GaAs-based QC laser group in the Dept. Of Physics and Astronomy at the University of Sheffield. At their request, QC lasers were fabricated for them from samples of their wafers shown in Table 60. Not all wafers grown at the EPSRC Central Facility produced devices that lased. In fact, only one wafer (M1599) out of the first four sent (M1597, M1598, M1599 and M1600) was found to produce lasing devices. The presence of a high density of

large oval defects on the wafers had indicated that perhaps the growth conditions had not been at an optimum. Having made adjustments to their growth parameters, their second attempts (M1744, M1745, M1746 and M1747) gave a better yield with lasing QC structures being produced from three out of the four wafers produced. In particular, wafer M1746 (following the design of Gmachl *et al.*[11] for emission at $\lambda \approx 8$ μm) gave a vastly greater performance than any of the previous efforts, but still not as good as reported by Gmachl *et al.*.[11] Results from one of the lasers fabricated from wafer M1746 were presented in Section 8.7.

Wafer number	Date of growth	Emission wavelength	Wafer design	T_{max}	P_{max} at $T \approx 11$ K
B748	Aug. 96	~ 5 μm	Faist *et al.*[8]	no lasing	
B804	Nov. 97	~ 5 μm	Faist *et al.*[8]	~ 120 K	~ 30 mW
A1376	Feb. 99	~ 5 μm	Faist *et al.*[8]	~ 210 K	~ 400 mW

Table 59 Wafers grown in the Dept. E. & E. Eng., Uni. Of Glasgow, from which QC laser structures were made. T_{max} was the highest operation temperature of the laser, and P_{max} was the peak optical power measured at $T \approx 11$ K. Both values were for ~15 μm-wide mesa-etched lasers operating in pulsed-mode (pulse duration ≤ 100 ns, repetition rate ≤ 5kHz).

Wafer number	Date received	Emission wavelength	Wafer design	T_{max}	P_{max} at $T \approx 11$ K
M1597	June 98	~ 8.4 μm	Sirtori *et al.*[9]	no lasing	
M1598	June 98	~ 8 μm	Sirtori *et al.*[10]	no lasing	
M1599	June 98	~ 4.6 μm	US patent no. 5, 509, 025	~ 120 K	~ 20 mW
M1600	June 98	~ 5 μm	Faist *et al.*[8]	no lasing	
M1744	Jan. 99	~ 5 μm	Faist *et al.*[8]	~ 120 K	~ 30 mW
M1745	Jan. 99	~ 8.4 μm	Sirtori *et al.*[9]	no lasing	
M1746	Jan. 99	~ 8 μm	Gmachl *et al.*[11]	~ 250 K	~ 0.8 W
M1747	Jan. 99	~ 4.6 μm	US patent no. 5, 509, 025	~ 120 K	~ 20 mW

Table 60 Wafers grown for Dr. Cockburn's Group by the EPSRC Central Facility, Uni. Of Sheffield, from which QC laser structures were made. See caption of Table 59 for definitions of T_{max} and P_{max}.

Wafers B804 and M1744 both followed the same $\lambda \approx 5$ μm design by Faist *et al.*, with the only (known) difference being that but one was grown at the Sheffield and one at Glasgow MBE facility. Comparing their respective values of T_{max} and P_{max} from Table 59 and Table 60, we can see that the results from both wafers were not only disappointing in terms of performance, but also remarkably similar. Based on the evidence available at the time, the only conclusion that could be reached was that both MBE facilities were not capable of the demanding growth involved in reproducing the QC structures adequately. Several mechanisms through which the MBE growth could have been responsible were envisaged and with these possibilities in mind it was time for our MBE group at the University of Glasgow to have a third attempt at the structure (wafer A1376). Referring again to Table 59, the lasers made from this wafer A1376 far outperformed those from any of the previous $\lambda \approx 5$ μm wafers we had used, but still fell well short of the performance standards set by Faist *et al.*. The fabrication process was unchanged, so the only conclusion at the time was that it had indeed been the quality of the MBE growth which had been at fault. The work proceeded using the best wafers available, namely A1376 and M1746.

8.9 Summary

A range of waveguides and fabrication techniques were employed in an effort to improve the performance of our QC lasers in terms of their T_0, J_{th}, I_{th} and output power using the results from our mesa-etched QC lasers as a the standard to improve upon. At the same time, efforts were made to understand the source of relatively poor performance common to them all.

8.9.1 General laser performance

The experimental evidence suggested that the QC active core was faithfully reproduced, and that it was the optical waveguide which was the source of the poor laser performance. The measurements uncovered the following evidence to that effect:

1. The $T_0 \approx 110$ K of our mesa-etched lasers agreed closely with that of Faist *et al.* (see Table 2) which was a good indication that the active waveguide core was of high quality.

2. The threshold current and slope efficiency of the 3 mm-long, 15 μm-wide mesa-etched QC laser indicated that the waveguide losses were $\alpha_w \approx 30$ cm^{-1}, whereas the optical modelling and the value reported by Faist *et al.* (see Table 2) was $\alpha_w \approx 13$ cm^{-1}. From the optical modelling, this would be consistent with a laser which had an InP substrate doping level significantly greater than 3×10^{18} cm^{-3}. Indeed, it was discovered that the substrate used was doped in the range 4×10^{18} cm^{-3} to 8×10^{18} cm^{-3}, whereas it should have been only 1×10^{18} cm^{-3}.

3. We saw from the comparison of the LI and IV curves in Figure 122, and from the plot of $\partial V/\partial I$ versus the drive current in Figure 121, that the loss of resonant tunnelling injection occurred *after* the major fluctuations in the measured optical output power. The IV characteristic had no features that related to changes in the LI curve until the point at which resonant tunneling injection was lost. This strongly suggests that there were no problems with the alignment of the energy levels in the QC active core and that it was faithfully reproduced. However, changes in the collection efficiency of light, i.e. changes in the far-field distribution would account for the observed fluctuations in the LI curves.

4. Measurements of the far-field profiles at different currents provided evidence that the far-field distributions did change with drive current. The collection efficiency was indeed changing as a function of the drive current. This accounted for the fluctuations seen in the LI curves. Changes in the far-field profiles implied that there were changes in the lasing transverse modes inside the laser cavity.

5. The shape of the far-field profile just above threshold suggested that higher order transverse modes had a lower threshold current than the fundamental mode. This agreed with the optical modelling. When compared with calculated far-field profiles, the shapes of the measured far-field profiles at higher drive currents suggested the lasing of two or more transverse modes during the current pulse.

It is therefore concluded that the lasers performance was hampered by the use of an excessively doped InP substrate. A repeat growth using the correct substrate should bring about a radical improvement in the performance of all the lasers studied.

8.9.2 Individual performance of lasers

8.9.2.1 Mesa-etch QCL

These devices exhibited relatively low values of T_0, high output beam divergence, and the lasing of higher order transverse modes. Further, the number of lasing transverse modes changed with drive current and gave rise to variations in the output beam profiles with current. In their favour, they showed low threshold currents owing to a good spatial overlap of the optical gain with optical mode.

8.9.2.2 Shallow-etched QCL

Very little characterisation meant that few conclusions could be reached for this structure, but it was confirmed that the shallow-etched QC laser suffered from elevated threshold currents. In agreement with Gmachl *et al.*,[3] the most likely explanation was that the structure did not provide very good electrical confinement, so that there was not a very good overlap of the optical mode with the optical gain.

An upwards kink in the LI at $I \approx 5.8$ A, perhaps indicated the appearance of another transverse mode with a higher collection efficiency. From the optical modelling of the far-field of the device, this was a reasonable explanation.

8.9.2.3 Mesa-etched QC array lasers

Array lasers were fabricated which exhibited a higher T_0 compared to the single mesa-etched lasers, in agreement with the thermal modelling, but further experimental studies are required to investigate the source of the improvement properly.

8.9.2.4 PSWOX QCLs

The performance of the first QC lasers fabricated using thermal wet oxidation were presented which greatly simplified the fabrication of the lasers and led to some improvements in the laser performance. Compared to their mesa-etched counterparts, these PSWOX QC lasers exhibited higher collected peak output powers, very narrow and stable output beam divergence as a function of drive current, and high values of T_0 despite the very high currents required to establish lasing. The high threshold currents suggested that there was very poor electrical confinement. This was not unexpected since the native oxide layer was shallow. With the improvement of the oxidation process to a point where the entire 2.5 μm-thick upper cladding can be oxidised, the current confinement should rival that of the shallow-etch QCL.

With the large current spreading, one might expect a low $\partial P/\partial I$, especially seeing as it was demonstrated that the only laser emission emanated from the ~ 20 μm region below the oxide aperture. In contrast, a good $\partial P/\partial I$ was measured which implied that virtually all of the additional current injected above threshold actually generated photons and contributed to the output power. Furthermore, some LI curves exhibited an upwards curvature with increasing current/optical power i.e. a gradually increasing $\partial P/\partial I$. An increase in the $\partial P/\partial I$ could be interpreted as an increase in the ratio of useful current to current lost via lateral spreading. Therefore, for some reason the current appeared to gradually stop spreading and inject directly into the active core below the oxide aperture. Lastly, the $\partial V/\partial I$ curve followed a continual downwards trend all the way to the current limit of the pulse generator. It was suggested that all these effects could be explained by a reduction in the $\partial V/\partial I$ of the lasing region relative to the non-lasing regions. This was envisaged to occur as a result of a stimulated emission-enhancement of the electron transport through the QC structure.

8.10 References

[1] J. Faist, A. Tredicucci, F. Capasso, C. Sirtori, D. L. Sivco, J. N. Baillargeon, A. L. Hutchison, A. Y. Cho, 'High-Power Continuous-Wave Quantum Cascade Lasers', *IEEE J. Quantum Electron.*, 34 (2) 336, Febuary 1998.

[2] C. Sirtori, F. Capasso, J. Faist, A. L. Hutchinson, D. L. Sivco, A. Y. Cho, "Resonant Tunneling in Quantum Cascade Lasers", *IEEE J. Quantum Electron.*, 34 (9) 1722, September 1998.

[3] C. Gmachl, F. Capasso, J. Faist, A. L. Hutchinson, A. Tredicucci, D. L. Sivco, J. N. Baillargeon, S. G. Chu, A. Y. Cho, 'Continuous-wave and high-power pulsed operation of index-coupled distributed feedback quantum cascade laser at $\lambda \approx 8.5$ μm', *Appl. Phys. Lett.* **72** (12), 23 March 1998.

[4] Hitran Database.

[5] P. Petit, P. Legay, G. Le Roux, G. Patriarche, G. Post, M. Quillec, "Controlled Steam Oxidation of AlInAs for Microelectronics and Optoelectronics Applications", *Journal of Electronic Materials*, **26** (12), L32, 1997.

[6] A. Yariv, *Quantum Electronics*, Third Edition, John Wiley & Sons, Inc., New York, 1989.

[7] C. Gmachl, F. Capasso, A. Tredicucci, D. L. Sivco, R. Kohler, A. L. Hutchison, A. Y. Cho, 'Dependence of the Device Performance on the Number of Stages in Quantum-Cascade Lasers', *IEEE J. Selected Topics in Quantum Electron.*, **5** (3) 808, May/June 1999.

[8] J. Faist, F. Capasso, C. Sirtori, D. L. Sivco, J. N. Baillargeon, A. L. Hutchinson, S. G. Chu, A. Y. Cho, 'High power mid-infrared (λ~5 μm) quantum cascade lasers operating above room temperature', *Appl. Phys. Lett.* **68** (26), 24 June 1996.

[9] C. Sirtori, J. Faist, F. Capasso, D. Sivco, A. L. Hutchinson, A. Y. Cho, 'Quantum cascade laser with plasmon-enhanced waveguide operating at 8.4 μm wavelength', *Appl. Phys. Lett.* **66** (24), 12 June 1995.

[10] C. Sirtori, J. Faist, F. Capasso, D. L Sivco, A. L. Hutchinson, S. N. George Chu, A. Y. Cho, 'Continuous wave operation of midinfrared (7.4-8.6 μm) quantum cascade lasers up to 110 K temperature', *Appl. Phys. Lett.* **68** (13), 25 March 1996.

[11] C. Gmachl, A. Tredicucci, F. Capasso, A. L. Hutchinson, D. L. Sivco, J. N. Baillargeon, A. Y. Cho, 'High-power $\lambda \approx 8$ μm quantum cascade lasers with near optimum performance', *Appl. Phys. Lett.* **72** (24), 15 June 1998.

Chapter 9 Conclusions and Future work

QC lasers were fabricated following the design reported by Faist *et al.*[1] and were characterised by our collaborators. Towards the end of the work, the real extent of the J_{th} of our devices was revealed with the discovery of the problem with the calibration of the current in the measurements (see Section 7.3), the dielectric permittivity modelling uncovered the extent of the dependence of n and α on the doping level (see Section 3.6.3), and the optical modelling gave results to indicate high values of α_w and J_{th} for excessive substrate doping levels as well as indicating the existence of higher order transverse mode with low thresholds (see Section 4.4.1). Far-field measurements made in the closing stages confirmed the lasing of higher order modes with the calculated far-field patterns matching those observed experimentally. All of these to came together at the end to reveal the true sources of the poor performance in our QCLs. That was the presence of, and hopping between, higher order transverse modes, and the high loss resulting from an excessively high doping level of the InP substrate.

Both Glasgow and Sheffield used n^+ InP substrates in which the n-type doping level was quoted by the manufacturers as being between 4×10^{18} cm^{-3} and 8×10^{18} cm^{-3}. Further, the large variation in the QC laser performance observed between different wafer growths could be explained by the random selection of the wafers doping level within the range 4×10^{18} cm^{-3} to 8×10^{18} cm^{-3}. This simple oversight may have helped to frustrate our original objectives, but at least we now have a much greater understanding of the QC laser, and are in a strong position to capitalise on the work carried out once replacement QC wafers are grown.

The optical modelling, which was instrumental in resolving the anomalous behaviour of our QC lasers, comprised of two parts. First, modelling of the dielectric permittivity gave values of n and α for InP, $In_{0.52}Al_{0.48}As$ and $In_{0.53}Ga_{0.47}As$ as a function of the free-carrier density and wavelength. These values were used in the 2D optical modelling of the waveguide, which was in turn was used calculate the threshold gain and far-field distribution of the waveguide modes. The results agreed well with the observed QC laser behaviour, predicting which modes lased first, as well as their far-field distributions. Other significant findings of the optical modelling were that poor electron mobility at high n_e was found to increase the calculated loss coefficient, and in order to obtain low loss 'plasma-enhanced' waveguides with high optical confinement, it is important to grow high quality semiconductor material with high values of electron mobility. The optical loss of InP was found to be intrinsically lower than that of InAlAs, making InP more suitable optically, as well as thermally, as a cladding material. Finally, the modelling highlighted that care must be taken to avoid making the plasma frequency drop below the optical frequency, otherwise high optical losses will be incurred.

Future work might use the optical modelling to improve the waveguide design so that only the fundamental mode is guided. Development of the optical waveguide modelling itself could include the modelling of structures with metallic layers on the sidewalls and the modelling of surface-plasmon modes and the coupling between them and the optical mode(s). Experimental work could be performed, such as reflectivity measurements using FTIR spectrometry, to determine the refractive index and loss coefficient of InP, $In_{0.52}Al_{0.48}As$ and $In_{0.53}Ga_{0.47}As$ in the mid-IR as a function of the doping level and wavelength.

2D non-linear thermal modelling of a variety of QC laser structures, such as arrays and buried heterostructures was carried out. The modelling indicated that there was a large temperature increase of the active waveguide core would occur under CW operation. The presence of a temperature gradient across the active waveguide core was also revealed, which was especially pronounced in devices mounted epilayer-up

(except in the BH QCL structure). This is expected to be detrimental to the QC laser performance for the reasons already detailed in Section 5.1, and should be minimised. The magnitude of the gradient was reduced by using epilayer-down mounting or a BH QC laser design, making these configurations favourable. In terms of the lowest temperature elevation of the QC waveguide core in CW-mode, the best performers were the narrow-mesa QC array lasers, followed closely by buried heterostructures (BH) QCLs and then epilayer-down-mounted InP-clad QCLs. On a purely thermal basis, the array lasers even rivalled an epilayer-down mounted BH QCL, even when the array was mounted epilayer-up. This was attributed mainly to the delocalising of the generated heat, avoiding the non-linear temperature rise caused by the temperature-dependence of the semiconductor thermal resistance. Other results included evidence to show that using an InP upper cladding layer was of little benefit in terms of CW operation, unless the device was mounted epilayer-down. Mounted-epilayer down, its heat dissipation was much improved and rivalled that of the buried heterostructures. These findings are very relevant to the field given that other QC groups are now developing complicated technologies such as buried heterostructures, whereas, the modelling suggests that this may a lot of effort for only a little gain. However, the BH QCLs are likely to have other benefits besides the thermal ones. Further work could include modelling of the transient temperatures that will occur in pulsed-mode operation.

Novel design and fabrication of QC lasers was demonstrated with the PSWOX QCL. Despite the high waveguide losses due to the substrate, the PSWOX QCL still performed very well. Optically they were far superior to our mesa-etched QC lasers, possessing a very low divergence output beam whose far-field profile was stable with increasing drive current. The lasers ability to dissipate heat was also superior over its counterparts, as demonstrated by its high characteristic temperature T_0. However, this particular structure was let down by the very poor electrical confinement which led to substantial threshold currents. Future research might first focus on increasing the depth of the native oxide in order to reduce lateral current spreading and threshold currents. Other avenues of research might to explore whether an enhancement of the electrical confinement by stimulated emission occurs in these devices possessing inherently poor electrical confinement. An investigation into the source of the unusually high T_0 might also be considered.

9.1 References

[1] J. Faist, F. Capasso, C. Sirtori, D. L. Sivco, J. N. Baillargeon, A. L. Hutchinson, S. G. Chu, A. Y. Cho, 'High power mid-infrared (λ~5 μm) quantum cascade lasers operating above room temperature', *Appl. Phys. Lett.* **68** (26), 24 June 1996.

Appendix A Derivation of the density of states

For an electron confined to a 3-dimensional space of volume $V = L_x L_y L_z$, the spacing of points in k space are $2\pi/L_x$ in x, $2\pi/L_y$ in y, and $2\pi/L_z$ in z, giving the k space volume per electron state as,

$$\frac{(2\pi)^3}{V}.$$

Representing the energies E and $E + dE$ by surfaces of spheres with radii k and $k + dk$, the volume of a shell between k and $k + dk$ is $4\pi k^2\, dk$. The number of electron states between k and $k + dk$ is,

$$2\frac{V}{(2\pi)^3}4\pi k^2 dk,$$

where the factor of 2 is to account for the two electron spin states. The number of states per unit volume between k and $k + dk$ is then,

$$\frac{k^2}{\pi^2}dk.$$

The number of electron states between E and dE per unit volume is,

$$N(E)dE = \frac{k^2}{\pi^2}dk,$$

which can be rearranged to,

$$N(E) = \frac{k^2}{\pi^2}\frac{dk}{dE}.$$

Appendix B Device Fabrication Procedures

B.1 Mesa-etched and Rib-mesa lasers and Arrays

B.1.1 Formation of waveguide

1. Scribe and cleave wafer into rectangular areas 8 mm parallel to the major flat [$0\bar{1}\bar{1}$] and 7 mm parallel to the minor flat [$0\bar{1}1$]. *To give clear indication of crystal plane direction if a crystallographic etch is to be used.*

2. Cleaning procedure: 5 minutes ultrasonic in Opticlear, rinse with acetone. 5 minutes ultrasonic in acetone, rinse with methanol. 5 minutes ultrasonic in methanol, rinse well with running RO water. Blow dry.

3. Spin resist procedure: spin S1818 resist for 30 seconds at 4000 rpm. Carefully remove large resist build-up from corners with flat end of tweezers.

4. Pre-bake resist procedure: place on a watch glass in an oven at 90°C for 30 minutes.

5. Expose outer periphery on Karl Suss with 'exposedge' mask pattern. Requires large exposure time, approx. 40 seconds (integrator setting on) due to greater resist layer thickness. *Will allow close contact of next mask and prevent breakage of sample arising from an uneven distribution of mask-sample contact. Karl Suss much better at build-up removal than other mask aligners.*

6. Remove mask from the Karl Suss and turn sample face down on a piece of rubylith. Expose reverse surface for approx. 50 seconds. *Will facilitate good parallelism of the sample to the etch mask by removal of unwanted resist on the underside of the sample and prevent sample breakage arising from an uneven pressure distribution.*

7. Develop resist procedure: thoroughly mix 1:1 solution of S1818 developer and RO water. Place sample in a petri dish containing the mixed solution for 75 seconds, agitating the sample every 15 seconds. Rinse well in RO water. Blow dry.

8. Place in oven at 90°C for 3 minutes. *Evaporate any residual water from surface.*

9. Select ferric waveguide mask (e.g. 10 μm window/20 μm waveguide/10 μm window spaced 500μm) and align the mask pattern such as to give windows parallel to long edge of sample (major flat). Bring mask into contact and expose for the time recommended for S1818 resist.

10. Repeat developing procedure (step 7).

11. Post-bake resist procedure: place on a watch glass in an oven at 120°C for 30 minutes. Let sample cool.

12. Wet etch the exposed semiconductor layer using H_3PO_4:H_2O_2:H_2O (1:8:1) at room temperature with no agitation. The etch time depends on the particular QC wafer design and desired etch depth. For the mesa-etched $\lambda = 5$ μm QC lasers (e.g. wafer A1376), an etch time of 4 minutes was used.

13. Once etching is completed, remove the resist etch mask using acetone in an ultrasonic bath for 2 minutes followed by rinses in methanol and RO water. Blow dry.

B.1.2 Insulation layer and Formation of Contact Window

1. Deposit insulating layer (e.g. silica, nitride, or alumina). See discussion at beginning of section.
2. Spin resist procedure.
3. Pre-bake resist procedure.
4. Expose outer periphery with 'exposedge2' mask pattern for approx. 40 seconds. *The new periphery exposure mask is needed to include the removal of the build-up at the step etched as a consequence of the 'exposedge' mask used in step 5 of the ridge formation.*
5. Remove mask from the mask aligner and turn sample face down on a piece of rubylith. Expose reverse surface for approx. 50 seconds.
6. Develop resist procedure.
7. Place in oven at 90°C for 3 minutes.
8. Align appropriately sized windows to waveguide centre using Karl Suss mask aligner. Bring the mask into contact and expose for normal exposure S1818 time. *This requires a mask with window widths approximately equal to waveguide width minus 4-6μm.*
9. Develop resist procedure.
10. Post-bake at 120°C for 30 minutes.
11. Dry etch silica in C_2F_6 plasma.

B.1.3 Contacts and Thinning

1. Ultrasonic cleaning in acetone, rinse with methanol then RO water and blow dry.
2. Spin S1818 resist on a glass coverslip for few seconds. Place sample pattern-side-up onto slip and dry in oven for 30 minutes. *Mounting of sample for contact deposition.*
3. Deoxidised in 1:1 HCl:H2O for 30 seconds. Rinse in RO water. Dry in nitrogen oven for 30 minutes at 90°C. *Prepares both InGaAs surface and silica surface for contact deposition.*
4. Give to technician for immediate deposition of a p-type contact (Ti/Pd/Au). *A p-type contact may be used as the InGaAs contact layer is very heavily n-type doped. The Ti/Pd/Au is preferential since it adheres well to the silica layer, allowing ultrasonic wire bonding.*
5. Spin S1818 resist on a glass coverslip for few seconds. Place sample pattern-side-down onto slip and bake in oven for 30 minutes. *Mounting of sample for thinning and n-type contact deposition.*
6. Mount coverslip onto metal chuck with wax. Slice off corners of coverslip protruding over chuck edge using a razor blade. *Use of coverslip avoids contact of wax with sample.*
7. Thin InP substrate from 350 μm to 200μm with 9μm aluminium oxide powder and from 200 μm to 150 μm with 3μm aluminium oxide powder. Heat chuck until wax just melts and remove the coverslip. *Thinning reduces the distance from the epilayer to the heatsink and improves the cleaving process*
8. Polish sample by etching with a HBr:Nitric:H_2O aged 1:1:10 solution. Agitate sample in acid until surface begins to look shiny, but not completely smooth. *Polishing in acid removes aluminium oxide grit and*

smoothes the surface further. However, leave the sample slightly rough to facilitate contact adhesion. Agitation required since the reaction is diffusion-limited and etches non-uniformly without stirring.

9. Repeat steps 2 to 4, but deposit an n-type contact (Au/Ge/Au/Ni/Au) instead. *Reverse contact deposition on the InP substrate.*

10. Remove from coverslip with acetone, rinse with methanol, RO water, then blow dry. *The sample should be left to soak in acetone until it drops off without much encouragement – forcing the sample will damage/scratch the contact layer, or even break the delicate sample.*

B.1.4 Cleaving process

1. Set scriber load to as low as possible.
2. Scribe at edge and cleave along line 1 as shown in Figure 154.
3. Scribe each half on the outer edge at points 2 and 3. Cleave along lines 2 and 3.
4. Inspect facets produced by cleaving using the Dye Bonding machine. If unsatisfactory, scribe and cleave again at least 500μm from the edge.
5. Scribe at edge and cleave along line 4 (vary position or number of scribe marks to produce lasers of different lengths).

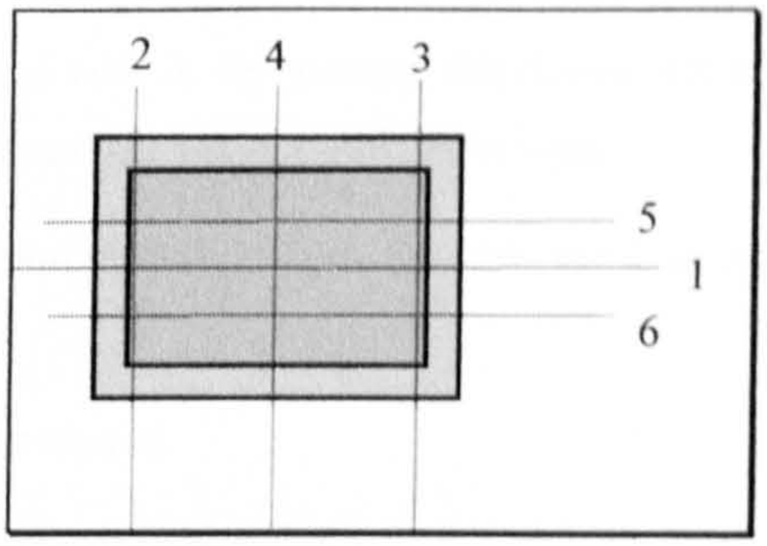

Figure 154 Cleaving of sample.

6. Scribe between each waveguide and cleave to produce single laser bars (e.g. points 5 and 6).

B.1.5 Mounting process

1. Sharpen the ends of 3 wooden cotton swabs sticks to a fine point: a 'flux stick' for applying flux, a 'device stick' for moving the laser around on the mount, and one to hold the mount steady.
2. Place the gold-coated heatsink onto the heating stage and heat to ~100°C.
3. Apply a thin coating of flux to the surface of the mount. Cover an area ~ 2 times the device length by ~5 times the device width.
4. Flatten the end of a piece of In wire using the flat of a razor blade. Then proceed to slice off a thin bar of In. *The amount of indium required depends on the area of the bond to be formed. Too little indium will result in an incomplete coverage and a poor thermal and mechanical bond. Too much In may cause a short-circuit to the top of the laser, or the laser to rise up onto a pool of indium. This results in a poor orientation of the laser bar w.r.t. the heatsink surface and also places a larger thermal resistance between the laser and the copper heatsink.*
5. Using the flux stick, transfer the slither of indium to the fluxed mount. Position the indium ~0.5mm to the left of where the device is intended to be mounted. Cover the indium in a thin layer of flux. *The total amount of flux is dependant on the amount of indium used and the device area. Too little and the indium will oxidise, wetting will be poor, and the bond incomplete. Too much, and the flux may flow up the side of the device facilitating a short-circuit, or the laser facets may become covered in flux and possibly indium.*

6. Select a laser bar, and using sharp tweezers, place the device onto the area of the mount which was fluxed, about 1mm to the right of the indium. Using the clean device stick prod and push the top-right edge of the laser bar to drag the device across the fluxed surface to the rest adjacent to the indium. *This ensures a uniform coating of flux on the underside of the laser. When moving the device try not to allow the 'device stick' to come into contact with the flux-covered mount. The point of the stick would collect flux from the mount and transfer it onto side and top of the device.*

7. Increase the set point of the heater controller to the temperature at which the indium will melt. Maintain the temperature at about 5 degrees above the indicated melting point. The indium should kept molten for the minimum length of time to prevent oxidation and a poor solder joint.

8. Using the device stick, prod the laser bar into contact with the edge of the molten indium. Then slowly draw the device away from the indium, which should be dragged with it. By moving the device left to right, backwards and forwards (or even rotating through 360°) spread the indium into a thin layer.

9. Once convinced that the underside of the laser is completely covered with indium, position the laser at (and perpendicular to) the mount edge.

10. Remove the heatsink from the heater and place on a metal surface to cool.

11. Any unwanted flux may be removed by soaking and rinsing the sample in acetone.

B.1.6 Electrical connections

1. Half cover a ceramic pad using a glass slide. Solder a 30mm length of wire 0.2mm diameter enamelled wire to the exposed half. *The glass side prevents solder covering all of the small pad.*

2. Repeat for a second pad.

3. Prepare a 1:2 mixture of UHU:acetone. Quickly dip the underside of the ceramic pad into the mixture and then press onto the surface of the mount ~3 mm from the laser diode. *The thinning of the UHU with acetone reduces the curing time.*

4. Repeat for second pad.

5. Place the mount onto a heater at ~100°C. The glue will expand and bubble as the solvents escape. Gently press the pads down to maintain contact with the heatsink surface.

6. Remove after 1 minute and cool. The glue will set once cooled.

7. Make gold wire bonds (25μm diameter wire) from the top of the laser diode to one pad, and from the heatsink surface to the other pad. The number of wire bonds required depends on the current that will be used to operate the device.

B.1 PSWOX lasers

In general, the fabrication of the PSWOX lasers was quite simple and involved the following stages:

5. Deposition, and then patterning of silica oxidation mask by one photolithographical sequence and two short wet etch steps.

6. Planar selective thermal wet oxidation (PSWOX).

Planar selective thermal wet oxidation was used to convert (or partially convert) the exposed areas of $In_{0.52}Al_{0.48}As$ into an electrically insulating, low refractive index native-oxide. By forming two 10 μm or 60 μm-wide stripes of native-oxide, say 20μm apart, a 20 μm-wide laser stripe could be formed with both optical and electrical confinement.

7. Formation of contact window through silica mask on the waveguide by one photolithographical sequence and one dry wet etch step. The planar geometry was advantageous as more uniform layers of photoresist were obtained. This made the photolithographical stage involved in the formation of the contact window both easier and more reliable than in the case of the mesa-etched lasers.

   One problem encountered after a thermal wet oxidation run was that the silica in close proximity to the native oxide stripes was found to be much more resistant to dry etching than usual (and virtually impervious to wet etching). It was postulated that this may have been due to diffusion of In or As species out of the native oxide and into the silica during the thermal wet oxidation. Inspection under a optical microscope showed that the silica close to the native oxide stripes had changed in colour slightly, perhaps indicating a change in refractive index due to such contaminants. Under the standard conditions used with our dry etch machine (C_2F_6 plasma), 200 nm of PECVD SiO_2 would normally have been removed within 6 minutes. In contrast, it was found that ~ 14 minutes was necessary to open the contact window on the PSWOX devices. Note that only the SiO_2 in close proximity (~ 10μm) to the regions of native oxide had exhibited an increased resistance to etching; the SiO_2 elsewhere on the same sample etched as normal.

8. Evaporation of the upper metal contact layer followed by thinning of the InP substrate and deposition of the lower metal contact layer onto the polished substrate. Cleaving, mounting and making the electrical connections.

   These stages were all identical to those detailed for the mesa-etched and rib-mesa laser (see ?).

B.1.7 Formation of the oxidation mask

The following steps lead to the formation of the silica oxidation mask, part of which will also form the electrical insulation layer. The waveguide pattern must be parallel to the edge of the sample to permit the formation of mirrors normal to the laser cavity through cleaving.

1. Scribe and cleave wafer into rectangular areas 8 mm parallel to the major flat $[0\bar{1}\bar{1}]$ and 7 mm parallel to the minor flat $[0\bar{1}1]$. *To give clear indication of crystal plane direction if a crystallographic etch is to be used.*

2. Cleaning procedure: 5 minutes ultrasonic in Opticlear, rinse with acetone. 5 minutes ultrasonic in acetone, rinse with methanol. 5 minutes ultrasonic in methanol, rinse well with running RO water. Blow dry.

3. Deposit 200nm of SiO_2 by PECVD.

4. Spin resist primer for 30s at 4000 rpm. *Promotes adhesion of the subsequent resist layer to the silica.*

5. Spin resist procedure: spin S1818 resist for 30s at 4000 rpm. Carefully remove large resist build-up from corners with flat end of tweezers.

6. Pre-bake resist procedure: place on a watch glass in an oven at 90°C for 30 minutes.

7. Expose outer periphery on Karl Suss with 'exposedge' mask pattern. Requires large exposure time, approx. 40 seconds (integrator setting on) due to greater resist layer thickness. *Will allow close contact of next mask and prevent breakage of sample arising from an uneven distribution of mask-sample contact. Karl Suss much better at build-up removal than other mask aligners.*

8. Remove mask from the Karl Suss and turn sample face down on a piece of rubylith. Expose reverse surface for approx. 50 seconds. *Will facilitate good parallelism of the sample to the etch mask by removal of unwanted resist on the underside of the sample and prevent sample breakage arising from an uneven pressure distribution.*

9. Develop resist procedure: thoroughly mix 1:1 solution of S1818 developer and RO water. Place sample in a petri dish containing the mixed solution for 75 seconds, agitating the sample every 15 seconds. Rinse well in RO water. Blow dry.

10. Place in oven at 90°C for 3 minutes. *Evaporate any residual water from surface.*

11. Select ferric waveguide mask (e.g. 10μm window/20μm waveguide/10μm window spaced 500μm) and align the mask pattern such as to give windows parallel to long edge of sample (major flat). Bring mask into contact and expose for the time recommended for S1818 resist.

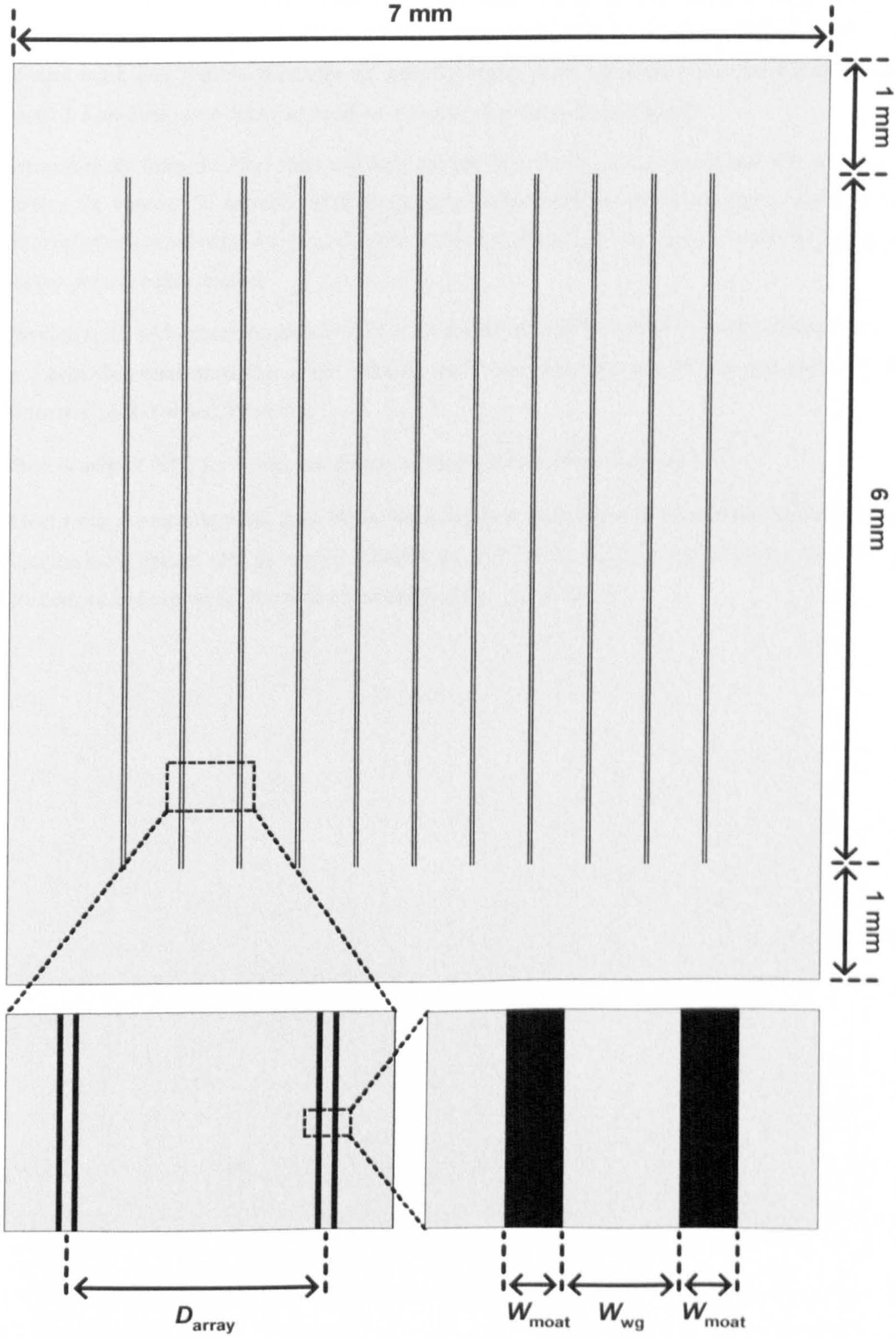

Figure 155 Illustration of one of the photolithographical masks used to define the waveguides.

12. Repeat developing procedure (step 7).
13. Post-bake resist procedure: place on a watch glass in an oven at 120°C for 30 minutes. Let sample cool.
14. Wet etch through the exposed SiO_2 layer using silica etch (buffered 4:1 HF solution). This should take ~15-20 seconds for 200nm SiO_2.

15. Once etching is completed, remove the resist etch mask using acetone in an ultrasonic bath for 2 minutes followed by rinses in methanol and RO water. Blow dry.

16. Etch exposed epilayers using 1:1:200 H_2SO_4:H_2O_2:H_2O (room temperature, no stirring) to expose InAlAs cladding layer. Etch rate ~40nm/min; 140 seconds was used for wafer previous PSWOX.

17. Rinse sample in RO water.

18. Agitate sample in a small beaker of neat concentrated H_2SO_4 for 20 seconds. *Believed to remove surface oxides formed during H_2SO_4:H_2O_2:H_2O etching which would otherwise influence the forthcoming wet oxidation rate/uniformity. The resist was removed in step 14 since it would have been attacked by the sulphuric acid etch in step 17.*

19. Rinse well in RO water.

20. Oxidation proceeded immediately after etch to avoid possible atmospheric oxidation.

B.1.8 Planar Selective Wet Thermal Oxidation (PSWOX)

The following steps will convert the exposed InAlAs layer to an electrically insulating, low refractive index native oxide. Two stripes of the native oxide separated by unconverted InAlAs will form the optical waveguide and confine the electrical current therein.

1. Rinse out and fill water flask with fresh RO water directly from the tap in cleanroom – fill to approximately same level every time (generally full). *RO water contaminates very easily due to its affinity for ions.*
2. Check position of three T-valves, they should be as follows:

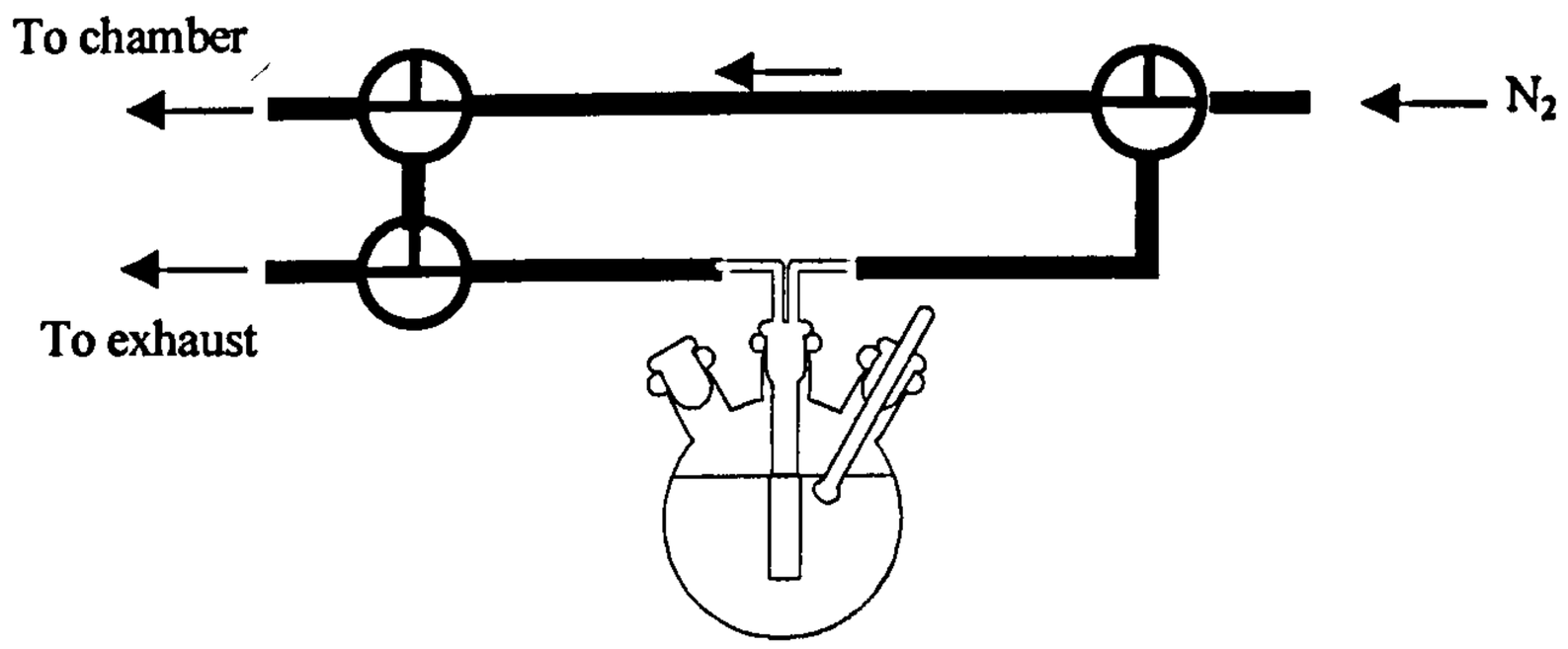

3. Switch on mantle at setting 5 (maximum) to begin heating the water.
4. Undo screws holding reaction chamber retaining ring and lift off reaction chamber glass cover.
5. Place sample(s) on specimen stage on a piece of clean InP wafer. *The InP wafer avoids damage to the InP substrate by means of the dissociation of phosphorous.*
6. Replace reaction chamber cover and fasten firmly (but not over-tight) using screws.
7. Switch on heater tape to setting 3. *Prevent condensation of water vapour in the delivery tube between the water flask and the furnace.*
8. Open needle valve until the flow on the gauge is 200 sccm allowing N_2 to pass into reaction chamber to purge it.

9. Wait until temperature in water flask reaches a few degrees above the desired temperature, then close the needle valve and rotate the T-valves to the following (the N_2 will now flow through the bubbler to the exhaust):

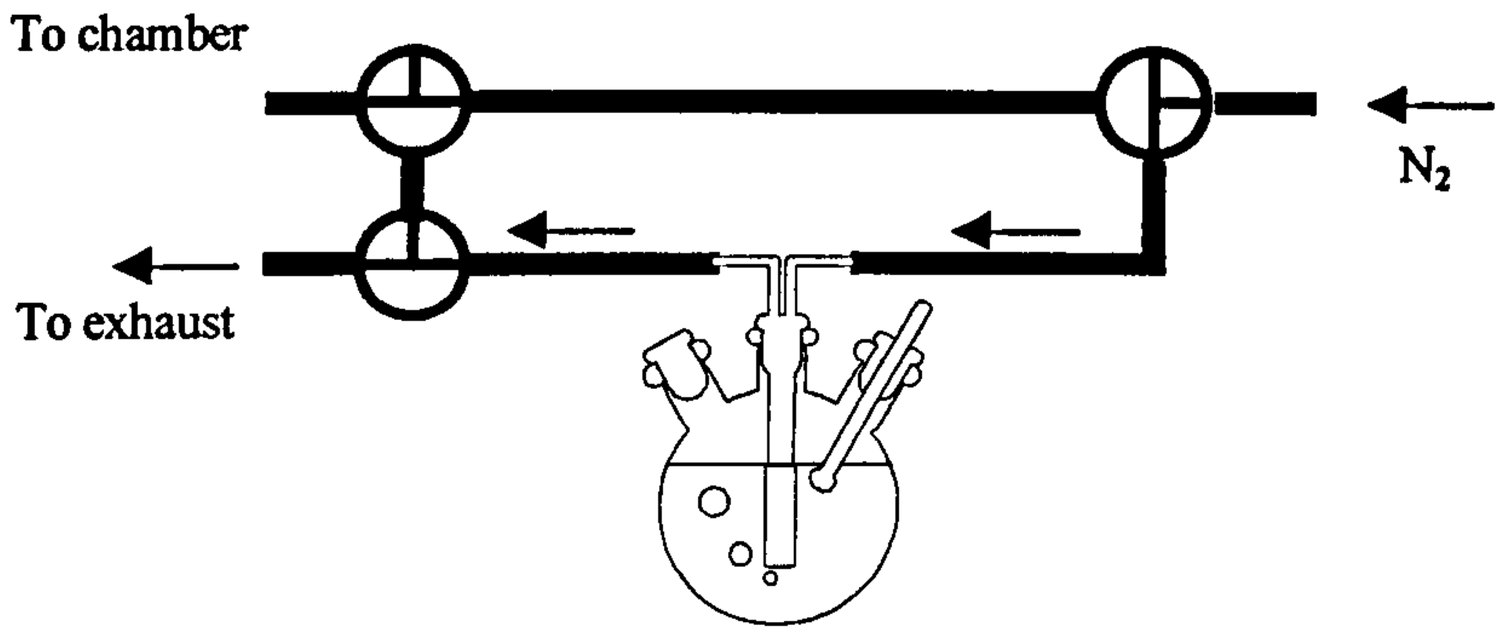

10. Reduce the setting on the mantle to the appropriate level for the desired temperature T_W. *Water temperature is also dependant on nitrogen flow through water. It was found that Setting 3 gave a water temperature of ~98°C for a flow rate of 500 sccm.*
11. Open the needle valve until the gauge reads the desired flow rate Q for oxidation and allow the temperature in the flask to stabilise to T_W.
12. Switch on reaction chamber controller. The flashing number in the centre display gives the current temperature. The number below is the set operating temperature and can be adjusted using the up/down buttons beneath the display. Adjust the set operating temperature to T_F = 500°C.
13. Switch heater switch on reaction chamber controller to ON. Sample stage should now begin to heat up to set temperature.
14. When the stabilised water temperature is reached, close needle valve to shut off gas flow. Rotate T-valves so output from bubbler goes to reaction chamber only:

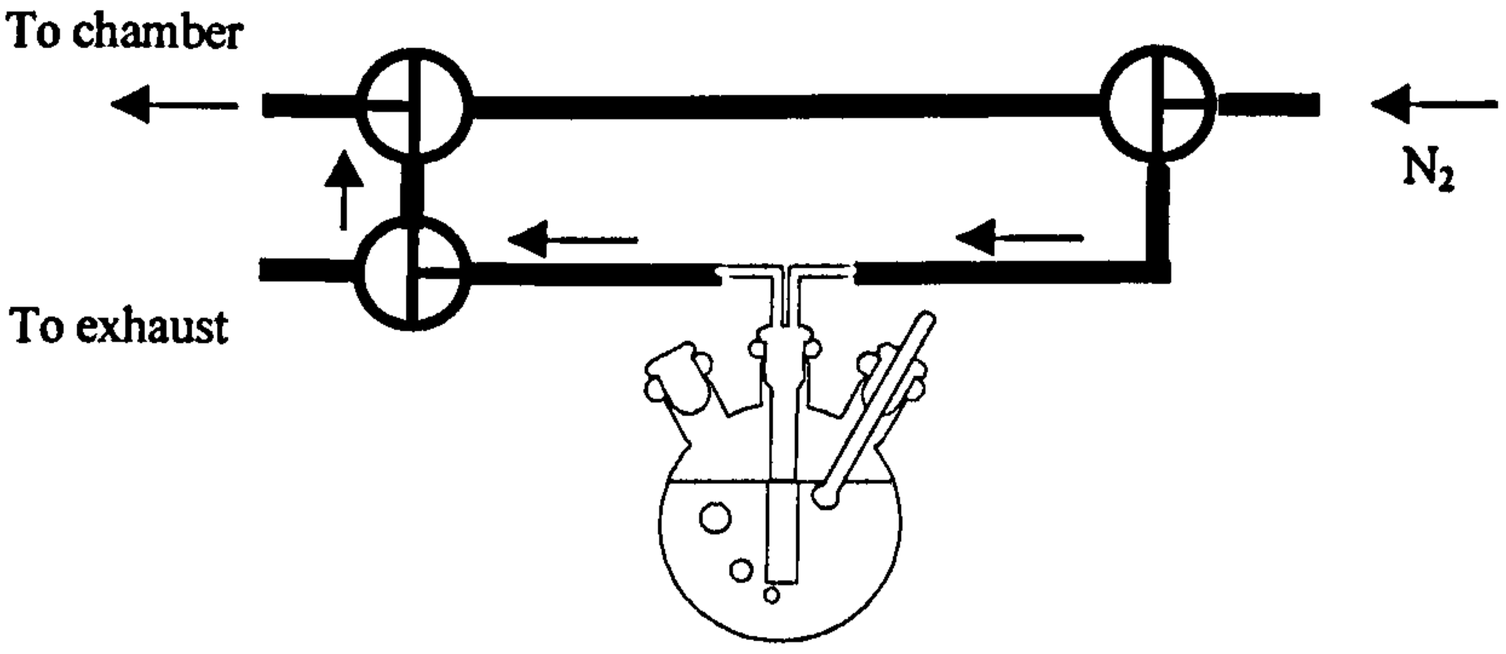

15. Open needle valve until flow is Q. Gas should now be passing through the water bubbler. Start timing from now, and monitor the temperature readings regularly over duration of the oxidation run.
16. At the end of the run, switch the heater off. Quickly close the needle valve, re-set the T-valves to by-pass the bubbler, then re-open needle valve so that 200 sccm dry-gas flow goes to the reaction chamber until room temperature is reached.

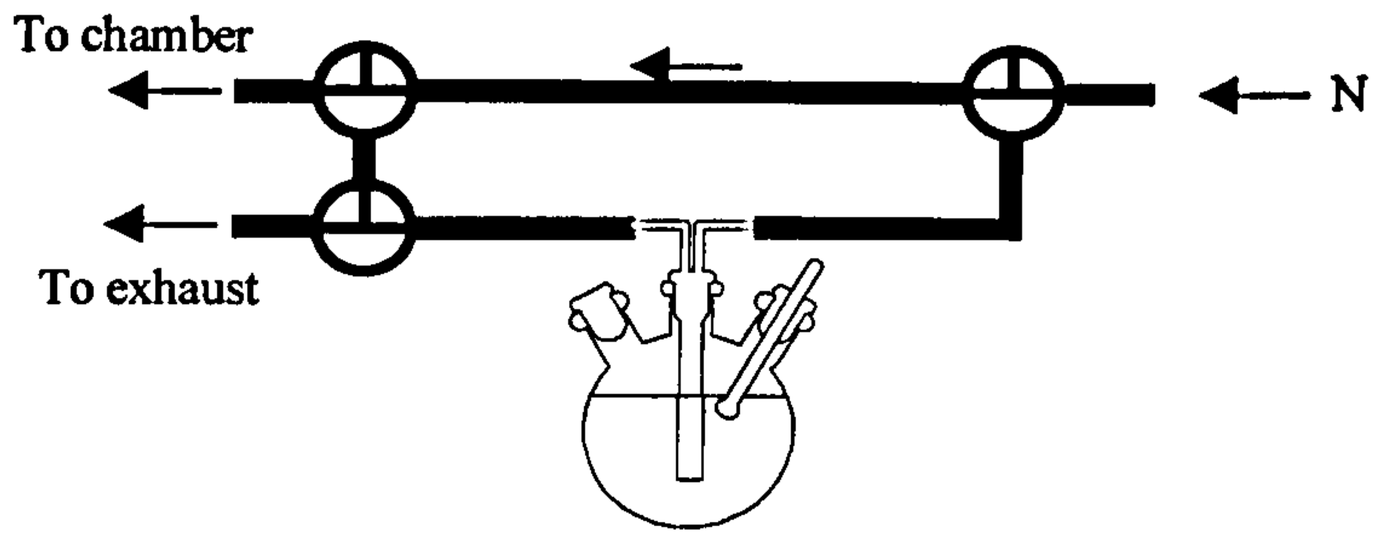

B.1.9 Formation of the Contact window

On the waveguide, a contact window must be made through the insulation layer (also served as the oxidation mask) to allow the metal contact layer to inject current into the diode.

1. Spin resist procedure.
2. Pre-bake resist procedure.
3. Expose outer periphery with 'exposedge2' mask pattern for approx. 40 seconds. *The new periphery exposure mask is needed to include the removal of the build-up at the step etched as a consequence of the 'exposedge' mask used in step 5 of the ridge formation.*
4. Remove mask from the mask aligner and turn sample face down on a piece of rubylith. Expose reverse surface for approx. 50 seconds.
5. Develop resist procedure.
6. Place in oven at 90°C for 3 minutes.
7. Align appropriately sized windows to waveguide centre using Karl Suss mask aligner. Bring the mask into contact and expose for normal exposure S1818 time. *This requires a mask with window widths approximately equal to waveguide width minus 4-6μm.*
8. Develop resist procedure.
9. Post-bake at 120°C for 30 minutes.
10. Dry etch silica in C_2F_6 for 14 minutes. *This is much longer than the standard dry etch time for 200nm SiO_2, but the silica between in close proximity to the native oxide stripes had been found to be much more resistant to dry (and wet) etching than usual.*

The remaining procedure is virtually identical to that for mesa-etched or rib-mesa QC lasers. Follow the procedure detailed in Sections B.1.2 to B.1.6 , omitting only step 1. of B.1.2